Dynamical Tuning of a Signal Recycled Gravitational Wave Detector

–

Dynamical Effects and Sensitivity Gain of Dynamical Tuning during Detection of a Chirp Signal from Compact Binary Coalescences

Dmitry Simakov

geboren am 15. November 1986 in Brezhnev, UdSSR

2014

Abstract

This thesis is the study of a particular method of detection of gravitational wave chirp signals from coalescing compact binary stars – the so-called dynamical tuning, i.e. amplification of the signal via tracking of its instantaneous frequency by the tuning of the signal-recycled detector. A quasi-stationary approximation presented here describes the sensitivity of dynamical tuning with respect to the full noise budget. However fast movement of the signal recycling mirror, required at the last stages of chirp, having high rate of frequency change, causes a non-stationary detection regime. Time-domain consideration describes the signal and noise evolution in the non-stationary detector, neglecting radiation pressure noise. The time-domain analysis of a dynamically tuned detection is presented for GEO 600, a Michelson-based gravitational wave detector with folded arms, which are modeled by simple straight arms. We prove that the shot noise, injected from the dark port and optical losses, remains white. The analysis of the transient effects shows that during the perfect tracking of the chirp frequency only transients from amplitude changes arise. The signal-to-noise-ratio gain, calculated in this thesis, is ~ 17 for a shot-noise limited detector and ~ 7 for a detector with displacement noise. With further development model may also describe non-stationary dynamical tuning in the other operating gravitational wave detectors, such as LIGO, Virgo, as well as the planning Einstein Telescope and KAGRA, that have the additional Fabry-Perot cavity in arms.

Keywords: gravitational waves, chirp signals, signal recycling, GEO 600, dynamical tuning

Kurzzusammenfassung

Diese Dissertation untersucht eine besondere Methode der Detektion von Gravitations-
wellen-Chirpsignalen von verschmelzenden kompakten Doppelsternsystemen – das so-
gennante dynamische Tuning, d.h. die Verstärkung des Signals indem ein Interfero-
meter mit Signal-Recycling auf die instantane Frequenz des Signals abgestimmt wird.
Eine quasi stationäre Annäherung kann benutzt werden um den Empfindlichkeits-
gewinn durch das dynamische Tuning zu berechnen. Aber die hohe Änderungsrate
der Abstimmungsfrequenz in der letzten Phase des Chirpsignals bedingt eine schnel-
le Bewegung des Signal-Recycling-Spiegels, welche eine nicht stationäre Betrachtung
notwendig macht. Die Betrachtung im Zeitbereich beschreibt die Entwicklung von Si-
gnal und Rauschen in einem nicht stationärem Detektor, dabei wird das Strahlungs-
druckrauschen vernachlässigt. Die Analyse einer Detektion von Gravitationswellen
mit dynamischem Tuning im Zeitbereich wird für GEO 600 entwickelt. GEO 600 ist
ein interferometrischer Gravitationswellendetektor, basierend auf einem Michelson-
Interferometer mit gefalteten Armen, welche in dieser Arbeit als einfache ungefal-
tete Arme modelliert werden. Es wird bewiesen, dass das Photonenschrotrauschen
vom Darkport und von den optischen Verlusten weiss bleibt. Die Analyse transienter
Effekte zeigt, dass während der dynamischen Signalverfolgung des Chirpsignals nur
Transienten vom Änderungen der Amplitude auftreten. Die Verstärkung im Signal-
zu-Rauschverhältnis ist ~ 17 für einen schrotrauschbegrenzten Detektor, und ~ 7
für einen Detektor mit thermischem Rauschen. Ein weiterentwickeltes Modell könnte
auch nichtstationäres dynamisches Tuning in anderen Gravitationswellendetektoren
mit Fabry-Perot Resonatoren in den Armen beschreiben, z.B. für LIGO, Virgo, das
geplante Einstein Telescope und KAGRA.

Schlüsselwörter: Gravitationswellen, Chirpsignale, Signal-Recycling, GEO 600, dy-
namisches Tuning

Acknowledgements

$\mathcal{S}$ INCE this work summarizes my scientific experience up to this moment, I would like to thank all the people who have contributed into my development as a scientist.

First of all I would like to thank the Braginsky group of quantum and precision measurements in the physical faculty of the Moscow State University, and personally Farid Khalili and Stefan Danilishin, for my undergraduate studies. Thank to your professionalism, kindness and sense of humor I have absorbed deep interest and respect to the gravitational wave science, and have obtained a solid scientific grounds, which allowed me to pass through the difficulties of this PhD work.

I want to thank Harald Lück and Karsten Danzmann for inviting me to Albert Einstein Institute, and for giving me the great opportunity for this outstanding experience, to make the real gravitational wave science in touch with the front-end detectors and experiments.

I would like to extend my appreciation to the people who have helped me with the scientific part of this work: to Harald Lück for supervising my job, to Sergey Tarabrin for endless hours of fruitful discussions, explaining fine points in physics of GW detectors, to Farid Khalili for giving the professional overview of my work from scientific point of view, to Denis Vasilyev for giving a glance to my work from the non-related to GW society point of view, to Valentin Averchenko for the discussion of the mathematical issues, to Parameswaran Ajith and especially Frank Ohme for explaining the behavior of compact binaries, to Andrzej Krolak for discussion of the dynamical tuning idea.

A special thank to GEO 600 group of AEI and to the quantum optomechanical group of Klemens Hammerer, who surrounded me during my work in AEI and were good friends, for the warm company, for support and for consistent spare time.

I would like to mention Farid Khalili, Holger Wittel and Sergey Tarabrin for proof reading this text and for giving important remarks concerning my work.

A big thank you to Evgenia Granova for the carefully made thesis template she shared with me. It is full of nice-looking and impressively convenient details.

I feel also grateful to my parents for their moral support during my whole PhD work. It was especially valuable in the difficult period time I had to face at some

point.

Finally I would like to express my gratefulness to the whole AEI crew, and personally to Karsten Danzmann and Melanie Hase for creating and supporting of the great working environment, and for a humane attitude towards the students and employees. It's hard to imagine, how much efforts does it require to make it work like this. I do appreciate it.

Contents

List of Figures

List of Tables

Gravitational wave observations

G RAVITATIONAL WAVES (GWs) are quadrupole curvatures of space-time, propagating with the speed of light. They were predicted first by Albert Einstein in 1916 [1] as a solution of his general relativity equations. A more thorough mathematical explanation of this solution is derived in [2–4]. There are various sources of gravitational waves predicted among the most highly-energetic known astrophysical phenomena, with fast quadrupole motion of compact large masses. The most convenient and well-known sources are supernovas, coalescences of binary systems, and rotations of pulsars [2, 3, 5–7]. There are also predictions for stochastic background GW radiation [8, 9], for the detection of which the correlated data from several detectors is required [10]. Among the more exotic sources of GWs we can mention the relic background radiation with frequencies up to 10^{10} Hz [11, 12], predicted by the string theory cosmological model [13]. Some astrophysical models predict also GWs at optical spectrum, e.g. caused by relic black holes evaporation [14].

Compact binary stars, such as neutron stars or black holes, emit a special kind of gravitational waves, usually referred to as a chirp signal, as they inspiral towards each other and then coalesce. The chirp signal gives us unique information about matter and space-time non-linear dynamics, as the GWs are emitted from regions with strong space-time curvature. The efforts in improving the sensitivity of the second generation GW detectors increase the expected observable event rate up to $1000 \ \mathrm{yr}^{-1}$ [15, 16]. Compact binary coalescence (CBC) and corresponding GW signal are conventionally split into three stages: inspiral, merger and ring down. The Post-Newtonian approximation of General relativity (GR) [17–20] allows prediction of the larger part of the inspiral stage. At this stage the signal has a sinusoidal shape with frequency and amplitude increasing in time. The latter stages of inspiral, and both merger and ring down stages are modeled by Numerical Relativity, and then all stages

are continuously sewed together.

Once a signal is measured and compared to the templates, one can extract the information about masses and spins of the inspiraling binary objects, as well as the equation of state of dense nuclear matter in case of the merging neutron stars [21, 22]. Therefore sensitive detection of the chirp signal might verify of falsify GR or alternative theories of gravity via comparing their predictions with the measured parameters. Schutz in [23] also proposed that the Hubble constant can be independently determined in a new and potentially accurate way by observation of the inspiral stage of the chirp GWs.

The first experiments to detect gravitational waves took place in 1967 by Joseph Weber from Maryland University [24]. The antenna in his experiments was a large aluminum cylinder, 2 meter long and 1 meter in diameter, suspended on steel wires. The resonant frequency of the antenna was 1660 Hz, and the sensitivity of piezo-based probes was of the order of 10^{-16} m. A gravitational wave, passing the detector, could excite the resonant oscillations in it with an amplitude large enough to detect. To exclude the influence of local noise, two detectors of this kind were installed with 2 km distance from each other. In his paper Weber has reported about a number of simultaneous signals with very small probability that they are accidental. Webber stated that the origin for some of these events could be gravitational waves.

Later the experiments of Weber were repeated, but with negative results: there were no signals detected. After the recent analysis of the overall data it was concluded, that the events, which Webber has taken as gravitational waves, were data processing artifacts [25]. The intensity and the rate of Weber's signals required the vicinity of the Sun to be full of events of supernova scale. Nevertheless, thanks to Weber, the attention of the scientists was attracted to the gravitational wave detection task.

The first convincing prove of the GW existence was published in 1981 in [26]. Taylor and Weisberg showed that the binary pulsar PSR 1913+16, discovered previously by Hulse and Taylor [27], loses energy in agreement with gravitational wave emission rate. However, the direct observation of a gravitational wave is yet to come.

The currently operating gravitational wave detectors can be divided into interferometric and bar resonant ones. There are only two resonant bar detectors left, MiniGRAIL and Auriga [28, 29], both operating at cryogenic temperature. Weber's detector had also a bar resonant configuration.

Ground-based laser interferometers, such as LIGO, GEO 600 and Virgo make the most sensitive detectors of GWs [30–35]. GEO 600 is keeping the science run nowadays, in the period 2011 - 2015, while LIGO and Virgo are switched off and are being upgraded to their advanced configurations. There are also two missions for gravitational wave laser interferometers planned for the future: the Eintstein telescope [36, 37], 10-km scale underground cryogenic detector and the 10 million kilometer scale space mission eLIGO/NGO recently confirmed by European Space agency [38, 39].

GEO 600

GEO 600 is a joint British/German gravitational wave detector [34] located near Hanover. Its main aims are currently the gravitational wave detection and test of the techniques of advanced detectors. Initially GEO 600 was planned as a 3 km underground detector in the Harz mountains [40]. Due to the financial reasons, the approved configuration of GEO 600, differing significantly from the initial proposal, was begun to be constructed on September 1995 in its current place with only 600 m long arms. The first stable operation mode of the detector took place in December 2001, also with a short coincidence run with the LIGO detectors [41]. From August 2002 until October 2010 GEO 600 joined 6 joint scientific data run with LIGO.

The GWs upon reaching the Earth become only tiny perturbations of space-time metric causing a small variation of the proper distances between the quasi-free-falling test masses of laser interferometer. According to this reason GEO 600, as well as all the mentioned above operating and planned GW detectors, are based on the traditional Michelson topology. The simplest layout of Michelson-based detector (see figure 0.1) is the following: the interferometer consists of a balanced 50/50 beamsplitter, perfectly reflecting end-mirrors and additional mirrors for signal and power amplification, referred to as a signal recycling mirror (SRM) and a power recycling mirror (PRM) respectively. GEO 600 uses a laser source with a master/slave Nd:YAG laser with wavelength of 1064 nm [42]. Interferometers usually operate near the dark fringe in the output port, meaning that the laser beams reflected from the end-mirrors destructively interfere on the beamsplitter. Since the Michelson topology is only susceptible to the '+'-polarized GWs, the latter cause antisymmetric (differential) motion of the interferometer's end-mirrors relative to the beamsplitter. This breaks the destructive interference on the beam splitter allowing a tiny part of the optical field carrying the information about the GW signal to reach the photodetector. This signal field gets recirculated by the SRM, forming the differential mode of the interferometer in the effective signal recycling cavity (SRC). The PRM in the laser port creates the common mode of the interferometer in the power recycling cavity (PRC) by recirculating mean laser power reflected from the end-mirrors performing symmetric (common) motion. Therefore the common mode does not contain any information about the GW signal and in the rest of this paper we only consider the differential mode. This dual recycling technique was first proposed and tested by [43, 44]. In addition to this layout most of the existing detectors, such as Virgo, LIGO and ET, have Fabry-Perot cavities instead of the end-mirrors of Michelson. GEO 600 has folded arms with an overall optical length of 1200 m.

The signals on the photodiode are detected using special techniques. Recently the output readout was changed from one of such techniques, called RF or heterodyne readout [45], to the a self-homodyne, DC readout [34, 46–50]. The reason for this change to another way of detection was in an additional vacuum noise from twice the modulation frequency, as it described in [3].

Parameters of the SRC are determined by the properties of the SRM: the frequency bandwidth of the cavity is defined by the SRM transmittance, while the detuning of laser carrier frequency from cavity resonance is defined by the microscopic position of
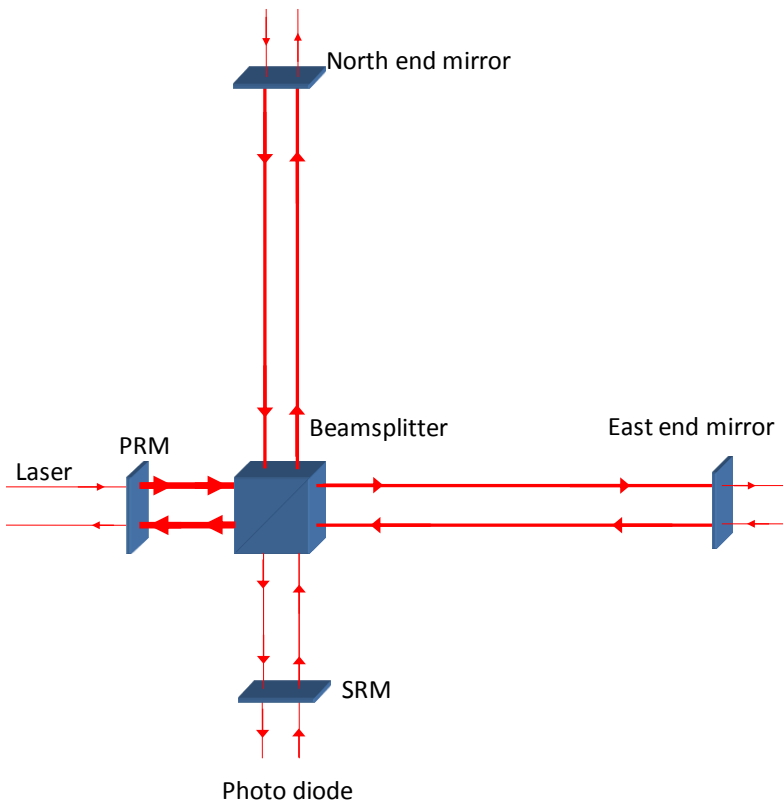
Figure 0.1.: Scheme of the simplified GEO 600 layout considered in this thesis

the SRM. In this sense the SRC is equivalent to a simple Fabry-Perot cavity. The SRC can be tuned to any desired signal frequency via proper choice of the cavity detuning. Currently all GW detectors operate stationary in time, meaning that the parameters of the SRC are fixed. There are two typical regimes of detection of chirp signals in this case: a wide-band operation and a narrow-band operation. In the former regime the detector is sensitive to the entire frequency band of the chirp signal, but at moderate sensitivity. Contrary, in the narrow-band regime the detector is much more sensitive, but only in the narrow band around the signal frequency the SRC is tuned to. Since the chirp signal at the inspiral stage is a sine function with frequency increasing in time, the peak sensitivity of the narrow-band-operated detector will only be achieved during the short interval of time, when the particular instantaneous frequency of the chirp approximately coincides with the detuning of the SRC. The study of the optimization of the detection of the chirp signals by a stationary detector is presented in [51].

Dynamical tuning

Another option for the detection of a chirp signal was proposed by Krolak and Meers in [52]: real-time tuning of the SRC to the instantaneous frequency of a signal via positioning of the SRM, i.e. real-time signal tracking. This method of detection is referred to as dynamical tuning. However the analysis in [52] was performed under the following approximations: (i) a shot-noise limited detector, and (ii) slow enough motion of the SRM such that the detector can be considered as a quasi-stationary one, i.e. all the optical fields evolve adiabatically on the time-scale of the motion of the SRM. The latter approximation also sets the limiting instant of time until which the signal can be observed before entering the regime of rapid frequency increase, where quasi-stationary approximation doesn't hold. To agree with these approximations, the authors considered the detection only of the part of the chirp signal with the instantaneous frequency varying from 100 up to 500 Hz.

Overview of this thesis

The method we develop in this thesis allows us treating the problem of dynamical tuning outside the approximations, described above. It should be noted that we do not consider the problem of signal prediction; we only assume that the initial time evolution of the signal is known, for instance, from the low-frequency data of other GW detectors, such that subsequent evolution of the signal can predicted. The other idea to wait for the certain frequency, and then predict the further frequency behavior on the fly, as it is proposed in [52] and developed in [53]. During this work we develop the model of GW detectors from the basics, first repeating the already known steps, then coming to the new results.

Stationary GW detectors in frequency domain

The response of a stationary operated detector to GWs and to all kinds of noise sources is usually calculated in frequency domain. In this part we mostly repeat the analysis, performed by [47], and calculate the sensitivities for a Fabry-Perot cavity and for GEO 600 layout. This considerations allows to formulate a quasi-stationary approximation for dynamical tuning. For the detailed analysis see references [33, 54–58].

In the first chapter we consider the field propagation inside the simplest layout of gravitational wave detectors, a Fabry-Perot cavity. According to the scaling law [59], a dual recycled Michelson interferometer with straight arms or Fabry-Perot cavity in the arms, may also be effectively reduced to a single Fabry-Perot cavity. Originally Fabry-Perot cavities were invented and have been successfully used as instruments to resolve close spectral lines of incoherent light, e.g. during the optical astronomical observations [60–63]. In the era of lasers the ability of Fabry-Perot cavities to store a coherent light made them an integral part of almost every laser [64, 65]. The same property made them useful for gravitational wave detections [66]. To detect gravitational waves, a Fabry-Perot cavity should be very long and should have movable mirrors. The description of fields in it is based on the reflection from the moving mirrors, introducing a negligible frequency dependence due to relativistic effects. The reflections together with wave properties of light define the resonance conditions, described by Airy function. The small jitters of the mirrors, caused by the gravitational waves, introduce very small but measurable field deviations inside and outside the cavity, allowing to extract the information about GWs: theoretically with homodyne detection, and experimentally with Pound-Driver-Hall method [67]. Apart from the GW influence, there are also the fluctuations of the measured fields, caused by Brownian motion of the optical surfaces, and by quantum fluctuations of electromagnetic field. Radiation pressure introduces the additional noisy displacement, caused by the injected quantum noise, and the optical spring effect, forming the second (after optical) resonance of the cavity. Both signal and noise deviations from stationary regime are very small, and this allows to effectively separate fields inside the detector into the zeroth and the first order terms, and neglect the higher order terms. The response of a Fabry-Perot cavity to these fluctuations defines the sensitivity to a signal, making a well-known result typical for all laser GW-detectors.

The second chapter studies the more complex layout of a dual-recycled Michelson-based interferometer. The fields inside the Michelson configuration [68] are explicitly divided into a common and a differential mode. The scaling law [59], defining the opto-mechanical equivalence between the signal recycling mode of the detector and a single Fabry-Perot cavity, is presented in details for their fields, forces and sensitivities. There was also shown the boundary between the common and the differential modes, caused by the dark-fringe offset, required for DC readout [69]. This boundary however is negligible. Based on the standard stationary sensitivity for GEO 600 the quasi-stationary model for dynamical tuning may be developed. The shot-noise quasi-stationary dynamical tuning was considered by [52]. In this work we add the new influence of displacement noises and radiation pressure effects into this approximation.

Non-stationary GW detectors in time-domain

The frequency of the part of a chirp GW changes very fast. It kicks the detector performing dynamical tuning out of the stationary regime, so frequency domain analysis becomes not adequate. Therefore, we want to make a new model of the non-stationary detector in time-domain. The consideration used in this part is based on the difference equation, introduced by Malik Rakhmanov in his thesis [70].

The shot noise in gravitational wave detectors is described as an injection from the dark port and from the lossy elements [71]. In the third chapter we develop a time-domain non-stationary model for the response of the detector to shot noise, transforming the difference equations into an infinite sum, and neglecting radiation pressure effects. The detector response takes the form of a series over an infinite number of round trips of the light inside the SRC [70, 72], the so-called impulse response. This model allows to study and simulate the autocorrelation function of the output shot noise in case of both ground state and squeezed state dark-port injections.

It is also possible to simulate similarly the non-stationary response of the detector to the end-mirror motion caused by GWs, as it is presented in chapter 4. It is also described by an impulse response of a similar appearance. Several configurations of the Michelson based interferometer were studied: the one with straight arms, the one with delayed lines and the one with Fabry-Perot cavity in the arms. For the first two tasks, the explicit impulse responses were found, for the latter the corresponding non-trivial difference equation was posed. The impulse responses allow to study the response of the detector on the step-wise change of signal parameters as well as of the SRM position. Similar to dynamic resonance to the phase fluctuation of the inner cavity field, introduced in [70], we present a dynamical resonance to a chirp frequency, when the GW phase change during one round-trip is compensated by the SRM detuning. We define and study a so-called resonant tracking, when the detector keeps dynamically resonance during the whole chirp signal detection. We established that detection during perfect resonant tracking of a chirp signal with negligible rate of amplitude displays a so-called virtual stationarity, when the field oscillations inside the detector possess the corresponding stationary value. Since the displacement noise, caused by seismic, gravity gradient and Brownian influences on the mirror surface, is also an end-mirror motion, and its differential component influences the output, it is possible to simulate the component of the thermal noise in the output photocurrent, using the response to the end-mirror motion. We also find the inverse impulse response that could restore the GW signal from the output current.

In chapter 5 we study the behavior of the non-stationary detector with a DC read-out. The "DC" component obtains a complex non-stationary shape after evolution inside the detector. We developed the formula for the photocurrent components, caused by this zero-order field component, and its beating with the signal first-order signal component. The transient effects of this configuration, and the shot noise were also studied.

Simulations of signal detection

In chapter 6 we repeat the Neyman-Pearson criteria for detection of the signals with known shape on the Gaussian noise background. We specify the SNR, defined in the criteria, for a shot noise and a thermal noise limited detection. The more difficult task of calculating the SNR on the background of both noises was formulated explicitly.

The final seventh chapter is dedicated to the simulation. We present the algorithm, allowing to simulate numerically the output current for the configurations, considered in this thesis. And we use the signals, simulated for the Michelson configuration, for the estimations of SNR gain of the dynamically tuned interferometer, assuming the limitation of sensitivity by the thermal and by the shot noise separately, with respect to the currently existing GEO 600 configuration. We also compare the time-domain non-stationary result with the frequency-domain quasi-stationary one to estimate the influence of transient dynamical effects.

Part I.

Stationary GW detectors in frequency domain

1.1. Reflecting from moving mirror. Linear correction due to special relativity

L ET us consider the scheme consisting of two beams: one propagating to the left, and one propagating to the right, both interacting with a mirror (see FIG. 1.1). We assume one polarization of the light, and direct the x-axes parallel to the beam, propagating to the left. The z-axes is chosen parallel to the electrical field oscillations of the field, then the z-component of the field is

$$
\hat{E}_a(t) = \sqrt{\frac{2\pi\hbar\omega_{\mathrm{p}}}{\mathcal{A}c}}(A(t)e^{-i\omega_{\mathrm{p}}t} + A^*(t)e^{i\omega_{\mathrm{p}}t})+
$$

$$
+ \int\limits_0^\infty \sqrt{\frac{2\pi\hbar\omega}{\mathcal{A}c}}[\hat{\mathsf{a}}(\omega)e^{-i\omega t} + \hat{\mathsf{a}}^\dagger(\omega)e^{i\omega t}]\frac{d\omega}{2\pi} \quad (1.1)
$$

with the notations presented in table 1.1. Since electrical field E, magnetic field H and wave vector field k always form the right-hand set of vectors, we direct y-axes along the corresponding magnetic field vector. In this thesis, all the waves, propagating to the left turn to those propagating to the right and vice versa by reflecting, therefore their electric fields will be oppositely directed. Any other polarization of light may be considered similarly, therefore the consideration described here is general.

The fields throughout this work are divided in two clearly distinctive parts. The first part is a classic carrier light in the zeroth order approximation. It is sourced by a very stationary laser, in this case $A(t) = A$, $C(t) = C$. It can be considered

Table 1.1.: Notations and definitions used in field expressions in this thesis

Notation	Definition
ω_{p}	the frequency of the carrier laser
c	the speed of light
$\mathcal{A}$	the cross-section of the beam
A, B, C, D	laser field amplitude (see FIG. 1.1)
$\hat{\mathrm{a}}(t), \hat{\mathrm{b}}(t), \hat{\mathrm{c}}(t), \hat{\mathrm{d}}(t)$	the small field perturbations, including quantum noise

stationary, because all the noisy processes and perturbations, introduced by mirrors motion, are very small and can be neglected in comparison to the amplitude of the carrier light. The fields of the zeroth approximation are denoted with big letters: A, B, C and D, corresponding to the location (see FIG. 1.1). All the perturbations, caused mainly by (i) the injected ground state quantum fluctuations: $\hat{\mathrm{a}}(\Omega)$ and $\hat{\mathrm{c}}(\Omega)$ in this case, and (ii) the microscopic mirror motion: for this mirror $X_{\mathrm{m}}(\Omega)$, are very small and assumed to be of the same order. We denote them with small latin letters, indicating the point of consideration, and with hats, meaning some part of it has quantum nature.

The electrical field of the two electromagnetic waves, depicted in FIG. 1.1 and propagating to the left, is described by $E(t, x) = E(t - x/c)$, while the field of the waves propagating to the right is by $E(t, x) = E(t + x/c)$. These beams are spatially separated by the mirror, depicted as the blue plane: each descended beam ends on the mirror and is partly reflected and partly transmitted into the outcome beams, starting on the mirror. The descending and the reflected beams are depicted separately for convenience, though spatially they coincide. The point of reflection is moving with the mirror, but for convenience of the model we use the initial position of the mirror with the coordinate x_{m}, depicted as the dashed shape, as a reference to connect all the four described beams. Strictly speaking, at least two beams do not exist at this point, but we can extrapolate them, forming a virtual link between the left and the right beams. The z-components of electric fields in the referent point at arbitrary instance t are:

$$\hat{E}_{\mathrm{a}}(t, -x_{\mathrm{m}}) = \hat{E}_{\mathrm{a}}(t + x_{\mathrm{m}}/c), \tag{1.2a}$$

$$\hat{E}_{\mathrm{b}}(t, -x_{\mathrm{m}}) = \hat{E}_{\mathrm{b}}(t - x_{\mathrm{m}}/c), \tag{1.2b}$$

$$\hat{E}_{\mathrm{c}}(t, -x_{\mathrm{m}}) = \hat{E}_{\mathrm{c}}(t - x_{\mathrm{m}}/c), \tag{1.2c}$$

$$\hat{E}_{\mathrm{d}}(t, -x_{\mathrm{m}}) = \hat{E}_{\mathrm{d}}(t + x_{\mathrm{m}}/c). \tag{1.2d}$$

The y-components of the magnetic fields, defined by the directions and values of
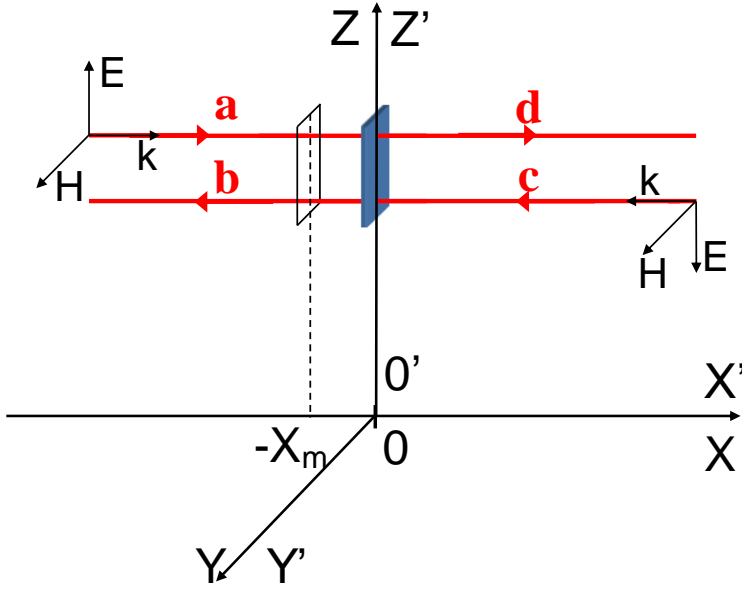
Figure 1.1.: Laser reflecting from a moving mirror

the corresponding wave vectors and electric fields, are

$$\hat{H}_{\mathrm{a}}(t, -x_{\mathrm{m}}) = \hat{E}_{\mathrm{a}}(t + x_{\mathrm{m}}/c), \tag{1.3a}$$

$$\hat{H}_{\mathrm{b}}(t, -x_{\mathrm{m}}) = -\hat{E}_{\mathrm{b}}(t - x_{\mathrm{m}}/c), \tag{1.3b}$$

$$\hat{H}_{\mathrm{c}}(t, -x_{\mathrm{m}}) = -\hat{E}_{\mathrm{c}}(t - x_{\mathrm{m}}/c), \tag{1.3c}$$

$$\hat{H}_{\mathrm{d}}(t, -x_{\mathrm{m}}) = \hat{E}_{\mathrm{d}}(t + x_{\mathrm{m}}/c). \tag{1.3d}$$

In the special relativity it is convenient to consider the reflection from the mirror in the instantaneously comoving inertial frame, where at some local instance the mirror is resting and the reflection is described classically. We introduce the laboratory and the comoving frames as it shown in FIG. 1.1, with the beginning of coordinates at the actual mirror position. Coordinates, time and properties of waves, corresponding to the laboratory frame, are denoted without primes: $x, y, z, t, \vec{E}, \vec{H}, \vec{k}, \omega$, while the corresponding values in the comoving frame are denoted with primes: $x', y', z', t', \vec{E}', \vec{H}', \vec{k}', \omega'$. The Lorentz transformations from the laboratory to the

moving frame:

$$x' = -\beta\gamma ct_0 + \gamma x - \beta\gamma ct, \tag{1.4a}$$

$$t' = t_0 + \gamma t - \beta\gamma\frac{x}{c}, \tag{1.4b}$$

$$E'_{\text{a,d}}(x',t') = (\gamma + \beta\gamma)E_{\text{a,d}}(x,t), \tag{1.4c}$$

$$E'_{\text{b,c}}(x',t') = (\gamma - \beta\gamma)E_{\text{b,c}}(x,t), \tag{1.4d}$$

$$\omega' = (\gamma - \beta\gamma)\omega, \tag{1.4e}$$

where $\beta = \frac{v}{c}$, $\gamma = \frac{1}{\sqrt{1-\frac{v^2}{c^2}}}$ and the term $-\beta\gamma ct_0$ is chosen to set the point of reflection event at $x' = 0$.

The events of the waves in the instance t_0 in laboratory frame occur in different instances of time in the comoving frame, so the reflection will happen at

$$x'_1 = 0, \tag{1.5a}$$

$$t'_1 = \gamma t_1, \tag{1.5b}$$

when the mirror rests. The reference point with coordinates $(-x_{\text{m}}, t_0)$ transforms into

$$x'_2 = -\gamma\beta ct_0 + \gamma(-x_{\text{m}}) - \beta\gamma ct_0, \tag{1.6a}$$

$$t'_2 = \gamma t_1 - \beta\gamma\frac{-x_{\text{m}}}{c}. \tag{1.6b}$$

The fields at the referent points and at the reflection are:

$$E'_{\text{a,d}}(x_2, t_2) = (\gamma + \beta\gamma)E_{\text{a,d}}(-x_{\text{m}}, t_1), \tag{1.7a}$$

$$E'_{\text{a,d}}(x'_1, t'_1) = (\gamma + \beta\gamma)E_{\text{a,d}}(0, t_1), \tag{1.7b}$$

$$E'_{\text{b,c}}(x_2, t_2) = (\gamma - \beta\gamma)E_{\text{b,c}}(-x_{\text{m}}, t_1), \tag{1.7c}$$

$$E'_{\text{b,c}}(x'_1, t'_1) = (\gamma - \beta\gamma)E_{\text{b,c}}(0, t_1). \tag{1.7d}$$

The fields at the reflection event, calculated from the fields at the referent points in the comoving frame using the Lorentz transformation (1.4),(1.6-1.7), and keeping only the terms of the first order of smallness: (i) with respect to $\frac{v}{c}$ in the Lorentz transformations, (ii) with respect to $k_{\text{p}}x_{\text{m}}(t)$ in the phase shift, and (iii) with respect to $\hat{a}$, $\hat{b}$, $\hat{c}$ and $\hat{d}$ in the field amplitude, read:

$$\hat{E}'_{\text{a}}(t'_0, 0) = \sqrt{\frac{2\pi\hbar\omega_{\text{p}}}{Ac}}Ae^{-i\omega_{\text{p}}t_0} - \sqrt{\frac{2\pi\hbar\omega_{\text{p}}}{Ac}}\left(\frac{-\dot{x}_{\text{m}}(t_0)}{c} + ik_{\text{p}}x_{\text{m}}\right)Ae^{-i\omega_{\text{p}}t_0} +$$

$$+ \int_0^\infty \sqrt{\frac{2\pi\hbar\omega}{Ac}}[\hat{a}(\omega)e^{-i\omega t_0}]\frac{d\omega}{2\pi} + h.c. \tag{1.8a}$$

$$\hat{E}'_{\mathrm{b}}(t'_0, 0) = \sqrt{\frac{2\pi\hbar\omega_{\mathrm{p}}}{\mathcal{A}c}} B e^{-i\omega_{\mathrm{p}}t_0} - \sqrt{\frac{2\pi\hbar\omega_{\mathrm{p}}}{\mathcal{A}c}} \left(\frac{\dot{x}_{\mathrm{m}}(t_0)}{c} - ik_{\mathrm{p}}x_{\mathrm{m}}(t_0) \right) B e^{-i\omega_{\mathrm{p}}t_0} +$$

$$+ \int_0^\infty \sqrt{\frac{2\pi\hbar\omega}{\mathcal{A}c}} [\hat{\mathrm{b}}(\omega)e^{-i\omega t_0}] \frac{d\omega}{2\pi} + h.c. \quad (1.8b)$$

$$\hat{E}'_{\mathrm{c}}(t'_0, 0) = \sqrt{\frac{2\pi\hbar\omega_{\mathrm{p}}}{\mathcal{A}c}} C e^{-i\omega_{\mathrm{p}}t_0} - \sqrt{\frac{2\pi\hbar\omega_{\mathrm{p}}}{\mathcal{A}c}} \left(\frac{\dot{x}_{\mathrm{m}}(t_0)}{c} - ik_{\mathrm{p}}x_{\mathrm{m}}(t_0) \right) C e^{-i\omega_{\mathrm{p}}t_0} +$$

$$+ \int_0^\infty \sqrt{\frac{2\pi\hbar\omega}{\mathcal{A}c}} [\hat{\mathrm{c}}(\omega)e^{-i\omega t_0}] \frac{d\omega}{2\pi} + h.c. \quad (1.8c)$$

$$\hat{E}'_{\mathrm{d}}(t'_0, 0) = \sqrt{\frac{2\pi\hbar\omega_{\mathrm{p}}}{\mathcal{A}c}} D e^{-i\omega_{\mathrm{p}}t_0} - \sqrt{\frac{2\pi\hbar\omega_{\mathrm{p}}}{\mathcal{A}c}} \left(\frac{-\dot{x}_{\mathrm{m}}(t_0)}{c} + ik_{\mathrm{p}}x_{\mathrm{m}}(t_0) \right) D e^{-i\omega_{\mathrm{p}}t_0} +$$

$$+ \int_0^\infty \sqrt{\frac{2\pi\hbar\omega}{\mathcal{A}c}} [\hat{\mathrm{d}}(\omega)e^{-i\omega t_0}] \frac{d\omega}{2\pi} + h.c. \quad (1.8d)$$

The boundary conditions on the resting in the comoving frame mirror is:

$$\hat{E}'_{\mathrm{b}}(t'_0, 0) = -R_{\mathrm{m}}\hat{E}'_{\mathrm{a}}(t'_0, 0) + iT_m\hat{E}'_{\mathrm{c}}(t'_0, 0), \qquad (1.9a)$$

$$\hat{E}'_{\mathrm{d}}(t'_0, 0) = -R_{\mathrm{m}}\hat{E}'_{\mathrm{c}}(t'_0, 0) + iT_{\mathrm{m}}\hat{E}'_{\mathrm{a}}(t'_0, 0), \qquad (1.9b)$$

where T_{m} and R_{m} are the amplitude transmittance and the reflectivity of the mirror, bound through the energy conservation equation $T_{\mathrm{m}}^2 + R_{\mathrm{m}}^2 = 1$. The losses here are neglected.

This equations give in the zeroth approximation:

$$B = -R_{\mathrm{m}}A + iT_{\mathrm{m}}C, \qquad (1.10a)$$

$$D = -R_{\mathrm{m}}C + iT_{\mathrm{m}}A. \qquad (1.10b)$$

It is more convenient to consider the coordinate of the end-mirror in the Fourier domain:

$$X(\Omega) = \int_{-\infty}^\infty x_{\mathrm{m}}(t)e^{i\Omega t}dt \qquad (1.11)$$

In the terms of the spectrum, $\dot{x}_{\mathrm{m}}(t)$ differs from $x_{\mathrm{m}}(t)$ by factor of $\Omega = \omega - \omega_p$, therefore the term with $\dot{x}_{\mathrm{m}}(t)$ would transform $k_p X(\Omega)$ into $kX(\Omega)$, where $k = \frac{\omega}{c}$. The first approximations, based on this transformation, reads:

$$\hat{\mathrm{b}}(\omega) = -R_{\mathrm{m}}\hat{\mathrm{a}}(\omega) - 2iR_{\mathrm{m}}\sqrt{k_p k}X(\omega - \omega_p)A_x + iT_{\mathrm{m}}\hat{\mathrm{c}}(\omega), \qquad (1.12a)$$

$$\hat{\mathrm{d}}(\omega) = -R_{\mathrm{m}}\hat{\mathrm{c}}(\omega) + 2iR_{\mathrm{m}}\sqrt{k_p k}X(\omega - \omega_p)C_x + iT_{\mathrm{m}}\hat{\mathrm{a}}(\omega). \qquad (1.12b)$$
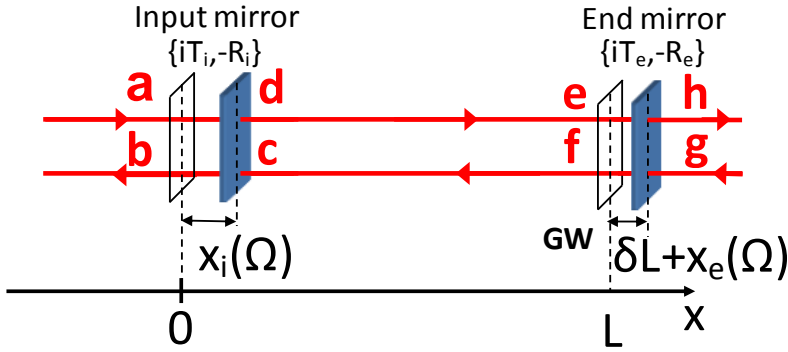
Figure 1.2.: Electromagnetic field in a Fabry-Perot cavity

$$\hat{b}^\dagger(\omega) = -R_m\hat{a}^\dagger(\omega) + 2iR_m\sqrt{k_p k}X(\omega_p - \omega)A_x^* - iT_m\hat{c}^\dagger(\omega), \tag{1.12c}$$

$$\hat{d}^\dagger(\omega) = -R_m\hat{c}^\dagger(\omega) - 2iR_m\sqrt{k_p k}X(\omega_p - \omega)C_x^* - iT_m\hat{a}^\dagger(\omega). \tag{1.12d}$$

One can see, that (1.12a),(1.12c) describes reflection to the left, and (1.12b),(1.12d) describes reflection to the right.

1.2. Fields in Fabri-Perot cavity with two moving mirrors

Two parallel mirrors form a Fabri-Perot cavity (see FIG. 1.2), the simplest topology of gravitational wave detectors. Gravitational waves cause microscopic motion of the right mirror, and these motions along with the thermal motion of both mirror, are measured by the Fabry-Perot cavity through the field perturbations, introduced by them.

Inside the cavity the fields of the zeroth approximation, denoted, as usual, with big letters, corresponding to their points, is sourced by the laser $A(t) = A$. All the perturbations, caused mainly by (i) the injected ground state quantum fluctuations: $\hat{a}(\Omega)$ and $\hat{g}(\Omega)$, and (ii) the microscopic mirror motion $X_i(\Omega)$ and $X_e(\Omega)$, are very small and both assumed to be of the first order of smallness. We denote them with small latin letters, indicating the point of consideration, and with hats, meaning some part of it has quantum nature.

Denote the boundary conditions on the mirrors for the zeroth approximation fields:

$$B = -R_i A + iT_i C, \tag{1.13a}$$

$$C = iT_i A - R_i D, \tag{1.13b}$$

$$F = -R_e E. \tag{1.13c}$$

The propagation of light inside the cavity continuously shifts its phase. There is a length of the cavity L, corresponding to exactly the whole number of the wavelengths of the carrier light during the round trip, meeting the resonant condition $e^{ik_{\mathrm{p}}2L} = 1$. We call the cavity of this length, resonant to the carrier laser or tuned. The displacement of a mirror from its tuned position δL introduces into zeroth-order mode fields the additional phase detuning $\delta_{\phi,0} = 2k_{\mathrm{p}}\delta L$ of the cavity from the resonance. Therefore:

$$E = Ce^{i\delta_{\phi,0}/2}, \tag{1.14a}$$

$$D = Fe^{i\delta_{\phi,0}/2}. \tag{1.14b}$$

The solution of these equations is the expression for the field inside the cavity dependent from the detuning:

$$C = \frac{iT_{\mathrm{i}}A}{1 - R_{\mathrm{i}}R_{\mathrm{e}}e^{i\delta_{\phi,0}}}. \tag{1.15}$$

The factor $\dfrac{1}{1 - R_{\mathrm{i}}R_{\mathrm{e}}e^{i\delta_{\phi,0}}}$, which is usually referred to as Airy function, describes the resonant features of the cavity. The maximum of this function at $\delta_{\phi,0} = 0$ corresponds to the resonance. The detuning phaseshift $\delta_{\phi,0}$ may be expressed in terms of round-frequency shift δ, referred to also as detuning, from the cavity resonance.

$$\delta_{\phi,0} = \delta 2\tau. \tag{1.16}$$

Here τ is the time of one-way trip of light inside the cavity: $\tau = L/c$.

The detuning γ, at which the field amplitude inside the detector differs from the resonant value by factor of $\sqrt{2}$, is called *half-bandwidth*, and its dependence on the optical properties of mirrors, i.e. their transmittances, may be obtained from the (1.15):

$$\gamma = \frac{T_{\mathrm{i}}^2 c}{4L} + \frac{T_{\mathrm{e}}^2 c}{4L}. \tag{1.17}$$

Here and everywhere in the chapter we use the following assumptions:

$$\delta_{\phi,0} \ll 1, \quad T_{\mathrm{i}}, T_{\mathrm{e}} \ll 1. \tag{1.18}$$

The mirrors influence on the half-bandwidth independently. So it is convenient to associate an individual bandwidth to each of them:

$$\gamma_{\mathrm{i}} = \frac{T_{\mathrm{i}}^2 c}{4L}, \tag{1.19a}$$

$$\gamma_{\mathrm{e}} = \frac{T_{\mathrm{e}}^2 c}{4L}. \tag{1.19b}$$

The physical meaning of each of the values is a bandwidth of a Fabry-Perot cavity, where the non-considered mirror is replaced by the ideally reflecting one. Easy to see that $\gamma = \gamma_{\mathrm{e}} + \gamma_{\mathrm{i}}$.

The Airy function (1.15), expressed in these values, is:

$$\frac{1}{1 - R_e R_i e^{i\delta_{\phi,1}}} = \frac{1}{(\gamma - i\delta)2\tau}. \tag{1.20}$$

The evolution of the first order terms of the field, carrying the information about mirrors motion, is calculated from (1.12a) for the reflection to the left and (1.12b) for the reflection to the right as following:

$$\hat{b}(\omega) = -R_i\hat{a}(\omega) - 2iR_i\sqrt{k_p k}X_i(\Omega)A + iT_i\hat{c}(\omega), \tag{1.21a}$$

$$\hat{d}(\omega) = -R_i\hat{c}(\omega) + 2iR_i\sqrt{k_p k}X_i(\Omega)C + iT_i\hat{a}(\omega), \tag{1.21b}$$

$$\hat{f}(\omega) = -R_i\hat{e}(\omega) - 2iR_e\sqrt{k_p k}X_e(\Omega)E + iT_e\hat{h}(\omega), \tag{1.21c}$$

$$\hat{h}(\omega) = -R_i\hat{g}(\omega) + iT_e\hat{e}(\omega). \tag{1.21d}$$

Here $\Omega = \omega - \omega_p$ is a frequency of mirror motion, causing the corresponding modulation sidebands. The field $\hat{a}(\omega)$ on the input mirror is injected oscillations of ground state mode of electromagnetic field. The end-mirrors are usually highly reflective, they have minor losses and do not transmit anything. However, due to fluctuation-dissipation theorem (FDT), the noise, corresponding to the losses on the mirror and everywhere in the cavity, is equivalent to the injected ground state mode $\hat{g}(\omega)$ through the mirror with transmittance T_e equal to losses of the end mirror. The injected fields $\hat{a}(\omega)$ and $\hat{g}(\omega)$ are objects to the following commutation relation:

$$\left[\hat{a}(\omega), \hat{a}^\dagger(\omega')\right] = 2\pi\delta(\omega - \omega') \tag{1.22}$$

The equations for the propagation of the first order approximation fields are:

$$\hat{e}(\omega) = \hat{d}(\omega)e^{i\delta_{\phi,1}/2}, \tag{1.23a}$$

$$\hat{c}(\omega) = \hat{f}(\omega)e^{i\delta_{\phi,1}/2}, \tag{1.23b}$$

where $\delta_{\phi,1} = \dfrac{2\omega\delta L}{c}$ is a phase detuning of the sideband from its resonance, and δL is a constant displacement of the cavity mirrors from the resonant position.

The solution for the fields in cavity, found from (1.21) and (1.23) is then

$$\hat{b}(\omega) = \frac{1}{1 - R_e R_i e^{i\delta_{\phi,1}}}\left[\hat{a}(\omega)(R_e e^{i\delta_{\phi,1}} - R_i) - T_i\hat{s}_e(\omega)e^{i\delta_{\phi,1}/2} + \right.$$

$$\left. + T_i R_e e^{i\delta_{\phi,1}}2R_i\sqrt{k_p k}X_i(\Omega)C\right] - 2iR_e\sqrt{k_p k}X_i(\Omega)A, \tag{1.24a}$$

$$\hat{c}(\omega) = \frac{i\hat{s}_e(\omega)e^{i\delta_{\phi,1}/2} - iR_e e^{i\delta_{\phi,1}}\hat{s}_i(\omega)}{1 - R_i R_e e^{i\delta_{\phi,1}}}, \tag{1.24b}$$

$$\hat{d}(\omega) = \frac{i\hat{s}_i(\omega) - iR_i e^{i\delta_{\phi,1}/2}\hat{s}_e(\omega)}{1 - R_i R_e e^{i\delta_{\phi,1}}}, \tag{1.24c}$$

$$\hat{e}(\omega) = \frac{i\hat{s}_i(\omega)e^{i\delta_{\phi,1}/2} - iR_i e^{i\delta_{\phi,1}}\hat{s}_e(\omega)}{1 - R_i R_e e^{i\delta_{\phi,1}}}, \tag{1.24d}$$

$$\hat{f}(\omega) = \frac{i\hat{s}_e(\omega) - iR_e e^{i\delta_{\phi,1}/2}\hat{s}_i(\omega)}{1 - R_i R_e e^{i\delta_{\phi,1}}}, \tag{1.24e}$$

where the injections of light into the cavity from the input and the end mirrors are correspondingly:

$$\hat{s}_i(\omega) = 2R_i\sqrt{k_p k}X_i(\Omega)C + T_i\hat{a}(\omega), \tag{1.25a}$$

$$\hat{s}_e(\omega) = -2R_e\sqrt{k_p k}X_e(\Omega)E + T_e\hat{g}(\omega). \tag{1.25b}$$

For the simplification of this solution we make the following assumptions and redenotations. We assume here and everywhere in the chapter that optical frequency ω_p is much larger than all other frequencies:

$$\Omega \ll \omega_p, \tag{1.26}$$

that cavity, as it was mentioned before, is short enough and mirrors are highly reflective (1.18).

We denote:

$$\ell(\Omega) = \gamma_e + \gamma_i - i(\delta + \Omega), \tag{1.27a}$$

$$X(\Omega) = X_e(\Omega) - X_i(\Omega), \tag{1.27b}$$

therefore the motion of two mirrors are equivalent to the motion of the one mirror only. We introduce the new, "rotated" annihilation and creation operators:

$$\hat{a}_{new}(\omega) = \frac{\ell^*(\Omega)}{\ell(\Omega)}\frac{\sqrt{\gamma_i}\hat{a}(\omega) - \sqrt{\gamma_e}\hat{g}(\omega)}{\sqrt{\gamma}}, \tag{1.28a}$$

$$\hat{g}_{new}(\omega) = \frac{\sqrt{\gamma_i}\hat{g}(\omega) + \sqrt{\gamma_e}\hat{a}(\omega)}{\sqrt{\gamma}}, \tag{1.28b}$$

that, as it may be easily checked, obey the same commutation relations as the original ones:

$$\left[\hat{a}_{new}(\omega)\hat{a}_{new}^\dagger(\omega')\right] = 2\pi\delta(\omega - \omega') \tag{1.29a}$$

$$\left[\hat{g}_{new}(\omega)\hat{g}_{new}^\dagger(\omega')\right] = 2\pi\delta(\omega - \omega'). \tag{1.29b}$$

Using these assumptions and notations, we get the following expression for the field disturbances, caused by the ground state injections and the mirror motions:

$$\hat{b}(\omega) = \frac{\sqrt{\gamma_i}\hat{a}(\omega) - \sqrt{\gamma_e}\hat{g}(\omega)}{\sqrt{\gamma}} + \sqrt{\frac{\gamma_i}{\tau}}\frac{2k_p EX(\Omega)}{\ell(\Omega)}, \tag{1.30a}$$

$$-\hat{c}(\omega) = \hat{d}(\omega) = \hat{e}(\omega) = -\hat{f}(\omega) = i\sqrt{\frac{\gamma}{\tau}}\frac{\hat{a}(\omega)}{\ell^*(\Omega)} + \frac{i\omega_p EX(\Omega)}{L\ell(\Omega)}. \tag{1.30b}$$

The equations for annihilation operators, may be obtained similarly from (1.12c) and (1.12d) using the same transformations, described in this section. It is easy to show that the result is a complex conjugate of (1.30), meaning the creation operator transforms to the annihilation ones, classic field components transform to their complex conjugate and the functions $X(\Omega), \ell(\Omega)$ transform correspondingly to $X(-\Omega), \ell^*(\Omega)$. So, we get:

$$\hat{b}^\dagger(\omega) = \frac{\sqrt{\gamma_i}\hat{a}^\dagger(\omega) - \sqrt{\gamma_e}\hat{g}^\dagger(\omega)}{\sqrt{\gamma}} + \sqrt{\frac{\gamma_i}{\tau}}\frac{2\omega_p E^* X(-\Omega)}{c\ell^*(\Omega)}, \tag{1.31a}$$

$$-\hat{c}^\dagger(\omega) = \hat{d}^\dagger(\omega) = \hat{e}^\dagger(\omega) = -\hat{f}^\dagger(\omega) = -i\sqrt{\frac{\gamma}{\tau}}\frac{\hat{a}^\dagger(\omega)}{\ell(\Omega)} + \frac{-i\omega_p E^* X(-\Omega)}{L\ell^*(\Omega)}. \tag{1.31b}$$

1.3. Radiation pressure force on a mirror. Ponderomotive forces

All the fields and forces in this section, and everywhere in the thesis, are considered in CGS-system (see appendix A). Let us consider a beam falling perpendicularly on the mirror. Both electric and magnetic fields are perpendicular to the wave vector and, therefore, parallel to the mirror surface. Electric field pushes the charged particles of the mirror surface parallel to the surface, and magnetic force, acting on this pushed charges, causes a force, perpendicular to the mirror surface. The single beam, falling perpendicular to the surface of the mirror, will have the following electric and magnetic field in Cartesian basis, the components of which correspond to two independent polarizations, as it shown in FIG. 1.1:

$$\vec{B}(t) = E_z \vec{e}_y - E_y \vec{e}_z, \tag{1.32a}$$

$$\vec{E}(t) = E_y \vec{e}_y + E_z \vec{e}_z. \tag{1.32b}$$

The electromagnetic wave pushes the current in the surface of the mirror:

$$\vec{j}(t) = j_x \vec{e}_x - j_y \vec{e}_y + j_z \vec{e}_z. \tag{1.33}$$

The x-component of the Lorentz force (A.7), caused by the light on the mirror, is then:

$$F_l(t) = \frac{W(t)}{c}. \tag{1.34}$$

Here we've used that (i) within the framework of CGS, the electric field in a wave equals to the magnetic field, (ii) the wave vector, the electric field and magnetic field form the right-hand set of vectors, (iii) the electric field multiplied by the charges of current gives us the force and (iv) the electric force multiplied by the velocity of charges, extracted from the current, gives the power.

The power $W(t)$ can be expressed through volume energy $w(t)$:

$$W(t) = w(t)\mathcal{A}c, \tag{1.35}$$

which can be itself expressed through electric field:

$$w(t) = \frac{|E(t)|^2}{4\pi}. \tag{1.36}$$

The following formula shows, that the Lorentz force, pushing the mirror, is predetermined by the electric field of the wave.

$$F_{\mathrm{l}}(t) = \frac{|E(t)|^2}{4\pi}\mathcal{A}. \tag{1.37}$$

The high frequency oscillations of the Lorentz's force are unobservable on the mirror, so the force, we percept as the radiation pressure force, is only an averaged (per an optical period) part of it:

$$F_{\mathrm{p}}(t) = \overline{F_{\mathrm{l}}(t)}. \tag{1.38}$$

Each mirror of the cavity in the FIG. 1.2 is pushed by four beams: one falling and one outgoing at each side of the mirror, i.e.:

$$F_{\mathrm{tot}} = F_{\mathrm{pe}} + F_{\mathrm{pf}} - F_{\mathrm{pg}} - F_{\mathrm{ph}}. \tag{1.39}$$

Throughout this thesis the radiation pressure is considered on the mirrors bounding a cavity, in this case a Fabry-Perot cavity, and therefore only two of the beams applies the major force: the two from the inside of the cavity.

The expression for the squared modulus of the field, taken in the general form from (1.1), contains two significant terms: the squared modulus of the zeroth approximation term and the cross multiplication of the terms of the zeroth and the first order. The first term is of the zeroth order and describes the strong constant pressure of the carrier light. This value for a single beam is:

$$W_0 = h\omega_{\mathrm{p}}|E|^2. \tag{1.40}$$

The second term, of the first order, describes the smaller, but in principle measurable, influence of the perturbations in the field. The residuary term, formed by multiplication of two small quantities, has the second order of smallness and is therefore negligible. The radiation pressure of zeroth order is always constant, it is counterbalanced by the forces of actuators and of the suspension pendulum, and is of no interest. Radiation pressure in the first approximation of the both a descending E

and a reflected F beams, which affect the dynamics of the detector, has the following appearance:

$$\hat{F}_{\mathrm{p}}(t) = 2\frac{\hbar\omega_{\mathrm{p}}}{c}\int\limits_{-\infty}^{\infty}\left[E^*\hat{\mathrm{e}}(\omega_{\mathrm{p}} + \Omega) + E\hat{\mathrm{e}}^{\dagger}(\omega_{\mathrm{p}} - \Omega)\right]e^{-i\Omega t}\frac{d\Omega}{2\pi}. \tag{1.41}$$

This expression was obtained in assumption of high mirror reflectivity, meaning the approximate equality of the descending and reflected beams, and neglecting the influence of optical frequency oscillation

$$R_{\mathrm{E}} \approx 1, \tag{1.42a}$$

$$\Omega \ll \omega_{\mathrm{p}}. \tag{1.42b}$$

The formula for radiation pressure, obtained by substituting of the explicit expression for the field, considered on the mirror inside the Fabry-Perot cavity (1.24),

$$\hat{F}_{\mathrm{p}}(t) = \int\limits_{-\infty}^{\infty}(\hat{F}_{\mathrm{fluct}}(\Omega) - K(\Omega)X(\Omega))e^{-i\Omega t}\frac{d\Omega}{2\pi}, \tag{1.43}$$

consists of the fluctuational:

$$\hat{F}_{\mathrm{fluct}}(\Omega) = \frac{2i\hbar\omega_{\mathrm{p}}}{c}\sqrt{\frac{\gamma}{\tau}}\left[\frac{E^*\hat{\mathrm{a}}(\omega_{\mathrm{p}} + \Omega)}{\ell^*(\Omega)} - \frac{E\hat{\mathrm{a}}^{\dagger}(\omega_{\mathrm{p}} - \Omega)}{\ell(-\Omega)}\right] \tag{1.44}$$

and the ponderomotive $K(\Omega)X(\Omega)$ parts with:

$$K(\Omega) = \frac{4\omega_{\mathrm{p}}W_0\delta}{cL\ell(\Omega)\ell^*(-\Omega)}, \tag{1.45}$$

where W_0 is the power from (1.40).

1.4. Dynamics of the mirrors in the Fabry-Perot cavity

The mirrors in a gravitational-wave detector are suspended as pendulums with the low-frequency resonance, therefore they are well isolated and can be considered as free masses at frequencies of GW. According to the Newton's second law, the motion of the mass center of such a mirror is caused by the external forces, which we divide into radiation pressure force $F_{\mathrm{p}}(\Omega)$, and the other non-optical external forces $F_{\mathrm{no}}(\Omega)$. Easy to show, that radiation pressure has the equal influence on both mirrors within approximations $R \approx 1$ and $\Omega \ll \omega_{\mathrm{p}}$. The non-optical external forces include the external displacement noise forces $F_{\mathrm{dis}}(\Omega)$ and the influence of gravitational waves, which is a force in a local-Lorentz frame $F_{\mathrm{gw}}(\Omega)$. The equations for the central masses of the mirrors (see FIG. 1.2) read:

$$-m_{\mathrm{i}}\Omega^2 X_{\mathrm{cm\ i}}(\Omega) = -F_{\mathrm{p}}(\Omega) + F_{\mathrm{no\ i}}(\Omega), \tag{1.46a}$$

$$-m_{\mathrm{e}}\Omega^2 X_{\mathrm{cm\ e}}(\Omega) = F_{\mathrm{p}}(\Omega) + F_{\mathrm{no\ e}}(\Omega), \tag{1.46b}$$

where

$$F_{\text{NO i}}(\Omega) = F_{\text{ex i}}(\Omega), \tag{1.47a}$$

$$F_{\text{NO e}}(\Omega) = F_{\text{ex e}}(\Omega) + F_{\text{gw e}}(\Omega). \tag{1.47b}$$

The field on the output (1.30,1.31) is sensitive not only to the central mass displacement of the mirror $X_{\text{cm}}(\Omega)$, but also to the displacement of the surface with respect to the mass center $X_{\text{surf}}(\Omega)$, caused by internal thermal noises of the mirror, so for the measured displacement components of (1.27b) we have:

$$X_{\text{i}}(\Omega) = X_{\text{cm i}}(\Omega) + X_{\text{surf i}}(\Omega), \tag{1.48a}$$

$$X_{\text{e}}(\Omega) = X_{\text{cm e}}(\Omega) + X_{\text{surf e}}(\Omega). \tag{1.48b}$$

The optical spring, however, affects only to the motion of mass centers, therefore the displacement of surface is left unaffected.

The solution of (1.46), obtained by taking into account the optical spring part of F_{p}, gives the following expression for the measured displacement:

$$X(\Omega) = \frac{-\hat{F}_{\text{fluct}}(\Omega) - \hat{F}_{\text{ex}}(\Omega) + m\Omega^2 X_{\text{surf}}(\Omega) - F_{\text{gw}}(\Omega)}{m\Omega^2 - K(\Omega)}, \tag{1.49}$$

with the equivalent quantities:

$$m = \frac{m_{\text{e}} m_{\text{i}}}{m_{\text{e}} + m_{\text{i}}}, \tag{1.50a}$$

$$F_{\text{ex}}(\Omega) = \frac{m_{\text{i}} F_{\text{dis e}}(\Omega) - m_{\text{e}} F_{\text{dis I}}(\Omega)}{m_{\text{e}} + m_{\text{i}}}, \tag{1.50b}$$

$$X_{\text{surf}}(\Omega) = X_{\text{surf E}}(\Omega) - X_{\text{surf i}}(\Omega), \tag{1.50c}$$

$$F_{\text{gw}}(\Omega) = \frac{m}{m_{\text{e}}} F_{\text{gw e}}(\Omega). \tag{1.50d}$$

We see that optomechanical properties of the Fabry-Perot cavity may be described by the mechanics of a cavity with one fixed mirror. There's a correspondence between the masses, position of mass centers and the fields of these equivalent systems. The displacement noise in general case is not the subject to this equivalence.

1.5. Detection of the output field in a Fabry-Perot cavity. Spectral density of coordinate, force and correlated noise

The motion of the mirror, caused by the GW, is measured by the Fabry-Perot cavity via the phase shift of the output field b (see FIG. 1.2) with respect to the initial mirror position, corresponding to the preset detuning of the mirror. The field is detected by a homodyne detection, by interfering it with the so called local oscillator, the reference

beam, synchronized with the carrier laser, with some preset homodyne phase ϕ_{lo}. The interference of the output signal with the local oscillator on a beam splitter gives a sum and a difference of their fields. By the subtraction of the signals from detection of these two fields, we keep only the following term:

$$\hat{I}_{\mathrm{det}}(t) \sim \overline{\hat{E}_b(t) \sin(\omega_{\mathrm{p}} t + \phi_{\mathrm{lo}})}. \tag{1.51}$$

The substitution of the field (1.1) with its amplitude (1.30a) give the explicit expression for the signal in the photocurrent:

$$\hat{I}_{\mathrm{sig}}(t) = \frac{1}{i} \int\limits_{-\infty}^{\infty} \sqrt{\frac{2\pi\hbar\omega}{\mathcal{A}c}} \left(\hat{r}(\Omega) + k(\Omega) X(\Omega) \right) e^{-i\Omega t} \frac{d\Omega}{2\pi}, \tag{1.52}$$

where

$$\hat{\mathrm{r}}(\Omega) = \left[\frac{\sqrt{\gamma_{\mathrm{I}}}}{\sqrt{\gamma}} \hat{\mathrm{a}}(\omega_{\mathrm{p}} + \Omega) - \frac{\sqrt{\gamma_{\mathrm{e}}}}{\sqrt{\gamma}} \hat{\mathrm{g}}(\omega_{\mathrm{p}} + \Omega) \right] e^{i\phi_{\mathrm{lo}}} - $$
$$- \left[\frac{\sqrt{\gamma_{\mathrm{I}}}}{\sqrt{\gamma}} \hat{\mathrm{a}}^\dagger(\omega_{\mathrm{p}} - \Omega) - \frac{\sqrt{\gamma_{\mathrm{e}}}}{\sqrt{\gamma}} \hat{\mathrm{g}}^\dagger(\omega_{\mathrm{p}} - \Omega) \right] e^{-i\phi_{\mathrm{lo}}} \tag{1.53a}$$

and

$$k(\Omega) = \sqrt{\frac{\gamma_{\mathrm{I}}}{\tau}} \frac{2\omega_{\mathrm{p}}}{c} \left[\frac{e^{i\phi_{\mathrm{lo}}} E}{\ell(\Omega)} - \frac{e^{-i\phi_{\mathrm{lo}}} E^*}{\ell^*(-\Omega)} \right]. \tag{1.53b}$$

The ground state oscillation $\hat{\mathrm{r}}(\Omega)$ gives an additional noise to the detected signal, and is referred to as shot noise. For some tasks it is more convenient to present the shot noise reduced to mirror motion:

$$\hat{x}(\Omega) = \frac{\hat{r}(\Omega)}{k(\Omega)}, \tag{1.54}$$

a so-called coordinate noise. It is a quantity, describing the properties of the real detected shot noise, as if it arose from some imaginary noisy mirror motion.

In Heisenberg picture the noise of a quantum quantity $\hat{\alpha}(\Omega)$, caused by the ground state oscillations, reads

$$2\pi\delta(\Omega - \Omega') S_\alpha(\Omega) = \left\langle 0 \left| \hat{\alpha}(\Omega)\hat{\alpha}^\dagger(\Omega') \right| 0 \right\rangle_{\mathrm{sym}}, \tag{1.55}$$

The spectral density of coordinate noise (1.54) is therefore:

$$S_x(\Omega) = \frac{c^2\tau}{16\gamma_{\mathrm{I}}\omega_{\mathrm{p}}^2 |E|^2} \frac{|\mathcal{D}(\Omega)|^2}{(\delta\cos\phi_{\mathrm{h}} + \gamma\sin\phi_{\mathrm{h}})^2 + \Omega^2 \sin^2\phi_{\mathrm{h}}}, \tag{1.56}$$

where

$$\phi_{\mathrm{h}} = \phi_{\mathrm{lo}} + \phi_{\mathrm{argE}}, \tag{1.57}$$

and

$$\mathcal{D}(\Omega) = (i\Omega + \gamma)^2 + \delta^2. \tag{1.58}$$

The homodyne angle ϕ_{h} determines the quadrature of the output field detected by the homodyne detector. For tuned detector $\delta = 0$ the minimal noise corresponds to the quadrature with $\phi_{\mathrm{h}} = \dfrac{\pi}{2}$, carrying the GW signal, which is conventionally called phase quadrature. The orthogonal quadrature with $\phi_{\mathrm{h}} = 0$ gives us the infinite noise in a tuned case, meaning absence of the signal component. This quadrature is called amplitude. Detuning changes the quadrature carrying the signal component. The angle ϕ_{h} minimizing the noise for each detuning δ, determines the quadrature carrying the signal.

The coordinate noise operator consists of two factors: the shot noise on the photodetector $\hat{r}(\Omega)$ and transfer function of the Fabry-Perot cavity $k(\Omega)$. Easy to show that the shot noise is white:

$$S_r(\Omega) = 1. \tag{1.59}$$

Therefore the frequency dependence of the coordinate noise comes from the resonant transfer function, and is the inverse square of it $S_x(\Omega) = \dfrac{1}{|k^2(\Omega)|}$.

The other influence of the ground state oscillations is radiation pressure noise $F_{\mathrm{fluct}}(\Omega)$, the spectral density of which, according to (1.44) and (1.55), is:

$$S_F(\Omega) = \frac{4\hbar^2 \omega_{\mathrm{p}}^2 \gamma}{c^2 \tau} \left| E \right|^2 \frac{\gamma^2 + \delta^2 + \Omega^2}{\left| \mathcal{D}(\Omega) \right|^2}. \tag{1.60}$$

The electrical field on the mirror, caused by the injected fluctuations, is proportional to transfer function of the cavity, therefore the radiation pressure noise, acting on the mirror, has the resonant properties. The fluctuating force is proportional to the quantum oscillations inside cavity, and therefore is also proportional to the transfer function of the cavity. The influence of the force on the mirror motion is affected by the optomechanical term $K(\Omega) - m\Omega^2$. Therefore, the radiation pressure noise in a simple case, with strong detuning and negligible optical spring, (i) decreases as $\frac{1}{\Omega^2}$ at low frequencies, (ii) has local steepness increasing and decreasing around the tuning frequency and (iii) decreases as $\frac{1}{\Omega^4}$ at high frequencies.

Since both parts of quantum noise, the coordinate (1.54) and the radiation pressure (1.44) noises, are caused by the ground state oscillations injected from the input mirror, they are not independent. The correlation for the two quantities α and β caused by the injections in general case in the same Heisenberg picture reads similarly to (1.55):

$$2\pi\delta(\Omega - \Omega') S_{\alpha\beta} = \frac{1}{2} \left\langle 0 \left| \hat{a}(\Omega) \hat{\beta}^{\dagger}_{fluct}(\Omega') \right| 0 \right\rangle_{\mathrm{sym}}. \tag{1.61}$$

Substituting the corresponding expressions we get the correlation between coordinate and force noises:

$$S_{xF} = -\frac{\hbar}{2} \frac{\delta \sin\phi_{\mathrm{h}} - \gamma \cos\phi_{\mathrm{h}} + i\Omega \cos\phi_{\mathrm{h}}}{\gamma \sin\phi_{\mathrm{h}} + \delta \cos\phi_{\mathrm{h}} - i\Omega \sin\phi_{\mathrm{h}}}. \tag{1.62}$$

1.6. Detection of gravitational waves. The noise, reduced to GW strain

The gravitational waves are the perturbations of the metrics of time-space. The strain of the wave passing the detector perpendicular to its plane has two polarizations

$$h(\Omega) = h_+(\Omega) + h_\times(\Omega). \tag{1.63}$$

Since the cavity is placed along the x-axis, it will be sensitive to $h_+(\Omega)$ polarization only. Gravitational wave, passing the detector, in the local-Lorentz frame acts on the end mirror of the cavity with the moving force, which reads in linear approximation:

$$F_{\text{GW}} = m\Omega^2 L h_+(\Omega). \tag{1.64}$$

The influence of the desired quantity $h_+(\Omega)$ in the measured photo current is worsen by the mentioned sources of noises that are conventionally reduced to the GW strain:

$$\hat{I}_{\text{det}} = \frac{1}{i} \int\limits_{-\infty}^{\infty} \sqrt{\frac{2\pi\hbar\omega}{\mathcal{A}c}} k_1(\Omega)(\hat{h}(\Omega) + h_+(\Omega))e^{-i\Omega t}\frac{d\Omega}{2\pi}, \tag{1.65}$$

where

$$\hat{h}(\Omega) = \frac{2}{m\Omega^2 L}(m\Omega^2 - K(\Omega))\hat{x}(\Omega) - \frac{2}{m\Omega^2 L}\hat{F}_{\text{fluct}}(\Omega) + \frac{2}{L}X_{\text{dis}}(\Omega), \tag{1.66a}$$

$$k_1(\Omega) = k(\Omega)\frac{m\Omega^2 L}{2(m\Omega^2 - K(\Omega))}. \tag{1.66b}$$

The term $X_{\text{dis}}(\Omega)$ is formed here from the displacement of the surface mirror with respect to mass center $X_{\text{mc}}(\Omega)$ and the equivalent free mass displacement corresponding to the external noise forces $-\dfrac{F_{\text{ext}}}{m\Omega^2}$. It describes the displacement noise of the mirror surface, both external and internal thermal, with respect to the inertial frame. So this noise, reduced to the GW strain, is independent from the optical spring effect and the optical cavity configuration. The displacement noise is usually stationary:

$$S_{\text{dis}}(\Omega)2\pi\delta(\Omega - \Omega') = \langle X_{\text{dis}}(\Omega)X_{\text{dis}}(\Omega')\rangle \tag{1.67}$$

It is also the subject to the dissipation-fluctuation theorem.

The spectral density of the whole quantum noise, reduced to the gravitational wave strain, may be obtained from the corresponding terms of (1.66a) into (1.55). The The spectral density resulting from this operation, as well as the previous frequency-domain quantities dependent on Ω, is double-sided, meaning it is determined for both positive and negative sideband frequencies. However the positive frequencies are usually much clearer intuitively, therefore the noise is conventionally described by single-sided spectral density, differing from the double sided by factor of 2. So,

transforming term with cross-corelated noise we obtain:

$$S_+^h(\Omega) = \frac{8}{m^2\Omega^4 L^2} \left(|K(\Omega) - m\Omega^2|^2 S_x(\Omega) + \right.$$
$$\left. + 2\Re\left[(K(\Omega) - m\Omega^2)S_{xF}(\Omega)\right] + S_F(\Omega) + S_{\mathrm{dis}}(\Omega) \right). \quad (1.68)$$

For convenience we omit the index "+" below.

GEO 600

2.1. GEO 600. Fields in equivalent cavities

G EO 600 is a ground-based detector operating near Hanover, Germany. Its main optical layout is shown in figure 2.1 and is described in introduction. The only difference of this layout from the actual one is the folded arms, and this difference will be considered later in section 2.3.

The electromagnetic fields inside GEO 600 may be described using the same physical grounds as the fields of a Fabry-Perot cavity in chapter 1: the propagation through the vacuum, the reflection from the mirrors, the radiation pressure, the losses, replaced by the equivalent transparency of the end mirror. The physical parameters of the GEO 600 elements we use in this work are represented in table 2.1 along with their expressions, descriptions and typical values in the current operation regime. The parameters of the laser used in GEO 600 one can find in table 2.2.

The fields in GEO 600 may be effectively separated into the power and the signal recycling cavities: the first is formed by the PRM and the end-mirrors, the latter one is formed by the SRM and the end-mirrors. The expressions for the fields, corresponding to these two cavities read:

$$
\hat{e}(\omega) = \approx \frac{i\sqrt{\frac{\gamma_{\mathrm{p}}}{\tau}}\hat{a}(\omega)e^{ikL_{\mathrm{i}}} + i\frac{k_{\mathrm{p}}}{\tau}X_{\mathrm{src}}(\Omega)E + i\sqrt{\frac{\gamma_{\mathrm{f}}}{\tau}}\hat{q}_1(\omega)}{\gamma_{\mathrm{p}} + \gamma_{\mathrm{f}} - i\Omega} -
$$
$$
- \frac{\frac{1}{2}\left(\gamma_{\mathrm{e}} - \gamma_{\mathrm{n}} + i\delta\omega_{df}\right)\hat{\mathrm{h}}(\omega)}{\gamma_{\mathrm{p}} + \gamma_{\mathrm{f}} - i\Omega}, \quad (2.1)
$$
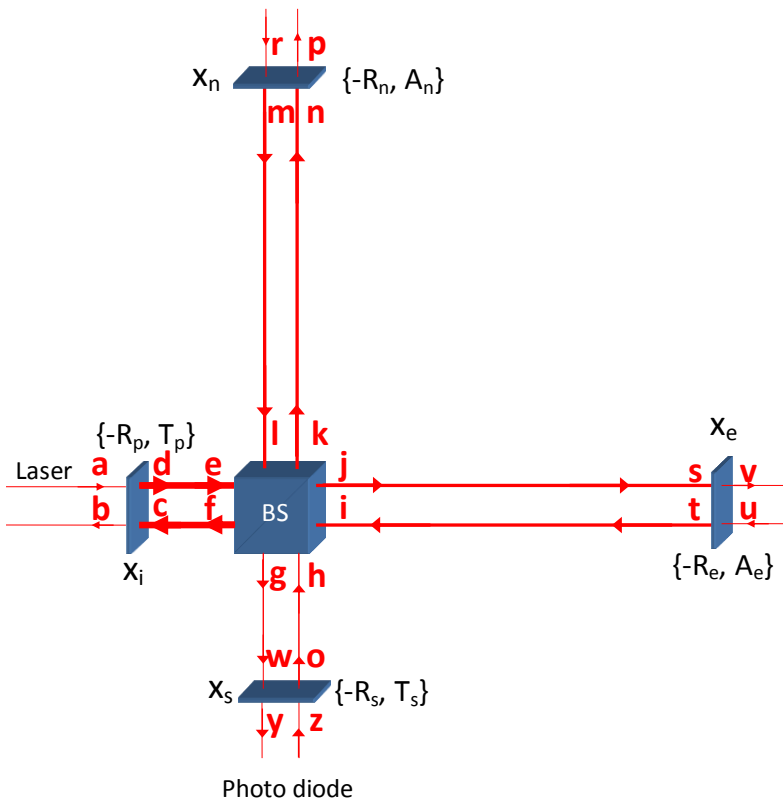
Figure 2.1.: Electromagnetic field in GEO 600

Table 2.1

Symbol	Quantity	Expressions via other quantities	Typical value
$\lvert A_\mathrm{m}\rvert^2$	Power losses on each mirror and BS		130 ppm (10^{-6})
$\lvert A_\mathrm{bs}\rvert^2$	Scattering on the beamsplitter		60 ppm
A_e	Amplitude losses in the east arm	$\sqrt{3\lvert A_\mathrm{m}\rvert^2 + \lvert A_\mathrm{bs}\rvert^2}$	2.5×10^{-2}
A_n	Amplitude losses in the north arm	$\sqrt{3\lvert A_\mathrm{m}\rvert^2}$	2.0×10^{-2}
A_f	Amplitude losses in the equivalent end mirror	$\sqrt{\dfrac{A_\mathrm{e}^2 + A_\mathrm{n}^2}{2}}$	2.3×10^{-2}
T_p	Amplitude transmittance of the power recycling mirror (PRM)	$\sqrt{900\ \mathrm{ppm}}$	3.0×10^{-2}
T_s	Amplitude transmittance of the current signal recycling mirror (SRM)	$\sqrt{0.1}$	0.32
T_s	Amplitude transmittance of the SRM, optimal for dynamical tuning	A_f	2.3×10^{-2}
γ_e	Half-bandwidth of the equivalent interferometer with mirror reflectivities -1 and A_e	$\dfrac{A_\mathrm{e}^2 c}{4L}$	26.9 1/s
γ_n	Half-bandwidth corresponding to north mirror	$\dfrac{A_\mathrm{n}^2 c}{4L}$	24.4 1/s
γ_p	Half-bandwidth corresponding to PRM	$\dfrac{T_\mathrm{p}^2 c}{4L}$	56.3 1/s

Table 2.1 – continued from previous page

Symbol	Quantity	Expressions via other quantities	Typical value
γ_s	Half-bandwidth corresponding to SRM	$\dfrac{T_s^2 c}{4L}$	1250 1/s
γ_f	Half-bandwidth corresponding to the equivalent end mirror	$\dfrac{\gamma_e + \gamma_n}{2}$	25.6 1/s
L	Length of one-way trip of light in arm		1200 m
τ	Time of one-way trip of light in arm	$\dfrac{L}{c}$	4.0×10^{-6} s
δL_{df}	Dark-fringe length offset	$\dfrac{\delta \phi_f c}{2\omega_p}$	12 pm (40 pm?)
$\delta \phi_f$	Dark-fringe phase offset	$\dfrac{2\omega_p \delta L_{df}}{c}$	1.4×10^{-4} rad
$\delta \omega_{df}$	Dark-fringe offset of arms' eigenfrequency	$\dfrac{\delta \phi_f}{2\tau}$	18 rad/s
δ	Frequency detuning of signal recycling cavity	$2\omega_p \dfrac{L_s + L}{c}$	1-10000 1/s
m_m	Mass of an actual GEO 600 end-mirror		5,6 kg
m_e	Mass of an equivalent GEO 600 end-mirror in a straight arm	$\dfrac{m_m}{5}$	1,12 kg

Table 2.1 – continued from previous page

Symbol	Quantity	Expressions via other quantities	Typical value
m	Mass of an equivalent Fabry-Perot cavity end mirror	$\dfrac{m_{\mathrm{e}}}{2}$	2,24 kg
m_{bs}	Mass of a beamsplitter in GEO 600		9,3 kg

Table 2.1.: Parameters of GEO 600 used in this thesis

and

$$
\hat{\mathrm{h}}(\omega) \approx \frac{i\sqrt{\dfrac{\gamma_{\mathrm{s}}}{\tau}}\hat{z}(\omega)e^{ikL_{\mathrm{s}}} + i\sqrt{\dfrac{\gamma_{\mathrm{f}}}{\tau}}\hat{q}_2(\omega)e^{ikL_{\mathrm{s}}} + \dfrac{R_{\mathrm{s}}k_{\mathrm{p}}}{\tau}X(\Omega)E}{\gamma_{\mathrm{s}} + \gamma_{\mathrm{f}} - i\left(\delta + \Omega\right)} -
$$
$$
- iR_{\mathrm{s}}\frac{\gamma_{\mathrm{e}} - \gamma_{\mathrm{n}} + i\delta\omega_{\mathrm{df}}}{2\left(\gamma_{\mathrm{s}} + \gamma_{\mathrm{f}} - i\left(\delta + \Omega\right)\right)}\hat{e}(\omega). \quad (2.2)
$$

The equations (2.1) and (2.2) are equivalent to the expression of the fields inside a Fabry-Perot cavity (compare with (1.24b) and (1.25b)). The field in the power recycling cavity carries the information about the common end-mirror motion (B.42) and the differential mode of ground-state field injections (B.39b), while the one in signal recycling cavity – about the differential end-mirror motion (B.55), as if it was caused by the motion of the equivalent mirror, and the common mode of ground-state field injections (B.51). The field from the orthogonal modes are injected only with the leaking from signal recycling mode due to dark-fringe offset and the differential end-mirror losses.

The detailed derivation of these two fields as well as the influence of leaks from orthogonal modes are presented in appendix (B).

2.2. Detection of the field in GEO 600

The field $\hat{\mathrm{h}}(\omega)$ from (B.59) with neglected corrections from the leaks is equivalent to the field inside the Fabry-Perot cavity (1.24a,1.24b). The only difference is the zeroth order field in the term with the differential end-mirrors motion: in the expression for the Fabry-Perot cavity it is caused by the field on the end-mirror, while in GEO 600 it is caused by the field E on the beamsplitter, the phase of which corresponds to a phase of light on the distance L_{s} from the SRM. It means that field on the output of the detector is described with the following equation, equivalent to (1.30a):

$$
\hat{y}(\omega) = \frac{\sqrt{\gamma_{\mathrm{s}}}\hat{z}(\omega) - \sqrt{\gamma_{\mathrm{f}}}\hat{q}_2(\omega)}{\sqrt{\gamma}} - i2\sqrt{\frac{\gamma_{\mathrm{s}}}{\tau}}Ek_{\mathrm{p}}\frac{X(\Omega)}{\ell(\Omega)}e^{-ik_{\mathrm{p}}L_{\mathrm{s}}}e^{i\delta_\phi/2}, \quad (2.3)
$$

Table 2.2.: Laser parameters used in this thesis

Symbol	Quantity	Expressions via other quantities	Typical value
W_a	Input laser power	$\hbar\omega_\mathrm{p}\lvert A\rvert^2$	3.2 W
W_e	Power inside power recyclling cavity	$W_A \dfrac{T_\mathrm{p}^2}{\left(\dfrac{T_\mathrm{p}^2}{2} + \dfrac{A_\mathrm{f}^2}{2} + 3\dfrac{A_\mathrm{m}^2}{2}\right)^2}$	4.08 kW Experimental at 2013 2 - 5 kW
λ	Wavelength of laser light		1064 nm
ω_p	Pumping frequqncy of laser light	$\dfrac{2\pi c}{\lambda}$	1.8×10^{15} rad/s
ω	Considered frequency of quantum field		1.8×10^{15} rad/s
Ω	Considered frequency of signal and noise spectrum	$\omega - \omega_\mathrm{p}$	$10 - 10000$ rad/s

where the new, rotated, annihilation operators are introduced similar to (1.28):

$$\hat{z}_{\text{new}}(\omega) = \frac{\ell_2^*(\Omega)}{\ell_2(\Omega)} \frac{\sqrt{\gamma_s}\hat{z}(\omega) + \sqrt{\gamma_f}\hat{q}_2(\omega)e^{i\delta_\phi/2}}{\sqrt{\gamma_2}}, \tag{2.4a}$$

$$\hat{q}_{2(\text{new})}(\omega) = \frac{-\sqrt{\gamma_s}\hat{q}_2(\omega)e^{i\delta_\phi/2} + \sqrt{\gamma_f}\hat{z}(\omega)}{\sqrt{\gamma_2}}. \tag{2.4b}$$

This field together with the dark-fringe offset (B.34) is detected on the photodiode. The first order term is obtained after the filtering out the zeroth order dc-component:

$$I_{\text{det}}(t) = \frac{2\pi\hbar\omega_p}{\mathcal{A}c} Y_0 \int\limits_{-\infty}^{\infty} \left(\hat{r}(\Omega) + k(\Omega)X(\Omega)\right) e^{-i\Omega t} \frac{d\Omega}{2\pi}, \tag{2.5}$$

where:

$$\hat{r}(\Omega) = \sqrt{\frac{\gamma_s}{\gamma}} \left(e^{-i\phi_Y}\hat{z}(\omega_p + \Omega) + e^{i\phi_Y}\hat{z}^\dagger(\omega_p - \Omega)\right) -$$

$$- \sqrt{\frac{\gamma_f}{\gamma}} \left(e^{-i\phi_Y}\hat{q}_2(\omega_p + \Omega) + e^{i\phi_Y}\hat{q}_2^\dagger(\omega_p - \Omega)\right), \quad (2.6a)$$

$$k(\Omega) = i2\sqrt{\frac{\gamma_s}{\tau}}\frac{\omega_p}{c}|E| \left[-\frac{e^{i\phi_h}}{\ell(\Omega)} + \frac{e^{-i\phi_h}}{\ell^*(-\Omega)}\right], \tag{2.6b}$$

where

$$\phi_h = \arctan\frac{\delta\omega_{\text{df}}}{\gamma_n - \gamma_e} - \arctan\frac{\delta}{\gamma_s + \gamma_e} \tag{2.7}$$

is a homodyne angle (compare to (1.57)).

We have introduced a so-called displacement noise in section 1.5, that describes the equivalent noise of the mirror displacement caused by shot noise on the photodetector. The spectral density of this noise can be calculated from (1.54) using (1.55):

$$S_x(\Omega) = \frac{c^2\tau}{16\gamma_s\omega_p^2|E|^2} \frac{|\mathcal{D}(\Omega)|^2}{\left(\delta\cos\phi_h + \gamma_2\sin\phi_h\right)^2 + \Omega^2\sin^2\phi_h}, \tag{2.8}$$

where

$$\mathcal{D}(\Omega) = (i\Omega + \gamma_2)^2 + (\delta)^2, \tag{2.9a}$$

and

$$\gamma_2 = \gamma_s + \gamma_f. \tag{2.9b}$$

Comparing (2.8) and (1.56) one can see the equivalence of the coordinate noise of GEO 600 to the coordinate noise of a Fabry-Perot cavity.
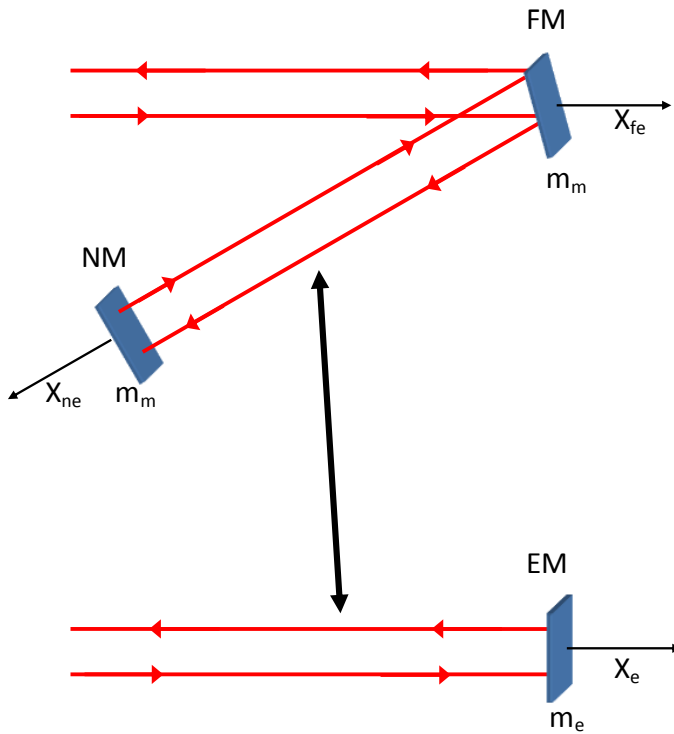
Figure 2.2.: GEO folded arm. A straight arm, equivalent to it

2.3. Equivalent straight arm

In contrast to the original Michelson interferometer with a single mirror in the arms, and to other gravitational wave detectors with Fabry-Perot cavities an arms, GEO 600 has so-called folded arms. The second mirror in the folded arm, is placed near the beamsplitter above the beam, forming a delay line instead of a Fabry-Perot cavity (see figure 2.2).

The dynamics of the mirrors, moved by radiation pressure and gravitational waves, is expressed in the following equations:

$$-m_{\mathrm{m}} X_{\mathrm{mc\ fe}}(\Omega)\Omega^2 = -m_{\mathrm{m}}\frac{L}{4}\Omega^2 h(\Omega) + 2\hat{F}_{\mathrm{p}}(\Omega), \qquad (2.10\mathrm{a})$$

$$-m_{\mathrm{m}} X_{\mathrm{mc\ ne}}(\Omega)\Omega^2 = \hat{F}_{\mathrm{p}}(\Omega), \qquad (2.10\mathrm{b})$$

where L is an optical length of the arm.

Similar to the dynamics of the mirrors of a Fabry-Perot cavity, described in section 1.4, the mirrors of the folded arms are also affected by the internal and the external noisy forces, causing an additional displacement of their mass centers and of surfaces with respect to mass centers. These displacements influence on both the measured quantity, and on the optical spring effects of radiation pressure. Similar to the dynamics of the Fabry-Perot cavity, this noisy displacements can be expressed as an equivalent displacement noise in the output signal. However, it doesn't affect the optomechanical properties of the detector with respect to the gravitational wave influence. Therefore, in this section we omit the consideration of the displacement noises, assuming laser measures the displacement of the mass centers of the mirrors, caused by radiation pressure and gravitational waves only.

Under these assumptions, the overall phase shift, caused by the reflection from the folded arm, may be described by the reflection (see (1.4)) from the equivalent mirror with the displacement:

$$X_{\mathrm{e}}(\Omega) = 2X_{\mathrm{fe}}(\Omega) + X_{\mathrm{ne}}(\Omega) = \frac{L}{2}h(\Omega) - \frac{\hat{F}_{\mathrm{p}}(\Omega)}{m_{\mathrm{e}}\Omega^2}, \qquad (2.11)$$

the response of which to the radiation pressure and to the gravitational wave is explained by the equivalent mass

$$m_{\mathrm{e}} = \frac{m_M}{5}, \qquad (2.12)$$

and distance L from the beamsplitter to the equivalent mirror.

The optical properties of the mirror are defined by the reflectivities of the mirrors:

$$R_{\mathrm{e}} = (-R_{\mathrm{fe}})^2(-R_{\mathrm{ne}}). \qquad (2.13)$$

2.4. Radiation pressure force on the end-mirrors. Spectral density of radiation pressure. Correlation between coordinate and radiation pressure noise

The differential motion of the equivalent end-mirrors (B.55) measured on the photodiode is affected and disturbed by radiation pressure. The ponderomotive force is dependent on the motion of the mirror surfaces, i.e. both mass center positions and the displacements of the surface with respect to mass center. This relative motion of the surface however do not affect the influence of gravitational waves and radiation pressure on the output signal, it only transforms the displacement noises in non-trivial way. Since the displacement motions are not the object of this work, we would omit the relative displacement of the surface, assuming the optical spring effect depends only on the mass center position.

The motion law of the two equivalent end-mirrors of GEO 600 (see figure 2.1) is following:

$$- m_\mathrm{e}\Omega^2 X_\mathrm{n}(\Omega) = \hat{F}^\mathrm{n}_\mathrm{fluct}(\Omega) - K^\mathrm{n}(\Omega)\left(X_\mathrm{n}(\Omega) - X_\mathrm{e}(\Omega)\right) + F_\mathrm{gw}(\Omega), \qquad (2.14a)$$

$$- m_\mathrm{e}\Omega^2 X_\mathrm{e}(\Omega) = \hat{F}^\mathrm{e}_\mathrm{fluct}(\Omega) - K^\mathrm{e}(\Omega)\left(X_\mathrm{n}(\Omega) - X_\mathrm{e}(\Omega)\right) - F_\mathrm{gw}(\Omega), \qquad (2.14b)$$

where $\hat{F}^\mathrm{n}_\mathrm{fluct}(\Omega)$, $\hat{F}^\mathrm{e}_\mathrm{fluct}(\Omega)$, $K^\mathrm{n}(\Omega)$ and $K^\mathrm{e}(\Omega)$ are defined by formula (1.41) The force, acting by the gravitational wave on the mirror:

$$F_\mathrm{gw}(\Omega) = \frac{1}{2} m_\mathrm{e}\Omega^2 L h(\Omega). \qquad (2.15)$$

The optical behavior of the signal recycling mirror, as it was shown in section B.6, is equivalent to the Fabry-Perot cavity with a mirror making differential motion (B.55). The dynamical behavior of this equivalent mirror is described as following:

$$X(\Omega) \equiv \frac{\hat{F}_\mathrm{fluct}(\Omega) + \dfrac{1}{2} m\Omega^2 L h(\Omega)}{K(\Omega) - m\Omega^2}, \qquad (2.16)$$

where the following equivalent quantities are introduced:

$$\hat{F}_\mathrm{fluct}(\Omega) \equiv \hat{F}^\mathrm{e}_\mathrm{fluct}(\Omega) - \hat{F}^\mathrm{n}_\mathrm{fluct}(\Omega) =$$

$$- \frac{2\hbar\omega_\mathrm{p}}{c} \times \left(\frac{\sqrt{\dfrac{\gamma_\mathrm{s}}{\tau}}\hat{z}(\omega_\mathrm{p} + \Omega) + \sqrt{\dfrac{\gamma_\mathrm{f}}{\tau}}\hat{q}_2(\omega_\mathrm{p} + \Omega)}{\gamma_\mathrm{s} + \gamma_\mathrm{f} - i\left(\delta + \Omega\right)} E^* + \right.$$

$$\left. + \frac{\sqrt{\dfrac{\gamma_\mathrm{s}}{\tau}}\hat{z}^\dagger(\omega_\mathrm{p} - \Omega) + \sqrt{\dfrac{\gamma_\mathrm{f}}{\tau}}\hat{q}_2^\dagger(\omega_\mathrm{p} - \Omega)}{\gamma_\mathrm{s} + \gamma_\mathrm{f} + i\left(\delta - \Omega\right)} E \right) \qquad (2.17a)$$

$$K(\Omega) \equiv K^{\mathrm{e}}(\Omega) - K^{\mathrm{n}}(\Omega) = \frac{2\hbar\omega_{\mathrm{p}}^2|E|^2\delta}{c^2\tau\ell_2(\Omega)\ell_2^*(-\Omega)}, \qquad (2.17\mathrm{b})$$

$$m = \frac{m_{\mathrm{e}}}{2}, \qquad (2.17\mathrm{c})$$

$$\ell_2(\Omega) = \gamma_{\mathrm{s}} + \gamma_{\mathrm{f}} - i(\delta + \Omega). \qquad (2.17\mathrm{d})$$

The fluctuational forces and optical rigidity, defined by the zeroth order field E and equivalent mirror motion $X(\Omega)$, are deduced from (B.6), (B.7) and (1.41). From these quantities follows the equivalent mass m of the Fabry-Perot cavity, describing dynamical properties of the detector. The spectral density of the equivalent radiation pressure noise, found with (1.55) from (2.17a), reads:

$$S_F(\Omega) = \frac{4\hbar^2\omega_{\mathrm{p}}^2\gamma_2}{c^2\tau}|E|^2\frac{\gamma_2^2 + \delta^2 + \Omega^2}{|\mathcal{D}_2(\Omega)|^2}. \qquad (2.18)$$

The correlation between radiation pressure and coordinate noises is, according to (1.61), using (1.54):

$$S_{xF}(\Omega) = -\frac{\hbar}{2}\frac{\delta\sin\phi_h - \gamma_2\cos\phi_h + i\Omega\cos\phi_h}{\gamma_2\sin\phi_h + \delta\cos\phi_h - i\Omega\sin\phi_h}. \qquad (2.19)$$

The noise, reduced to the gravitational wave, is determined by (2.5), (2.6) and (2.16):

$$\hat{h}(\Omega) = \frac{2}{m\Omega^2 L}\left[\left(K(\Omega) - m\Omega^2\right)\hat{x}(\Omega) + \hat{F}(\Omega)\right]. \qquad (2.20)$$

Therefore, the doubled, single-sided spectral density of the full quantum noise of GEO 600, scaled to gravitational wave strain may be found from this expression:

$$S_+^h(\Omega) = \frac{8}{m^2\Omega^4 L^2}\left(\left|K(\Omega) - m\Omega^2\right|^2 S_x(\Omega) + \right.$$
$$\left. + 2\Re\left[\left(K(\Omega) - m\Omega^2\right)S_{xF}(\Omega)\right] + S_{\mathrm{f}}(\Omega)\right). \qquad (2.21)$$

For convenience we again omit the index "+" below.

2.5. Radiation pressure noise on a beamsplitter

The GEO 600 is a detector without Fabry-Perot cavities in arms, therefore the full power of the laser beam interacts also with the beamsplitter. The part of the beam, reflecting from the beamsplitter applies a pressure, including the noisy influence due to the shot noise and ponderomotive force, similar to the beam, reflecting from the mirror. This pressure causes the jittering of the beamsplitter, and this causes the additional noise disturbances into the output field.

The motions of the beamsplitter, depicted in figure 2.3, introduces the disturbances of phase shift into the reflected light. The phase of light on the scale of the beamsplitter size may be represented with the following function:

$$\phi(x,y) = \phi(0,y)e^{ik_{\mathrm{p}}x}. \qquad (2.22)$$
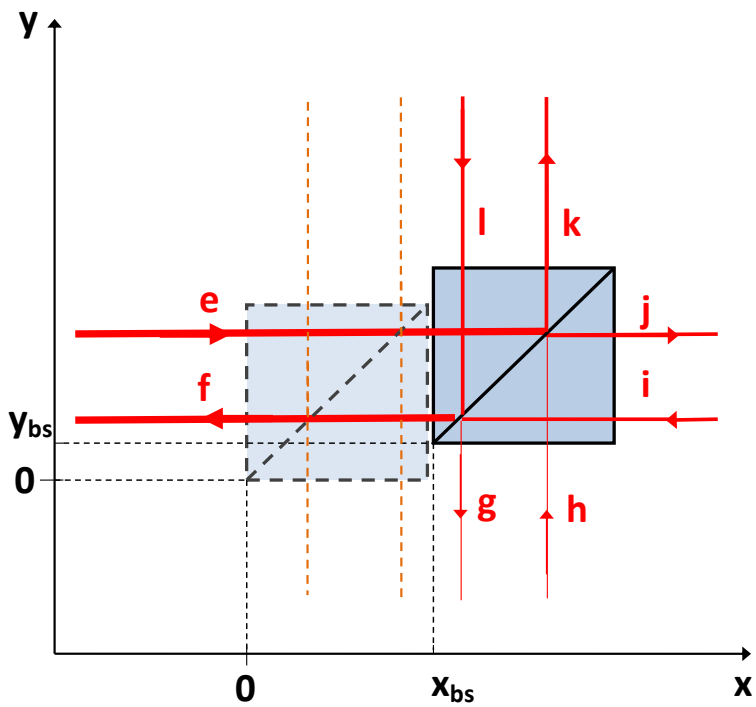
Figure 2.3.: Motions and fields of a beamsplitter

The equation for the reflecting mirror surface is following:

$$y(\Omega) = x(\Omega) - X_{\text{bs}}(\Omega) + Y_{\text{bs}}(\Omega) \tag{2.23}$$

The shift between phases of the beams at the displaced and at resting beamsplitter is then:

$$\delta\phi = \phi(x(\Omega), y(\Omega)) - \phi(y(\Omega), y(\Omega)) \approx i k_{\text{p}} X_{\text{r}}(\Omega), \tag{2.24}$$

where

$$X_{\text{r}}(\Omega) = X_{\text{bs}}(\Omega) - Y_{\text{bs}}(\Omega) \tag{2.25}$$

is an optical displacement, or displacement of the reflection point, of the beamsplitter.

The small phase shifts for the zeroth approximation fields introduces the corrections of the first order of smallness, therefore the corrections, introduced by fields falling from the dark port are negligible. The displacement of the beamsplitter introduces the phase shift only to the beams, propagating into x-axes, because the distance between the point of reflection and the the north mirror doesn't change. There will be no additional phase shift into the transmitted beams.

The following perturbations of the fields at the point of reflection caused by the beamsplitter motions make the influence to the measurements:

$$\hat{e}_{\text{r}}(\omega) = \hat{e}(\omega) + i k_{\text{p}} X_{\text{r}}(\Omega) E, \tag{2.26a}$$

$$\hat{i}_{\text{r}}(\omega) = \hat{i}(\omega) - i k_{\text{p}} X_{\text{r}}(\Omega) I, \tag{2.26b}$$

$$\hat{f}_{\text{r}}(\omega) = \hat{f}(\omega) - i k_{\text{p}} X_{\text{r}}(\Omega) F. \tag{2.26c}$$

These perturbations introduce the following corrections into the input-output relations of GEO 600 (see section B.1):

$$\hat{k}(\omega) = i\frac{\sqrt{2}}{2}\hat{h}(\omega) - \frac{\sqrt{2}}{2}\hat{e}(\omega) - i\frac{\sqrt{2}}{2}k_{\text{p}}X_{\text{r}}(\Omega)E, \tag{2.27a}$$

$$\hat{f}(\omega) = i\frac{\sqrt{2}}{2}\hat{i}(\omega) - \frac{\sqrt{2}}{2}\hat{l}(\omega) - i k_{\text{p}}X_{\text{r}}(\Omega)E, \tag{2.27b}$$

$$\hat{g}(\omega) = i\frac{\sqrt{2}}{2}\hat{l}(\omega) - \frac{\sqrt{2}}{2}i\hat{(\omega)} + \frac{1}{2}k_{\text{p}}X_{\text{r}}(\Omega)E. \tag{2.27c}$$

They introduce the corresponding corrections into the first order fields of the power and of the signal recycling modes:

$$\hat{h}(\omega) = i\sqrt{\frac{\gamma_2}{\tau}}\frac{e^{i\delta_\phi/2}}{\ell_2^*(\Omega)}\hat{z}_{new}(\omega) + \frac{k_{\text{p}}E}{\tau\ell_2(\Omega)}\left(X(\Omega) - \frac{1}{2}X_{\text{r}}(\Omega)\right)e^{i\delta_\phi}, \tag{2.28a}$$

$$\hat{e}(\omega) = -\sqrt{\frac{\gamma_1}{\tau}}\frac{\hat{a}_{new}(\omega)}{\ell_1^*(\Omega)} - i\frac{k_{\text{p}}E}{\tau\ell_1(\Omega)}\left(X_{\text{I}}(\Omega) + X_{\text{src}}(\Omega) + \frac{3}{4}X_{\text{r}}(\Omega)\right). \tag{2.28b}$$

Here there were used the rotated annihilation operators: from (2.4) and

$$\hat{a}_{\text{new}}(\omega) = \frac{\ell_1^*(\Omega)}{\ell_1(\Omega)} \frac{\sqrt{\gamma_P}\hat{a}(\omega) + \sqrt{\gamma_f}\hat{q}_1(\omega)}{\sqrt{\gamma_1}}, \tag{2.29a}$$

$$\hat{q}_{1(\text{new})}(\omega) = \frac{-\sqrt{\gamma_P}\hat{q}_1(\omega) + \sqrt{\gamma_f}\hat{a}(\omega)}{\sqrt{\gamma_1}}. \tag{2.29b}$$

The field inside the signal recycling cavity with the resting beamsplitter is sensitive to the differential motion of mirror, caused by the gravitational waves. The motion of the beamsplitter, caused by the radiation pressure, however introduces the additional perturbations to the field, effectively changing the signal end-mirror motion to $X(\Omega) - \frac{1}{2}X_r(\Omega)$ instead of $X(\Omega)$.

This equivalent mirror motion defines the signal in the photodiode current via (2.5):

$$I_{\text{det}}(t) = \frac{2\pi\hbar\omega_P}{\mathcal{A}c} Y_0 \int\limits_{-\infty}^{\infty} \left(\hat{r}(\Omega) + k(\Omega)\left(X(\Omega) - \frac{1}{2}X_r(\Omega) \right) \right) e^{-i\Omega t} \frac{d\Omega}{2\pi}, \tag{2.30}$$

where $\hat{r}(\Omega)$ and $k(\Omega)$ are identical to those from (2.6). Therefore the beamsplitter pushed by the radiation pressure noise doesn't change the coordinate noise $S_x(\Omega)$ (2.8).

The consideration of the radiation pressure noise requires the joint consideration of dynamics of the beamsplitter and the end-mirrors.

The laser fields on the beamsplitter, the radiation pressure of which is set in (1.41), push considerably from the north in the vertical direction, also from the east and from the PRM side in horizontal direction. The fields, pushing from the direction of the SRM is negligible, since the fields are very small there. The corresponding combination of the Newtons' Law equations for the coordinates of the beamsplitter, defines the displacement of the reflection surface $X_r(\Omega)$ caused by this radiation pressure as following:

$$-m_{\text{bs}}\Omega^2 X_r(\Omega) = \hat{F}_{\text{bs}}(\Omega), \tag{2.31}$$

where the equivalent force, causing the displacement is

$$\hat{F}_{\text{bs}}(\Omega) = \frac{2\hbar\omega_P}{c} \left(E^*\hat{e}(\omega_P + \Omega) + E\hat{e}^\dagger(\omega_P - \Omega) \right) - $$
$$- 2i\frac{\hbar\omega_P}{c} \left(E^*\hat{h}(\omega_P + \Omega) - E\hat{h}^\dagger(\omega_P - \Omega) \right), \quad (2.32)$$

and m_{bs} is the mass of the beamsplitter.

The dynamics of the end mirrors, caused by radiation pressure (1.41) and gravitational wave can be described in the following way (compare to (2.14)):

$$-m\Omega^2 X(\Omega) = \hat{F}(\Omega) + \frac{1}{2}m\Omega^2 Lh(\Omega), \tag{2.33}$$

where

$$\hat{F}(\Omega) = 2i\frac{\hbar\omega_P}{c} \left(E^*\hat{h}(\omega_P + \Omega) - E\hat{h}^\dagger(\omega_P - \Omega) \right). \tag{2.34}$$

The joint dynamics of the beamsplitter and the differential mirror motion may be simplified by the division of the fields, acting on it, to those from the power recycling cavity and from the signal recycling cavity. The radiation pressure, caused by fields from the signal recycling cavity is equal to the equivalent force $\hat{F}(\Omega)$, acting on the differential motion of the end-mirrors. Therefore, the radiation pressure on the beamsplitter may be represented in the following way:

$$\hat{F}_{\mathrm{bs}}(\Omega) = \Delta\hat{F}(\Omega) - \hat{F}(\Omega), \tag{2.35}$$

where the pressure from the fields of the power recycling cavity is additional to the usual fields from the signal recycling cavity:

$$\Delta\hat{F}(\Omega) = \frac{2\hbar\omega_{\mathrm{p}}}{c}\left(E^*\hat{e}(\omega_{\mathrm{p}}+\Omega) + E\hat{e}^\dagger(\omega_{\mathrm{p}}-\Omega)\right). \tag{2.36}$$

The field $\hat{e}(\omega)$, as it follows from (2.28b), contains the dependence on the optical displacement of the beamsplitter, therefore should introduce the optical rigidity into this motion. However, the optical spring factor $K_{\mathrm{PRC}}(\Omega)$ in the Fabry-Perot cavity, to which the power recycling cavity is equivalent, is proportional to the detuning of the cavity according to (2.17b). To achieve the maximal light power, the power recycling cavity is tuned to the carrier frequency of the laser, therefore $K_{\mathrm{PRC}}(\Omega)$ equals to zero.

As it follows from (1.41) and (2.28a), the radiation pressure force $\hat{F}(\Omega)$, acting on the differential end-mirror motion in the signal recycling cavity, can be described in the following way (compare with (2.16)):

$$\hat{F}(\Omega) = \hat{F}_{\mathrm{fluct}}(\Omega) - K(\Omega)\left(X(\Omega) - \frac{1}{2}X_{\mathrm{r}}(\Omega)\right), \tag{2.37}$$

where $\hat{F}_{\mathrm{fluct}}(\Omega)$ and $K(\Omega)$ are the same as in (2.17a) and (2.17b) correspondingly.

The joint dynamics of the beamsplitter and the end-mirrors in the signal recycling mode is described by the following Newton equations:

$$-m\Omega^2 X(\Omega) = \hat{F}_{\mathrm{fluct}}(\Omega) - K(\Omega)X(\Omega) + K(\Omega)X_{\mathrm{r}}(\Omega) + m_{\mathrm{e}}\Omega^2 Lh(\Omega), \tag{2.38a}$$

$$-m_{bs}\Omega^2 X_{\mathrm{r}}(\Omega) = \Delta\hat{F}(\Omega) - 2\hat{F}_{\mathrm{fluct}}(\Omega) + 2K(\Omega)X(\Omega) - 2K(\Omega)X_{\mathrm{r}}(\Omega). \tag{2.38b}$$

The solution of this equation system gives the following motion of the end-mirror in the equivalent signal recycling cavity:

$$X(\Omega) - \frac{1}{2}X_{\mathrm{r}}(\Omega) = \frac{\hat{F}_{\mathrm{fluct}}(\Omega)\left(1+\dfrac{m}{m_{\mathrm{bs}}}\right) - \dfrac{\Delta\hat{F}_{\mathrm{fluct}}(\Omega)}{2}\dfrac{m}{m_{\mathrm{bs}}} + \dfrac{m}{2}\Omega^2 Lh(\Omega)}{K(\Omega)\left(1+\dfrac{m}{m_{\mathrm{bs}}}\right) - m\Omega^2}. \tag{2.39}$$

$\hat{F}_{\mathrm{fluct}}(\Omega)$ in this expression is equivalent to the one in (2.17a). Since the coordinate noise also doesn't change, the expressions for the spectral density for the coordinate $S_x(\Omega)$, radiation pressure $S_F(\Omega)$ and correlation noise $S_{xF}(\Omega)$ are the same, as in section 2.4.

The spectral density of the radiation pressure of the fields in the power recycling mode, calculated with (1.55), reads:

$$S_{\Delta F} = \frac{4\hbar^2 \omega_{\mathrm{p}}^2 \gamma_1 |E|^2}{c^2 \tau (\gamma_1^2 + \Omega^2)}. \tag{2.40}$$

Then the single-sided spectral density of the full quantum noise of GEO 600 with the included radiation pressure on the beamsplitter, scaled to gravitational wave strain, is following:

$$S_+^h(\Omega) = \frac{8}{m^2 \Omega^4 L^2} \left(\left| K(\Omega) \left(1 + \frac{m}{m_{\mathrm{bs}}} \right) - m\Omega^2 \right|^2 S_x(\Omega) + \right.$$

$$+ 2\Re \left[\left(K(\Omega) \left(1 + \frac{m}{m_{\mathrm{bs}}} \right) - m\Omega^2 \right) \left(1 + \frac{m}{m_{\mathrm{bs}}} \right) S_{xF}(\Omega) \right] +$$

$$\left. + \left(1 + \frac{m}{m_{\mathrm{bs}}} \right)^2 S_{\mathrm{f}}(\Omega) + \frac{m^2}{m_{\mathrm{bs}}^2} S_{\Delta F} \right). \tag{2.41}$$

As usual, we omit index "+" below.

The asymptotic case of the beam splitter with the infinite mass m_{bs} corresponds to the detector with the resting beamsplitter. Logically, under this assumption (2.41) turns to (2.21).

The influence of the radiation on the beamsplitter, considered in this section, is shown on the figure 2.4, where spectral densities of GEO 600 with and without radiation pressure on the beamsplitter are represented.

2.6. Squeezed vacuum

The sensitivity of GEO 600 is shot-noise limited at the high frequencies. The quantum effects cause the uncertainties, or noise, in two orthogonal light quadratures, e.g. the number of photons and their phase. The quantum noise of both quadratures is equal in the ground state, and is subject to the uncertainty principle of Heisenberg. The injection of the squeezed vacuum [54, 71, 73–75] into the dark-port decreases the noise along one of the light quadratures, increasing it in the orthogonal one, keeping the uncertainty principle. The scheme of the shot-noise injection is depicted on figure 2.5. Mathematically it is described by the changing of the ground state shot noise at the dark port into:

$$|\zeta\rangle = \hat{S}(R) |0_\zeta\rangle \tag{2.42}$$

The correction to the annihilation and creation operator of the injected to the dark port fields $\hat{z}(\omega)$ and $\hat{z}^\dagger(\omega)$, caused by the squeezed state at the dark port is described by the equation (A7) in [54]:

$$\hat{S}^\dagger(R)\hat{z}(\omega_{\mathrm{p}} + \Omega)\hat{S}(R) = \hat{z}(\omega_{\mathrm{p}} + \Omega)\cosh R + \hat{z}^\dagger(\omega_{\mathrm{p}} - \Omega)e^{2i\theta}\sinh R, \tag{2.43a}$$

$$\hat{S}^\dagger(R)\hat{z}^\dagger(\omega_{\mathrm{p}} - \Omega)\hat{S}(R) = \hat{z}^\dagger(\omega_{\mathrm{p}} - \Omega)\cosh R + \hat{z}(\omega_{\mathrm{p}} + \Omega)e^{-2i\theta}\sinh R. \tag{2.43b}$$
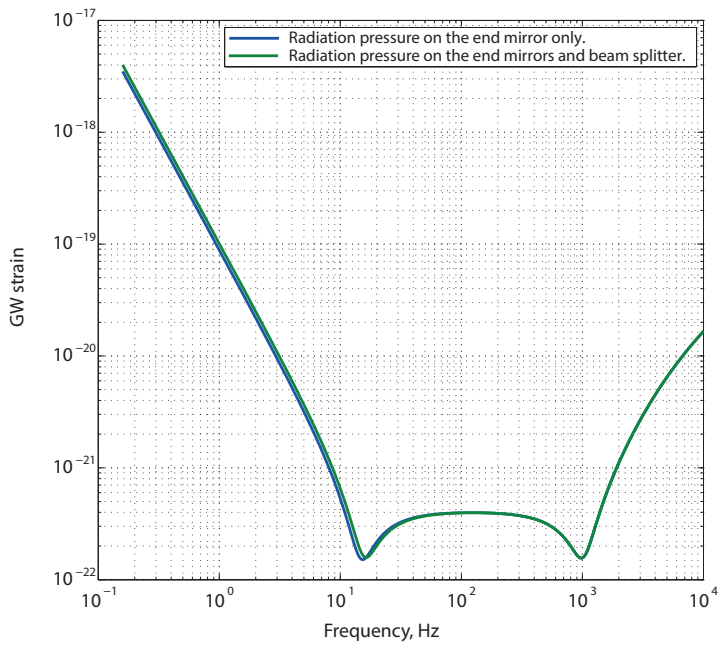
Figure 2.4.: Comparison of spectral densities of the quantum noise in GEO 600 with and without influence of the radiation pressure on the beamsplitter.
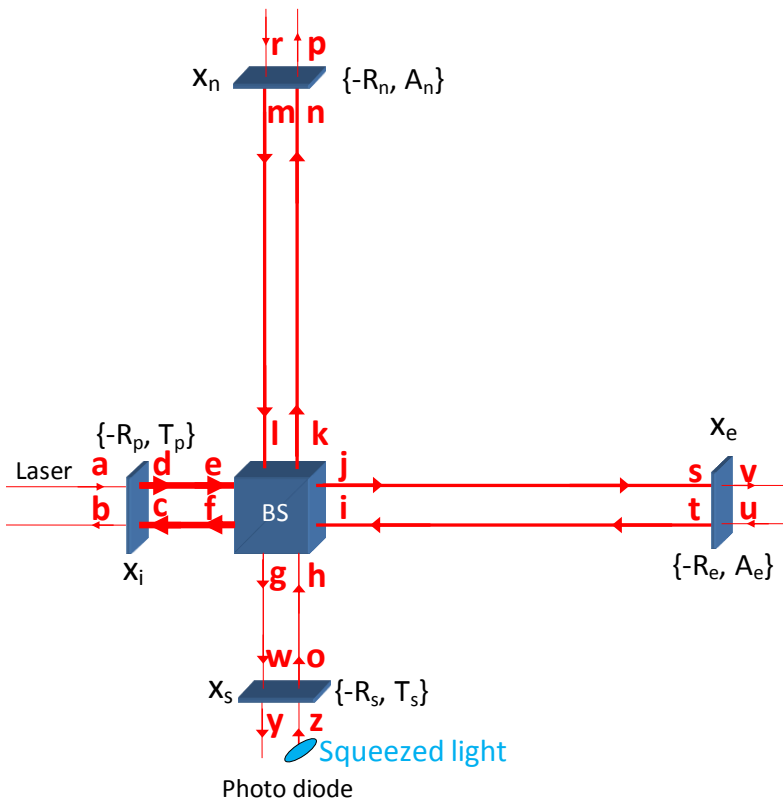
Figure 2.5.: GEO with squeezed vacuum

It should be mentioned here, that this squeezing transformation is applied to initial, non-rotated annihilation and creation operator.

This modification leads to the new expressions for the coordinate and the radiation pressure force and correlated parts of quantum noise. The substitution of the new dark-port injected field into (2.6) and (2.17a), expressed in the non-rotated operators, turns them into:

$$\hat{x}(\Omega) = A_1(\Omega)\hat{z}^\dagger(\omega_{\mathrm{p}} - \Omega) + A_2(\Omega)\hat{z}(\omega_{\mathrm{p}} + \Omega)_+$$
$$+ A_3(\Omega)\hat{q}^\dagger(\omega_{\mathrm{p}} - \Omega) + A_4\hat{q}(\omega_{\mathrm{p}} + \Omega), \quad (2.44a)$$

$$\hat{F}(\Omega) = B_1(\Omega)\hat{z}^\dagger(\omega_{\mathrm{p}} - \Omega) + B_2(\Omega)\hat{z}(\omega_{\mathrm{p}} + \Omega) +$$
$$+ B_3(\Omega)\hat{q}^\dagger(\omega_{\mathrm{p}} - \Omega) + B_4(\Omega)\hat{q}(\omega_{\mathrm{p}} + \Omega), \quad (2.44b)$$

where

$$A_1 = \left[\frac{\ell(-\Omega) - 2\gamma_{\mathrm{f}}}{\ell^*(-\Omega)} \cosh R + \frac{\ell^*(\Omega) - 2\gamma_{\mathrm{f}}}{\ell(\Omega)} \sinh R e^{2i\theta_1} \right] \frac{e^{i\phi_Y}}{k(\Omega)}, \quad (2.45a)$$

$$A_2 = \left[\frac{\ell(-\Omega) - 2\gamma_{\mathrm{f}}}{\ell^*(-\Omega)} \sinh R e^{-2i\theta_1} + \frac{\ell^*(\Omega) - 2\gamma_{\mathrm{f}}}{\ell(\Omega)} \cosh R \right] \frac{e^{-i\phi_Y}}{k(\Omega)}, \quad (2.45b)$$

$$A_3 = \frac{2\sqrt{\gamma_{\mathrm{S}}\gamma_{\mathrm{f}}} e^{i\phi_Y}}{\ell^*(-\Omega)} \frac{1}{k(\Omega)}, \quad (2.45c)$$

$$A_4 = \frac{2\sqrt{\gamma_{\mathrm{S}}\gamma_{\mathrm{f}}} e^{-i\phi_Y}}{\ell(\Omega)} \frac{1}{k(\Omega)}, \quad (2.45d)$$

and

$$B_1 = -2\frac{\hbar\omega_{\mathrm{p}}}{c}|E|\sqrt{\frac{\gamma_{\mathrm{S}}}{\tau}} e^{i\phi_{\mathrm{E}}} \left(e^{2i(\theta_1 - \phi_{\mathrm{h}})} \sinh R + \cosh R \right) \frac{1}{\ell^*(-\Omega)}, \quad (2.46a)$$

$$B_2 = -2\frac{\hbar\omega_{\mathrm{p}}}{c}|E|\sqrt{\frac{\gamma_{\mathrm{S}}}{\tau}} e^{-i\phi_{\mathrm{E}}} \left(e^{-2i(\theta_1 - \phi_{\mathrm{h}})} \sinh R + \cosh R \right) \frac{1}{\ell(\Omega)}, \quad (2.46b)$$

$$B_3 = -2\frac{\hbar\omega_{\mathrm{p}}}{c}|E|\sqrt{\frac{\gamma_{\mathrm{S}}}{\tau}} e^{i\phi_{\mathrm{E}}} \frac{1}{\ell^*(-\Omega)}, \quad (2.46c)$$

$$B_4 = -2\frac{\hbar\omega_{\mathrm{p}}}{c}|E|\sqrt{\frac{\gamma_{\mathrm{S}}}{\tau}} e^{-i\phi_{\mathrm{E}}} \frac{1}{\ell(\Omega)}, \quad (2.46d)$$

The spectral densities of the coordinate, radiation pressure and correlated parts of quantum noise, followed from here, read:

$$S_x(\Omega) = \frac{1}{2} \left(|A_1(\Omega)|^2 + |A_2(\Omega)|^2 + |A_3(\Omega)|^2 + |A_4(\Omega)|^2 \right), \quad (2.47a)$$

$$S_{xF}(\Omega) = \frac{1}{2} \left(A_1(\Omega)B_1^*(\Omega) + A_2(\Omega)B_2^*(\Omega) + A_3(\Omega)B_3^*(\Omega) + A_4(\Omega)B_4^*(\Omega) \right), \quad (2.47b)$$

$$S_{\mathrm{f}}(\Omega) = \frac{1}{2} \left(|B_1(\Omega)|^2 + |B_2(\Omega)|^2 + |B_3(\Omega)|^2 + |B_4(\Omega)|^2 \right), \quad (2.47c)$$

In expression for S_{xF} we can use that $e^{i(\phi_{\mathrm{E}} - \phi_Y)} = e^{-i\phi_{\mathrm{h}}}$.
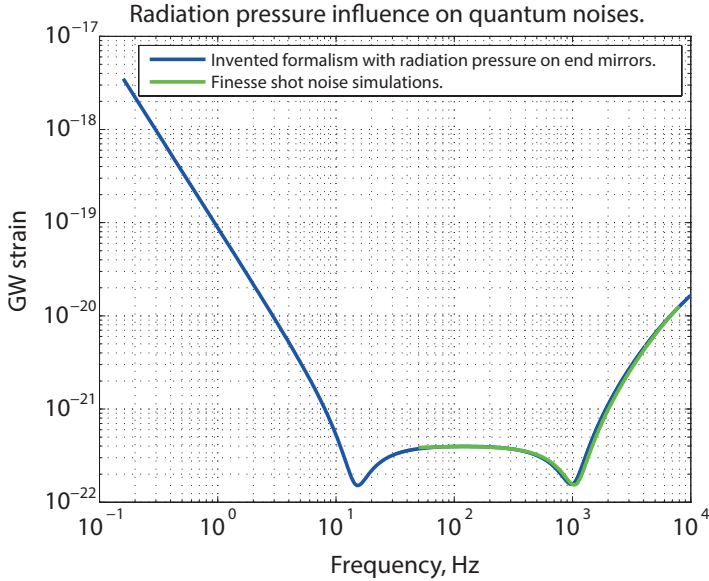
Figure 2.6.: Comparison of the spectral densities of the quantum shot noise, predicted by the model of this chapter for GEO 600, with the predictions of Finesse. The configuration of the detector here slightly differs from the real configuration of GEO 600

2.7. Comparison of the frequency-domain model with the results of Finesse. Fitness with experimental results

The frequency-domain model of the quantum noises, represented in this chapter, is rather general. It predicts the sensitivity of GEO 600 depending from all its parameters, including the masses, positions and the optical parameters of elements, and properties of electromagnetic fields in the detector.

There is a widely accepted computer program Finesse [76], designed by Andreas Freise to simulate the shot noise of GW detectors. The results of the model were checked numerous number of times, and are trusted by the experimentalists working in the field for GW detetors. We compared the shot noise of the GEO 600 configuration simulated by Finesse and calculated, using (2.21). The noises represented in figure 2.6 are calculated under the following assumptions: (i) the power on the beamsplitter $W_e = 2$ kW, (ii) the detuning of the signal recycling cavity $\delta = 1$ kHz, (iii) the transmittance of the SRM, defining the bandwidth of the signal recycling cavity, $T_s^2 = 2$ %. The other parameters for the detector are taken from the tables 2.1, 2.2. The model, described in this chapter fits to the results of the Finesse very well.

The quantum noise in GEO 600 are dominate at high frequencies. At the other frequencies the other noise overcome it. Therefore the proper comparison of the
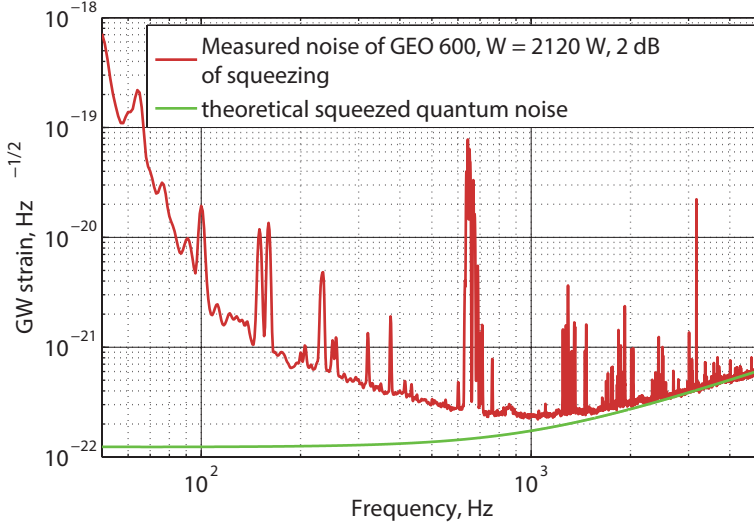
Figure 2.7.: Comparison of the theoretical noise prediction and the experimental GEO 600 noise

current frequency-domain model is only possible at high frequencies. In figure 2.7 the model of squeezed quantum noise, defined by (2.21,2.47), is compared to the real GEO 600 noise measured on march, the 5th, 2013. GEO was operating at the following parameters: (i) the power on the beamsplitter $W_e = 2, 1$ kW, (ii) tuned detector $\delta = 0$ kHz, (iii) the new low-reflectivity SRM with $T_s^2 = 10$ %, (iv) and the squeezed dark-port injection with the squeezing factor of 2 dB at the detector output. The other parameters for the detector are also taken from the tables 2.1, 2.2. The predictions of the model for the squeezed quantum noise coincide with the actually measured noise.

Therefore, the model, described in this chapter, fits to the existing model of Finesse, and to the real measured noise in GEO 600 and is, therefore, trustworthy.

2.8. Quasi-stationary approximation of dynamical tuning

The GW detector, more precisely the sensitive to GWs signal recycling mode, is equivalent to a Fabry-Perot cavity. The shot noise on the photodiode, defined by $\hat{r}(\Omega)$ in (2.6a), is white, and its intensity is independent from the parameters of the detector. The amplification of the GW inside the detector $k(\Omega)$(2.6b), according to the Airy function, has resonant features, defined mostly by the parameters of the SRM: the halfbandwidth γ_s is defined by the transmittance of the SRM (B.32a), and the resonant frequency δ, or detuning, is defined by the displacement of the SRM
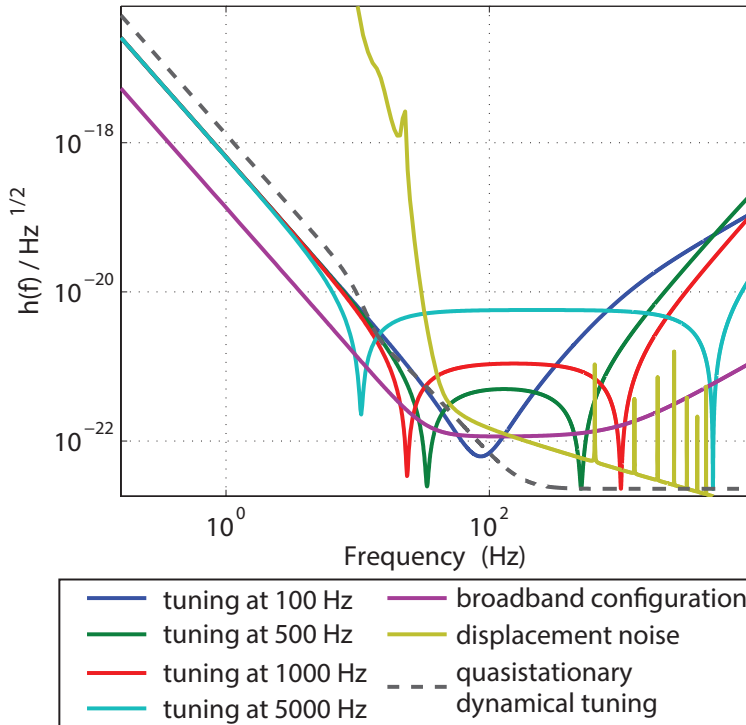
Figure 2.8.: Comparison of broad-band and narrow-band tunings. Effective quasi-stationary quantum noise for dynamical tuning

from its resonant position (B.32b).

     There are two typical operational regimes of the detector: (i) a narrow-band one, when the small γ defines a high amplification of the signal in the low frequency band, and (ii) a broad-band regime, when the high γ defines a moderate amplification for a broad-band signal. Comparison of these regimes is presented in figure 2.8, where the quantum noise of broad-band configuration is compared to the quantum noise of the narrow-band configuration. All the noise curves, presented on the plot, are calculated by the formula (2.21): the broad-band configuration contains the tuned SRM with 10 % transmittance, in the narrow-band configuration the position of the SRM corresponds to the tuning frequency, and has the 0,1 % transmittance. The peak sensitivity at 100 Hz is less than at higher frequencies, because of the noticeable influence of the radiation-pressure effects.

     The broad-band regime is good for the signal with wide spectrum, while the narrow-band regime fits to the signal sinusoidal signal with the constant frequency. The chirp signal from the compact binary coalescences has a special in this sense shape: it has a sinusoidal shape, with the carrier frequency significantly changing in time. Meers and Krolak [52] have proposed a new way of precise detection of the chirp signal: its

instantaneous frequency may be followed by the detuning of the detector.

When the frequency changes sufficiently slow, the fields in the detector approximately keep their stationary values, and this regime of detection may be considered as quasi-stationary. The model for the quasi-stationary, in frame of which the results in [52] were obtained, is following: each value of the carrier frequency lasts infinitely long, and the changes of the interferometer detuning take an infinite amount of time to occur. The spectrum of such a signal component would consist of the single frequency component, and it will "see" only one point of the noise spectral density, corresponding to this frequency. After the frequency of a signal passes the whole bandwidth, the continuum of these points form a new, effective curve of spectral density during the dynamical tuning detection. This effective spectral density, the set of the optical resonances, is also depicted in figure 2.8. The quasi-stationary quantum noise curve may be therefore calculated from (2.21), by setting the optical resonance condition for each signal frequency: $\delta = \Omega$.

The quasi-stationary quantum noise, based on the following of the signal frequency by the optical resonance of the cavity, is not optimal at lower frequency, as it shown figure 2.8. Due to the optical spring the detector tuned optically e.g. to 500 Hz has another resonance at the frequency around 70 Hz, where it provides much higher sensitivity, than the detector, tuned optically to this frequency. The comparison of quasi-stationary shot-noise and full quantum noise for the dynamical tuning, calculated from (2.21) and (2.8), is depicted in figure 2.9. As it follows from this figure, the contribution of the radiation pressure effect becomes negligible at frequencies above 200 Hz, and the shot noise becomes the good approximation for the quantum noise. This value depends on the laser power inside the detector as well as the transmittance of the SRM. This particular number was obtained for the power 2 kW and the SRM of $T_S = 420$ ppm. Additionaly, the sensitivity below 100 Hz is dominated by technical noise.

The quasi-stationary approximation is applicable, when the velocity of the mirror, defined by the signal instantaneous frequency change, is rather small. On the figure 2.10, on the plot of chirp signal and its frequency, the area from 100 Hz to 500 Hz, considered in [52] as quasi-stationary, is depicted. The frequency of signal above 500 Hz changes very fast in a short time. The SRM, moving to follow this frequency, is shifted faster, than it requires for the field to reach steady state. Therefore the dynamical tuning of the marked signal section from 500 Hz to the end of merger, where the signal frequency reaches the maximal value ans stops to change, cannot be described in the quasi-stationary approximation.

Though the area of the non-stationary dynamical tuning detection is very short in comparison to the overall signal, it contains the information about the last stage of inspiral and about the merger of two binary elements. This part of the coalescence could verify or falsify the GR with the new precision, and carries the information about the state of dense nuclear matter in case of neutron stars. The response of the detector during the non-stationary detection of this section cannot be modeled in quasi-stationary approximation and requires therefore the non-stationary model.
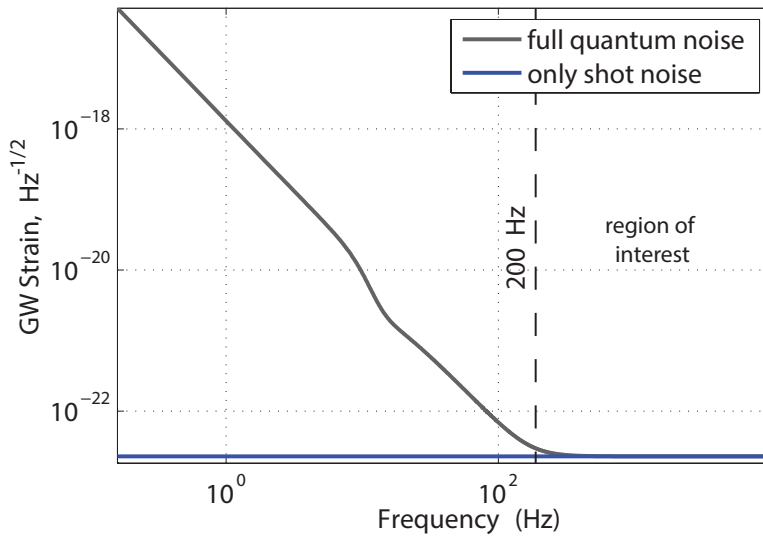
Figure 2.9.: Comparison of the full quantum noise and the shot noise only for quasi-stationary model of the dynamical tuning
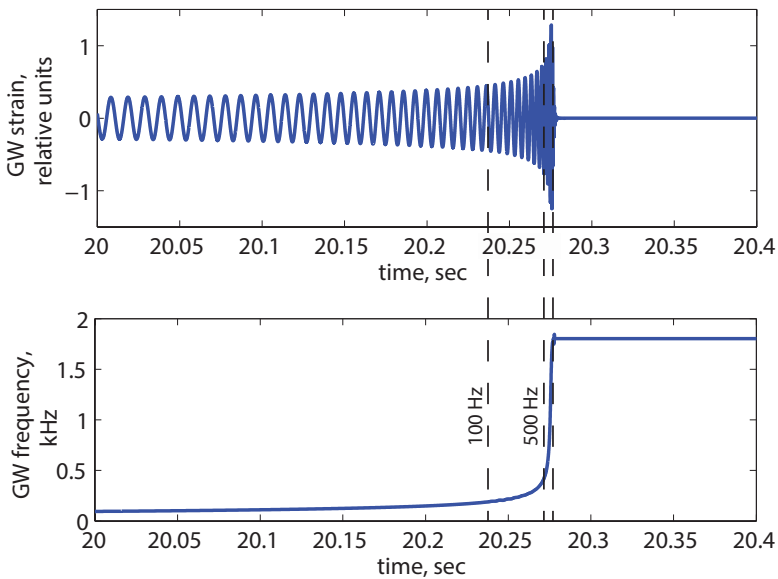
Figure 2.10.: Chirp signal and its instantaneous frequency. The signal section fitting for quasi-stationary approximation

Part II.

Non-stationary GW detectors in time-domain

THE properties of a stationary detector, considered in the previous chapter, make it appropriate for a special kind of the chirp signals detection, a so called dynamical tuning, when the frequency of the signal is followed by the optical resonance of detector. The frequency-domain model gives a quasi-stationary approximation of the dynamical tuning, emphasizing the area of its applicability. There is a short section with rapidly increasing, beginning from 500 Hz, where the detector falls out of the quasi-stationary regime (see figure 2.10).

The study of the radiation pressure established the frequency band above 200 Hz, where the quantum noise is shot noise dominated with negligible influence of radiation-pressure effects. This shot noise dominated frequency band covers the band of non-stationary detection regime during dynamical tuning. Therefore it is convenient to study the non-stationary dynamical detection only of the certain part of the GW, starting from the 200 Hz instantaneous frequency, by inventing a time-domain model for the detector response on the shot noise, displacement noise, GWs, and neglecting radiation-pressure effects.

The stationary detector is modeled as a linear system with constant parameters. It is very convenient to describe its response in the frequency domain, because every frequency component of the input influence causes the output signal with the same frequency, and can be considered separately. This response is described with a transfer function $R(\Omega)$ (see for example $k(\Omega)$ (2.6b)), and for some input $z(\Omega)$ one can easily find the output:

$$y(\Omega) = R(\Omega)z(\Omega) \tag{2.48}$$

When parameters of the detector, such as position of the SRM in the case of dynamical tuning, change fast enough, the frequency domain loses its charming attraction, because a single frequency component on the input causes the output with a finite-band spectrum, and the transfer function has no sense. It is possible to build a frequency-domain model, including all this finite band responses, but it is much more intuitively clear to switch to the time-domain.

In time domain we split the input influence in the infinitely short delta-impulses and sum the output responses of the detector on them. This reaction is called an impulse response $L(t_1, t_2)$ and is analogous to the transfer function in the frequency-domain. The signal on the output is then:

$$y(t) = \int\limits_{-\infty}^{t} L(t, t_1)z(t_1)dt_1 \tag{2.49}$$

It is easy to show, that in the stationary case the impulse response depends from the single argument:

$$L(t_1, t_2) = L(t_1 - t_2), \tag{2.50}$$

and it is bounded to the transfer function via the Fourier transform:

$$R(\Omega) = \int\limits_{-\infty}^{\infty} L(\tau)e^{-i\Omega\tau}d\tau. \tag{2.51}$$

55

The impulse response defines the signals and noise on the output of the detector, as response on the input injections.

The sensitivity of the detector in the frequency-domain is defined by the signal spectrum y(Ω) and the spectral density of noise $S(\Omega)$. Similarly to this, the sensitivity of the detector in time-domain is defined by the signal y(t) and the properties of noise, described by the autocorrelation function $B(t_1, t_2)$. The autocorrelation function in the stationary case is also a function of one variable and is bounded to the spectral density via the Fourier transform:

$$S(\Omega) = \int\limits_{-\infty}^{\infty} B(\tau)e^{-i\Omega\tau}d\tau. \tag{2.52}$$

This chapter is dedicated to the autocorrelation function of the shot noise in time-domain.

Analysis of shot noise

T HE shot noise of the detector is caused by ground state oscillations of the electro-
magnetic field in the vacuum. These oscillations may be assumed as injections
into the dark-port or in the end-mirrors of the field [71], described by the quantum
part of the equation (1.1) with the annihilation and creation operator as the field
amplitude. The non-stationary evolution of the injected field, obeying the equations
of Maxwell, may be described by the impulse response operator, which is obtained in
this chapter.

The losses in the arms and on the optics introduce additional shot noise, which
may be equivalently described as injections in the end-mirrors. The evolution of
these injections is represented by their own impulse response operator.

Finally, the evolution of the squeezed injection is considered similarly to shot noise.

3.1. Noise in time domain

The noise in the detector is a response on different inevitable stochastic processes,
occurring at almost every part of the detector. The main sources of noise are the
thermal fluctuations of the mirror coating and the ground state oscillations of the
electromagnetic fields. The basics, this consideration is grounded on, are presented
in [77]. The stochastic noisy process may be described by a *random function $\xi(t)$* of
a real variable t, meaning it has a random value for each t. This function is called a
random process if t is time. The autocorrelation function, describing the stochastic

properties of the random process, is defined as follows:

$$B_\alpha(t_1, t_2) = m\{\alpha(t_1)\alpha(t_2)\} = \int\limits_{-\infty}^{\infty} a_1 a_2 w_a(a_1 a_2, t_1, t_2) da_1 da_2. \qquad (3.1)$$

Here the moment of the function is denoted by m. The stochastic processes are denoted by greek letters, e.g. $\alpha(t)$, corresponding to the latin letter of the considered physical quantity, here a. The values that the noise takes at the instances of time t_1, t_2 we denote a_1, a_2. $w_x(a_1, a_2, t_1, t_2)$ is the two dimensional probability density function, defining the stochastic properties of the process.

    The operators of physical quantities are time-dependent in Heisenberg picture. The autocorrelation function of any such quantity of the shot noise, injected with state $|\psi\rangle$ is then:

$$B_\alpha(t_1, t_2) = m\{\alpha(t_1)\alpha(t_2)\} = \langle \psi \,|\hat{a}(t_1)\hat{a}(t_2)|\, \psi\rangle_{\text{sym}}, \qquad (3.2)$$

where ψ is the quantum state, $\hat{a}(t)$ is the quantum operator of the considered quantity. The autocorrelation function of the noise process a is analogous to the spectral density in frequency-domain (1.55).

    The ground state shot noise is an inevitable side-effect of measuring the perturbations in electromagnetic field, caused by GWs. As it was mentioned in the previous chapter, the current on the photodiode as the result of each homodyne or the DC-readout detection, is the physical value we measure directly.

    The electrical field of the ground noise electromagnetic oscillations are described with (1.1). The result of the homodyne detection (1.51) of this field is:

$$\hat{I}_{\text{det}}(t) = \frac{1}{2i} \int\limits_{-\infty}^{\infty} \sqrt{\frac{2\pi\hbar\omega_p}{\mathcal{A}c}} [\hat{a}(\omega_p + \Omega)e^{i\phi_{\text{lo}}} - \hat{a}^\dagger(\omega_p - \Omega)e^{-i\phi_{\text{lo}}}]e^{-i\Omega t}\frac{d\Omega}{2\pi}, \qquad (3.3)$$

where $\Omega = \omega - \omega_p$ is a is frequency of a sideband modulation. The current in the photodiode, depending on the different parameters of the measuring device, is determined up to some constant factor. For distinctness, we use the same factor for the homodyne detection here as on the right-hand side of (1.51).

    The autocorrelation function for the shot noise, calculated from the definition (3.2), reads:

$$B_\alpha(t_1, t_2) = C_z \delta(t_1 - t_2), \qquad (3.4)$$

where

$$C_z = \frac{\pi\hbar\omega_p}{2\mathcal{A}c} \qquad (3.5)$$

is a constant. The shot noise is delta-correlated, and therefore is white. Strictly speaking, it is white only under the assumption of the low-frequency sidebands of carrier frequency $\Omega \ll \omega_{\text{p}}$ – at higher frequencies there appears a frequency dependence.

    The squeezed noise is a modified shot noise, that has a decreased uncertainty along one quadrature, and an increased one along the perpendicular quadrature. If we now

measure the current $\hat{I}_{\text{det}}(t)$ from the squeezed state $|\alpha\rangle = \hat{S}(\Omega)\,|0_{\text{a}}\rangle$, using (2.43), we get the following autocorrelation function for it:

$$B_{\text{sq}}(t_1, t_2) = C_z \left(\cosh 2R - \sinh 2R \cos(2\theta + 2\phi_{\text{lo}}) \right) \delta(t_1 - t_2). \qquad (3.6)$$

We can see that depending on the squeezing angle θ we reach the quadrature with minimal (squeezed noise) and with maximal noise intensity (anti-squeezed noise):

$$B_{\text{min}}(t_1, t_2) = C_z e^{-2R} \delta(t_1 - t_2), \qquad (3.7a)$$

$$B_{\text{max}}(t_1, t_2) = C_z e^{2R} \delta(t_1 - t_2), \qquad (3.7b)$$

that differ from the shot noise by exponent with the squeezed factor R.

The shot noise injected into the dark port of the detector interacts optically and via radiation pressure with the GW detector and is reflected back towards the photodiode afterwards. Though both injected and reflected noises are random, the reflected one is defined by the input one: the field on the output is defined by the field on the input in the previous instances time.

The injections of shot noise in the detector, as it was shown in the section B.1, propagate between the elements, change their amplitudes and are split on the mirrors and beamsplitter, all according to the Maxwell's equations. Mathematically it is impossible to describe the phase shift of the real oscillating input signal, using only arithmetical operations: it also requires manipulations with the wave, shifted by the $\frac{\pi}{2}$ in the oscillations at the optical frequency of the input signal. Therefore instead of the impulse response function we introduce the impulse response operator:

$$y(t) = \int\limits_{-\infty}^{t} \mathcal{L}(t, t')[z(t')]dt', \qquad (3.8)$$

describing also the phase shift.

For the shot noise the considered input and output of the interferometer are z and y correspondingly, as it depicted in figure 2.1. It is convenient to consider the transformations of a wave, using the complex amplitude, when the real signal is represented as the real part of some complex number. The phase of the signal is considered then as argument of the complex quantity, and the amplitude – as its modulus.

The sinusoidal wave on the input of the detector may be represented in this picture as the following:

$$z(t) = \Re(e^{-i\omega t}) = \Re(e^{i\omega t}). \qquad (3.9)$$

The transformation of the input field, caused by the reflection from the detector, and described by the impulse response operator $\mathcal{L}(t, t')$, may be modeled by a complex function, describing the phase shift and amplitude ratio between the fields on the input and on the output at the instances t' and t correspondingly. The same phase shift in this complex function, also referred to as complex impulse response, corresponds to

the positive and to the negative argument of function, depending on the sign of the argument of the wave:

$$\int\limits_{-\infty}^{t} \mathcal{L}(t, t_1) \Re(e^{-i\omega t_1}) dt_1 \equiv \int\limits_{-\infty}^{t} |L_c(t, t_1)|\, e^{-i\varphi_L(t,t_1)} e^{-i\omega t_1}) dt_1 =$$

$$= \int\limits_{-\infty}^{t} \Re(L_c(t, t_1) e^{-i\omega t_1}) dt_1. \quad (3.10a)$$

$$\int\limits_{-\infty}^{t} \mathcal{L}(t, t_1) \Re(e^{-i\omega t_1}) dt_1 = \int\limits_{-\infty}^{t} \Re(L_c^*(t, t_1) e^{i\omega t_1}) dt_1. \quad (3.10b)$$

Therefore the impulse operator $\mathcal{L}(t, t_1)$ is by definition a complex impulse function $L_c(t, t_1)$ for the negatively oscillating exponent, and its conjugate $L_c^*(t, t_1)$ for the positively oscillating exponent.

The response of the detector on the monochromatic signal is dependent on the frequency of the input signal as a parameter. In the complex domain it reads:

$$R(t, \omega) \equiv \int\limits_{-\infty}^{t} L_c(t, t_1) e^{i\omega t_1} dt_1 \quad (3.11)$$

According to Fourier transform, we could "construct" an arbitrary input signal from the monochromatic signals of different frequencies. This property also mean that we can "construct" the complex impulse response from the responses on the monochromatic signals on different frequency. In other words, as it follows from (3.10a) the complex impulse response is a Fourier transform of this parametrized response on monochromatic waves:

$$L_c(t, t_1) = \int\limits_{-\infty}^{\infty} \frac{d\omega}{2\pi} R(t, \omega) e^{i\omega t_1}. \quad (3.12)$$

The field of the shot noise (1.1), injected from the dark port, is also an integral of the components with the positive and negative frequencies. Then, the shot noise on the output, followed from (3.10a) and (B.23), reads:

$$y(t) = \int\limits_{-\infty}^{t} dt_1 \int\limits_{0}^{\infty} \frac{d\omega}{2\pi} \sqrt{\frac{2\pi\hbar\omega}{\mathcal{A}c}} \left[\hat{a}(\omega) L_c(t, t_1) e^{-i\omega t_1} + \hat{a}^\dagger(\omega) L_c^*(t, t_1) e^{i\omega t_1} \right]. \quad (3.13)$$

The current on the photodiode after a homodyne detection (1.51) reads:

$$\hat{I}_{\text{det}}(t) = \frac{1}{2i} \int\limits_{-\infty}^{t} dt_1 \int\limits_{-\infty}^{\infty} \frac{d\Omega}{2\pi} \sqrt{\frac{2\pi\hbar\omega}{\mathcal{A}c}} \left[\hat{a}(\omega_p + \Omega) L_c(t,t_1) e^{i\omega_p(t-t_1)} e^{i\phi_{\text{lo}}} - \right.$$

$$\left. - \hat{a}^\dagger(\omega_p - \Omega) L_c^*(t,t_1) e^{-i\omega_p(t-t_1)} e^{-i\phi_{\text{lo}}} \right] e^{-i\Omega t_1} \quad (3.14)$$

And the autocorrelation function of this noise:

$$B_{\text{vac}}(t_1, t_2) = C_z \int_{-\infty}^{t_1} dt_1' \Re\left(L_s(t_1, t_1') L_s^*(t_2, t_1') \right), \quad (3.15)$$

where $L_s(t_1, t_1')$ is an auxiliary function introduced as

$$L_s(t_1, t_1') = L_c(t_1, t_1') e^{i\omega_p(t_1 - t_1')}, \quad (3.16)$$

here "s" stands for "shot-noise".

The photocurrent of squeezed input, reflected from the detector, reads:

$$\hat{I}_{\text{sq}}(t) = \frac{1}{2i} \int\limits_{-\infty}^{t} dt_1 \int\limits_{-\infty}^{\infty} \frac{d\Omega}{2\pi} \sqrt{\frac{2\pi\hbar\omega}{\mathcal{A}c}} \times$$

$$\times \left[\hat{a}(\omega_p + \Omega) \left(L_s(t,t_1) e^{i\phi_{\text{lo}}} \cosh R - L_s^*(t,t_1) e^{-2i\theta} e^{-i\phi_{\text{lo}}} \sinh R \right) + \right.$$

$$\left. + \hat{a}^\dagger(\omega_p - \Omega) \left(-L_s^*(t,t_1) e^{-i\phi_{\text{lo}}} \cosh R + L_s(t,t_1) e^{2i\theta} e^{i\phi_{\text{lo}}} \sinh R \right) \right] e^{-i\Omega t} \frac{d\Omega}{2\pi}. \quad (3.17)$$

The autocorrelation function for this noise:

$$B_{\text{sq}}(t_1, t_2) = C_z \int\limits_{-\infty}^{t_1} dt_1' \left| L_s(t_1, t_1') L_s(t_2, t_1') \right| \times$$

$$\times \left[\cosh 2R \cos(\varphi_s(t_1, t_1') - \varphi_s(t_2, t_1')) - \right.$$

$$\left. - \sinh 2R \cos(\varphi_s(t_1, t_1') + \varphi_s(t_2, t_1') + 2\theta + 2\phi_{\text{lo}}) \right], \quad (3.18)$$

where the argument of the auxiliary function is presented explicitly:

$$L_s(t, t_1) = \left| L_s(t, t_1) \right| e^{i\varphi_s(t, t_1)}. \quad (3.19)$$

3.2. Complex impulse response on the shot noise, injected into the dark port

The explicit expression for the complex impulse response of the detector on the shot noise, as it was mentioned in the previous section, may be obtained from the response

of the detector on a monochromatic input signal. We first consider the response of the detector on an arbitrary signal

In appendix C it was shown that fields inside the detector, for all their realistic frequencies, reflect back from the end-mirror completely to the signal recycling mode. According to propagation of the light in arms, as it is depicted in figure 2.1 it reads:

$$\hat{g}(t) = \frac{1}{2} R_n \hat{h} \left(t - 2\frac{2L_n}{c} \right) - \frac{1}{2} R_e \hat{h} \left(t - 2\frac{L_e}{c} \right). \tag{3.20}$$

Let us consider the response on an injection into the dark port by the source $Z_0(t)$, placed at such a distance from the source to the BS L_0 to have a whole number of waves there. The field reflected from the beamsplitter and the injections through the SRM are connected through the following equation:

$$\hat{h}(t) = -\frac{1}{2} R_s R_n \hat{h} \left(t - 2\frac{L_s \left(t - \frac{L_s}{c} \right) + L_n}{c} \right) +$$

$$+ \frac{1}{2} R_s R_n \hat{h} \left(t - 2\frac{L_s \left(t - \frac{L_s}{c} \right) + L_e}{c} \right) + iT_s \hat{z}_0 \left(t - \frac{L_0}{c} \right). \tag{3.21}$$

This equation is a difference equation for the field and is a convenient form for the description of the signal. It is also used in the other time-domain analysis of GW detectors [70, 72].

From this equation we can get the response to a monochromatic input signal

$$\hat{z}_0(t) = e^{-i\omega t} \tag{3.22}$$

under the following assumptions and using the following methods.

1) During dynamical tuning we move the SRM, i.e. change the length between the beamsplitter and the SRM with time $L_s(t)$, to follow the chirp signal frequency. However, the motions of the mirror are slow enough with respect to the characteristic duration of the light propagation inside the detector. To keep the high precision of the model, the displacement of the mirror during one round-trip 2τ is taken into account, while its displacement, the propagation from the beamsplitter to the SRM, is negligible $L_s \left(t - \frac{L_s}{c} \right) \approx L_s(t)$.

2) For the time-delay of the signal, and for the signal frequencies the difference of lengths between arms is negligible:

$$\tau \approx \frac{L_e}{c} \approx \frac{L_n}{c}. \tag{3.23}$$

3) The dark-port condition is represented as follows (see notations in table 2.1):

$$2k_p L_e = 2k_p L_e - \delta\phi_f, \tag{3.24a}$$

$$2k_p L_n = 2k_p L_n + \delta\phi_f \tag{3.24b}$$

4) The reflection of the field back to the SRM from the arms is described as following:

$$\frac{1}{2}\left(R_e e^{-i\delta\phi_f} + R_N e^{i\delta\phi_f}\right) = R_f e^{i\phi_f}, \tag{3.25}$$

where up to the first order of the smallness:

$$R_f \equiv \frac{1}{2}\sqrt{R_n^2 + R_e^2 + 2R_n R_e \cos 2\delta\phi_f} \approx \frac{1}{2}(R_n + R_e) \tag{3.26a}$$

and

$$\phi_f \equiv \arctan\left(\frac{R_e - R_n}{R_e + R_n}\tan\delta\phi_f\right) \approx 0. \tag{3.26b}$$

5) The equation (3.21) may be solved for the case of the monochromatic input signal (3.22). Using method of mathematical induction one can prove the following solution for the field inside the signal recycling cavity:

$$\hat{h}(t) = \sum_{n=1}^{\infty} iT_s e^{-i\omega t} \left(R_f R_s\right)^n \times$$

$$\times \left(e^{i2\tau\Omega}\right)^n \exp\left(\sum_{k=1}^{n} i2k_p x(t - 2(k-1)\tau)\right) + iT_S e^{-i\omega t}. \tag{3.27}$$

The field in this point defines also the field on the photodetector outside the cavity. Assume, the distance from the beamsplitter to the photodetector introduces the same phase shift, the whole number of 2π, as the distance from the source of injection into the dark port. The field at the output detector gives us the response of the detector on the input signal:

$$R(t,\omega) = \sum_{n=2}^{\infty} T_s^2 \left(R_F\right)^n R_s^{n-1} \left(e^{i2\tau\Omega}\right)^n \exp\left(\sum_{k=1}^{n-1} i2k_p x(t - 2k\tau)\right) +$$

$$+ T_s^2 e^{-i\omega t} e^{i2\tau\Omega} R_f - R_s e^{-i\omega t}\exp\left(-2ik_p x(t)\right). \tag{3.28}$$

From this response of the detector on the harmonic signal, substituting (3.28) into (3.12), we get the complex impulse response:

$$L_c(t, t_1) = e^{i\omega_p(t_1 - t)}\left[\sum_{n=2}^{\infty} T_s^2 R_f^n R_s^{n-1} \exp\left(\sum_{k=1}^{n-1} i2k_p x(t - 2k\tau)\right) \times \right.$$

$$\times \delta(t_1 - t + 2n\tau) + T_s^2 R_f \delta(t_1 - t + 2\tau) -$$

$$\left. - R_s \exp\left(-2ik_p x(t)\right)\delta(t_1 - t)\right]. \tag{3.29}$$

The physical meaning of the complex response, in contrast to the usual impulse response, is a response not on the delta-shaped quantity of the input field, but on the delta-shaped modulation of the wave with optical frequency ω_p. In this model we can really assume an infinitely short duration of the modulation as the elementary

components of the signals. However, this model is valid for signals with some finite duration of more than 10^{-9} seconds, according to the boundary conditions on the spectrum bandwidth described in appendix C.

The delta-like impulse of a laser light modulation is injected in the SRM at the instance t_1. The bigger part of the incident light is reflected from the SRM with the reflectivity R_s. The rest is injected inside the signal recycling cavity. Accroding to the model the injected part during its propagation inside the detector is split on the beamsplitter towards the arms, and assembles back on the beamsplitter after the reflection from the end-mirrors. Hence it is convenient to consider the evolution of the perturbations, caused by dark port injection, as the propagation of the amplitude modulation inside the single equivalent Fabry-Perot cavity formed by the SRM and the end-mirror with the reflectivity R_f. The time the light requires for the round trip inside the equivalent cavity is 2τ. The smaller part of this delta-impulse that reaches the SRM after the reflection from the arms is transmitted with the coefficient T_S, while the rest of it is reflected with, respectively, R_S. The reflected part comes back to the SRM after another full roundtrip, and the process repeats infinitely. As the result we have an infinite number of decaying "echo"-impulses with corresponding amplitudes $C_0, C_1, C_2, ...$ on the photodiode. The decay factor during one round trip is $R_s R_f$, and the phase shift between two consequent impulses, k-th and (k+1)-th, reads

$$\Delta\phi_k(t) = 2k_p x(t'_k), \tag{3.30}$$

where $t'_k = t + 2k\tau$ is the reflection instance of the k-th impulse, and x(t) is the microscopic displacement of the SRM from the resonant position of the equivalent cavity (see also appendix (D)).

The auxiliary function $L_s(t, t_1)$ from (3.16), found from (3.29) reads:

$$L_s(t, t_1) = \sum_{n=2}^{\infty} T_s^2 R_f^n R_s^{n-1} \exp\left(\sum_{k=1}^{n-1} i2k_p x(t - 2k\tau)\right) \times$$
$$\times \delta(t_1 - t + 2n\tau) + T_s^2 R_f \delta(t_1 - t + 2\tau) -$$
$$- R_s \exp\left(-2ik_p x(t)\right) \delta(t_1 - t). \tag{3.31}$$

This function describes the evolution of the modulations without the time-evolution of the optical oscillations, or the evolution of the "frozen" optical wave. In other words, it describes the evolution of the field inside the detector in the rotated frame.

To simplify the notation of the complex impulse response, denote the phase of k-th term from (3.29) as $\varphi_k(t)$. Using the accumulated phase shift (D.2-D.4), defined in appendix D they can be expressed by the simple formula:

$$\varphi_n(t) = \Phi_{N-1} - \Phi_{N-n}, \forall n \geq 0. \tag{3.32}$$

Using the phase shift, noted in such a way, the complex impulse response (3.29) gets the following look:

$$L_c(t, t_1) = e^{\omega_p(t_1 - t)} \sum_{n=1}^{\infty} T_s^2 \exp\left(i\varphi_n(t)\right) R_f^n R_s^{n-1} \delta(t_1 - t + 2n\tau) - R_s \delta(t_1 - t) \exp i\varphi_0(t).$$

$$\tag{3.33}$$
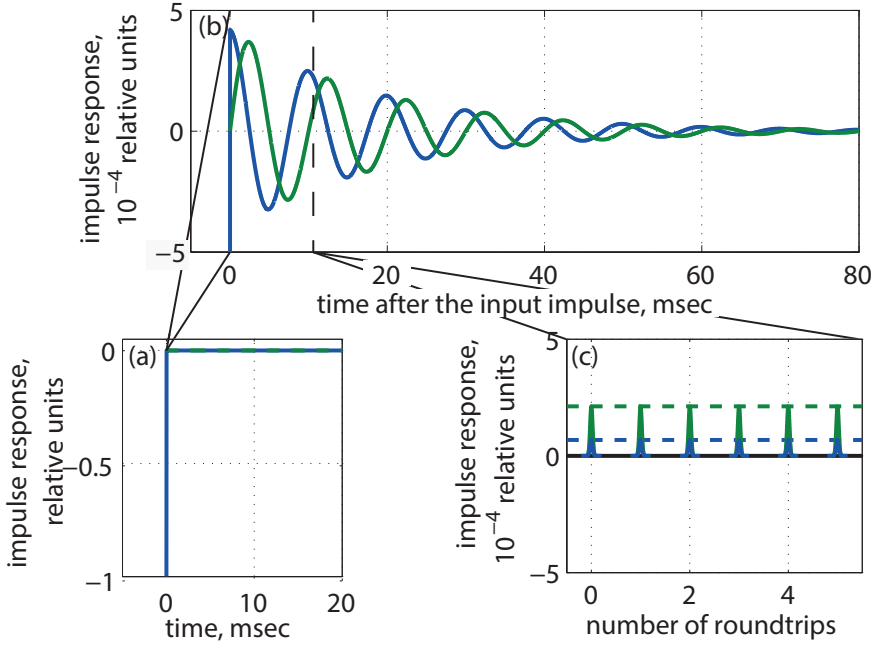
Figure 3.1.: Two quadratures of the auxiliary impulse response $L_s(t, t_1)$ on the vacuum quantum oscillations, injected from the dark port: (a) on a large amplitude scale, depicting the direct reflection of the impulse from the SRM inpulse, (b) on a small amplitude scale, representing SRM transmission from the inner SRC oscillations and decay, (c) on a short time scale, picturing the discrete nature of the impulse function and the round-trip time

And the auxiliary impulse response (3.16) turns in these notations to:

$$L_s(t, t_1) = \sum_{n=1}^{\infty} T_s^2 \exp\left(i\varphi_n(t)\right) R_f^n R_s^{n-1} \delta(t_1 - t + 2n\tau) - R_s \delta(t_1 - t) \exp i\varphi_0(t) \quad (3.34)$$

The typical plot of the impulse response for the GEO 600 with the signal recycling cavity tuned to 100 Hz, and with other parameters, presented in tables 2.1 and 2.2, is in figure 3.1.

3.3. Output noise autocorrelation function

The autocorrelation function of the output shot noise, caused by the injections into the dark-port, may be calculated by the substitution of the auxiliary impulse response $L_s(t, t_1)$ from (3.34) into the general expression for the shot noise autocorrelation function (3.15). The result of the integration of two delta functions, arising in the

obtained formula, is also a delta function:

$$\int\limits_{-\infty}^{\min(t_1,t_2)} dt_1' \delta(t_1' - (t_1 - \Delta t_1))\delta(t_1' - (t_2 - \Delta t_2)) = \delta(t_1 - \Delta t_1 - t_2 + \Delta t_2),$$

$$(\Delta t_1, \Delta t_2 \geq 0). \quad (3.35)$$

After the integration of these delta-functions multiplications and combining the terms, we could also express the phases of each term via the accumulated phase shifts (D.2-D.4) from appendix (D):

$$\varphi_n(t_1) - \varphi_m(t_1 + 2(m - n)\tau) = \Phi_{N_1-1} - \Phi_{N_1+m-n-1}; \forall n, m \geq 0. \quad (3.36)$$

Here we used that the accumulated phase shifts are zero for the negative indices.

As the result we get the following expression:

$$B_{\text{vac}}(t_1, t_2) = C_z \sum_{n=1}^{\infty} \sum_{m=1}^{\infty} T_s^4 \cos\left(\Phi_{N_1-1} - \Phi_{N_1+m-n-1}\right) R_f^{n+m} R_s^{n+m-2} \delta(t_2 - t_1 - 2(m-n)\tau) -$$

$$- C_z \sum_{n=1}^{\infty} T_s^2 \cos\left(\Phi_{N_1-1} - \Phi_{N_1-n-1}\right) R_f^n R_s^n \delta(t_2 - t_1 + 2n\tau) -$$

$$- C_z \sum_{n=1}^{\infty} T_s^2 \cos\left(\Phi_{N_1-1} - \Phi_{N_1+n-1}\right) R_f^n R_s^n \delta(t_1 - t_2 + 2n\tau) + C_z R_s \delta(t_1 - t_2) \quad (3.37)$$

For the further simplification of this expression we do the following steps.

1) We redefine $N = N_1 - 1$ for the convenience of the indices notation.

2) The double sum in (3.37) has terms with repeating arguments of delta functions, with equal $n - m$. These terms may combined by introducing of the new set of indices:

$$m' = n - m, \quad (3.38\text{a})$$
$$n' = n + m. \quad (3.38\text{b})$$

In the sum with the new indices m' changes from $-\infty$ to ∞ with step one, and n' changes from $|m'| + 2$ to ∞ with step 2.

3) The two single sum with index changing from 1 to ∞ may be combined to a single sum with the new index changing from $-\infty$ to ∞ with the step 1, by changing the index in one of this terms $n \to -n$, and by inserting an additional term, corresponding to $n = 0$.

Each sum has summands that consist of the same set of delta functions, therefore these two sums may be simply combined, giving the following expression as the result:

$$B_{\text{vac}}(t_1, t_2) =$$

$$= C_z \sum_{n=-\infty}^{\infty} \cos(\Phi_N - \Phi_{N-n}) R_F^{|n|} T_S^2 R_S^{|n|} \left[\frac{-1 + R_F^2}{1 - R_F^2 R_S^2}\right] \delta(t_1 - t_2 - 2n\tau) +$$

$$+ C_z \delta(t_1 - t_2). \quad (3.39)$$

If the output shot noise is caused only by the injections from the dark port, i.e. by the ideally reflective end-mirrors $R_{\mathrm{f}} = 0$, the whole sum becomes zero, and the auto-correlation function becomes equal to the one of the injected noise:

$$B_\eta(t_1, t_2) = C_z \delta(t_1 - t_2). \tag{3.40}$$

It means that though the detector with the SRM moving during a detection trans-forms the fields of the injected shot noise in a non-stationary way, they keep their autocorrelation function the same.

The finite transmittance and the losses of the end-mirrors, however, changes the noise on the output: it becomes correlated. The values of the noise are correlated every natural number of the round-trips, and the correlation decreases with the increasing of this number.

However, the imperfections in the arms and in the end-mirrors introduce their own additional injections into the output shot noise, which are therefore inseparable from the described above. If there are losses in the detector, the output noise, caused only by the injections in the SRM, has no physical meaning, and should be treated only together with the shot noise injections on the losses.

3.4. Complex impulse response on the shot noise, injected into the end-mirrors

In this section we repeat the calculation from section 3.2, finding the complex impulse response for the injection in the end-mirrors.

We remember the outcome of appendix C, that for all realistic frequencies of the fields inside the detector are reflected back from the end-mirror completely to the signal recycling mode.

According to the propagation of the fields in the detector, for the field, reflected from the arms and sourced by the injection of the shot noise in the end arms, we can write the following difference equation (see figure 2.1 for notations):

$$\hat{\mathrm{h}}(t) = \frac{1}{2} R_{\mathrm{s}} \left[R_{\mathrm{e}} \hat{\mathrm{h}} \left(t - 2\frac{L_{\mathrm{s}}(t)}{c} - 2\frac{L_{\mathrm{e}}}{c} \right) - R_{\mathrm{n}} \hat{\mathrm{h}} \left(t - 2\frac{L_{\mathrm{s}}(t)}{c} - 2\frac{L_{\mathrm{n}}}{c} \right) \right] +$$

$$+ \hat{\mathrm{u}} \left(t - 2\frac{L_{\mathrm{s}}(t)}{c} - \frac{L_{\mathrm{e}}}{c} \right) (iA_{\mathrm{e}}) \left(-\frac{\sqrt{2}}{2} \right) (-R_{\mathrm{s}}) + \hat{\mathrm{r}} \left(t - 2\frac{L_{\mathrm{s}}(t)}{c} - \frac{L_{\mathrm{n}}}{c} \right) (iA_{\mathrm{n}}) \left(i\frac{\sqrt{2}}{2} \right) (-R_{\mathrm{s}}).$$

$$\tag{3.41}$$

To calculate the complex impulse responses to the injection in the end-mirrors, we inject separately the complex exponent into the north mirror:

$$\hat{\mathrm{r}}(t) = e^{-i\omega t}, \tag{3.42a}$$

$$\hat{\mathrm{u}}(t) = 0, \tag{3.42b}$$

and into the east mirror:

$$\hat{r}(t) = 0, \tag{3.43a}$$

$$\hat{u}(t) = e^{-i\omega t} \tag{3.43b}$$

The final expressions could be obtained under the following assumptions, repeating those of section 3.2.

1) During dynamical tuning we move the SRM, i.e. change the length between the beamsplitter and the SRM with time $L_s(t)$, to follow the chirp signal frequency. However, the motions of the mirror are slow enough with respect to the characteristic duration of the light propagation inside the detector. To keep the high precision of the model, the displacement of the mirror during one round-trip 2τ is taken into account, while its displacement, while the light propagates from the beamsplitter to the SRM, is negligible $L_s\left(t - \dfrac{L_s}{c}\right) \approx L_s(t)$.

2) For the time-delay of the signal, and for the signal frequencies the difference of lengths between the arms is negligible:

$$\tau \approx \frac{L_e}{c} \approx \frac{L_n}{c}. \tag{3.44}$$

3) The dark-port condition is represented as following (see notations in table 2.1):

$$2k_p L_e = 2k_p L_e - \delta\phi_f, \tag{3.45a}$$

$$2k_p L_n = 2k_p L_n + \delta\phi_f \tag{3.45b}$$

4) The reflection of the field back to the SRM from the arms is described as following:

$$\frac{1}{2}\left(R_e e^{-i\delta\phi_f} + R_n e^{i\delta\phi_f}\right) = R_f e^{i\phi_f}, \tag{3.46}$$

where up to the first order of smallness:

5) For the monochromatic signal injected at the north and the east end-mirrors correspondingly (3.42-3.43), the equation (3.41) may be solved, using the method of mathematical induction. For each injection we have the following fields inside the detector correspondingly:

$$\hat{h}_n(t) = iA_n \frac{\sqrt{2}}{2} R_s e^{-i\omega t} e^{i\Omega\tau} \sum_{n=0}^{\infty} R_f^n R_s^n e^{i2n\Omega\tau} e^{\sum\limits_{k=0}^{n} 2ik_p x(t-2k\tau)}. \tag{3.47a}$$

$$\hat{h}_e(t) = iA_e \frac{\sqrt{2}}{2} R_s e^{-i\omega t} e^{i\Omega\tau} \sum_{n=0}^{\infty} R_f^n R_s^n e^{i2n\Omega\tau} e^{\sum\limits_{k=0}^{n} 2ik_p x(t-2k\tau)}. \tag{3.47b}$$

These fields in this point, as for the dark-port injections, define the field on the photodetector outside the cavity. The photodetector is the same, i.e. on the same

distance of the the whole number of the wavelengths from the beamsplitter. The responses on the monochromatic injections in the end-mirrors are correspondingly:

$$
R_{\mathrm{n}}(t,\omega) = A_{\mathrm{n}} T_{\mathrm{s}} \frac{\sqrt{2}}{2} e^{-i\omega t} e^{i\Omega\tau} +
$$

$$
+ A_{\mathrm{n}} T_{\mathrm{s}} \frac{\sqrt{2}}{2} e^{-i\omega t} e^{i\Omega\tau} \sum_{n=1}^{\infty} (R_{\mathrm{f}} R_{\mathrm{s}})^n \, e^{i2n\Omega\tau} e^{\sum_{k=1}^{n} 2ik_{\mathrm{p}} x(t-2k\tau)}. \quad (3.48\mathrm{a})
$$

$$
R_{\mathrm{e}}(t,\omega) = A_{\mathrm{e}} T_{\mathrm{s}} \frac{\sqrt{2}}{2} e^{-i\omega t} e^{i\Omega\tau} +
$$

$$
+ A_{\mathrm{e}} T_{\mathrm{s}} \frac{\sqrt{2}}{2} e^{-i\omega t} e^{i\Omega\tau} \sum_{n=1}^{\infty} (R_{\mathrm{f}} R_{\mathrm{s}})^n \, e^{i2n\Omega\tau} e^{\sum_{k=1}^{n} 2ik_{\mathrm{p}} x(t-2k\tau)}. \quad (3.48\mathrm{b})
$$

From these responses of the detector on the harmonic signal, substituting (3.48) into (3.12), and using phase shift trains (D.2) from appendix D, we get the complex impulse responses:

$$
L_{\mathrm{c,n\to d}} = A_{\mathrm{n}} T_{\mathrm{s}} \frac{\sqrt{2}}{2} e^{i\omega_{\mathrm{p}}(t_1 - t)} \left[\delta\left(t_1 - t + \tau\right) + \right.
$$

$$
\left. + \sum_{n=1}^{\infty} (R_{\mathrm{f}} R_{\mathrm{s}})^n \, e^{i\phi_n(t)} \delta\left(t_1 - t + \tau + 2n\tau\right) \right]. \quad (3.49\mathrm{a})
$$

$$
L_{\mathrm{c,e\to d}} = A_{\mathrm{e}} T_{\mathrm{s}} \frac{\sqrt{2}}{2} e^{i\omega_{\mathrm{p}}(t_1 - t)} \left[\delta\left(t_1 - t + \tau\right) + \right.
$$

$$
\left. + \sum_{n=1}^{\infty} (R_{\mathrm{f}} R_{\mathrm{s}})^n \, e^{i\phi_n(t)} \delta\left(t_1 - t + \tau + 2n\tau\right) \right]. \quad (3.49\mathrm{b})
$$

Here the indices n $\to$ d and e $\to$ d mean correspondingly "north to detector" and "east to detector".

The physical meaning of these complex responses is also a response on the delta-shaped modulation, but here it shows a bit different behavior of the impulse on the detector.

The delta-like impulse of a laser light modulation is injected in the end-mirror. The field requires time τ to pass the beamsplitter, and reach the SRM. The smaller part reaching the SRM is partly transmitted through and partly reflected from it, and then makes the round-trips, as it was described in section 3.2.

The impulse responses in the rotating frame are then:

$$
L_{\mathrm{s,n\to d}}(t, t_1) = A_{\mathrm{n}} T_{\mathrm{s}} \frac{\sqrt{2}}{2} \left[\delta\left(t_1 - t + \tau\right) + \right.
$$

$$
\left. + \sum_{n=1}^{\infty} (R_F R_S)^n \, e^{i\phi_n(t)} \delta\left(t_1 - t + \tau + 2n\tau\right) \right]. \quad (3.50\mathrm{a})
$$
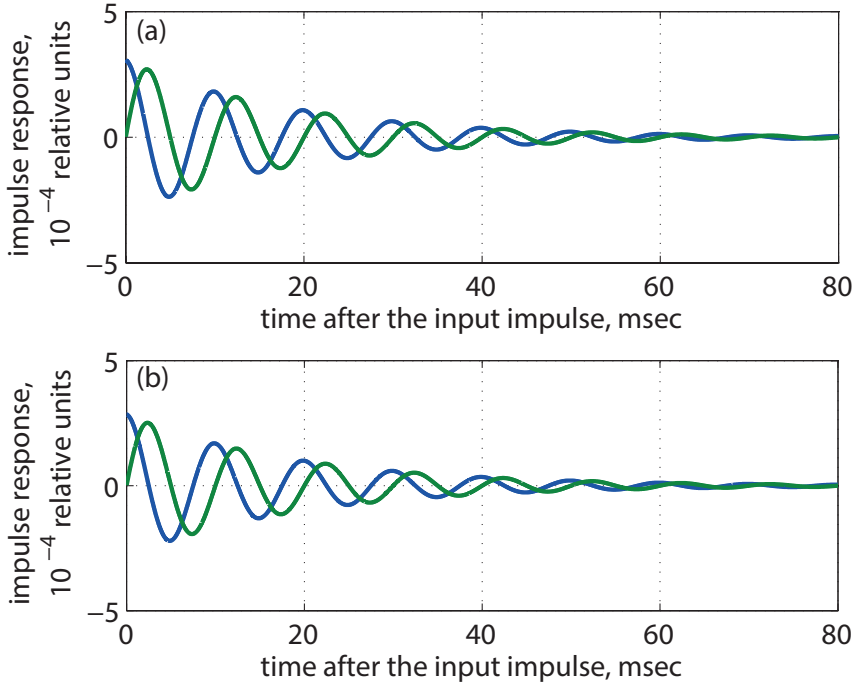
Figure 3.2.: Two quadratures of the impulse response on the vacuum quantum oscillations, injected from the equivalent end-mirrors: (a) from the north end-mirror, (c) from the east end-mirror

$$L_{s,e\to d}(t,t_1) = A_e T_s \frac{\sqrt{2}}{2} \left[\delta\left(t_1 - t + \tau\right) + \right.$$

$$\left. + \sum_{n=1}^{\infty} \left(R_F R_S\right)^n e^{i\phi_n(t)} \delta\left(t_1 - t + \tau + 2n\tau\right) \right]. \quad (3.50b)$$

The typical plots of the impulse responses for the shot noise, injected from the end-mirrors, for the GEO 600 with the signal recycling cavity tuned to 100 Hz, and with other parameters, presented in tables 2.1 and 2.2, are in figure 3.2.

3.5. Autocorrelation function of output noise, sourced from the end mirrors

One can calculate the autocorrelation functions of the output shot noise, caused by the injections of the ground state oscillations in the end mirrors, substituting $L_s(t,t_1)$ from (3.50a) into (3.15). The expressions for the autocorrelation functions after integrating over two delta functions, as in (3.35), and substituting accumulated phase shift (D.12)

read correspondingly:

$$B_{\eta(\mathrm{n})}(t_1, t_2) = \frac{1}{2} C_z A_{\mathrm{n}}^2 T_{\mathrm{s}}^2 \left[\delta\left(t_2 - t_1\right) + \right.$$

$$+ \sum_{n=1}^{\infty} (R_{\mathrm{f}} R_{\mathrm{s}})^n \cos(\Phi_{N_1-1} - \Phi_{N_1-n-1}) \delta\left(t_2 - t_1 + 2n\tau\right) +$$

$$+ \sum_{n=1}^{\infty} (R_{\mathrm{f}} R_{\mathrm{s}})^n \cos(\Phi_{N_1+n-1} - \Phi_{N_1-1}) \delta\left(t_1 - t_2 + 2n\tau\right) +$$

$$+ \sum_{n=1}^{\infty} \sum_{m=1}^{\infty} (R_{\mathrm{f}} R_{\mathrm{s}})^{n+m} \cos(\Phi_{N_1-1} - \Phi_{N_1+m-n-1}) \delta\left(t_1 - t_2 + 2(m-n)\tau\right) \Bigg]. \quad (3.51\mathrm{a})$$

$$B_{\eta(\mathrm{e})}(t_1, t_2) = \frac{1}{2} C_z A_{\mathrm{e}}^2 T_{\mathrm{s}}^2 \left[\delta\left(t_2 - t_1\right) + \right.$$

$$+ \sum_{n=1}^{\infty} (R_{\mathrm{f}} R_{\mathrm{s}})^n \cos(\Phi_{N_1-1} - \Phi_{N_1-n-1}) \delta\left(t_2 - t_1 + 2n\tau\right) +$$

$$+ \sum_{n=1}^{\infty} (R_{\mathrm{f}} R_{\mathrm{s}})^n \cos(\Phi_{N_1+n-1} - \Phi_{N_1-1}) \delta\left(t_1 - t_2 + 2n\tau\right) +$$

$$+ \sum_{n=1}^{\infty} \sum_{m=1}^{\infty} (R_{\mathrm{f}} R_{\mathrm{s}})^{n+m} \cos(\Phi_{N_1-1} - \Phi_{N_1+m-n-1}) \delta\left(t_1 - t_2 + 2(m-n)\tau\right) \Bigg]. \quad (3.51\mathrm{b})$$

Here η corresponds to the point y in (2.1), where the noise is measured.

The simplifications here repeat those of 3.3. Let us write them explicitly in this section as well:

1) We redefine $N = N_1 - 1$ for the convenience of the indices notation.

2) The double sum in (3.51a) has terms with repeating arguments of delta functions, with equal $n - m$. These terms may be combined by introducing a new set of indices:

$$m' = n - m, \quad (3.52\mathrm{a})$$

$$n' = n + m. \quad (3.52\mathrm{b})$$

In the sum with the new indices m' changes from $-\infty$ to ∞ with step one, and n' changes from $|m'| + 2$ to ∞ with step 2.

3) The two single sums with index going from 1 to ∞ may be combined to a single sum with index ranging from $-\infty$ to ∞ with the step 1, by changing the index in one of this terms $n \to -n$, and by inserting an additional term, corresponding to $n = 0$.

Each sum has summands, that consist of the same set of delta functions, therefore these two sums may be simply combined, giving the following expression as result:

$$B_{\eta(\mathrm{n})}(t_1, t_2) = \frac{1}{2} C_z A_{\mathrm{n}}^2 T_{\mathrm{s}}^2 \sum_{n=-\infty}^{\infty} \cos(\Phi_N - \Phi_{N-n}) \frac{(R_{\mathrm{f}} R_{\mathrm{s}})^{|n|}}{1 - [R_{\mathrm{f}} R_{\mathrm{s}}]^2} \delta(t_1 - t_2 - 2n\tau), \quad (3.53\mathrm{a})$$

$$B_{\eta(\mathrm{e})}(t_1, t_2) = \frac{1}{2} C_z A_{\mathrm{e}}^2 T_{\mathrm{s}}^2 \sum_{n=-\infty}^{\infty} \cos(\Phi_N - \Phi_{N-n}) \frac{(R_{\mathrm{f}} R_{\mathrm{s}})^{|n|}}{1 - [R_{\mathrm{f}} R_{\mathrm{s}}]^2} \delta(t_1 - t_2 - 2n\tau) \quad (3.53\mathrm{b})$$

The autocorrelation function from two uncorrelated noises is the sum of their autocorrelation functions. Therefore, the total output noise from the injections into the end-mirrors reads:

$$B_{\eta(\mathrm{f})}(t_1, t_2) = C_z (R_{\mathrm{f}} R_{\mathrm{s}})^{|n|} T_{\mathrm{s}}^2 \sum_{n=-\infty}^{\infty} \cos(\Phi_N - \Phi_{N-n}) \frac{1 - R_{\mathrm{f}}^2}{1 - [R_{\mathrm{f}} R_{\mathrm{s}}]^2} \times$$
$$\times \, \delta(t_1 - t_2 - 2n\tau). \quad (3.54)$$

One could recognize in this expression the part of (3.39). Easy to see, that the total noise, formed by the ground state injections in the dark-port and in the end mirrors gives us the white noise:

$$B_{\mathrm{vac}}^{\mathrm{tot}}(t_1, t_2) = C_z \delta(t_1 - t_2). \quad (3.55)$$

Therefore the output noise of GEO 600 with the moving SRM stays white, independently from its motion law and from the losses on the end-mirrors, and, correspondingly, from the injection of the ground-state oscillations in them. There are two laws leading to this result: the energy conversation law on the mirrors $T^2 + R^2 = 1$ and fluctuation dissipation theorem, connecting the losses and injection of the noise in the detector.

This result is also consistent with the results obtained in the frequency-domain consideration in chapter 2, where the quantum noise on the photodiode is represented by operator $\hat{r}(\Omega)$, defined in (2.6a). The spectral density of that noise is constant, and therefore, the autocorrelation function is detla-function. The constants of these two noises fit to each other up to the amplitude of the local oscillator during homodyne detection.

3.6. Squeezed light

The shot noise on the photodetector is formed by the shot noise, injected into the dark port and injected into the end-mirrors. To reduce the level of noise at some quadrature, the squeezed quantum noise instead of the ground state noise is injected into the dark port. The squeezed noise evolves inside the detector and is detected on the photodetector along with the injections from the end-mirrors.

The autocorrelation function of the part of the noise, caused only by the squeezing injections, obtained by the substitution of the auxiliary delta response (3.34) into the general formula for the squeezed noise (3.18), reads:

$$B_{\mathrm{sq}}(t_1, t_2) = C_z \sum_{n=0}^{\infty} \sum_{m=0}^{\infty} A_n A_m \delta(t_2 - t_1 - (m-n)\tau) \left[\cos(\varphi_n'(t_1) - \varphi_m'(t_2)) \cosh 2R - \right.$$
$$\left. - \cos(\varphi_n'(t_1) + \varphi_m'(t_2)) \sinh 2R \right], \quad (3.56)$$

where the following variables were introduced for simplicity:

$$A_0 = -R_{\text{s}} \tag{3.57a}$$

$$A_n = T_{\text{s}}^2 R_{\text{f}}^n R_{\text{s}}^{n-1}, n > 0, \tag{3.57b}$$

$$\varphi_n'(t) = \varphi_n(t) + \phi_{\text{lo}} + \theta. \tag{3.57c}$$

A_n are the amplitudes of the terms of the linear response in the rotated frame (see (3.34)).

It is convenient to describe the influence of the ground state oscillations, injected from the end-mirrors as the difference between the total shot noise (3.55) and the ground state injections from the dark port, that can be represented as (3.56) with the squeezing factor R equals to zero. The result reads:

$$B_{\text{sq}}(t_1, t_2) = C_z \delta(t_1 - t_2) +$$

$$+ C_z \sum_{n=0}^{\infty} \sum_{m=0}^{\infty} A_n A_m \delta(t_2 - t_1 - (m - n)\tau) \left[\cos(\varphi_n'(t_1) - \varphi_m'(t_2))(\cosh 2R - 1) - \right.$$

$$\left. - \cos(\varphi_n'(t_1) + \varphi_m'(t_2)) \sinh 2R \right], \quad (3.58)$$

Squeezed noise, given by the formula (3.56) may be simulated numerically.

Analysis of differential end-mirror motion.

A GRAVITATIONAL wave affects the fields inside the detector via differential end-mirror motion. The impulse response, describing the modulations of the field inside the detector, caused by this motion, is described in this chapter. The explicitly found impulse response allows to analyze some features of the dynamical tuning. We can establish the exact conditions of the resonant tracking, and also the transformations it introduces to the shape of the detected GW signal.

A bunch of influences on the detector, referred together to as displacement noise, causes a stochastic end-mirror motion. The response of the detector on the differential mode of this motion also has non-stationary features, due to SRM motion. The impulse response to the differential motion allows to calculate the autocorrelation function of the displacement noise, the main components of which are the seismic fluctuations, gravity gradient noise, and Brownian noise of the mirror coatings and of the suspension.

The signal on the output of the detector would have the deformed shape with respect to the incident GW. However, this transformation, defined by the impulse response, has one to one correspondence, and therefore, it is possible to restore, or deconvolute, the initial GW shape from the measured one on the photodiode.

As it was shown in the previous chapter, a part of the current, measured on the photodiode, is caused not by the differential mirror motion, but from the shot noise. Therefore, a real deconvoluted signal would have a part not corresponding to the real mirror-motion. The deconvolution of this noise was also described in this chapter.

The DC-readout is a more realistic way of detecting GWs than homodyne detection. However it gives a different signal on the photodetector. The last part of this chapter will be dedicated to the signals and noise in the current from the photodetector during the DC-readout.

4.1. Impulse response at the dark port

4.1.1. Recycled Michelson configuration

GEO 600 measures the differential end-mirror motion, caused by gravitational waves. An arbitrary motion of the end-mirrors, $x_e(t)$ and $x_n(t)$ respectively, produces a sideband in the signal-recycling cavity. This wave falling on the beamsplitter from the dark port is reflected back from the end-mirrors completely. The component of the field, sourced by the end-mirror motion, together with its round-trip evolution gives the following difference equation:

$$\hat{h}(t) = R_s k_p e^{2ik_p x(t)} E R_1(t - \tau) e^{i\varphi_1(t-\tau)} + R_s e^{2ik_p x(t)} R_f e^{i\phi_f} \hat{h}(t - 2\tau), \qquad (4.1)$$

where the end-mirror influence is described by the following expressions, obtained by a linear approximation with respect to the phase of dark-fringe offset:

$$R_1(t) \approx 2R_f x_d(t) + 2R_0 x_s(t) \qquad (4.2a)$$

$$\varphi_1 : (\sin \varphi_1(t) \approx \frac{R_e x_e(t) + R_n x_n(t)}{R_1} \delta\phi_f) \cap (\cos \varphi_1 \approx \frac{2R_f x_d(t) + 2R_0 x_s(t)}{R_1} \cos \delta\phi_f) \qquad (4.2b)$$

with the new quantities introduced for convenience:

$$R_f = \frac{R_e + R_n}{2} \approx 1, \qquad (4.3a)$$

$$R_0 = \frac{R_e - R_n}{2} \approx 3 \times 10^{-5}, \qquad (4.3b)$$

$$x_s(t) = \frac{x_e(t) + x_n(t)}{2}, \qquad (4.3c)$$

$$x_d(t) = \frac{x_e(t) - x_n(t)}{2}. \qquad (4.3d)$$

The quantities R_f and R_0 define the sensitivity of the detector to differential and common mirror motions correspondingly. Their typical values allow to neglect R_0, making the following approximation for them:

$$R_1(t) \approx 2R_f x_d(t), \qquad (4.4a)$$

$$\varphi_1(t) \approx 0. \qquad (4.4b)$$

The phase $\varphi_1(t)$ varies significantly from zero, when $R_1(t)$ has very small values. However, since we could neglect such values, large phases have no physical meaning.

With these approximation, the difference equation for the field inside the signal recycling cavity, sourced by the end-mirror motion, reads:

$$\hat{h}(t) \approx 2R_s R_f E k_p x_d(t - \tau) e^{2ik_p x(t)} + R_s R_f \hat{h}(t - 2\tau) e^{2ik_p x(t)}. \qquad (4.5)$$

The solution for the field, described for convenience in a different point of the signal recycling cavity is:

$$\hat{g}(t) = -2R_{\mathrm{f}}Ek_{\mathrm{p}}x_{\mathrm{d}}\left(t-\tau\right)-$$

$$-2\sum_{n=1}^{\infty}R_{\mathrm{f}}^{n+1}R_{\mathrm{s}}^{n}Ek_{\mathrm{p}}x_{\mathrm{d}}\left(t-2n\tau-\tau\right)e^{2ik_{\mathrm{p}}\sum_{k=1}^{n}x(t-2k\tau)}. \quad (4.6)$$

After taking into account the evolution of the sideband towards the dark-port, and its detection using a homodyne local oscillator (1.51), we get the influence of the differential end-mirror motion on the current in the photodetector:

$$I_{\mathrm{det}}(t) = \sum_{n=0}^{\infty}C_{n}\cos(\xi_{n}(t))x_{\mathrm{d}}\left(t-(2n+1)\tau\right), \quad (4.7)$$

where the amplitudes and the phase shifts of the terms are defined as following:

$$C_{0} = -2\sqrt{2}\sqrt{\frac{\pi\hbar\omega_{p}}{\mathcal{A}c}}R_{\mathrm{f}}T_{\mathrm{s}}|E|k_{\mathrm{p}}, \quad (4.8a)$$

$$C_{n} = C_{0}(R_{\mathrm{f}}R_{\mathrm{s}})^{n}, \quad (4.8b)$$

$$\xi_{0}(t) = \phi_{\mathrm{h}}, \quad (4.8c)$$

$$\xi_{n}(t) = \phi_{\mathrm{h}} + 2k_{\mathrm{p}}\sum_{k=1}^{n}x(t-2k\tau) \quad (4.8d)$$

and

$$\phi_{\mathrm{h}} = \phi_{\mathrm{lo}} + \phi_{\mathrm{e}} \quad (4.9)$$

is a homodyne angle, and ϕ_{e} is the phase of field E.

Unlike the response on the shot noise, the response on the differential mirror motion, though carried by the laser radiation, doesn't contain the optical oscillation part, and can therefore be described by the normal impulse response, i.e. the response to the delta-like input impulse:

$$L_{\mathrm{s}\to\mathrm{c}} = \sum_{n=0}^{\infty}C_{n}\cos(\xi_{n}(t))\delta\left(t_{1}-t+(2n+1)\tau\right). \quad (4.10)$$

The plot of the impulse response is depicted in FIG. 4.1. For the plot we use the parameters from tables 2.1 and 2.2.

The delta-like impulse in the differential motion of the end-mirrors modulates the phase of the laser fields at their surfaces. These fields are formed from the field E falling on the beamsplitter. The phases of two modulations in the arms have the opposite signs, therefore they interfere constructively towards the dark port on the beamsplitter forming the amplitude modulation, which has the shape of a short laser impulse. The interference is reversible, hence it is convenient to consider the evolution of the perturbations, caused by differential end-mirrors motion, as the propagation
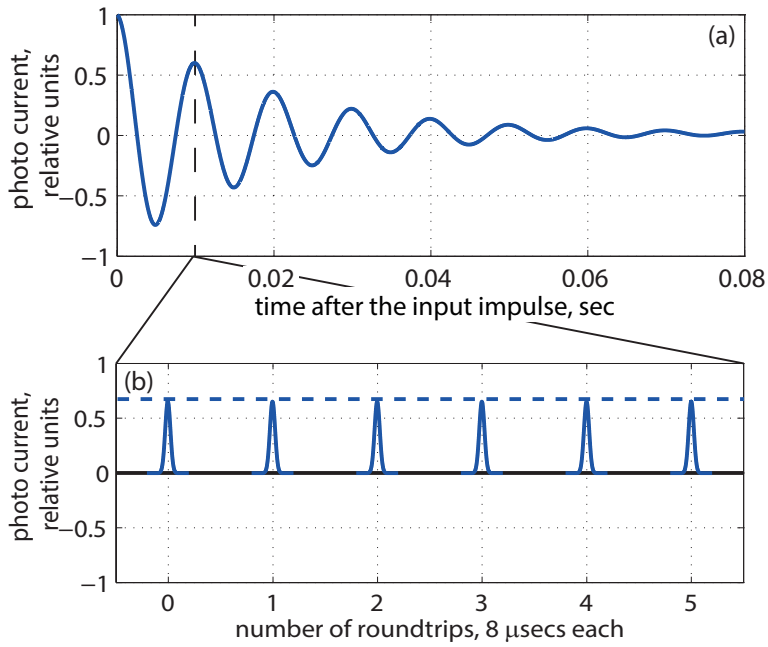
Figure 4.1.: The typical impulse response of the considered detector with a constant detuning $f_{\mathrm{tun}} = 100\,\mathrm{Hz}$: (a) in the response decay-time scale, (b) in the single round-trip time scale

of the amplitude modulation inside a single equivalent Fabry-Perot cavity formed by the SRM and the end-mirror with the reflectivity $R_{\rm f}$. The time the light requires for a round trip inside the equivalent cavity is 2τ. The smaller part of the laser impulse that reaches the SRM is transmitted with the coefficient T_S, while the rest of it is reflected with, respectively, R_S. The reflected part comes back to the SRM after the full roundtrip and the process repeats infinitely. As the result we have an infinite number of decaying "echo"-impulses with corresponding amplitudes $C_0, C_1, C_2, \ldots$ on the photodiode. The decay factor during one round trip is $R_S R_F$, and the phase shift between two consequent impulses, k-th and (k+1)-th, reads

$$\delta(t'_k) = 2k_{\rm p}x(t'_k), \tag{4.11}$$

where $t'_k = t_1 + (2k + 1)\tau$ is the reflection instance of the k-th impulse, and x(t) is the microscopic displacement of the SRM from the resonant position of the equivalent cavity.

It can be shown that the impulse response for the case of stationary detector with $x(t) = $const is a Fourier transform of the transfer function $k(\Omega)$ from the frequency-domain description of the detector, defined in (2.6b).

4.1.2. Delay line

The early proposals for GW detectors had the delay lines instead of Fabry-Perot cavities to increase the optical length of the arm and, therefore, the sensitivity to the GWs. Unlike the Fabry-Perot cavity, the light inside the delay line makes only the certain number of roundtrips before it is reflected back to the beamsplitter, as it depicted in figure 4.2. Similar to the layout with the Fabry-Perot cavities in arms, delay lines require additional mirrors near the beamsplitter. We denote the reflectivities of these closer mirrors as $R_{\rm ec}$ and $R_{\rm nc}$ for, correspondingly, the east and the north arms. The number of round trips in an early proposal [40] was $N_{\rm rt} = 40$. The current GEO 600 configuration has folded arms (see section 2.3), which are delay lines with $N_{\rm rt} = 2$.

If the GW has a slow frequency, the change displacement of the end-mirrors, caused by GWs, is insignificant during the time the light spends in a delay line. The reflection from the delay line in this case is equivalent to the reflection from a single arm with an optical length of the whole delay line, and with an end-mirror reflectivity equal to joint reflectivity of all the reflections during light travels there. A GW with high frequency may change the value of its strain fast enough to break the equivalence. For such frequencies the reflection from the arms with delay lines is described by the following equations, which are modifications of (B.7) and (B.5):

$$\hat{\rm i}_{\rm dl}(t) = -i\frac{\sqrt{2}}{2}R_{\rm e}^{N_{\rm rt}}R_{\rm ec}^{N_{\rm rt}-1}\hat{\rm e}(t - 2N_{\rm rt}\tau)-$$

$$-\frac{\sqrt{2}}{2}R_{\rm e}^{N_{\rm rt}}R_{\rm ec}^{N_{\rm rt}-1}\hat{\rm h}(t - 2N_{\rm rt}\tau) + \sum_{k=0}^{N_{\rm rt}-1}\sqrt{2}R_{\rm e}k_{\rm p}x_{\rm e}(t - \tau - 2k\tau)E\left(R_{\rm e}R_{\rm ec}\right)^k. \tag{4.12a}$$
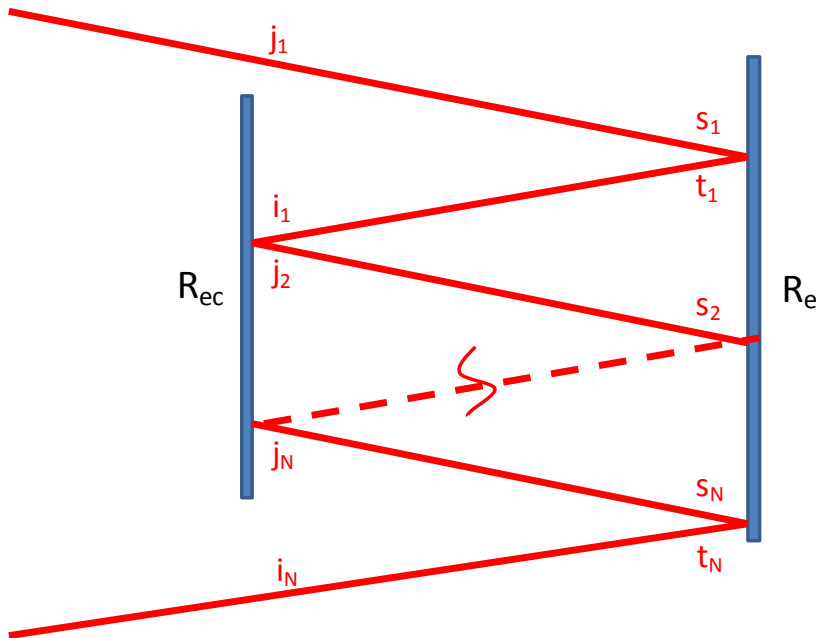
Figure 4.2.: Scheme of a delay line.

$$\hat{l}_{dl}(t) = \frac{\sqrt{2}}{2} R_n^{N_{rt}} R_{nc}^{N_{rt}-1} \hat{e}(t - 2N_{rt}\tau) +$$

$$+ i\frac{\sqrt{2}}{2} R_n^{N_{rt}} R_{nc}^{N_{rt}-1} \hat{h}(t - 2N_{rt}\tau) + \sum_{k=0}^{N_{rt}-1} \sqrt{2} i R_n k_p x_e(t - \tau - 2k\tau) E \left(R_n R_{nc}\right)^k. \tag{4.12b}$$

The maximal signal amplification is obtained, when the mirrors in a delay line are tuned to resonance, so the the signals, injected by the displaced mirrors, sum up in phase. In this subsection we assume the detector without the signal recycling mirror, therefore the phase, the field obtains propagating from the delay line to the photodetector, is unimportant. Under this considerations, and also under the dark-port conditions, similar to (4.1-4.5), the reflection from the arms with the delay line reads:

$$\hat{g}(t) \approx -R_f(N_{rt} - 1)\hat{h}(t - N_{rt}\tau) + 2 \sum_{k=0}^{N_{rt}-1} \frac{\omega_p}{c} E R_f(k) x_d(t - (2k+1)\tau), \tag{4.13}$$

where the new equivalent reflectivity after k round-trips in a delay line is introduced:

$$R_f(k) = \frac{R_n^{k+1} R_{nc}^k + R_e^{k+1} R_{ec}^k}{2}. \tag{4.14}$$

The propagation of this field to the detector, followed by the homodyne detection, defines the photocurrent, caused by the differential mirror motion. By setting a delta-shaped motion of the end-mirrors one gets the impulse response of a Michelson based detector with delay lines:

$$L_{s \to c(dl)}(t_1, t_1') = \sum_{k=0}^{N_{rt}-1} A_k \cos(\phi_h)\delta(t_1 - t_1' + \tau/2 + k\tau), \tag{4.15}$$

where

$$A_k = 4\sqrt{2}k_p|E|R_f(k). \tag{4.16}$$

4.1.3. Delay line with SRM.

The detector with delay lines may also be dynamically tuned to the detected chirp GW, by implementing and moving the SRM. The equation (4.13), describing the light injection due to the end-mirror differential motion, may be modified to describe the recycling:

$$\hat{h}(t) = -R_s R_f(N_{rt} - 1)\hat{h}(t - 2N_{rt}\tau)e^{2ik_p x(t)} -$$

$$- 2 \sum_{k=0}^{N_{rt}-1} k_p E R_s R_f(k)e^{2ik_p x(t)} x_d(t - \tau/2 - k\tau). \tag{4.17}$$
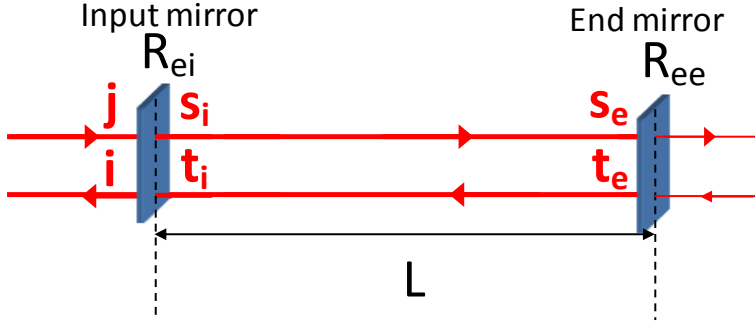
Figure 4.3.: Scheme of a Fabry Perot cavity in the arm.

The solution of this recurrent equation reads:

$$\hat{h}(t) = -2 \sum_{n=0}^{\infty} \sum_{k=0}^{N_{\text{rt}}-1} k_{\text{p}} E R_{\text{s}} R_{\text{f}}(k) \left(R_{\text{s}} R_{\text{f}}(N_{\text{rt}}-1) \right)^n e^{\sum_{j=0}^{n} 2ik_{\text{p}}x(t-2jN_{\text{rt}}\tau)} \times$$

$$\times x_{\text{d}}(t - (2nN_{\text{rt}} + 2k + 1)\tau). \quad (4.18)$$

After the calculation of the field evolution from the beamsplitter through the SRM and towards the point of the detection on the homodyne detector, and after the substituting the delta-like signal end-mirror motion we get the impulse response of the signal recycled detector with the delay line:

$$L_{\text{s}\to\text{c(dlsr)}}(t_1, t_1') =$$

$$= \sum_{n=0}^{\infty} \sum_{k=0}^{N_{\text{rt}}-1} A_{nk} \cos\left(\xi_n(t)\right) \delta(t_1 - t_1' + (2nN_{\text{rt}} + 2k + 1)\tau), \quad (4.19)$$

where

$$A_{nk} = -4\sqrt{2} k_{\text{p}} |E| T_{\text{s}} R_{\text{f}}(k) \left(R_{\text{s}} R_{\text{f}}(N_{\text{rt}}-1) \right)^n, \quad (4.20\text{a})$$

$$\xi_n(t) = \sum_{j=0}^{n} 2ik_{\text{p}}x(t - 2jN_{\text{rt}}\tau) - 2ik_{\text{p}}x(t) + \phi_{\text{h}} \equiv \phi_n(t) + \phi_h. \quad (4.20\text{b})$$

The phase shift $\xi_n(t)$, that the field gets during n roundtrips inside the detector, may also be described via the accumulated phase shift, introduced in appendix D.2, with phase-shift trains $\phi_n(t)$ defined in (D.16).

4.1.4. Fabry-Perot cavity in arm

All interferometric gravitational wave detectors, except for the one considered in this thesis, GEO 600, have Fabry-Perot cavities in the arms. The difficulty of considering this configuration in the time-domain is in the double cavity system.

The scheme of the detector is modified by adding a Fabry-Perot cavity in the arms, which is shown in figure 4.3. On the plot the new notations for the fields in the Fabry-Perot cavity of the east arm are presented, while the notations of the north arm are equivalent. The cavities in the arms are tuned in order to get the maximal field amplitude on the mirrors. The boundary conditions for east arm cavity are:

$$\hat{i}(t) = -R_{ei}\hat{j}(t) + iT_{ei}\hat{t}_i(t), \tag{4.21a}$$

$$\hat{s}_i(t) = -R_{ei}\hat{t}_i(t) + iT_{ei}\hat{j}(t), \tag{4.21b}$$

$$\hat{t}_i(t) = -R_{ee}\hat{s}_i(t - 2\tau) - 2iR_{ee}k_p x_e(t - \tau)S. \tag{4.21c}$$

The equivalent set of the equations for the north cavity mirrors reads:

$$\hat{l}(t) = -R_{ni}\hat{k}(t) + iT_{ni}\hat{m}_i(t), \tag{4.22a}$$

$$\hat{n}_i(t) = -R_{ni}\hat{m}_i(t) + iT_{nI}\hat{k}(t), \tag{4.22b}$$

$$\hat{m}_i(t) = -R_{ne}\hat{n}_i(t - 2\tau) - 2iR_{ne}k_p x_n(t - \tau)N. \tag{4.22c}$$

From this equations the fields, leaking out of a Fabry-Perot cavities may be expressed:

$$\hat{i}(t) = -R_{ei}\hat{j}(t) + T_{ei}^2 R_{ee} \sum_{k=0}^{\infty} \hat{j}(t - 2(k+1)\tau)(R_{ee}R_{ei})^k +$$
$$+ 2T_{ei}R_{ee} \sum_{k=0}^{\infty} k_p x_e(t - (2k+1)\tau)S(R_{ee}R_{ei})^k \tag{4.23a}$$

$$\hat{l}(t) = -R_{ni}\hat{k}(t) + T_{ni}^2 R_{ne} \sum_{k=0}^{\infty} \hat{k}(t - 2(k+1)\tau)(R_{ne}R_{ni})^k +$$
$$+ 2T_{ni}R_{ne} \sum_{k=0}^{\infty} k_p x_n(t - (2k+1)\tau)N(R_{ne}R_{ni})^k, \tag{4.23b}$$

The fields in the signal recycling cavity may be calculated as the corresponding interference of these two fields with the dark-port condition. Both paths of the field in the signal recycling cavity, propagating through the east and through the north arms, have the same distinguishable parts: (i) inside the Fabry-Perot cavity, where the one-way trip lasts for τ; and (ii) between the input mirror of the cavity and the SRM, for describing which the new quantity τ_{in} is introduced.

The fields on the end-mirrors, which is responsible for the leaks from the power recycling cavity due to the end-mirror motion, may be described in terms of the field E, falling on the beamsplitter:

$$S = -\frac{\sqrt{2}}{2}\frac{T_{ei}}{1 - R_{ee}R_{ei}}E, \tag{4.24a}$$

$$N = -i\frac{\sqrt{2}}{2}\frac{T_{ni}}{1 - R_{ne}R_{ni}}E. \tag{4.24b}$$

All the fields of the first order in (4.23) may be expressed from the field $h(t)$ a round-trip ago, and they read:

$$\hat{h}(t) = \sum_{k=0}^{\infty} R_{\mathrm{s}} A_{\mathrm{g}k} \hat{h}(t - 2\tau_{in} - 2k\tau)e^{2ik_{\mathrm{p}}x(t)} + R_{\mathrm{s}} B_{\mathrm{g}k} E x_{\mathrm{d}}(t - 2\tau_{in} - (2k+1)\tau)e^{2ik_{\mathrm{p}}x(t)},$$

(4.25)

where

$$A_{\mathrm{g}0} = -\frac{R_{\mathrm{ei}} + R_{\mathrm{ni}}}{2}, \tag{4.26a}$$

$$A_{\mathrm{g}k} = \frac{T_{\mathrm{ei}}^2 R_{\mathrm{ee}}(R_{\mathrm{ee}}R_{\mathrm{ei}})^k + T_{\mathrm{ni}}^2 R_{\mathrm{ne}}(R_{\mathrm{ne}}R_{\mathrm{ni}})^k}{2}, k > 0, \tag{4.26b}$$

$$B_{\mathrm{g}k} = \frac{T_{\mathrm{ei}}^2 R_{\mathrm{ee}}k_{\mathrm{p}}(R_{\mathrm{ee}}R_{\mathrm{ei}})^k}{1 - R_{\mathrm{ee}}R_{\mathrm{ei}}} + \frac{T_{\mathrm{ni}}^2 R_{\mathrm{ne}}k_{\mathrm{p}}(R_{\mathrm{ne}}R_{\mathrm{ni}})^k}{1 - R_{\mathrm{ne}}R_{\mathrm{ni}}}. \tag{4.26c}$$

The field on the output may be simulated numerically using the recurrent substitution of $h(t)$ into the formula. One could also try different approximations to simplify the equations, for example assuming the time of propagation between the input mirror of a Fabry-Perot and the SRM to be short $\tau_{\mathrm{in}} \ll \tau$, or the resonant tuning of the Fabry-Perot $2\omega_{\mathrm{p}}\tau = 2\pi k, k \in N$.

4.2. Particular cases of detected signal

The impulse responses of the different detector configurations, considered in the previous section, have a rather tricky dependence on the input end-mirror motion and the SRM displacement, revealing the complex behavior of the fields inside the detector. There are some very simple particular cases of the input signal and the SRM motion, for which the output signal may be calculated analytically. In this section we consider the output of the different detector layouts, namely recycled Michelson configuration, the configuration with a delay line in the arms with and without the SRM for the following partial cases: stationary case, when the input signal has a constant amplitude and frequency, and the SRM has a constant position; and a step-wise change of every of these parameters in a very fast way, keeping the other parameters constant.

4.2.1. Recycled Michelson configuration

Let us consider the recycled Michelson configuration, the impulse response of which is defined by (4.10). The following partial cases are interesting to us.

Stationary case

Here the response of the detector with constant detuning to a signal with constant frequency and constant amplitude is considered:

$$x_{\mathrm{d}}(t) = \mathbb{A}_0 \cos(\Omega t), \tag{4.27a}$$
$$2k_{\mathrm{p}}x(t) = \delta. \tag{4.27b}$$

After the expansion of both cosines in the expression of the photocurrent, obtained by the substitution of (4.27a) into (4.10), according to Euler's formula into complex exponents, the four infinite geometric series appear. After solving these series, every pair of the resulting expressions with the same arguments of the complex exponents may be summed, turning into:

$$I_{\mathrm{det}}(t) = C_0 \mathbb{A}_0 \frac{1}{2} \left\{ \frac{\cos(\Omega t - \Omega\tau + \phi_{\mathrm{h}} - \zeta_1)}{\sqrt{1 - 2R\cos(2\Omega\tau - \delta) + R^2}} + \right.$$
$$\left. + \frac{\cos(\Omega t - \Omega\tau - \phi_{\mathrm{h}} - \zeta_2)}{\sqrt{1 - 2R\cos(2\Omega\tau + \delta) + R^2}} \right\}, \tag{4.28}$$

where

$$\zeta_1 = \arctan\frac{R\sin(\Omega\tau - \delta)}{1 - R\cos(\Omega\tau - \delta)}, \tag{4.29a}$$
$$\zeta_2 = \arctan\frac{R\sin(\Omega\tau + \delta)}{1 - R\cos(\Omega\tau + \delta)}. \tag{4.29b}$$

We also denote here and below in this thesis for the simplicity the total reflectivity during a round-trip:

$$R \equiv R_{\mathrm{s}}R_{\mathrm{f}}. \tag{4.30}$$

The two terms in this equation correspond to two sidebands, caused by the signal end-mirror oscillations, deformed by the resonant Airy function of the detector. This result is obviously consistent with the result, considered in the frequency domain with the equations (2.5) and (2.6b).

When the detector is tuned to one of the sidebands, i.e. $\delta = 2\Omega\tau$, the denominator of the corresponding terms becomes very small with respect to the other term, and it overwhelms the non-resonant sideband:

$$I_{\mathrm{det}}(t) \approx C_0 \mathbb{A}_0 \frac{1}{2} \frac{\cos(\Omega t - \Omega\tau + \phi_{\mathrm{h}})}{1 - R} \tag{4.31}$$

Both terms in (4.28) oscillate at the GW-frequency, which one can see after merging of the terms:

$$I_{\mathrm{det}}(t) = C_0 \frac{1}{2} B \cos(\Omega t - \Omega\tau + \phi_{\mathrm{h}} - \theta), \tag{4.32}$$

where

$$B = \frac{1}{\mathcal{A}_1^2} + \frac{1}{\mathcal{A}_2^2} + \frac{2}{\mathcal{A}_1 \mathcal{A}_2} \cos(\zeta_1 - \zeta_2), \tag{4.33a}$$

$$\theta = \arctan \frac{\frac{1}{\mathcal{A}_1} \cos \zeta_1 + \frac{1}{\mathcal{A}_2} \cos \zeta_2}{\frac{1}{\mathcal{A}_1} \sin \zeta_1 + \frac{1}{\mathcal{A}_2} \sin \zeta_2}, \tag{4.33b}$$

$$\mathcal{A}_1 = \sqrt{1 - 2R\cos(2\Omega\tau - \delta) + R^2}, \tag{4.33c}$$

$$\mathcal{A}_2 = \sqrt{1 - 2R\cos(\Omega\tau + \delta) + R^2}. \tag{4.33d}$$

Step-wise change of amplitude

One can mathematically set the case of the stationary detector, with constant detuning, detecting the signal with constant frequency and step-wise change of the amplitude:

$$x_{\mathrm{d}}(t) = \begin{cases} \mathbb{A}_1 \cos(\Omega t), t < t_1, \\ \mathbb{A}_2 \cos(\Omega t), t >\geq t_1, \end{cases} \tag{4.34a}$$

$$2k_{\mathrm{p}}x(t) = \delta. \tag{4.34b}$$

Before the change of the amplitude $t < t_1$ the system still remains stationary, and has no "idea" about the future transient. The output current for this area of the signal is:

$$I_{\mathrm{det}}(t) = \frac{1}{4}\mathbb{A}_1 C_0 \left\{ \frac{\exp(i(\Omega t - \Omega\tau + \phi_{\mathrm{h}}))}{1 - R\exp(-i(2\Omega\tau - \delta))} + \frac{\exp(-i(\Omega t - \Omega\tau + \phi_{\mathrm{h}}))}{1 - R\exp(i(2\Omega\tau - \delta))} + \right.$$
$$\left. + \frac{\exp(i(\Omega t - \Omega\tau - \phi_{\mathrm{h}}))}{1 - R\exp(-i(2\Omega\tau + \delta))} + \frac{\exp(-i(\Omega t - \Omega\tau - \phi_{\mathrm{h}}))}{1 - R\exp(i(2\Omega\tau + \delta))} \right\}. \tag{4.35}$$

This expression is another form of (4.28), written without merging of the terms with the same frequency.

The four infinite geometric series, describing the build up of the signal, are separated after the change of amplitude into the finite part, describing the part of the current, sourced by the fragment of GW with the new amplitude, and the residuary, sourced by the part of GW with the old amplitude:

$$I_{\mathrm{det}}(t) = \frac{1}{4}C_0 \left\{ \exp\left(i\left(\Omega t - \Omega\tau + \phi_{\mathrm{h}}\right)\right) \times \right.$$
$$\times \frac{\mathbb{A}_2 + (\mathbb{A}_1 - \mathbb{A}_2)\left(R\exp\left(-2i\Omega\tau + i\delta\right)\right)^{\lfloor \frac{t-t_1}{\tau} + \frac{1}{2}\rfloor}}{1 - R\exp\left(-2i\Omega\tau + i\delta\right)} +$$
$$+ \exp\left(i\left(\Omega t - \Omega\tau - \phi_{\mathrm{h}}\right)\right) \times$$
$$\left. \times \frac{\mathbb{A}_2 + (\mathbb{A}_1 - \mathbb{A}_2)\left(R\exp\left(-2i\Omega\tau - i\delta\right)\right)^{\lfloor \frac{t-t_1}{\tau} + \frac{1}{2}\rfloor}}{1 - R\exp\left(-2i\Omega\tau - i\delta\right)} + h.c. \right\}. \tag{4.36}$$

To analyze the frequency components of this signal in the photocurrent, the equation (4.36) should be respresented in the following way:

$$
I_{\text{det}}(t) \approx \frac{1}{4} C_0 \left\{ \frac{\mathbb{A}_2 \exp\left(i\left(\Omega t + \phi_{\text{h}}\right)\right)}{1 - R\exp\left(-2i\Omega\tau + i\delta\right)} + \right.
$$
$$
+ \frac{(\mathbb{A}_1 - \mathbb{A}_2)\left(R^{\frac{t-t_1}{2\tau}} \exp\left[i\left(\frac{\delta t}{2\tau} - \frac{\delta t_1}{2\tau} + \Omega t_1 + \phi_h\right)\right]\right)}{1 - R\exp\left(-2i\Omega\tau + i\delta\right)} +
$$

$$
+ \frac{\mathbb{A}_2 \exp\left(i\left(\Omega t - \phi_{\text{h}}\right)\right)}{1 - R\exp\left(-2i\Omega\tau + i\delta\right)} +
$$
$$
\left. + \frac{(\mathbb{A}_1 - \mathbb{A}_2)\left(R^{\frac{t-t_1}{\tau}} \exp\left[i\left(-\frac{\delta t}{2\tau} + \frac{\delta t_1}{2\tau} - \Omega t_1 - \phi_h\right)\right]\right)}{1 - R\exp\left(-2i\Omega\tau + i\delta\right)} + h.c. \right\}. \quad (4.37)
$$

The stationary part of this expression has the frequency of the signal, while both transient components decay at the eigenfrequency of the detector. Also all the field, stored in the detector before the transition, switches instantaneously to the eigenfrequency of the detector, decaying on it, while the arising part has both frequency components, resulting into the stationary term with time. This transient behavior of the detector can be seen in figure 4.4 (a).

Step-wise change of frequency

The response of a stationary detector with constant detuning on the GW signal with constant amplitude but the step-wise change of the frequency may be described like this:

$$
x_{\text{d}}(t) = \begin{cases} \mathbb{A}_0 \cos(\Omega_1 t), t < t_1, \\ \mathbb{A}_0 \cos(\Omega_2 t), t \geq t_1, \end{cases} \quad (4.38a)
$$
$$
2k_{\text{p}}x(t) = \delta. \quad (4.38b)
$$

Before the step, the system, as in previous cases, is in the stationary state:

$$
I_{\text{det}}(t) = \frac{1}{4}C_0\mathbb{A}_0 \left\{ \frac{\exp(i(\Omega_1 t - \Omega_1\tau + \phi_{\text{h}}))}{1 - R\exp(-i(2\Omega_1\tau - \delta))} + \frac{\exp(-i(\Omega_1 t - \Omega_1\tau + \phi_{\text{h}}))}{1 - R\exp(i(2\Omega_1\tau - \delta))} + \right.
$$
$$
\left. + \frac{\exp(i(\Omega_1 t - \Omega_1\tau - \phi_{\text{h}}))}{1 - R\exp(-i(2\Omega_1\tau + \delta))} + \frac{\exp(-i(\Omega_1 t - \Omega_1\tau - \phi_{\text{h}}))}{1 - R\exp(i(2\Omega_1\tau + \delta))} \right\}. \quad (4.39)
$$

For the field evolution after the step the infinite sums of geometric series, split into
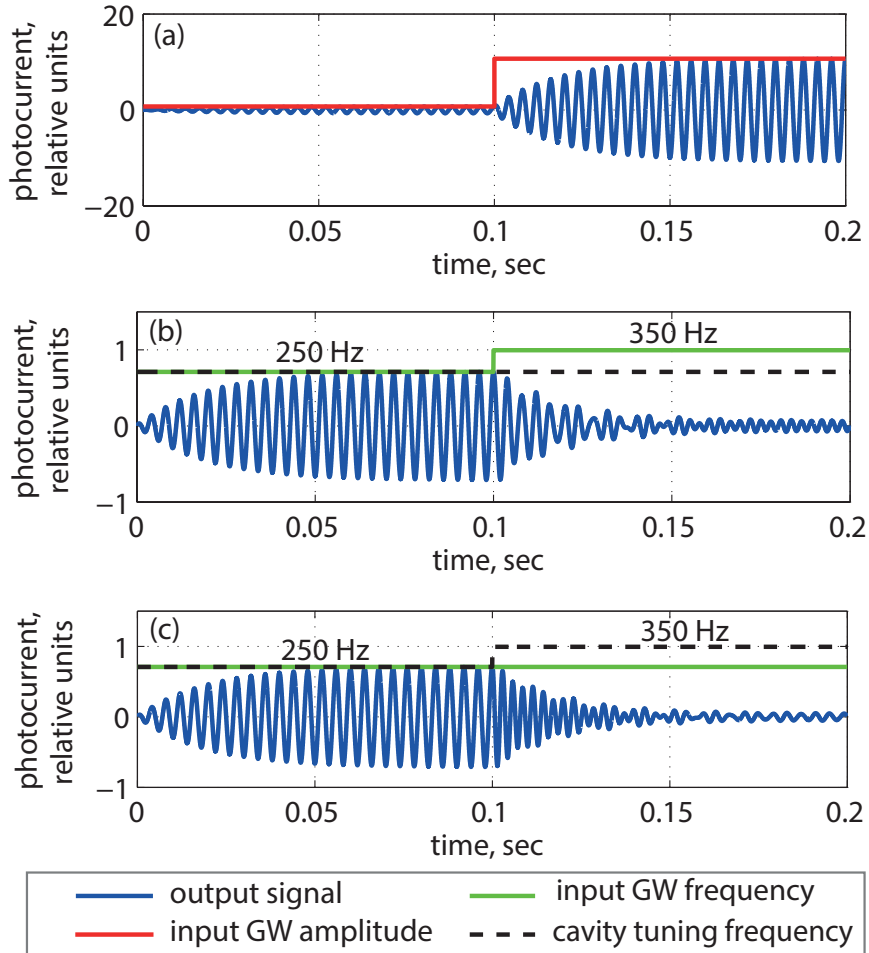
Figure 4.4.: The typical transients of the considered detector on the step-wise change of (a) $X(t)$, (b) $f(t)$, (c) $\delta(t)$

two parts, describing the response to the new and to the old signal frequency:

$$I_{\text{det}}(t) = \frac{1}{4}C_0\mathbb{A}_0\left\{\exp(i(\Omega_1 t - \Omega_1\tau + \phi_{\text{h}}))\frac{(R\exp(-2i\Omega_1 + i\delta\tau))^{\lfloor\frac{t-t_1}{2\tau}+\frac{1}{2}\rfloor}}{1 - R\exp(-2i\Omega_1\tau + i\delta))} + \right.$$

$$+ \exp(i(\Omega_2 t - \Omega_2\tau + (\Omega_1 - \Omega_2)t_1 + \phi_{\text{h}}))\frac{1 - (R\exp(-2i\Omega_2\tau + i\delta))^{\lfloor\frac{t-t_1}{2\tau}+\frac{1}{2}\rfloor}}{1 - R\exp(-2i\Omega_2\tau + i\delta)} +$$

$$+ \exp(i(\Omega_1 t - \Omega_1\tau - \phi_{\text{h}}))\frac{(R\exp(-2i\Omega_1 - i\delta\tau))^{\lfloor\frac{t-t_1}{2\tau}+\frac{1}{2}\rfloor}}{1 - R\exp(-2i\Omega_1\tau - i\delta))} +$$

$$\left. + \exp(i(\Omega_2 t - \Omega_2\tau + (\Omega_1 - \Omega_2)t_1 - \phi_{\text{h}}))\frac{1 - (R\exp(-2i\Omega_2\tau - i\delta))^{\lfloor\frac{t-t_1}{2\tau}+\frac{1}{2}\rfloor}}{1 - R\exp(-2i\Omega_2\tau - i\delta)} + h.c.\right\}.$$

$$(4.40)$$

To reveal explicitly the frequency component, this expression is represented in the following way:

$$I_{\text{det}}(t) \approx \frac{1}{4}C_0\mathbb{A}_0\left\{\left[\frac{R^{\frac{t-t_1}{2\tau}}\exp\left(i\frac{\delta t}{2\tau} - i\frac{\delta t_1}{2\tau} + i\Omega_1 t_1 + i\phi_{\text{h}}\right)}{1 - R\exp(-2i\Omega_1\tau + i\delta))} + \right.\right.$$

$$+ \frac{\exp(i(\Omega_2 t + (\Omega_1 - \Omega_2)t_1 + \phi_{\text{h}}))}{1 - R\exp(-i2\Omega_2\tau + i\delta)} - \left.\frac{R^{\frac{t-t_1}{2\tau}}\exp\left(i\frac{\delta t}{2\tau} - i\frac{\delta t_1}{2\tau} + i\Omega_1 t_1 + i\phi_{\text{h}}\right)}{1 - R\exp(-2i\Omega_2\tau + i\delta)}\right] +$$

$$+ \left[\frac{R^{\frac{t-t_1}{2\tau}}\exp\left(-i\frac{\delta t}{2\tau} + i\frac{\delta t_1}{2\tau} + i\Omega_1 t_1 - i\phi_{\text{h}}\right)}{1 - R\exp(-2i\Omega_1\tau - i\delta))} + \right.$$

$$\left.\left. + \frac{\exp(i(\Omega_2 t + (\Omega_1 - \Omega_2)t_1 - \phi_{\text{h}}))}{1 - R\exp(-i2\Omega_2\tau - i\delta)} - \frac{R^{\frac{t-t_1}{2\tau}}\exp\left(-i\frac{\delta t}{2\tau} + i\frac{\delta t_1}{2\tau} + i\Omega_1 t_1 - i\phi_{\text{h}}\right)}{1 - R\exp(-2i\Omega_2\tau - i\delta)}\right] + h.c.\right\}.$$

$$(4.41)$$

We can see in this case, similarly to the previous case, that the new stationary field oscillates at the signal frequency, while all transient processes, including the field accumulated before the frequency step, occur at the eigenfrequency of the detector. The response of the detector on the frequency step-change as well as the fields behavior one can see in figure 4.4 (b).

Step-wise change of detuning

The detection of a signal with constant amplitude and frequency, performed by the detector with a very fast, step-wise change of the detuning during the detection, is

described mathematically as following:

$$x_{\mathrm{d}}(t) = \mathbb{A}_0 \cos(\Omega t),\qquad(4.42\text{a})$$

$$2k_{\mathrm{p}}x(t) = \begin{cases} \delta_1, t < t_1 \\ \delta_2, t \geq t_1. \end{cases}\qquad(4.42\text{b})$$

The detection before the change of the detuning $t < t_1$ remains obviously stationary and repeats therefore the result (4.28):

$$I_{\mathrm{det}}(t) = \frac{1}{4}C_0\mathbb{A}_0 \left\{ \frac{\exp(i(\Omega t - \Omega\tau + \phi_{\mathrm{h}}))}{1 - R\exp(-i(2\Omega\tau - \delta_1))} + \frac{\exp(-i(\Omega t - \Omega\tau + \phi_{\mathrm{h}}))}{1 - R\exp(i(2\Omega\tau - \delta_1))} + \right.$$
$$\left. + \frac{\exp(i(\Omega t - \Omega\tau - \phi_{\mathrm{h}}))}{1 - R\exp(-i(2\Omega\tau + \delta_1))} + \frac{\exp(-i(\Omega t - \Omega\tau - \phi_{\mathrm{h}}))}{1 - R\exp(i(2\Omega\tau + \delta_1))} \right\}. \quad(4.43)$$

After the change of the detuning $t > t_1$ the output field, that was so far described as the single geometric series, can be divided in two new homogeneous parts: the finite one, describing the influence of the new detuning, and the residuary infinite sum, carrying the phase shifts from the old detunings, and after applying the formulas for the geometric series, one gets the following:

$$I_{\mathrm{det}}(t) = \frac{1}{4}C_0\mathbb{A}_0 \left\{ \exp(i(\Omega t - \Omega\tau + \phi_{\mathrm{h}})) \left[\frac{1 - (R\exp(-i(2\Omega\tau - \delta_2)))^{\lfloor \frac{t-t_1}{2\tau} + 1 \rfloor}}{1 - R\exp(-i(2\Omega\tau - \delta_2))} + \right. \right.$$
$$\left. + \exp\left(i(\delta_2 - \delta_1)\lfloor\frac{t-t_1}{1\tau}\rfloor\right) \frac{(R\exp(-i(2\Omega\tau - \delta_1)))^{\lfloor \frac{t-t_1}{2\tau} + 1 \rfloor}}{1 - R\exp(-i(2\Omega\tau - \delta_1))} \right] +$$
$$+ \exp(i(\Omega t - \Omega\tau - \phi_{\mathrm{h}})) \left[\frac{1 - (R\exp(-i(2\Omega\tau + \delta_2)))^{\lfloor \frac{t-t_1}{2\tau} + 1 \rfloor}}{1 - R\exp(-i(2\Omega\tau + \delta_2))} + \right.$$
$$\left. + \exp\left(-i(\delta_2 - \delta_1)\lfloor\frac{t-t_1}{2\tau}\rfloor\right) \frac{(R\exp(-i(2\Omega\tau + \delta_1)))^{\lfloor \frac{t-t_1}{2\tau} + 1 \rfloor}}{1 - R\exp(-i(2\Omega\tau + \delta_1))} \right] + h.c. \right\}. \quad(4.44)$$

Here $\lfloor a \rfloor$ means the whole part of the rational value a.

To see the actual frequencies of the oscillations, we should combine the complex

exponents in the terms:

$$
\begin{aligned}
I_{\text{det}}(t) \approx \frac{1}{4} C_0 \mathbb{A}_0 \Bigg\{ &\left[\frac{\exp(i(\Omega t + \phi_{\text{h}}))}{1 - R\exp(-i(2\Omega\tau - \delta_2))} + \right. \\
&+ \frac{R^{\frac{t-t_1}{2\tau}} \exp\left[i\left(\frac{\delta_2 t}{2\tau} - \frac{\delta_2 t_1}{2\tau} + \Omega t_1 + \phi_{\text{h}}\right)\right]}{1 - R\exp(-i(2\Omega\tau - \delta_2))} + \\
&+ \left. \frac{R^{\frac{t-t_1}{2\tau}} \exp\left[i\left(\frac{\delta_2 t}{2\tau} - \frac{\delta_2 t_1}{2\tau} + \Omega t_1 + \phi_{\text{h}}\right)\right]}{1 - R\exp(-i(2\Omega\tau - \delta_1))} \right] + \\
&+ \left[\frac{\exp(i(\Omega t - \phi_{\text{h}}))}{1 - R\exp(-i(2\Omega\tau - \delta_2))} + \right. \\
&+ \frac{R^{\frac{t-t_1}{2\tau}} \exp\left[i\left(-\frac{\delta_2 t}{2\tau} + \frac{\delta_2 t_1}{2\tau} + \Omega t_1 - \phi_{\text{h}}\right)\right]}{1 - R\exp(-i(2\Omega\tau - \delta_2))} + \\
&+ \left. \frac{R^{\frac{t-t_1}{2\tau}} \exp\left[i\left(-\frac{\delta_2 t}{2\tau} + \frac{\delta_2 t_1}{2\tau} + \Omega t_1 - \phi_{\text{h}}\right)\right]}{1 - R\exp(-i(2\Omega\tau - \delta_1))} \right] + h.c. \Bigg\} . \quad (4.45)
\end{aligned}
$$

Here we have neglected the phase-shifts in the field during a single round-trip due to the signal oscillations and the SRC-detuning.

The expression consists of four similar parts, each of them holds the terms of the exponents of one sign, corresponding to one of the sidebands. Each part consists of the three term, whose physical meaning can be expressed in two ways. The first term in each part describes the stationary condition, corresponding to the infinite time passed after the transition, while the second and the third terms describe the transients. The stationary process after the transition occurs at the signal frequency Ω, while all the transient processes occur at the new eigenfrequency $\frac{\delta}{2\tau}$ of the detector.

From another point of view, the field inside the detector may be divided into the decaying and arising one. The whole field, accumulated by the detector before the transition is described with the third term of each part. It decays with time, but, what is surprising, not on the signal frequency. The frequency of this field part switches instantaneously after the SRM displacement to the new eigenfrequency of the detector. The first two terms in each part of (4.45) describe the arising field in the detector, which is a superposition of the oscillations on the signal frequency and on the detector eigenfrequency, becoming in the end the monochromatic stationary signal with the signal frequency. This behavior is depicted on the plot of the detector response in figure 4.4 (c).

Composite step-wise change

The remarkable consequence of the described processes becomes apparent as both GW and of the SRC detuning frequency are changing synchronized, this is depicted in the figure 4.5(a). The perturbations caused by these changes are canceled, so the frequency of the output signal switches instantaneously from one value to another without any relaxation processes. Hence, only amplitude transient effects affect the output signal during the resonant tracking of the GW with both frequency and amplitude dependent on time. The response of the detector to the joint synchronized step-wise change of signal amplitude and the SRC detuning as well as all three considered parameters are presented in figure 4.5(b,c).

4.2.2. Delay line

The mirrors in the delay lines in both arms are assumed to have the equal reflectivity, and, therefore,

$$R_{\text{f}}(k) = R(0)R^{2k}. \tag{4.46}$$

Stationary case

The detection of a signal with constant amplitude and frequency by the configuration with delay lines is defined only by the GW:

$$x_{\text{d}}(t) = B_0 \cos(\Omega t). \tag{4.47}$$

For this the current, calculated from (7.8), is:

$$I_{\text{det}}(t) = \frac{1}{2}A_0 \left[\frac{[1 - (R^2 e^{-2i\Omega\tau})^{N_{\text{rt}}}]e^{i\Omega(t-\tau/2)}}{1 - R^2 e^{-2i\Omega\tau}} + \frac{[1 - (R^2 e^{2i\Omega\tau})^{N_{\text{rt}}}]e^{-i\Omega(t-\tau)}}{1 - R^2 e^{2i\Omega\tau}} \right]. \tag{4.48}$$

The current oscillates at frequency Ω with the amplitude:

$$I_{\text{amp}} = A_0 \frac{\sqrt{1 - 2R^{2N_{\text{rt}}}\cos(2N_{\text{rt}}\Omega\tau) + R^{2N_{\text{rt}}}}}{\sqrt{1 - 2R^2\cos(2\Omega\tau) + R^4}}. \tag{4.49}$$

Step-wise amplitude change

The detection of the signal with the amplitude, quickly changing at the instance t_1, is set as:

$$x_{\text{d}}(t) = \begin{cases} \mathbb{A}_1 \cos(\Omega t), t < t_1, \\ \mathbb{A}_2 \cos(\Omega t), t >\geq t_1, \end{cases} \tag{4.50}$$

The current before the step is stationary, as in (4.48), with the corresponding amplitude:

$$I_{\text{det}}(t) = \frac{1}{2}\mathbb{A}_1 A_0 \left[\frac{[1 - (R^2 e^{-2i\Omega\tau})^{N_{\text{rt}}}]e^{i\Omega(t-\tau/2)}}{1 - R^2 e^{-2i\Omega\tau}} + \frac{[1 - (R^2 e^{2i\Omega\tau})^{N_{\text{rt}}}]e^{-i\Omega(t-\tau)}}{1 - R^2 e^{2i\Omega\tau}} \right]. \tag{4.51}$$
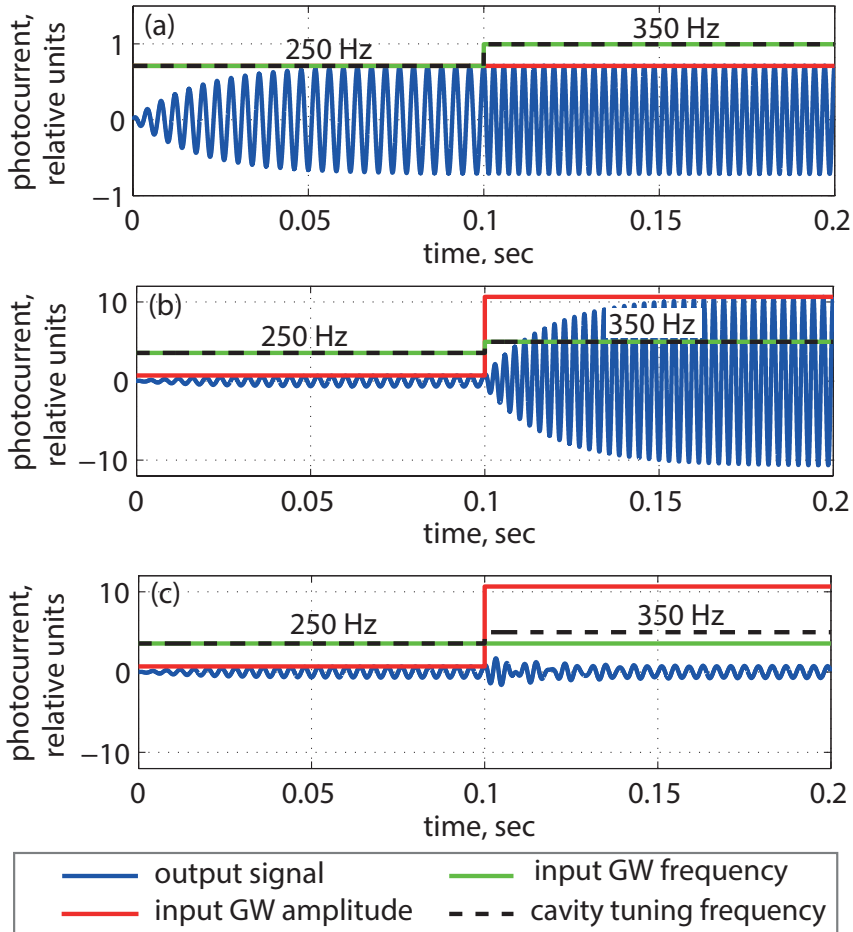
Figure 4.5.: The transients of the considered detector on the combinations of step-wise changes of (a) $f(t)$ and $\delta(t)$, (b) $X(t)$, $f(t)$ and $\delta(t)$, (c) $X(t)$ and $\delta(t)$

After the step the transient will last for $(2N_{\mathrm{rt}} - 2)\tau$. The signal during this time, $(t > t_1 + \tau/2) \cap (t < t_1 + (2N_{\mathrm{rt}} - 1)\tau)$, reads:

$$
I_{\mathrm{det}}(t) = \frac{1}{2}A_0 \left[\frac{[1 - \mathbb{A}_2(R^2 e^{-2i\Omega\tau})^{\lfloor \frac{t-t_1}{2\tau} + \frac{1}{2} \rfloor} - \mathbb{A}_1(R^2 e^{-2i\Omega\tau})^{\lfloor N_{\mathrm{rt}} - \frac{t-t_1}{2\tau} + \frac{1}{2} \rfloor}]e^{i\Omega(t-\tau)}}{1 - R^2 e^{-2i\Omega\tau}} + \right.
$$
$$
\left. + \frac{[1 - \mathbb{A}_2(R^2 e^{2i\Omega\tau})^{\lfloor \frac{t-t_1}{2\tau} + \frac{1}{2} \rfloor} - \mathbb{A}_1(R^2 e^{2i\Omega\tau})^{\lfloor N_{\mathrm{rt}} - \frac{t-t_1}{2\tau} + \frac{1}{2} \rfloor}]e^{-i\Omega(t-\tau)}}{1 - R^2 e^{2i\Omega\tau}} \right]. \quad (4.52)
$$

After this transition signal reaches its stationary oscillations:

$$
I_{\mathrm{det}}(t) = \frac{1}{2}\mathbb{A}_2 A_0 \left[\frac{[1 - (R^2 e^{-2i\Omega\tau})^{N_{\mathrm{rt}}}]e^{i\Omega(t-\tau)}}{1 - R^2 e^{-2i\Omega\tau}} + \frac{[1 - (R^2 e^{2i\Omega\tau})^{N_{\mathrm{rt}}}]e^{-i\Omega(t-\tau)}}{1 - R^2 e^{2i\Omega\tau}} \right]. \quad (4.53)
$$

4.2.3. Delay lines with SRM

We assume the delay line layout of the detector with the equal far and close mirrors in the arms:

$$
R = R_{\mathrm{s}} R_{\mathrm{m}}^{2N_{\mathrm{rt}}-1} \quad (4.54)
$$

Stationary case

The detection of a stationary oscillating signal with constant detuning of the detector may be described as following:

$$
x_{\mathrm{d}}(t) = \mathbb{A}_0 \cos(\Omega t), \quad (4.55a)
$$
$$
2k_{\mathrm{p}}x(t) = \delta. \quad (4.55b)
$$

The current on the photodiode will have the following behavior, obtained from (7.10):

$$
I_{\mathrm{det}}(t) = \frac{\mathbb{A}_0 A_0}{4} \left\{ \frac{e^{i\Omega(t-\tau)+i\phi_{\mathrm{h}}}(1 - (R_{\mathrm{m}}^2 e^{-2i\Omega\tau})^{N_{\mathrm{rt}}})}{(1 - R_{\mathrm{m}}^2 e^{-2i\Omega\tau})(1 - Re^{-2i\Omega N_{\mathrm{rt}}\tau}e^{i\delta})} + \right.
$$
$$
\left. + \frac{e^{i\Omega(t-\tau)-i\phi_{\mathrm{h}}}(1 - (R_{\mathrm{m}}^2 e^{-2i\Omega\tau})^{N_{\mathrm{rt}}})}{(1 - R_{\mathrm{m}}^2 e^{-2i\Omega\tau})(1 - Re^{-2i\Omega N_{\mathrm{rt}}\tau}e^{-i\delta})} + h.c. \right\} \quad (4.56)
$$

The amplitudes of oscillations of the two sidebands of this field are:

$$
I_{\mathrm{amp},1} = \frac{\mathbb{A}_0 A_0}{2} \frac{\sqrt{1 - 2R^{2N_{\mathrm{rt}}}\cos(2N_{\mathrm{rt}}\Omega\tau) + R^{2N_{\mathrm{rt}}}}}{\sqrt{1 - 2R^2 \cos(2\Omega\tau) + R^4}} \times
$$
$$
\times \frac{1}{\sqrt{1 - 2R\cos(\delta_\phi - 2\Omega N_{\mathrm{rt}}\tau) + R^2}}. \quad (4.57a)
$$

$$I_{\text{amp},2} = \frac{\mathbb{A}_0 A_0}{2} \frac{\sqrt{1 - 2R^{2N_{\text{rt}}}\cos(2N_{\text{rt}}\Omega\tau) + R^{2N_{\text{rt}}}}}{\sqrt{1 - 2R^2\cos(\Omega\tau) + R^4}} \times$$

$$\times \frac{1}{\sqrt{1 - 2R\cos(\delta_\phi + \Omega 2N_{\text{rt}}\tau) + R^2}}. \quad (4.57b)$$

The first amplitude gives a factor of 6 for the amplifications of resonant oscillations. This value is obtained with $T_s^2 = 400\text{ppm}$, $T_m^2 = 50$ ppm.

Step-wise change

The detection of a stationary oscillating GW signal with the interferometer with delay lines in the arms, and the detuning changing fast at the instance t_1:

$$x_{\text{d}}(t) = \mathbb{A}_0 \cos(\Omega t), \quad (4.58a)$$

$$2k_{\text{p}}x(t) = \begin{cases} \delta_1, t < t_1 \\ \delta_2, t \geq t_1. \end{cases} \quad (4.58b)$$

The signal remains stationary, before it feels the influence of the step $t < t_1$, similarly to (4.56):

$$I_{\text{det}}(t) = \frac{\mathbb{A}_0 A_0}{4} \left\{ \frac{e^{i\Omega(t-\tau)+i\phi_{\text{h}}}(1 - (R_{\text{m}}^2 e^{-2i\Omega\tau})^{N_{\text{rt}}})}{(1 - R_{\text{m}}^2 e^{-2i\Omega\tau})(1 - Re^{-2i\Omega N_{\text{rt}}\tau}e^{i\delta_1})} + \right.$$

$$\left. + \frac{e^{i\Omega(t-\tau)-i\phi_{\text{h}}}(1 - (R_{\text{m}}^2 e^{-2i\Omega\tau})^{N_{\text{rt}}})}{(1 - R_{\text{m}}^2 e^{-2i\Omega\tau})(1 - Re^{-2i\Omega N_{\text{rt}}\tau}e^{-i\delta_1})} + h.c. \right\} \quad (4.59)$$

The transient process for $t \geq t_1$ reads:

$$I_{\text{det}}(t) = \frac{\mathbb{A}_0 A_0}{4} \left\{ \frac{\exp(i(\Omega t - \Omega\tau + \phi_{\text{h}}))(1 - (R_{\text{m}}^2 e^{-2i\Omega\tau})^{N_{\text{rt}}})}{(1 - R_{\text{m}}^2 e^{-2i\Omega\tau})} \times \right.$$

$$\times \left[\frac{1 - (R\exp(-i(2\Omega N_{\text{rt}}\tau - \delta_2)))^{\lfloor \frac{t-t_1}{N_{\text{rt}}\tau}+1 \rfloor}}{1 - R\exp(-i(2\Omega N_{\text{rt}}\tau - \delta_2))} + \right.$$

$$\left. + \exp\left(i(\delta_2 - \delta_1)\frac{t-t_1}{\tau}\right) \frac{(R\exp(-i(2\Omega N_{\text{rt}}\tau - \delta_1)))^{\lfloor \frac{t-t_1}{2N_{\text{rt}}\tau}+1 \rfloor}}{1 - R\exp(-i(2\Omega N_{\text{rt}}\tau - \delta_1))} \right] +$$

$$+ \frac{\exp(i(\Omega t - \Omega\tau - \phi_{\text{h}}))(1 - (R_{\text{m}}^2 e^{-2i\Omega\tau})^{N_{\text{rt}}})}{(1 - R_{\text{m}}^2 e^{-2i\Omega\tau})} \times$$

$$\times \left[\frac{1 - (R\exp(-i(2\Omega N_{\text{rt}}\tau + \delta_2)))^{\lfloor \frac{t-t_1}{2N_{\text{rt}}\tau}+1 \rfloor}}{1 - R\exp(-i(2\Omega N_{\text{rt}}\tau + \delta_2))} + \right.$$

$$\left. + \exp\left(i(\delta_1 - \delta_2)\frac{t-t_1}{\tau}\right) \frac{(R\exp(-i(2\Omega N_{\text{rt}}\tau + \delta_1)))^{\lfloor \frac{t-t_1}{2N_{\text{rt}}\tau}+1 \rfloor}}{1 - R\exp(-i(2\Omega N_{\text{rt}}\tau + \delta_1))} \right] + h.c. \right\}. \quad (4.60)$$

4.3. Dynamical resonance conditions

4.3.1. Recycled Michelson configuration

The dynamical tuning of the detector is designed to detect a chirp signal, keeping the detector constantly in resonance to the changing instantaneous GW frequency. The sinusoidal chirp GW signal may be represented as following:

$$x_{\mathrm{d}}(t) = Re[X(t)e^{i\zeta(t)}], \tag{4.61}$$

where $X(t)$ is the slowly changing real amplitude and $\zeta(t)$ is a phase of sinusoidal wave.

The cavity is resonant to only one of the sidebands, while the other one is suppressed. The tuning to a sideband takes place, when during one roundtrip the phase shift of this sideband, caused by the GW oscillations, is canceled by the corresponding displacement of the SRM from the laser resonance position. Generally speaking, this condition is defined within one roundtrip and therefore we can express it mathematically for the non-stationary detector with the moving SRM. It is easy to see by substituting of the sinusoidal signal (4.61) into the impulse response, that for one of sidebands, appearing after a trigonometric transformations of the cosine product to their sum, the following condition makes all the terms of the corresponding series in-phase:

$$\zeta(t - (2n + 1)\tau) = \xi_n(t) + C, \tag{4.62}$$

where C is a constant. If this condition is satisfied, the sum of all the terms of the sideband is simply the sum of their amplitudes. Obviously, it gives the maximal possible field amplitude for the interference. The condition (4.62) is valid for every n and t, therefore by comparing the phases of the terms for the number of roundtrips $n = k$ and $n = k + 1$, the SRM motion, required to follow the gravitational wave resonantly, is the following:

$$x(t) = \frac{1}{2k_{\mathrm{p}}} \left[\zeta(t + \tau) - \zeta(t - \tau) \right]. \tag{4.63}$$

Since we assume the frequency of the signal to be determined, the phase of the signal reads:

$$\zeta(t) = \int_{t_0}^{t} f(t_1)dt_1. \tag{4.64}$$

The right side of (4.63), expressed via frequency $f(t)$, turns to the integral with the limits $t - \tau$ and $t + \tau$. The frequency changes in these limits insignificantly, and therefore we could approximate this change as a linear function drawn between the frequency values at the borders of the integration interval. The result of such an integration would be a square of trapezium:

$$x(t) = \frac{\tau}{k_{\mathrm{p}}} \frac{f(t - \tau) + f(t + \tau)}{2}. \tag{4.65}$$

This expression determines the required law of motion of the SRM, to keep the detector resonant to the instantaneous frequency at each instance of the time. The effect of being resonant to the time-variant frequency is called a *dynamic resonance*, and was considered first in the thesis of Malik Rakhmanov [70] as dynamical resonant condition for the fluctuations of the carrier frequency inside a Fabry-Perot cavity. In this work the dynamic resonance is defined for the source of an enhanced light inside the cavity, e.g. the sideband, injected into it and caused by the end-mirror motion.

It appears that the resonant motion of the SRM may be conveniently found from the accumulated phase shift, defined in appendix D. From (D.3-D.11a) it follows that:

$$x(t) = \frac{1}{2k_p} \left(\Phi_N - \Phi_{N-1} \right). \tag{4.66}$$

This formula is especially useful for the discrete simulations.

In this section we also can find from (4.66) and (4.63) the physical meaning of the accumulated phase shift, defined by the SRM motion:

$$\Phi_N - \Phi_0 = \zeta(t + \tau) - \zeta(t - 2N\tau + \tau). \tag{4.67}$$

It is a phase of the chirp GW, to which the corresponding motion of the SRM is resonant to.

For the negligible changes of the frequency during the roundtrip:

$$|f(t + \tau) - f(t - \tau)| \ll f(t), \tag{4.68}$$

the resonant condition is simplified down to the quasi-stationary condition:

$$x(t) = \frac{\tau}{k_{\mathrm{p}}} f(t). \tag{4.69}$$

4.3.2. Delay line with SRM

The signal recycled detector with delay lines may also detect chirp gravitational waves with dynamical tuning. Let us consider again the sinusoidal GW (4.61), neglecting its amplitude change.

In the Michelson configuration with straight arms, the field during a round-trip obtains only one injection. The light goes out of the delay-line as a package of such injections. Each of them carries the information about a single value of a GW, therefore the whole package carries the information about N_{rt} consequent values of GW, separated by the round-trip time. This package, being a superposition of some number of injected coherent waves with their phases and amplitudes, has its own phase and amplitude. Two consecutive packages make the strongest amplification of the signal when they are in phase. Describe the two last component packages for the

signal photocurrent, detected at the instance t, in the complex amplitudes:

$$I_1(t) = \sum_{k=0}^{N_{\mathrm{rt}}-1} A_{1k} e^{i\xi_1(t)} e^{-i\zeta(t-(2N_{\mathrm{rt}}+2k+1)\tau)}, \tag{4.70a}$$

$$I_2(t) = \sum_{k=0}^{N_{\mathrm{rt}}-1} A_{0k} e^{i\xi_0(t)} e^{-i\zeta(t-(2k+1)\tau)}, \tag{4.70b}$$

where $\xi_k(t)$ are defined by (4.20).

The phases of these components are:

$$\tan Z_1(t) = \frac{\sum\limits_{k=0}^{N_{\mathrm{rt}}-1} A_{1k} \sin(\Delta\phi_1(t) + \phi_h - \zeta_{N_{\mathrm{rt}}+k}(t))}{\sum\limits_{k=0}^{N_{\mathrm{rt}}-1} A_{1k} \cos(\Delta\phi_1(t) + \phi_h - \zeta_{N_{\mathrm{rt}}+k}(t))}, \tag{4.71a}$$

$$\tan Z_2(t) = \frac{\sum\limits_{k=0}^{N_{\mathrm{rt}}-1} A_{0k} \sin(\phi_h - \zeta_k(t))}{\sum\limits_{k=0}^{N_{\mathrm{rt}}-1} A_{0k} \cos(\phi_h - \zeta_k(t))}. \tag{4.71b}$$

with a single phase shift from (D.14):

$$\Delta\phi_1(t) = 2k_{\mathrm{p}} x(t - 2N_{\mathrm{rt}}\tau), \tag{4.72}$$

and new variable, defined as:

$$\zeta_n(t) = \zeta(t - (2n+1)\tau), n \in Z. \tag{4.73}$$

$\Delta\phi_1(t)$ is a phase shift, which field $Z_2(t)$ (and all other components of light) obtains during reflection from the SRM, before the last roundtrip. We could choose the microscopical position of the SRM such, so the field $Z_2(t)$ gets the same phase after the reflection from the delay line, as the package $Z_1(t)$, following after him. From this the explicit resonant condition for the SRM motion may be obtained:

$$x(t) = \frac{1}{2k_{\mathrm{p}}} \arctan \left(\frac{\sum\limits_{k=0}^{N_{\mathrm{rt}}-1} \sum\limits_{k'=0}^{N_{\mathrm{rt}}-1} A_{1k} A_{0k'} \sin(\zeta_{k'-N_{\mathrm{rt}}}(t) - \zeta_k(t))}{\sum\limits_{k=0}^{N_{\mathrm{rt}}-1} \sum\limits_{k'=0}^{N_{\mathrm{rt}}-1} A_{1k} A_{0k'} \cos(\zeta_{k'-N_{\mathrm{rt}}}(t) - \zeta_k(t))} \right). \tag{4.74}$$

The more intuitively clear result may be obtained under the following simple assumptions: (i) every mirror has the same reflectivity R_{f} (and the same losses), so the expressions for the delay-line reflectivity (4.14), and for the amplitudes of the impulses (4.20a) become:

$$R_{\mathrm{f}}(k) = R_{\mathrm{f}}^{2k+1}, \tag{4.75a}$$

$$A_{nk} = -4\sqrt{2}k_{\mathrm{p}}|E|T_{\mathrm{s}} R_{\mathrm{f}}^{2k+1} \left(R_{\mathrm{s}} R_{\mathrm{f}}^{2N_{\mathrm{rt}}-1} \right)^n; \tag{4.75b}$$

(ii) the frequency changes slow enough to neglect its variations during a round trip inside the delay line, so:

$$f(t + N_{\mathrm{rt}}\tau) - f(t - N_{\mathrm{rt}}\tau) \ll f(t), \tag{4.76a}$$

$$\zeta_n(t) - \zeta_m(t) = 2(n - m)f(t)\tau. \tag{4.76b}$$

Under these assumption the resonant condition (4.74) is simplified to the quasi-stationary expression:

$$x(t) = \frac{1}{2k_{\mathrm{p}}} 2N_{\mathrm{rt}} f(t)\tau. \tag{4.77}$$

This result is easy to understand. To keep the detector in resonance the SRM should introduce the same phase shift to the light, that changes in the gravitational wave during the full roundtrip.

4.4. Resonant tracking of the chirp sinusoidal signal

The dynamical resonant condition of a Michelson interferometer defines the position of the SRM, that adds the injections from GWs in-phase, or satisfying the dynamic resonant conditions (4.63). The detection of a GW, keeping the detector dynamically resonant, is called resonant tracking of the signal.

The response of the resonantly tracking detector to the chirp input signal may be obtained by substituting the dynamical resonant conditions (4.63) into (4.10):

$$L_{\mathrm{s}\to\mathrm{c}}(t, t_1) = \sum_{n=0}^{\infty} C_n \cos(\zeta_0(t) - \zeta_n(t) + \phi_{\mathrm{h}})\delta\left(t_1 - t + (2n + 1)\tau\right). \tag{4.78}$$

Here we have used the definitions for ζ_k from (4.73).

The response of the resonantly tracking detector to the input signal (4.61) may be calculated by substituting it in (4.78):

$$I_{\mathrm{det}}(t) = \sum_{n=0}^{\infty} C_n \cos(\zeta_0(t) - \zeta_n(t) + \phi_{\mathrm{h}})X\left(t - (2n + 1)\tau\right)\cos\zeta_n(t). \tag{4.79}$$

The multiplication of every two cosines in the series is a sum of the two cosines: with sum and with difference of their arguments, describing the behavior of two signal sidebands inside the cavity. The cosines with sum of the arguments have uncorrelated phases, while the phases of the cosines with the difference arguments become equal, i.e. the fields corresponding to them are summed up in-phase, therefore significantly overcoming the non-correlated side-band, which is neglected:

$$I_{\mathrm{det}}(t) \approx Z(t)\cos\left[\zeta_0(t) + \phi_h\right], \tag{4.80}$$

where

$$Z(t) = \frac{1}{2}\sum_{n=0}^{\infty} C_n X\left(t - (2n + 1)\tau\right). \tag{4.81}$$

The phase (and therefore frequency) behavior of the detected photocurrent repeats the one of the input gravitational wave, excepting a phase shift, corresponding to the time the light requires to travel from the end-mirrors to the photodiode. Therefore the resonant tracking changes only the time-variant amplitude $X(t)$ of the input signal. The more convenient appearance for amplitude $Z(t)$ of the photocurrent may be obtained by developing it into Taylor's series, and summing the resulting terms, corresponding to each derivative, as a geometric series, taking into account (4.8a,4.8b):

$$Z(t) = C_0 \frac{X(t-\tau)}{1-R} + C_0 \sum_{k=1}^{\infty} \frac{X^{(k)}(t-\tau)(-2\tau)^k}{(1-R)^{k+1}}, \tag{4.82}$$

where $X^{(k)}(t)$ is a k-th derivative of the time-dependent GW amplitude and

$$R = R_{\mathrm{f}} R_{\mathrm{s}}. \tag{4.83}$$

The first term in (4.82), describing the response on a GW with the negligibly slowly changing amplitude, corresponds to the photodetector signal from the quasi-stationary detection of the chirp (compare with (2.6b) with $\delta = \Omega$). However, it is not a quasi-stationary detector in the usual sence. Even though the instantaneous amplitude of the response is equal to the corresponding response of the stationary detector to the monochromatic GW, the typical times of the frequency change and of the SRM motion could be much less than the transient times of the detector. This kind of detection is referred to therefore as *virtually stationary*.

As it follows from (4.82), the speed of the amplitude change and its higher derivatives $X^{(k)}(t)$ break virtual stationarity, cause the transient processes preventing the detector from achieving the maximal, "quasi-stationary" amplification of the GW signal. The condition of virtual stationarity is convenient to describe in the relative perturbations caused by the derivatives of the GW amplitude, normalized by the virtual-stationary values:

$$\varepsilon_k(t) = \frac{X^{(k)}\left(t-\frac{\tau}{2}\right)}{X(t-\frac{\tau}{2})} \left(\frac{-2\tau}{1-R}\right)^k \approx \frac{X^{(k)}\left(t-\frac{\tau}{2}\right)}{X(t-\frac{\tau}{2})} (-0.02)^k, \tag{4.84}$$

where the numerical value was calculated for the typical GEO values of τ, T_{s} and A_{f} presented in table 2.1.

Another way of binding the amplitudes of GW and photocurrent may be found in the frequency domain. The time shifts of n round trips become the exponents with power n in the Fourier transform of (4.81). These factors make the series in this expression geometric, and after calculating its limit one gets:

$$Z(\Omega) = R(\Omega)X(\Omega). \tag{4.85}$$

So during resonant tracking the photocurrent amplitude is bound with the GW amplitude through the stationary transformation, characterized by the transfer function:

$$R(\Omega) = \frac{1}{2} \frac{C_0 e^{i\Omega\tau/2}}{1 - Re^{i\Omega\tau}} \tag{4.86}$$

The transfer function here is an Airy function for the equivalent Fabry-Perot cavity with the frequency bandwidth calculated from (1.17):

$$\gamma = \frac{T_{\rm s}^2 + A_{\rm f}^2}{4\tau}, \tag{4.87}$$

and equal to $8.3\,\mathrm{Hz}$. Here $A_{\rm f}^2 = 1 - R_{\rm f}^2$ is a transmittance (or losses) of the end-mirror of an equivalent FP cavity.

On the scale of considered frequencies ($10^2 - 10^4$ Hz) this bandwidth could be considered as very narrow.

So we could harmlessly linearize (4.86):

$$R(\Omega) = \frac{1}{2} \frac{C_0 e^{i\Omega\tau/2}}{1 - R - i\Omega\tau}. \tag{4.88}$$

As the outcome, the phase and the frequency behavior of the output signal repeats that of the input GW, while the amplitude at the output is smoothed with respect to the amplitude of the GW signal. In other words, during the resonant tracking the shape of the output signal is obtained by low pass filtering of the GW shape.

4.5. Thermal noise on the output

Apart from the quantum noises there is the number of noise sources resulting in the end-mirror displacement. The main sources of this displacement noise are the seismic, the thermal fluctuations of the mirror coating and of the suspension. The detector is sensitive to the differential end-mirror motion, and since the independent stochastic motion of the end-mirror has the differential component, this noise affects the sensitivity.

To calculate the sensitivity the signal and stochastic changes of the same value should be considered. In chapter 3 as well as in the first sections of the current chapter the shot noise and GW signals were considered in the variations of the photocurrent. To include properly the displacement noise in the sensitivity calculations, the fluctuations of the photocurrent, caused by them, should be found.

The displacement noise is the fluctuation of the optical elements in the interferometer, e.g. of mirrors, beamsplitter, etc. Normally the displacement noise may be described as the noisy motion of the end-mirrors. Since this motion is independent from any optical parameters of the detector, including the time-dependent detuning, it is stationary, even during the dynamical tuning. Its properties are described by the spectral density $S_{\rm dis}(\Omega)$ and the corresponding autocorrelation function:

$$B_{\rm dis}(\tau) = \int\limits_{-\infty}^{\infty} S_{\rm dis}(\Omega) e^{-i\Omega\tau} \frac{d\Omega}{2\pi}. \tag{4.89}$$

On the contrary, the displacement noise in the photocurrent is a stationary noise detected by a non-stationary detector, and therefore is also non-stationary. The

displacement noise in the end-mirrors $x_{\mathrm{dis}}(t)$ and in the photocurrent $I_{\mathrm{dis}}(t)$ are bound by the evolution of the fields inside the detector described by the impulse response to the differential end-mirror motion (4.10). From this boundary and the definition of an autocorrelation function (3.1) the properties of the noise in the photocurrent may be expressed from those of the end-mirror motion in the following way:

$$B_{\mathrm{i}}(t_1, t_2) = \int\limits_{-\infty}^{t_1} dt'_1 \int\limits_{-\infty}^{t_2} dt'_2 L_{\mathrm{s}\to\mathrm{c}}(t_1, t'_1) L_{\mathrm{s}\to\mathrm{c}}(t_2, t'_2) B_{\mathrm{dis}}(t'_1, t'_2). \qquad (4.90)$$

The explicit substitution of the impulse response gives the following expression for the output autocorrelation function:

$$B_{\mathrm{i}}(t_1, t_2) = \sum_{m=0}^{\infty} \sum_{n=0}^{\infty} C_m C_n \cos\left[\xi_m(t_1)\right] \cos\left[\xi_n(t_2)\right] B_{\mathrm{dis}}(t_2 - t_1 + 2(m-n)\tau). \quad (4.91)$$

The merging of the terms with the same argument of $B_{\mathrm{dis}}(t)$ may be done changing of the sum indices to

$$m' = m + n, \qquad (4.92\mathrm{a})$$
$$n' = m - n. \qquad (4.92\mathrm{b})$$

After substitution of the impulse amplitudes (4.8a,4.8b) we get:

$$B_{\mathrm{i}}(t_1, t_2) = \sum_{m'=0}^{\infty} \sum_{n'} C_0^2 R^{m'} \cos\xi_{\frac{m'+n'}{2}}(t_1) \cos\xi_{\frac{m'-n'}{2}}(t_2) B_{\mathrm{dis}}(t_2 - t_1 + 2n'\tau), \quad (4.93)$$

where m' covers values from 0 to infinity, and $n'\epsilon[-m', m']$ with the step of 2.

The properties of the end-mirror displacement noise are usually described by the spectral density function. The photocurrent autocorrelation function expressed through it may be obtained via the Fourier transform:

$$B_{\mathrm{i}}(t_1, t_2) =$$
$$= \int\limits_{-\infty}^{\infty} \frac{d\Omega}{2\pi} S(\Omega) \sum_{m=0}^{\infty} \sum_{n=0}^{\infty} C_m C_n \cos\xi_m(t_1) \cos\xi_n(t_2) e^{i\Omega(t_2 - t_1 + 2(m-n)\tau)}. \quad (4.94)$$

4.6. The signal deconvolution

The dynamical tuning of the chirp GW signal amplifies the signal part of the output photocurrent. On the contrast to the stationary operating detector, where spectrums of the output and the input signals are bound via transfer function, the dynamical tuning deforms the shape of the detected wave in a non-stationary way, so the restoration of the initial shape becomes an important task. The resonantly tracked signal is easy to restore by the deconvolution of the envelope in accordance with formula

(4.85). However, in real life the resonant tracking of the signal isn't perfect: the inevitable errors of the tracking makes this way of restoration wrong.

However, it is possible to restore the differential end-mirror from the measured photocurrent if we have also know the SRM motion during the detection, and therefore the impulse response function, precisely. Assume for convenience the homodyne angle equal to zero and write down the response on the arbitrary differential motion using (4.78) in the following way:

$$I_{\mathrm{det}}(t) = C_0 x_{\mathrm{d}}\,(t - \tau) +$$
$$+ R\left[\cos\left(2k_{\mathrm{p}}x(t - 2\tau)\right) I_{\mathrm{det}}(t - 2\tau) - \sin\left(2k_{\mathrm{p}}x(t - 2\tau)\right) \tilde{I}_{\mathrm{det}}(t - 2\tau)\right], \quad (4.95)$$

where we introduce the other, undetected quadrature of the photocurrent:

$$\tilde{I}_{\mathrm{det}}(t) \equiv \sum_{n=0}^{\infty} C_n \sin(\zeta(t - \tau) - \zeta(t - (2n + 1)\tau))x_{\mathrm{d}}\,(t - (2n + 1)\tau) =$$
$$= R\left[\sin\left(2k_{\mathrm{p}}x(t - 2\tau)\right) I_{\mathrm{det}}(t - 2\tau) + \cos\left(2k_{\mathrm{p}}x(t - 2\tau)\right) \tilde{I}_{\mathrm{det}}(t - 2\tau)\right]. \quad (4.96)$$

The last expression in this equation is a recurrent formula for $\tilde{I}_{\mathrm{det}}(t)$, using which we could explicitly express it through the measured photocurrent:

$$\tilde{I}_{\mathrm{det}}(t) = R \sin\left(2k_{\mathrm{p}}x(t - 2\tau)\right) I_{\mathrm{det}}(t - 2\tau) +$$
$$+ \sum_{k=2}^{\infty} R^k \prod_{l=1}^{k-1} \cos\left(2k_{\mathrm{p}}x(t - 2l\tau)\right) \sin\left(2k_{\mathrm{p}}x(t - 2k\tau)\right) I_{\mathrm{det}}(t - 2\tau). \quad (4.97)$$

After substituting this formula in (4.95) the differential end-mirror motion, and therefore, the inverse impulse response, may be found explicitly:

$$L_{\mathrm{c} \to \mathrm{s}}(t, t_1) = \sum_{n=0}^{\infty} \tilde{A}_n(t)\delta(t_1 - t + (2n - 1)\tau), \quad (4.98)$$

where:

$$\tilde{A}_0(t) = \frac{1}{C_0}, \quad (4.99\mathrm{a})$$

$$\tilde{A}_1(t) = -\frac{R}{C_0} \cos\left(2k_{\mathrm{p}}x(t - \tau)\right), \quad (4.99\mathrm{b})$$

$$\tilde{A}_2(t) = \frac{R^2}{C_0} \sin\left(2k_{\mathrm{p}}x(t - \tau)\right) \sin\left(2k_{\mathrm{p}}x(t - 3\tau)\right) \quad (4.99\mathrm{c})$$

$$\tilde{A}_n(t) = \frac{R^n}{C_0} \prod_{l=2}^{n-1} \cos\left(2k_{\mathrm{p}}x(t - (2l - 1)\tau)\right) \sin\left(2k_{\mathrm{p}}x(t - \tau)\right) \times$$
$$\times \sin\left(2k_{\mathrm{p}}x(t - (2n - 1)\tau)\right), n \geq 3. \quad (4.99\mathrm{d})$$

The following equation proves that the eigenbases of both direct and inverse impulse response transformations are full, and theoretically no information about the GW signal is lost during the resonant tracking:

$$\int\limits_{-\infty}^{\infty} L_{c\to s}(t,t_1)L_{s\to c}(t_1,t_1') = \delta(t-t_1').\tag{4.100}$$

4.7. Projection of the output quantum noise on the end-mirror motion

Both displacement noise and GW signals occur at the end-mirrors. Only shot noise is considered on the photodetector. So far the problem of sensitivity was studied on the photodetector, by calculating displacement noise and GW signal there. However, it may be easier to do on the end-mirrors. By the detection we don't really care, where the noise appeared, since two noises, having the same characteristics, but originated at different places, are indistinguishable for us. Therefore we could calculate the auto-correlation function of the virtual shot noise at the end-mirrors, or the noise reduced to the end-mirros: it will be the projected noise, which causes the corresponding white noise on the photodetector (3.55). Since we know the inverse impulse response of the detector (4.98), we can calculate the reduced noise. The delta-function allows to integrate the expression for the autocorrelation function once:

$$B_s^q(t_1,t_2) = C_z \int\limits_{-\infty}^{t_1} dt_1' L_{C\to S}(t_1,t_1')L_{C\to S}(t_2,t_1').\tag{4.101}$$

The inverse impulse response also depends on time as a sum of delta-functions, therefore we could perform the second integration, substituting the explicit expression of the impulse response:

$$B_s^q(t_1,t_2) = C_z \sum_{k=-\infty}^{\infty} \tilde{B}_k(t_1,t_2)\delta(t_2-t_1+k\tau),\tag{4.102}$$

In order to merge all the terms, where the delta-function has the same parameter, we introduce the new indices and a new variable:

$$k = m - n,\tag{4.103a}$$

$$l = m + n,\tag{4.103b}$$

$$\tilde{B}_k(t_1,t_2) = \sum_{l/2=-k}^{k} \tilde{A}_{(l-k)/2}(t_1)\tilde{A}_{(l+k)/2}(t_2),\tag{4.103c}$$

where the limits of the sum, depicted in this way, mean that l changes from $-2k$ to $2k$ with step 2.

DC Readout.

5.1. DC part of the output light

DC-READOUT is an important way to detect the field oscillations on the output, caused in the detector by GWs. In a stationary detector the DC-offset of the interference at the beamsplitter from the dark port causes a zero-order leak from the power recycling cavity. After the stationary amplification this leak result in the monochromatic laser radiation on the photodiode, being a very nice local oscillator (B.33), synchronized with the laser frequency fluctuations.

The motion of the SRM, performing the dynamical tuning, establishes a non-stationary response on the DC-offset source in the signal recycling cavity, complexifying the detection. In the stationary case the beating of the DC leak with the signal field may be extracted by low-pass filtering of a zero-order component. During the dynamical detection the parameters of the signal recycling cavity vary so rapidly, that the zeroth order component of the field, caused by the DC-offset, belongs no longer to the low-frequency region, arising the problem of the signal extraction.

Let us describe the evolution of the zero-order component in the detector with the DC-offset. The equation, describing the zero-order leak from the power recycling cavity due to dark fringe offset in time-domain, and its evolution during one round-trip inside the signal recycling cavity reads:

$$H_{\mathrm{dc}}(t) = E \left(-iR_{\mathrm{s}}R_2 e^{i\varphi_2} e^{2ik_{\mathrm{p}}x(t)} \right) + \left(R_{\mathrm{s}}R_{\mathrm{f}} e^{2ik_{\mathrm{p}}x(t)} \right) H(t - 2\tau), \qquad (5.1)$$

where

$$R_2 = \frac{1}{2}\sqrt{R_{\mathrm{e}}^2 + R_{\mathrm{n}}^2 - 2R_{\mathrm{e}}R_{\mathrm{n}}\cos(2\delta\phi_{\mathrm{f}})}, \tag{5.2a}$$

$$\varphi_2 = \operatorname{arccot}\left(\frac{R_{\mathrm{e}} - R_{\mathrm{n}}}{R_{\mathrm{e}} + R_{\mathrm{n}}}\cot\delta\phi_{\mathrm{f}}\right) \tag{5.2b}$$

The solution for the field in the signal recycling cavity is then:

$$H_{\mathrm{dc}}(t) = -i\sum_{n=0}^{\infty} R_{\mathrm{s}}^{n+1} R_{\mathrm{f}}^n R_2 E e^{2ik_{\mathrm{p}}\sum_{k=0}^{n} x(t-2k\tau)} e^{i\varphi_2}, \tag{5.3}$$

The explicit field on the photodiode, caused by the DC-leaks, may be found from the field inside the cavity, describing the evolution of light between the corresponding points:

$$E_{\mathrm{dc}}(t) = \sum_{n=0}^{\infty} B_n \cos(\omega_{\mathrm{p}} t - \xi_n(t)), \tag{5.4}$$

where

$$B_0 = -2\sqrt{2}\sqrt{\frac{\pi\hbar\omega_p}{\mathcal{A}c}} T_{\mathrm{s}} R_2 |E|, \tag{5.5a}$$

$$B_n = B_0 (R_{\mathrm{s}} R_{\mathrm{f}})^n, \tag{5.5b}$$

$$\xi_0(t) = \varphi_2 + \phi_{\mathrm{e}}, \tag{5.5c}$$

$$\xi_n(t) = \xi_0 + 2k_{\mathrm{p}}\sum_{k=1}^{n} x(t-2k\tau), \tag{5.5d}$$

and ϕ_e is a phase of light E.

The current of the photodiode for the detector with DC-readout is described by the following expression:

$$I_{\mathrm{det}} = \mathrm{const} \times \overline{|E_{\mathrm{dc}}(t) + E_{\mathrm{y}}(t)|^2} \approx I_{\mathrm{dc}}(t) + I_{\mathrm{y}}(t), \tag{5.6}$$

where $E_{\mathrm{y}}(t)$ is a first order term on the photodiode, caused by GWs and noise. The measured photocurrent, the zeroth and the first order terms of which are denoted correspondingly $I_{\mathrm{dc}}(t)$ and $I_{\mathrm{y}}(t)$, is proportional to the audio-frequency components of the detected laser power (below we set the corresponding constant to 1 for simplicity). The information about GW is carried only by the first order term, describing beating of the fields of the zeroth and of the first order. The zeroth order term, being only a non-stationarily amplified DC-leak from the power recycling cavity, is therefore undesirable. Its expression may be found explicitly by the substitution of (5.4) into (5.6):

$$I_{\mathrm{dc}}(t) = \frac{1}{2}\sum_{n=0}^{\infty}\sum_{m=0}^{\infty} B_n B_m \cos(\Phi_{N-n-1} - \Phi_{N-m-1}), \tag{5.7}$$

Where we used the accumulated phase shift from (D.11a). The zeroth-order component is defined by the SRM motion, and therefore can theoretically be simulated and subtracted from the measured signal, once this motion is measured precisely enough, leaving only the signal component.

5.2. The signal from the end-mirror motion in DC-readout

The field on the photodetector, sourced by the differential end-mirror motion is the same for both DC-readout and homodyne detection, and therefore can be taken from the section 4.1 directly:

$$E_{\mathrm{y}}(t) = \sum_{n=0}^{\infty} 2C_n \sin\left[\omega_{\mathrm{p}}t - \phi_e - (\Phi_{N-1} - \Phi_{N-n-1})\right] x_{\mathrm{d}}\left(t - (2n+1)\tau\right), \qquad (5.8)$$

where the amplitudes C_n are defined in (4.8a,4.8a), and the Φ_n is an accumulated phase shift, defined in appendix D by the expression (D.11a).

Therefore, the photocurrent component, caused by the end-mirror motion, and also we get the impulse response by setting the delta-function to the differential end-mirror motion:

$$L_{\mathrm{s}\to\mathrm{c}}^{\mathrm{dc}}(t, t_1) = \sum_{n=0}^{\infty} \sum_{m=0}^{\infty} B_n C_m \sin(\Phi_{N-n-1} - \Phi_{N-m-1} - \varphi_2)\delta\left(t - t_1 + (2n+1)\tau\right).$$
$$(5.9)$$

The restoration of the gravitational wave from the measured photocurrent is theoretically possible in a similar way to the described one in section 4.6.

5.3. Particular cases of detected signal

In this section we consider the partial cases of the signal detection with the detector, operating with time-varying position of the SRM and the DC-readout. The simplest cases are stationary detection, assuming the constant amplitude and frequency of the signal, and the constant detuning of the detector. Another case is the detection of such a signal with a step-wise change of the detuning. The fields, caused by the GW motion have two sidebands, however in this section we consider only one of them, assuming it to be close to resonance, effectively overwhelming the other one.

Stationary case

The operational regime of the detection with the constant detuning of the GW with the constant amplitude and frequency is defined by:

$$x_{\mathrm{d}}(t) = \mathbb{A}_0 \cos(\Omega t), \qquad (5.10a)$$
$$2k_{\mathrm{p}}x(t) = \delta. \qquad (5.10b)$$

The output current during this detection may be represented as two sets of infinite sums, corresponding to the zero and the first order terms, in the following way, defined

by (5.6), (5.7) and (5.9):

$$I_{\text{det}}(t) = \frac{1}{2} \sum_{n=0}^{\infty} \sum_{m=0}^{\infty} B_n B_m \cos\left((m-n)\delta\right) +$$

$$+ \sum_{n=0}^{\infty} \sum_{m=0}^{\infty} C_n B_m \sin\left((m-n)\delta + \varphi_2\right) \cos(\Omega(t - (2n+1)\tau)). \quad (5.11)$$

The zero-order term, found after a significant amount of trivial transformations of the geometric series read:

$$I_{\text{det},0} = \frac{B_0^2}{1 - 2R\cos\delta + R^2}. \quad (5.12)$$

The first-order current after even larger amount of the similar geometric series transformations, keeping only one sideband, assumed to be close to resonance:

$$I_{\text{det},1} \approx \mathbb{A}_0 C_0 B_0 \frac{\cos(\Omega t - \Omega\tau - \zeta)}{\sqrt{(1 - 2R\cos(\delta - 2\Omega\tau) + R^2)(1 - 2R\cos\delta + R^2)}}, \quad (5.13)$$

where

$$\zeta = \arctan\left\{\left[\cos\varphi_2 - R\cos(\delta - 2\Omega\tau + \varphi_2) - R\cos(\delta - \varphi_2) + \right.\right.$$
$$+ R^2\left(\cos(\delta - \varphi_2)\cos(\delta - 2\Omega\tau) + \sin(\delta - \varphi_2)\sin(\delta - 2\Omega\tau)\right)\right] /$$
$$/ \left[\sin\varphi_2 - R\sin(\delta - 2\Omega\tau + \varphi_2) + R\sin(\delta - \varphi_2) - \right.$$
$$\left.\left. - R^2\left(\sin(\delta - \varphi_2)\cos(\delta - 2\Omega\tau) - \cos(\delta - \varphi_2)\sin(\delta - 2\Omega\tau)\right)\right]\right\}. \quad (5.14)$$

Step-wise change of detuning

The step-wise change of the detuning during the detection of the monochromatic GW signal can be described as:

$$x_{\text{d}}(t) = \mathbb{A}_0 \cos(\Omega t), \quad (5.15a)$$

$$2k_{\text{p}}x(t) = \begin{cases} \delta_1, t < t_1 \\ \delta_2, t \geq t_1. \end{cases} \quad (5.15b)$$

The system before the step does not experience the stationary state:

$$I_{\text{det},1} \approx C_0 B_0 \frac{\cos(\Omega t - \Omega\tau - \zeta)}{\sqrt{(1 - 2R\cos(\delta_1 - 2\Omega\tau) + R^2)(1 - 2R\cos\delta_1 + R^2)}}, \quad (5.16)$$

For the calculation of the transients terms at $t > t_1$ we used Mathematica. The zero order terms reads:

$$I_{\text{det},0}(t) = \frac{B_0^2}{1 - 2R\cos\delta_2 + R^2} +$$

$$+ \frac{B_0^2 R^2 \sin^2\left(\frac{\delta_1 - \delta_2}{2}\right)}{(1 - 2R\cos\delta_1 + R^2)(1 - 2R\cos\delta_2 + R^2)} R^{\frac{2(t-t_1)}{\tau}} +$$

$$+ \frac{2B_0^2 R\left|\sin\left(\frac{\delta_1 - \delta_2}{2}\right)\right|}{\sqrt{1 + R^2 - 2R\cos\delta_1}(1 + R^2 - 2R\cos\delta_2)} R^{\frac{t-t_1}{\tau}} \cos\left(\frac{\delta_2}{\tau}t - \xi - \frac{\delta_2}{\tau}t_1\right), \quad (5.17)$$

where

$$\xi = \arctan\frac{\sin\delta_2 + R\sin(\delta_1 - \delta_2) - \sin\delta_1}{\cos\delta_1 + R(-1 + \cos(\delta_1 - \delta_2)) - \cos\delta_2}. \quad (5.18)$$

The first order component of the current is correspondingly:

$$I_{\text{det},1}(t) = \mathbb{A}_0 \left\{ \mathcal{B}_1 \cos(\Omega t - \xi_1) + \mathcal{B}_2 R^{\frac{t-t_1}{2\tau}+1} \cos\left[(\delta_1 - 2\Omega\tau)\frac{t - t_1}{2\tau} - \xi_2\right] + \right.$$

$$+ \mathcal{B}_3 R^{\frac{t-t_1}{2\tau}+1} \cos\left[(\delta_1 + 2\Omega\tau)\frac{t - t_1}{2\tau} - \xi_3\right] + \mathcal{B}_4 R^{\frac{t-t_1}{2\tau}+1} \cos\left[(\delta_2 - 2\Omega\tau)\frac{t - t_1}{2\tau} - \xi_4\right] +$$

$$+ \mathcal{B}_5 R^{\frac{t-t_1}{2\tau}+1} \cos\left[(\delta_2 + 2\Omega\tau)\frac{t - t_1}{2\tau} - \xi_5\right] + \mathcal{B}_6 R^{\frac{t-t_1}{2\tau}+1} \cos\left(l\delta_1 - \xi_6\right) + \mathcal{B}_7 R^{\frac{t-t_1}{2\tau}+1} \cos\left(\delta_2\frac{t - t_1}{2\tau} - \xi_8\right) +$$

$$\left. + \mathcal{B}_8 R^{2\left(\frac{t-t_1}{2\tau}+1\right)} \cos\left[(\delta_1 - \delta_2)\frac{t - t_1}{2\tau} - \xi_8\right] \right\}, \quad (5.19)$$

where

$$\mathcal{B}_1 = \frac{1}{1 - 2R\cos\delta_2 + R^2} \times$$

$$\times \frac{2R|\sin\delta_2\sin(\Omega\tau)|}{\sqrt{(1 - 2R\cos(\delta_2 - 2\Omega\tau) + R^2)(1 - 2R\cos(\delta_2 + 2\Omega\tau) + R^2)}} \quad (5.20a)$$

$$\mathcal{B}_2 = \frac{1}{2\sqrt{(1 + R^2 - 2R\cos\delta_1)(1 + R^2 - 2R\cos(\delta_2 - 2\tau\Omega))}}, \quad (5.20b)$$

$$\mathcal{B}_3 = \frac{1}{2\sqrt{(1 + R^2 - 2R\cos\delta_1)(1 + R^2 - 2R\cos(\delta_2 + 2\tau\Omega))}}, \quad (5.20c)$$

$$\mathcal{B}_4 = \frac{1}{2\sqrt{(1 + R^2 - 2R\cos\delta_2)(1 + R^2 - 2R\cos(\delta_2 - 2\tau\Omega))}}, \quad (5.20d)$$

$$\mathcal{B}_5 = \frac{1}{2\sqrt{(1 + R^2 - 2R\cos\delta_2)(1 + R^2 - 2R\cos(\delta_2 + 2\tau\Omega))}} \quad (5.20e)$$

$$\mathcal{B}_6 = \sqrt{\frac{1 + R^2 + R^2 \cos 2\phi_0 - 4R \cos \delta_1 \cos \phi_0 \cos(2\Omega\tau - \phi_0) + \cos 2(2\Omega\tau - \phi_0)}{2(1 + R^2 - 2R \cos \delta_2)(1 + R^2 - 2R \cos(\delta_1 - 2\Omega\tau))(1 + R^2 - 2R \cos(\delta_1 + 2\Omega\tau))}},$$
$$\text{(5.20f)}$$

$$\mathcal{B}_7 = \sqrt{\frac{1 + R^2 + R^2 \cos 2\phi_0 - 4R \cos \delta_2 \cos \phi_0 \cos(2\Omega\tau - \phi_0) + \cos 2(2\Omega\tau - \phi_0)}{2(1 + R^2 - 2R \cos \delta_2)(1 + R^2 - 2R \cos(\delta_2 - 2\Omega\tau))(1 + R^2 - 2R \cos(\delta_2 + 2\Omega\tau))}},$$
$$\text{(5.20g)}$$

$$\begin{aligned}
\mathcal{B}_8 = \Bigg\{ \Bigg[&\frac{R^2 - R(\cos \delta_2 + \cos(\delta_1 - 2\Omega\tau)) + \cos(\delta_1 - \delta_2 - 2\Omega\tau)}{2(1 + R^2 - 2R \cos \delta_2)(1 + R^2 - 2R \cos(\delta_1 - 2\Omega\tau))} - \\
&- \frac{R^2 - R(\cos[\delta_1 + \cos(\delta_2 - 2\Omega\tau)) + \cos(\delta_1 - \delta_2 + 2\Omega\tau)}{2(1 + R^2 - 2R \cos[\delta_1)(1 + R^2 - 2R \cos(\delta_2 - 2\Omega\tau))} + \\
&+ \frac{R^2 - R(\cos \delta_2 + \cos(\delta_1 + 2\Omega\tau)) + \cos(\delta_1 - \delta_2 + 2\Omega\tau)}{2(1 + R^2 - 2R \cos \delta_2)(1 + R^2 - 2R \cos(\delta_1 + 2\Omega\tau))} - \\
&- \frac{R^2 + \cos(\delta_1 - \delta_2 - 2\Omega\tau) - R(\cos \delta_1 + \cos(\delta_2 + 2\Omega\tau))}{2(1 + R^2 - 2R \cos \delta_1)(1 + R^2 - 2R \cos(\delta_2 + 2\Omega\tau))} \Bigg]^2 + \\
&+ \Bigg[\frac{R \sin(\delta_2 - R \sin \delta_1 - 2\Omega\tau) + \sin(\delta_2 - \delta_2 - 2\Omega\tau)}{2(1 + R^2 - 2R \cos \delta_2)(1 + R^2 - 2R \cos(\delta_2 - 2\Omega\tau))} - \\
&- \frac{-R \sin \delta_2] + R \sin(\delta_2 - 2\Omega\tau) + \sin(\delta_2 - \delta_2 + 2\Omega\tau)}{2(1 + R^2 - 2R \cos \delta_2)(1 + R^2 - 2R \cos(\delta_2 - 2\Omega\tau))} + \\
&+ \frac{R \sin \delta_2 - R \sin(\delta_2 + 2\Omega\tau) + \sin(\delta_2 - \delta_2 + 2\Omega\tau)}{2(1 + R^2 - 2R \cos \delta_2)(1 + R^2 - 2R \cos(\delta_1 + 2\Omega\tau))} + \\
&+ \frac{(R - \cos(\delta_2 + 2\Omega\tau)) \sin \delta_1 + (-R + \cos \delta_1) \sin(\delta_2 + 2\Omega\tau)}{2(1 + R^2 - 2R \cos \delta_1)(1 + R^2 - 2R \cos(\delta_2 + 2\Omega\tau))} \Bigg]^2 \Bigg\}^{\frac{1}{2}} \quad \text{(5.20h)}
\end{aligned}$$

$$\tan \xi_1 = -\frac{(-1 + R^2 + 2R \cos \delta_2 - 2R^2 \cos 2\Omega\tau) \sin 2\Omega\tau}{(-1 + R^2 - 2R \cos \delta_2 + 2R^2 \cos 2\Omega\tau)(1 - \cos 2\Omega\tau)}, \quad \text{(5.20i)}$$

$$\tan \xi_2 = \frac{-\cos(\delta_1 - \phi_0) + R(\cos \phi_0 - R \cos(\delta_2 - \phi_0 - 2\Omega\tau) + \cos(\delta_1 + \delta_2 - \phi_0 - 2\Omega\tau))}{\sin(\delta_1 - \phi_0) + R(\sin \phi_0 + R \sin(\delta_2 - \phi_0 - 2\Omega\tau) - \sin(\delta_1 + \delta_2 - \phi_0 - 2\Omega\tau))},$$
$$\text{(5.20j)}$$

$$\tan \xi_3 = \frac{-\cos(\delta_1 + \phi_0) + R(\cos \phi_0 - R \cos(\delta_2 + \phi_0 + 2\Omega\tau) + \cos(\delta_1 + \delta_2 + \phi_0 + 2\Omega\tau))}{\sin(\delta_1 + \phi_0) + R(-\sin \phi_0 + R \sin(\delta_2 + \phi_0 + 2\Omega\tau) - \sin(\delta_1 + \delta_2 + \phi_0 + 2\Omega\tau))},$$
$$\text{(5.20k)}$$

$$\tan \xi_4 = \frac{-\cos(\delta_2 - \phi_0) + R(\cos \phi_0 - R \cos(\delta_2 - \phi_0 - 2\Omega\tau) + \cos(2\delta_2 - \phi_0 - 2\Omega\tau))}{\sin(\delta_2 - \phi_0) + R(\sin \phi_0 + R \sin(\delta_2 - \phi_0 - 2\Omega\tau) - \sin(2\delta_2 - \phi_0 - 2\Omega\tau))},$$
$$\text{(5.20l)}$$

$$\tan \xi_5 = \frac{-\cos(\delta_2 + \phi_0) + R(\cos \phi_0 - R \cos(\delta_2 + \phi_0 + 2\Omega\tau) + \cos(2\delta_2 + \phi_0 + 2\Omega\tau))}{\sin(\delta_2 + \phi_0) + R(-\sin \phi_0 + R \sin(\delta_2 + \phi_0 + 2\Omega\tau) - \sin(2\delta_2 + \phi_0 + 2\Omega\tau))}$$
$$\text{(5.20m)}$$

$$\tan \xi_6 = \left[\frac{\cos(\delta_1 + \phi_0 - 2\Omega\tau) + R(-\cos\phi_0 + R\cos(\delta_2 + \phi_0) - \cos(\delta_1 + \delta_2 + \phi_0 - 2\Omega\tau))}{1 + R^2 - 2R\cos(\delta_1 - 2\Omega\tau)} + \right.$$
$$\left. + \frac{R^2\cos(\delta_2 - \phi_0) + \cos(\delta_1 - \phi_0 + 2\Omega\tau) - R(\cos\phi_0 + \cos(\delta_1 + \delta_2 - \phi_0 + 2\Omega\tau))}{1 + R^2 - 2R\cos(\delta_1 + 2\Omega\tau)} \right] /$$
$$/ \left[\frac{\cos(\delta_2 + \phi_0 - 2\Omega\tau) + R(-\cos\phi_0 + R\cos(\delta_2 + \phi_0) - \cos(2\delta_2 + \phi_0 - 2\Omega\tau))}{1 + R^2 - 2R\cos(\delta_2 - 2\Omega\tau)} + \right.$$
$$\left. + \frac{R^2\cos(\delta_2 - \phi_0) + \cos(\delta_2 - \phi_0 + 2\Omega\tau) - R(\cos\phi_0 + \cos(2\delta_2 - \phi_0 + 2\Omega\tau))}{1 + R^2 - 2R\cos(\delta_2 + 2\Omega\tau)} \right],$$

(5.20n)

$$\tan \xi_7 = \left[\frac{-\cos(\delta_2 + \phi_0 - 2\Omega\tau) + R(\cos\phi_0 - R\cos(\delta_2 + \phi_0) + \cos(2\delta_2 + \phi_0 - 2\Omega\tau)])}{1 + R^2 - 2R\cos(\delta_2 - 2\Omega\tau)} + \right.$$
$$\left. + \frac{-\cos(\delta_2 - \phi_0 + 2\Omega\tau) + R(-R\cos(\delta_2 - \phi_0) + \cos\phi_0 + \cos(2\delta_2 - \phi_0 + 2\Omega\tau))}{1 + R^2 - 2R\cos(\delta_2 + 2\Omega\tau)} \right] /$$
$$/ \left[\frac{\sin(\delta_2 + \phi_0 - 2\Omega\tau) + R(-\sin\phi_0 + R\sin(\delta_2 + \Phi_0) - \sin(2\delta_2 + \phi_0 - 2\Omega\tau))}{1 + R^2 - 2R\cos(\delta_2 - 2\Omega\tau)} + \right.$$
$$\left. + \frac{\sin(\delta_2 - \phi_0 + 2\Omega\tau) + R(R\sin(\delta_2 - \phi_0) + \sin\phi_0 - \sin(2\delta_2 - \phi_0 + 2\Omega\tau))}{1 + R^2 - 2R\cos(\delta_2 + 2\Omega\tau)} \right]$$

(5.20o)

$$\tan \xi_8 = \left[\frac{R^2 - R(\cos\delta_2 + \cos(\delta_1 - 2\Omega\tau)) + \cos(\delta_1 - \delta_2 - 2\Omega\tau)}{2(1 + R^2 - 2R\cos\delta_2)(1 + R^2 - 2R\cos(\delta_1 - 2\Omega\tau))} - \right.$$
$$- \frac{R^2 - R(\cos[\delta_1 + \cos(\delta_2 - 2\Omega\tau)) + \cos(\delta_1 - \delta_2 + 2\Omega\tau)}{2(1 + R^2 - 2R\cos[\delta_1)(1 + R^2 - 2R\cos(\delta_2 - 2\Omega\tau))} +$$
$$+ \frac{R^2 - R(\cos\delta_2 + \cos(\delta_1 + 2\Omega\tau)) + \cos(\delta_1 - \delta_2 + 2\Omega\tau)}{2(1 + R^2 - 2R\cos\delta_2)(1 + R^2 - 2R\cos(\delta_1 + 2\Omega\tau))} -$$
$$\left. - \frac{R^2 + \cos(\delta_1 - \delta_2 - 2\Omega\tau) - R(\cos\delta_1 + \cos(\delta_2 + 2\Omega\tau))}{2(1 + R^2 - 2R\cos\delta_1)(1 + R^2 - 2R\cos(\delta_2 + 2\Omega\tau))} \right]$$
$$/ \left[\frac{R\sin(\delta_2 - R\sin\delta_1 - 2\Omega\tau) + \sin(\delta_2 - \delta_2 - 2\Omega\tau)}{2(1 + R^2 - 2R\cos\delta_2)(1 + R^2 - 2R\cos(\delta_2 - 2\Omega\tau))} - \right.$$
$$- \frac{-R\sin\delta_2] + R\sin(\delta_2 - 2\Omega\tau) + \sin(\delta_2 - \delta_2 + 2\Omega\tau)}{2(1 + R^2 - 2R\cos\delta_2)(1 + R^2 - 2R\cos(\delta_2 - 2\Omega\tau))} +$$
$$+ \frac{R\sin\delta_2 - R\sin(\delta_2 + 2\Omega\tau) + \sin(\delta_2 - \delta_2 + 2\Omega\tau)}{2(1 + R^2 - 2R\cos\delta_2)(1 + R^2 - 2R\cos(\delta_1 + 2\Omega\tau))} +$$
$$\left. + \frac{(R - \cos(\delta_2 + 2\Omega\tau))\sin\delta_1 + (-R + \cos\delta_1)\sin(\delta_2 + 2\Omega\tau)}{2(1 + R^2 - 2R\cos\delta_1)(1 + R^2 - 2R\cos(\delta_2 + 2\Omega\tau))} \right].$$

(5.20p)

5.4. Shot noise in time domain with DC readout

The fields of the shot noise, caused by the ground state quantum oscillations, like the signal fields considered in the previous section, are not changing from replacing the

homodyne detection by the DC-readout. The photocurrent component, sourced by the shot noise, injected somewhere in the detector, is calculated as the beating of its field, described by the amplitude (3.13), with the zeroth order field:

$$
I_{\mathrm{sn}}(t) = 2\sum_{n=0}^{\infty}\int_{-\infty}^{t}dt_1\int_{-\infty}^{\infty}\frac{d\Omega}{2\pi}\sqrt{\frac{2\pi\hbar\omega_p}{\mathcal{A}c}}\frac{B_n}{2}\Big[\hat{a}(\omega_p+\Omega)L_{\mathrm{s}}(t,t_1)e^{-i\xi_n(t)} +
$$
$$
+\,\hat{a}^{\dagger}(\omega_p-\Omega)L_{\mathrm{s}}^{*}(t,t_1)e^{i\xi_n(t)}\Big]e^{-i\Omega t_1}\quad (5.21)
$$

The full shot noise is summed up by the injections into the dark-port and the end-mirrors (losses), the response of the detector to which is described by the impulse responses (3.34), (3.50a) and (3.50b). The autocorrelation function of the shot noise, caused by these injections reads:

$$
B_{\mathrm{dc}}(t_1,t_2) = 4\sum_{n=0}^{\infty}\sum_{m=0}^{\infty}B_nB_mC_z\Re\Big\{e^{i(\xi_m(t_2)-\xi_n(t_1))}\,\times
$$
$$
\times\int_{-\infty}^{\min(t_1,t_2)}dt_1'\,\Big[L_{\mathrm{s}}(t_1,t_1')L_{\mathrm{s}}^{*}(t_2,t_1') + L_{\mathrm{c,n\to d}}(t_1,t_1')L_{\mathrm{c,n\to d}}^{*}(t_2,t_1') +
$$
$$
+L_{\mathrm{c,e\to d}}(t_1,t_1')L_{\mathrm{c,e\to d}}^{*}(t_2,t_1')\Big]\Big\}\quad (5.22)
$$

The integral in this expression is by chance the expression for the shot noise auto-correlation function with the homodyne detection (3.15). Substituting the result of this integration, which was explicitly found in (3.55), we get:

$$
B_{\mathrm{dc}}(t_1,t_2) = 8I_{\mathrm{dc}}(t_1)C_z\delta(t_1-t_2).\qquad (5.23)
$$

So, during the dynamical tuning with DC-readout, the shot noise of the detector becomes non-stationary. Though it stays delta-correlated, the value of this correlation is proportional to the zeroth-order component.

Part III.

Simulations of signal detection

T HE photocurrent on the output of a GW detector consists always of a signal and a noise part, for both conventional and for a dynamically tuned detector. Dynamical tuning of the Michelson-based detector increases the amplification of the chirp gravitational wave in the whole frequency range with respect to the conventional stationary detector. However, the fast motion of the SRM, required for resonant tracking of the signal, causes a non-stationary operational regime of the detector. The time-domain model of the detector, considered in chapter II, describes these non-stationary transformations of both signals and noise, allowing to simulate their corresponding photocurrent components.

The successful detection of the GW component as well as the determination of its parameters depends also on the noise level. The comparison of the intensities of signals and of noise defines the sensitivity of the detector to the particular signal via a so called signal-to-noise-ratio (SNR). This quantity is independently defined through both Neyman-Pearson criteria, which is described in the chapter 6, and through the matched filtering (see e.g. [78]).

The calculations of the SNR require the explicitly calculated signal and the parameters of the noise in the output photocurrent, or reduced to any other quantity, e.g. to the end-mirror motion. The simulations of the output from chirp GW signals as well as the SNRs are analyzed in chapter 7. It allows us to compare the sensitivity of the dynamically tuned detection with respect to a conventional stationary detector.

6.1. Detection of the signal with noise in time domain. Neyman-Pearson approach. SNR

The calculation of the SNR for the dynamically tuned detection of a chirp signal is based on the maximum likelihood principle, first described by Neyman and Pearson [79] and applied for the detection of chirp GW signals in Gaussian noise, which is a good approximation after vetoing, e.g. in [80].

Assume the two hypotheses about the measured signal $x(t)$: (i) H_0, assuming a pure, without any signal, Gaussian noise $n(t)$ with the autocorrelation function $B(t, u)$ and, generally speaking, non-stationary; (ii) H_1, assuming the known signal $s(t)$ on the background of this noise:

$$x(t) = \begin{cases} n(t), 0 \le t \le T, \text{if } H_0 \text{ is true,} \\ s(t) + n(t), 0 \le t \le T, \text{if } H_1 \text{ is true.} \end{cases} \tag{6.1}$$

For these hypotheses the probability distribution to measure the discrete number of signal values at the instances of time $x_i = x(t_i), 0 \le i \le N$ reads:

$$p_0(x_i) = \frac{1}{(2\pi)^{N/2}|S_{kl}|^{-1/2}} \exp\left\{-\frac{1}{2}\sum_{i,j=0}^{N}[x_i - s(t_i)]S_{ij}^{-1}[x_j - s(t_j)]\right\}, \tag{6.2a}$$

$$p_1(x_i) = \frac{1}{(2\pi)^{N/2}|S_{kl}|^{-1/2}} \exp\left\{-\frac{1}{2}\sum_{i,j=0}^{N} x_i S_{ij}^{-1} x_j\right\}, \tag{6.2b}$$

where $S_{ij} \equiv E[(x_i - s(t_i))(x_j - s(t_j))]$ is the covariation matrix that describes the noise statistics.

The likelihood ratio for this signal is

$$\Lambda(x_i) \equiv \frac{p_1(x_i)}{p_0(x_i)} =$$

$$= \exp\left\{-\frac{1}{2}\sum_{i,j=0}^{N}[x_i - s(t_i)]S_{ij}^{-1}[x_j - s(t_j)] + \frac{1}{2}\sum_{i,j=0}^{N}x_i S_{ij}^{-1}x_j\right\}, \quad (6.3)$$

The logarithm of likelihood for the continuous measurement may be obtained by the change of the sum over each index to the integration over the corresponding moment of time and by the introduction of an auxiliary inverse function $q(t) = \int_0^T S^{-1}(t,t_1)s(t_1)dt_1$:

$$\log \Lambda[x(t)] = \int_0^T x(t)q(t)dt - \frac{1}{2}\int_0^T s(t)q(t)dt, \quad (6.4)$$

where $q(t)$ is the solution of the following integral equation:

$$s(t) = \int_0^T q(u)B(t,u)du. \quad (6.5)$$

The likelihood ratio $\Lambda[x(t)]$ depends on the measured data only through an integral called *detection statistics*:

$$G = \int_0^T x(t)q(t)dt. \quad (6.6)$$

According to the assumptions, every measured value $x(t)$ is Gaussian, therefore G, being their linear combination, is also Gaussian, and the parameters of its distribution are $< G >= d^2$ (for H_1) and $\sigma_G =< G^2 - < G >^2 >= d^2$, where

$$d^2 = \int_0^T s(t)q(t)dt \quad (6.7)$$

is the signal-to-noise ratio.

The signal $s(t)$ we measure in this work is a photocurrent $I_{\text{det}}(t)$, calculated with the impulse response to the end-mirror motion (see section 4.1). The main detected fractions of noise, with respect to which the SNR is calculated are the shot noise (3.55) and the end-mirror displacement noise (see section 4.5).

6.2. SNR for a shot-noise-limited detector

The dynamical tuning amplifies the same components of the thermal noise as of the GW signals. Therefore, the most noticeable increase of sensitivity would occur in a shot noise limited detection. The integral equation (6.5) after the explicit substitution of a white shot noise (3.55) reads:

$$s(t) = C_{\mathrm{z}} \int_0^T q(u)\delta(t-u)du = C_{\mathrm{z}}q(t), \tag{6.8}$$

and its solution becomes:

$$q(t) = \frac{s(t)}{C_{\mathrm{z}}}. \tag{6.9}$$

The SNR, obtained from (6.7), is for the white shot noise:

$$d^2 = \frac{1}{C_{\mathrm{z}}} \int_0^T s^2(t)dt. \tag{6.10}$$

Therefore, physically the SNR of the dynamically tuned and shot-noise limited detection is proportional to the overall energy of the signal during detection (i.e. to the integral over the squared amplitude).

From here it follows that only the amplification of the signal determines the sensitivity during the shot-noise-limited detection. The simulations of the signal on the photodiode are therefore enough to calculate the increase of sensitivity.

The non-stationarity of the noise during the detection with DC-readout (5.23) modifies the integral equation:

$$s(t) = 8C_z \int_0^T q(u)I_{\mathrm{dc}}(t)\delta(t-u)du = C_z q(t)W_{DC}(t), \tag{6.11}$$

the solution for which reads:

$$q(t) = \frac{s(t)}{8I_{\mathrm{dc}}(t)C_z}, \tag{6.12}$$

and the corresponding SNR is therefore:

$$d^2 = \frac{1}{C_z} \int_0^T \frac{s^2(t)}{8I_{\mathrm{dc}}(t)}dt. \tag{6.13}$$

6.3. SNR for a displacement-noise-limited detection

In the current design of the stationary operated detectors the shot noise and the displacement noise are on a similar level. The dynamical tuning significantly amplifies

both the signal and thermal noise, reducing the influence of the shot noise to the detection (see also section 2.8). The displacement-noise-limited detection could become therefore a convenient model with well-known results, applicable also for the dynamical tuning detection.

It is easy to show, that if the eigenbasis of the impulse response of the detector is full, or in other words the equation (4.100) is valid, the SNRs, calculated in both photocurrent and in the end-mirror motion are equivalent. Since the displacement noise on the end-mirrors is stationary independently from the SRM motion, it is more convenient to solve the sensitivity task there. For stationary noise:

$$B(t, u) = B(t - u) = \int\limits_{-\infty}^{\infty} S(\Omega) e^{-i\Omega(t-u)} \frac{d\Omega}{2\pi} \qquad (6.14)$$

the inverse function (6.5) may be conveniently found in the frequency domain:

$$\tilde{q}(\Omega) = \frac{\tilde{s}(\Omega)}{S(\Omega)}. \qquad (6.15)$$

And the expression for the SNR becomes therefore:

$$d^2 = \int\limits_{-\infty}^{\infty} \frac{|\tilde{s}(\Omega)|^2}{S(\Omega)} \frac{d\Omega}{2\pi}. \qquad (6.16)$$

6.4. Detector with thermal and shot noise

Even if the perfect tracking of a GW signal amplifies the displacement noise significantly higher than level of shot noise, the inevitable tracking errors could reduce the amplification, forcing to take the full noise, both shot and displacement, into account. After the substitution the expression for the noise autocorrelation function from (3.55) and (4.90), the integral equation for the inverse function reads:

$$s(t) = C_z q(t) + \int\limits_0^T q(u) B_i(t, u) du. \qquad (6.17)$$

The task of solution of this equation is non-trivial. It could theoretically be obtained from the numerical simulation of the $B_i(t, u)$, using (4.94), in the discrete form of matrix, and calculating its inverse matrix.

CHAPTER 7

Simulations of the signal

THERE are two partial cases of noise configurations of a dynamically tuned detector we consider in this work: a thermal noise limited and a shot noise limited ones. As it was shown in section 6.3, the SNR for the thermal noise limited dynamically tuned detection repeats that of the stationary detection, since the thermal noise and the signal are transformed in the same way. The calculation of the SNR during the shot-noise limited detection, is basically a detection of the photocurrent on a white-noise background, unaffected by the transitions inside the detector. Therefore, the calculation of the SNR is reduced to the simulation of the GW signal on the output.

The impulse response of the detector to the end-mirror motion, described in section 4.1, defines the current on the photodetector continuously. Unfortunately the influence of the SRM position affects the photocurrent in a complex non-trivial way, via phase shifts of the single round-trips, and therefore the explicit values of the photocurrent can be analytically calculated only in very simple cases, described and analyzed in section 4.2: (i) with the constant detuning, meaning the stationary detection, (ii) and with the step-wise changes, meaning the response to the Heaviside step-function. The linear motion of the mirror is already too complex to calculate the output analytically. The motion of the SRM, required for the dynamical tuning of the chirp signal, is much more complicated that the linear one, therefore the numerical simulation of the output signal is required.

It is possible however to simulate the output numerically with the good precision. During the development of the numerical algorithm for the output signal calculation the two questions should be addressed: (i) how to discretize the values in the detector to bind them efficiently, (ii) how to model the resulting discretized value of the output signal as full as possible, using the finite number of mathematical calculations. These

questions are considered in the first section of these chapter.

The second section is the final step of the work, performed in this thesis. The time-domain model for the signal simulations, invented in this work, is used for the simulations of the chirp GW signals, predicted by the current binary stars coalescence models. The explicitly simulated signals in the photocurrent allow to calculate and to analyze the resulting SNR.

7.1. Numerical algorithms of the simulations of the output signals

7.1.1. Recycled Michelson configuration.

The current, caused by a gravitational wave in the dynamically tuned Michelson based interferometer with a homodyne detector, may be calculated with (4.7). Though this formula describes the signal at any instance t of the continuous time, it has a discrete nature: it uses the values of input parameters, namely of the differential end-mirror motion and of the SRM displacement, only at certain previous isolated instances, divided by the round-trip time.

$$I_{\det}(t) = \sum_{n=0}^{\infty} C_n x_{\mathrm{d}}(t - (2n+1)\tau) \cos(\phi_n(t) + \phi_{\mathrm{h}}), \qquad (7.1)$$

where the amplitudes C_n are defined in (4.8a, 4.8b), and $\phi_n(t)$ is a phase shift train from (D.2).

We can define a one discrete set of the input parameters, separated by the round-trips, which will define in our simulations the output current, which will consequently also be a discretized output with the same separation:

$$I_N = \sum_{n=0}^{N-1} C_n x_{\mathrm{d},N-n} \cos(\Phi_N - \Phi_{N-n} + \phi_{\mathrm{h}}). \qquad (7.2)$$

Here discretized values were introduced in the following way:

$$I_N \equiv I(2(N-1)\tau), \qquad (7.3\mathrm{a})$$

$$x_N \equiv x(2(N-1)\tau), \qquad (7.3\mathrm{b})$$

$$x_{\mathrm{d},N} \equiv x_{\mathrm{d}}(2(N-1)\tau - \tau), \qquad (7.3\mathrm{c})$$

$$f_N \equiv f(2(N-1)\tau - \tau), \qquad (7.3\mathrm{d})$$

$$\Phi_1 \equiv 0, \qquad (7.3\mathrm{e})$$

$$\Phi_N \equiv \sum_{j=1}^{N-1} 2k_{\mathrm{p}} x_j, N \geq 1. \qquad (7.3\mathrm{f})$$

For clearness these values and their indices are depicted in figures 7.1 and 7.2. Φ_N in this consideration is an accumulated phase shift from appendix D, and defined by
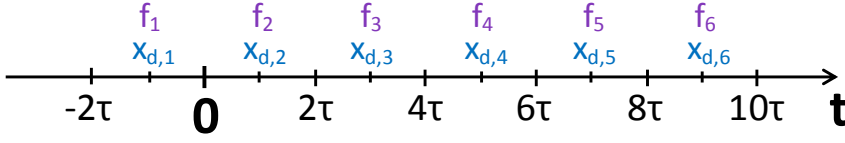
Figure 7.1.: Indices-time correspondence of gravitational wave signal and its frequency
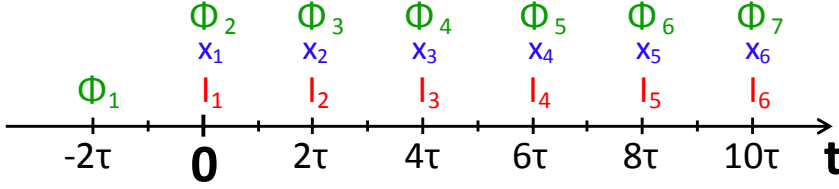
Figure 7.2.: Indices-time correspondence of the output signal, the SRM displacement and the accumulative phase

(D.11a) with $t_0 = 0$ (here the instance of the beginning was set to zero). The sum in (7.2) is interrupted at the beginning of the detection, assuming the signal beforehand to be zero.

This discretization allows to express the discretized number of the output values through the discretized set of the input values. However, a large sum in (7.2), in spite of being finite, seems quite challenging from the point of view of computational time, while interrupting it may affect the simulations precisions. To overcome this problem we may notice, that this sum, starting from $(M+1)$-st term, looks very similar to the full expression for the output value with an index $N - M - 1$. Physically, it means that the output light I_N is a light, reflected from the SRM $(M+1)$ roundtrips ago, a smaller part of which was transmitted through it and detected as I_{N-M-1}. The part remaining in the detector complement another M signal injections, becoming I_N. Therefore one could develop the following algorithm, where every new value for the output signal is calculated from the previous signal values, keeping therefore the full information about all the previous signal injections:

$$I_N = \sum_{n=0}^{M} C_n x_{\mathrm{d},N-n} \cos(\Phi_N - \Phi_{N-n} + \phi_{\mathrm{h}}) +$$
$$R^{M+1} \left[\cos(\Phi_N - \Phi_{N-M-1}) I_{N-M-1} - \sin(\Phi_N - \Phi_{N-M-1}) I_{\sin,N-M-1} \right], \quad (7.4)$$

where we have redefined after the explicit substitution of C_n:

$$R = R_F R_S. \tag{7.5}$$

The new quantity is also required for this simulation algorithm:

$$I_{\mathrm{sin},N} \equiv \sum_{n=0}^{N-1} A_n x_{\mathrm{d},N-n} \sin(\Phi_N - \Phi_{N-n} + \phi_{\mathrm{h}}) =$$

$$= \sum_{n=0}^{M} A_n x_{\mathrm{d},N-n} \sin(\Phi_N - \Phi_{N-n} + \phi_{\mathrm{h}}) +$$

$$+ R^{M+1} \left[\cos(\Phi_N - \Phi_{N-M-1}) E_{\mathrm{sin},N-M-1} + \sin(\Phi_N - \Phi_{N-M-1}) E_{N-M-1} \right]. \quad (7.6)$$

The physical meaning of this new value is the quadrature of the light on the detector, perpendicular to the one that is actually detected with the defined local oscillator.

The dynamical resonance condition (4.65), required to track the signal resonantly, reads in these discrete notations:

$$\Phi_n - \Phi_{n-1} = 2k_{\mathrm{p}} x_{n-1} = (f_{n-1} + f_n)\tau. \quad (7.7)$$

7.1.2. Delay line

In the delay line the light makes a finite and a small number of round-trips N_{rt} before being detected. Therefore, using the discretion (7.3), the following formula output signal of the corresponding configuration may be obtained from (4.15):

$$I_N = \sum_{n=0}^{N_{\mathrm{rt}}-1} A_n x_{\mathrm{d},N-n} \cos(\phi_{\mathrm{h}}), \quad (7.8)$$

where A_k is defined in (4.16).

7.1.3. Signal recycled delay line configuration

In a signal recycled detector with delay lines in the arms the light has to types of round-trips: between the mirrors of the delay line, and between two reflections from the SRM. The later we call *full round trip*. For the delay line with N_{rt} round trips inside we require therefore the following indices to specify the path of the light:

$$t_N = 2(N-1)\tau, \quad (7.9\mathrm{a})$$

$$N - 1 = (M-1)N_{\mathrm{rt}} + m - 1, \quad (7.9\mathrm{b})$$

$$m = N - \lfloor \frac{N}{N_{\mathrm{rt}}} \rfloor N_{\mathrm{rt}}, \quad (7.9\mathrm{c})$$

$$M = \lfloor N N_{\mathrm{rt}} \rfloor + 1, \quad (7.9\mathrm{d})$$

where $\lfloor a \rfloor$ denotes the whole part (of the floor) of a.

Using these notations, and (7.3), the following discrete formula is obtained from (4.19):

$$I_N = \sum_{n=0}^{\infty} \sum_{k=0}^{N_{\mathrm{rt}}-1} A_{nk} x_{\mathrm{d},N-nN_{\mathrm{rt}}-k} \cos(\Phi_{M,m} - \Phi_{M-n,m} + \phi_{\mathrm{h}}), \quad (7.10)$$

where A_{nk} is taken from (4.20a), and $\Phi_{M,m}$ is an accumulated phase shift for this configuration, defined in appendix D.2 by (4.20a).

The finite simulation formula, using the field value N_{rt} round trips ago (compare with (7.4)) is the following:

$$I_N = \sum_{k=0}^{N_{\mathrm{rt}}-1} A_{0k} x_{\mathrm{d},N-k} \cos\phi_{\mathrm{h}}+$$

$$+ R I_{N-N_{\mathrm{rt}}} \cos(2k_{\mathrm{p}} x_{N-N_{\mathrm{rt}}}) - R I_{N-N_{\mathrm{sin,rt}}} \sin(2k_{\mathrm{p}} x_{N-N_{\mathrm{rt}}}). \quad (7.11\mathrm{a})$$

The corresponding perpendicular quadrature of this quantity, required for the signal simulations is as follows:

$$I_{\sin,N} = \sum_{k=0}^{N_{RT}-1} A_{0k} x_{\mathrm{d},N-k} \sin\phi_{\mathrm{h}}+$$

$$+ R I_{N-N_{\mathrm{rt}}} \sin(2k_{\mathrm{p}} x_{N-N_{\mathrm{rt}}}) + R E_{\sin,N-N_{\mathrm{rt}}} \cos(2k_{\mathrm{p}} x_{N-N_{\mathrm{rt}}}). \quad (7.11\mathrm{b})$$

For the time, when the detection has begun quite recently, and the light hasn't finished the full round-trip, i.e. $N < N_{RT}$, the field and its perpendicular quadratures are subsequently:

$$I_N = \sum_{k=0}^{N} A_{0k} x_{\mathrm{d},N-k)} \cos\phi_{\mathrm{h}}, \quad (7.11\mathrm{c})$$

$$I_{\sin,N} = \sum_{k=0}^{N} A_{0k} x_{\mathrm{d},N-k} \sin\phi_{\mathrm{h}}. \quad (7.11\mathrm{d})$$

7.1.4. Recycled Michelson with DC readout

Since the current GW detectors operate with DC readout, the simulation of the fields in this case during dynamical tuning is important. Let us write down the equations for the fields on the photodetector (5.7,5.9) in the following way:

$$I_{\mathrm{det}}(t) = \frac{1}{2} \sum_{n=0}^{\infty} \sum_{m=0}^{\infty} B_n B_m \cos\left(\phi_m(t) - \phi_n(t)\right)+$$

$$+ \sum_{n=0}^{\infty} \sum_{m=0}^{\infty} C_n B_m \sin\left(\phi_m(t) - \phi_n(t) + \varphi_2\right) \times$$

$$\times x_{\mathrm{d}}(t - (2n+1)\tau). \quad (7.12)$$

In the case of dc-readout the assumption of the absence of the GW-signal before the detection doesn't cancel the dc-part of the field. We assume, that before the detection, the detector was waiting in the position $x(0)$, corresponding to the initial

signal frequency:

$$x(t) = x(0), t < 0, \tag{7.13a}$$

$$2k_{\mathrm{p}}x(0) = \phi_0 = 2f(0)\tau. \tag{7.13b}$$

In the expression (7.12), where the discretized values (7.3) are used, we could divide the infinite sum, corresponding to the evolution of the detector before the detection $t < 0, n > N - 1$ and during the detection $t < 0, n > N - 1$.

After some significant piece of mathematics the following discrete formula is obtained:

$$
\begin{aligned}
I_N = \frac{1}{2} \sum_{n=0}^{N-1} B_n \Bigg(\Re \left[e^{-i\Phi_{N-n}} S_N \right] + \\
+ \frac{B_0 R^N \cos\left(\Phi_{N-n} + \phi_0\right) - B_0 R^{N+1} \cos\Phi_{N-n}}{1 - 2R\cos\phi_0 + R^2} \Bigg) + \\
+ \frac{1}{2} \frac{B_0^2 R^{2N}}{1 - 2R\cos\phi_0 + R^2} + \sum_{n=0}^{N-1} C_n \Bigg(\Im \left[e^{-i(\Phi_{N-n} - \varphi_2)} S_N \right] - \\
- \frac{B_0 R^N \sin\left(\Phi_{N-n} + \phi_0 - \varphi_2\right) - B_0 R^{N+1} \sin\left(\Phi_{N-n} - \varphi_2\right)}{1 - 2R\cos\phi_0 + R^2} \Bigg) x_{\mathrm{d},N-n}. \quad (7.14)
\end{aligned}
$$

Here the quantity, describing the time evolution of the zeroth order dc-component, is introduced for the simplification:

$$S_N = \sum_{m=0}^{N-1} B_m e^{i\Phi_{N-m}}. \tag{7.15}$$

7.1.5. Signal deconvolution

The task of the deconvolution, studied in this thesis for the recycled Michelson interferometer, allows to restore the input signal from the output photocurrent. As it was mentioned, the discrete set of the output current, separated by the round-trip time, is bound to another set of the discrete values of the input signal. Therefore, we could use the discretization, defined in (7.3) and shown in figures 7.1 and 7.2, without any error from switching from the continuous to discrete data. The discrete set of the output current is bound with the discrete set of the input signal values, therefore, we could simulate the deconvolution for the one set of the bound data, using (4.98) and (4.99):

$$x_{\mathrm{d},N} = \sum_{n=0}^{N-1} \tilde{A}_{n,N} I_{N-n}, \tag{7.16}$$

where:

$$\tilde{A}_{0,N} = \frac{1}{C_0}, \tag{7.17a}$$

$$\tilde{A}_{1,N} = -\frac{R}{C_0} \cos\left(2\omega_p \frac{x((N-1)\tau - \tau)}{c}\right) = -\frac{R}{C_0} \cos\Delta\phi_{N-1}, \tag{7.17b}$$

$$\tilde{A}_{2,N} = \frac{R^2}{C_0} \sin\Delta\phi_{N-1}\sin\Delta\phi_{N-2}, \tag{7.17c}$$

$$\tilde{A}_{n,N} = \frac{R^n}{C_0} \prod_{l=2}^{n-1} \cos\Delta\phi_{N-l}\sin\Delta\phi_{N-1}\sin\Delta\phi_{N-n}, n \geq 3, \tag{7.17d}$$

$$\Delta\phi_N \equiv 2k_p x_N. \tag{7.17e}$$

The numerical calculation of this sum implies either a significant calculation time, or the inevitable error from interruption of the sum. However, similarly to the direct impulse response, the end-mirror displacement is calculated from the information about the previous output current signals, and, therefore can be used for the calculation of the next displacements by adding only the recent values of the photocurrent:

$$x_{d,N} = R\frac{\sin\Delta\phi_{N-1}\cos\Delta\phi_{N-2}}{\sin\Delta\phi_{N-2}}x_{d,N-1} + \frac{1}{C_0}I_N -$$
$$- R\frac{\sin(\Delta\phi_{N-1} + \Delta\phi_{N-2})}{\sin\Delta\phi_{N-2}}\frac{1}{C_0}I_{N-1} + R\frac{\sin\Delta\phi_{N-1}}{\sin\Delta\phi_{N-2}}\frac{R}{C_0}I_{N-2}. \tag{7.18}$$

7.2. Simulation results. The improvement of sensitivity from dynamical tuning

The main goal of any detector development is increasing the sensitivity of the signal detection. The sensitivity of a certain detection regime with an arbitrary, also non-stationary, known Gaussian noise budget to a given signal, is commonly described by the SNR defined in the previous chapter. The increase of sensitivity by the implementation of the dynamical tuning is very much dependent on the specific detector configuration. To estimate the realistic benefits from the dynamical tuning, the improvement of the SNR, caused by its implementation into an existing detector, should be calculated.

GEO 600 [34, 81] is the only currently operating detector, and is traditionally used for testing advanced technologies, such as signal recycling or squeezing. It could be a good candidate for the test or the science run implementations of the dynamical tuning. The response of GEO 600, assumed for simplicity with the folded arms replaced by straight ones with the same optical length, is described by (4.10) and is modelled, using (7.4) and (7.6). The current stationary regime of GEO 600, with respect to which we study the increasing of sensitivity, has a broad frequency band ($\sim 1000\,\text{Hz}$), established by a low-reflective SRM, and is therefore optimized for chirp signals. The dynamical tuning can be implemented into GEO 600 by: (i) installation of a new SRM
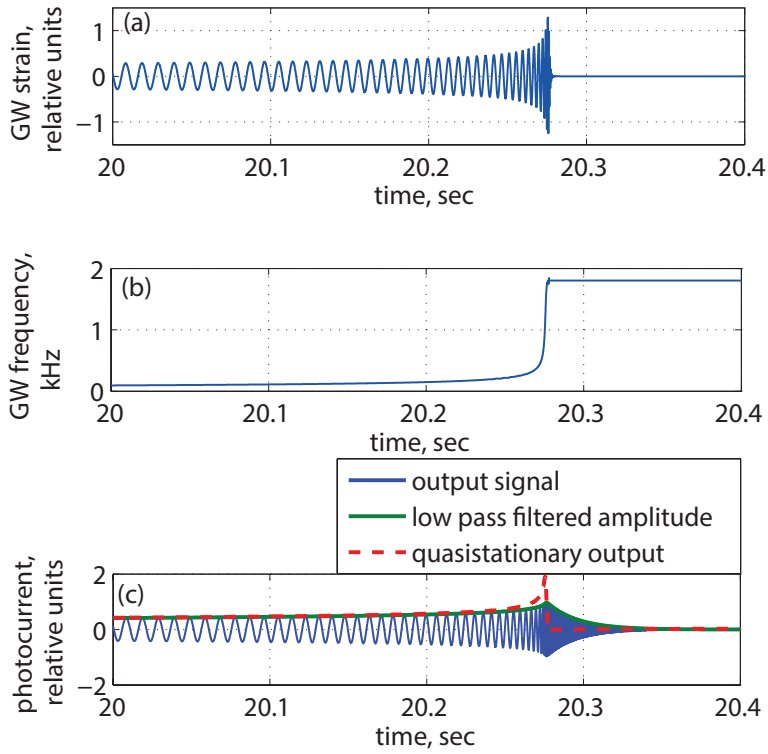
Figure 7.3.: (a) The gravitational wave signal from a 5+5 Solar mass spinless black hole binary. (b) The instantaneous frequency of this signal. (c) The resonantly tracked detection signal, compared to the low-pass-filtered GW amplitude and the output in quasistationary approximation
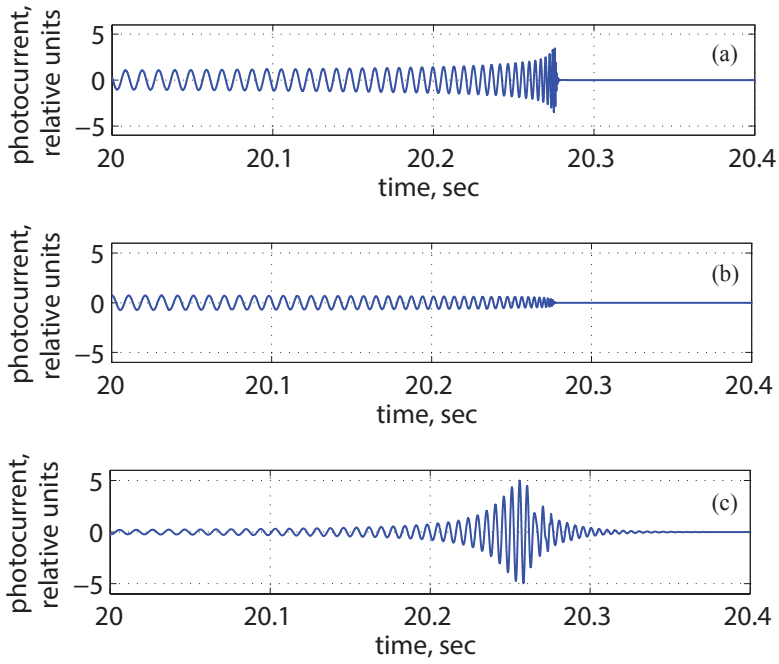
Figure 7.4.: The response to the GW of a stationary detector (a) in current GEO configuration, (b) with narrow-band sensitivity and tuned, and (c) with narrow-band sensitivity and detuned to 200 Hz
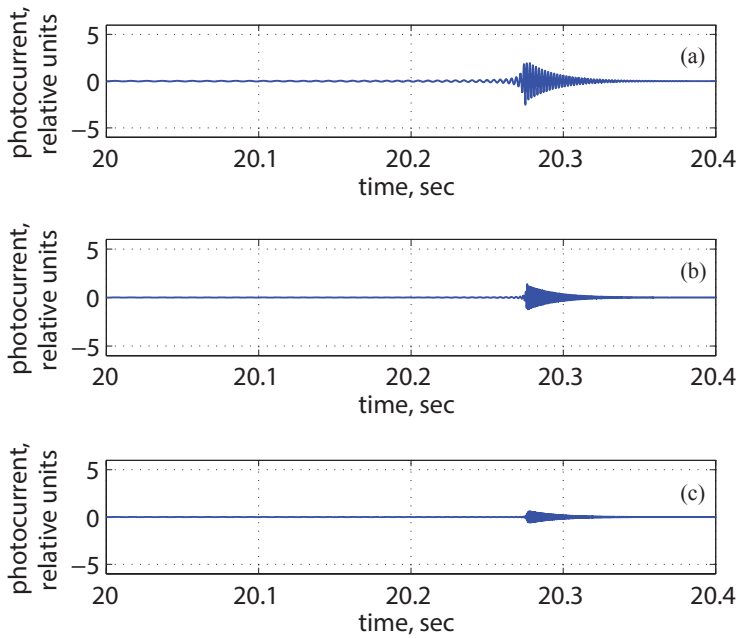
Figure 7.5.: The response to the GW of a stationary detector (a) with narrow-band sensitivity and detuned to 500 Hz, (b) with narrow-band sensitivity and detuned to 1000 Hz, and (c) with narrow-band sensitivity and detuned to 1800 Hz
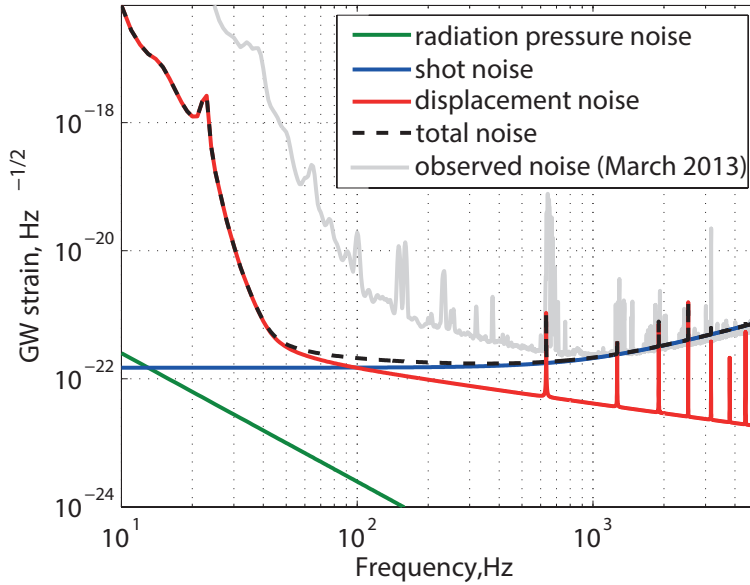
Figure 7.6.: The noise budget of GEO 600. The gain of the real noise at high frequencies is due to the injection of squeezed light

with high reflectivity, instead of the old one, to achieve the narrow-band regime, and (ii) moving the SRM very precisely, synchronized to the chirp frequency change, also keeping the detector locked. The sensitivity of the dynamically tuned detection is compared to the current operation mode of the detector, also referred to as reference configuration, or a reference detector. The parameters of GEO 600 and its laser used for the simulations are presented in tables 2.1 and 2.2, and the differences between the considered regimes are in the table 7.1.

The chirp signals, used for the simulations, are modeled by hybrid models [17–20] for an arbitrary set of masses and spins of the binary elements. In this work the sensitivity to only one group of signals is studied: to spinless binaries with equal masses and total mass ranging from 3 to 10 solar masses.

Since the hybrid model contains the time dependency of the instantaneous frequency of a chirp signal, it is possible to simulate its resonant tracking, using an algorithm for Michelson-based detectors (7.7). The example of such a simulation is presented in figure 7.3. In its parts (a) and (b) the latter stage of a chirp signal, emitted by the binary with 5+5 Solar masses, and its frequency are depicted. The simulation of the resonantly tracked detection of this signal is presented in figure 7.3 (c). The simulated output signal is compared to the low-passed filtering of the GW envelope according to (4.85) (see also the whole section (4.4)). These two results fit, validating both the numerical model and resonant tracking approximation. It also evident that the non-resonant sideband, neglected in the resonant tracking approximation, is really

Table 7.1.: GEO parameters, modified for the dynamical tuning

| Symbol	Quantity	Current configuration value	Value for dynamical tuning configuration
T_S^2	Power transmission on the signal recycling mirror (SRM)	0.1	420 ppm
δ	Frequency detuning of signal recycling cavity	0 Hz	resonant tracking

very small.

The comparison of the simulated response to the GW with the non-physical result of quasistationary (or mathematically equivalent virtually stationary, as described in section 4.4) approximation, shows where the amplitude of the signal changes very fast, kicking the detection out of both quasi-stationary and virtually stationary regime, namely at the instantaneous frequencies $f > 200$ Hz. This frequency region coincides with the one, depicted in figure 2.9, where the effect of radiation pressure noise is negligible. Therefore, the time-domain model, developed in this thesis, is required for the proper simulation of this part of the signal, and we may assume the detection to be free of radiation pressure effects.

For these reasons all the segments of the signals, the SNR-gain to which is calculated, are taken with the instantaneous frequency starting from 200 Hz. To study the dependence on the source masses, the sensitivity to the signal from the binary systems with equal components and with total masses ranging from 3 to 10 Solar masses is considered.

The sensitivity improvement of dynamical tuning is calculated with respect to the current configuration of the detector, the response of which to the signal in figure 7.3 is depicted in the same relative units in figure 7.4(a). To give an additional feeling of the narrow-band regime, a few detection results, performed in this regime for different detunings, is represented in figure 7.4(b,c) and in figure 7.5. In these plots the excitations of different signal frequency components are clearly seen.

The noise of the detector can be divided into three parts, according to their origins: shot noise, radiation pressure noise and thermal noise as it is shown in figure 7.6 [82,83]. We assume, that the real noise will be reduced to the theoretical predictions, and we use them for the sensitivity analysis. As it was mentioned before, the radiation pressure noise is negligible in the frequency band of our interest. The increase in sensitivity occurs from the enhancement of the GW signal in comparison to shot noise only, because dynamical tuning amplifies the same components of thermal noise as of GWs, keeping the constant sensitivity with respect to the thermal noise. Therefore first we study the sensitivity increasing in the shot noise limited assumption. GEO 600 is operating with squeezed shot noise. And for the dynamical tuning simulations we use the ground-state shot noise (without squeezing), for it is easier to simulate and is low enough to overcome the thermal noises, as it will be shown later.
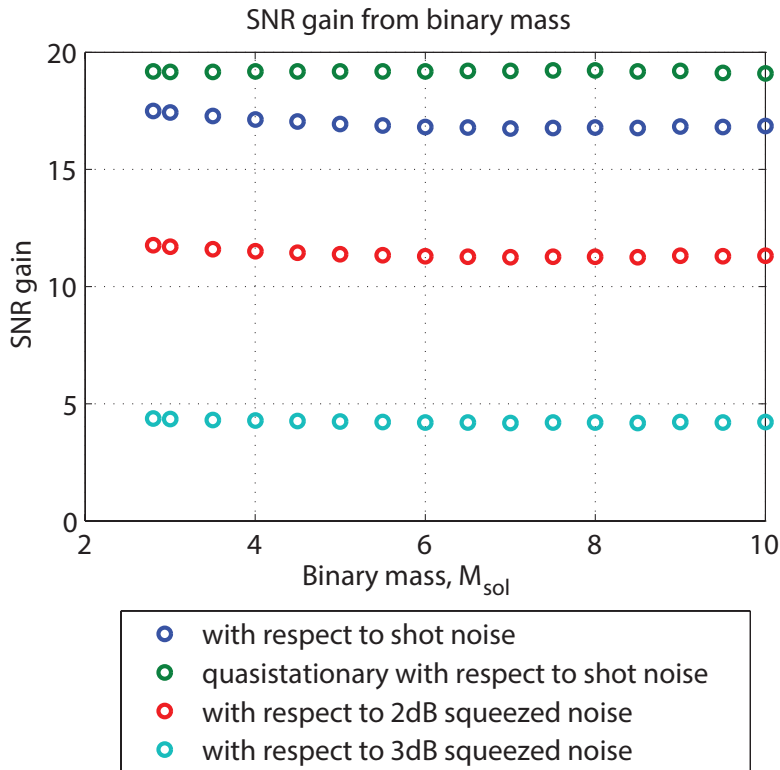
Figure 7.7.: The SNR gain of the dynamical tuning in comparison with the stationary broad-band regime. Both regimes are considered as shot noise limited

The ground state shot noise on the photodiode remains delta-correlated independently from the changed parameters of the SRM, namely its motion during the detection and its transmittance (see section 3.5). Therefore the SNR with respect to this noise, as it follows directly from (6.10), may be compared via the corresponding signal in the output current. The additional squeezing of the shot noise in the reference configuration reduces the SNR increase corresponding to the squeeze factor in (3.7). For this study we use the realistic squeezing factors [84, 85].

The gain in the SNR for the shot-noise limited detector for different squeezing factors of the reference configuration is presented in figure 7.7. It has values from ~ 5 to ~ 17, depending on the squeezing factor of the reference detector. It decreases slightly with increasing of the mass of the system. The SNR-gain with respect to the vacuum shot noise limited configuration, obtained in quasi-stationary approximation, is also depicted in the figure to estimate the dynamical effects of the detector. The output signal, simulated in this approximation, was presented before, in figure 7.3. It significantly differs from the real values, but due to slow change of frequency and amplitude for most of signal duration the integral effect of this difference is of the order of 15 %.

The thermal noise in figure 7.6 is comparable to the shot noise in the frequency band of interest. Since dynamical tuning decreases dramatically the influence of shot noise to the sensitivity, the influence of the thermal noise, which stays the same, becomes dominant, at least by factor of 12, as it shown in figure 7.8. Therefore the thermal noise limited detector makes a good approximation for the SNR gain achievable by dynamical tuning in a real detector, considered with both shot and thermal noise. The values for the SNR-gain, simulated in this thermal-noise-limited approximation is depicted in figure 7.9 with respected to the different squeezing factors in the reference regime. It has values varying from factor of ~ 3 to factor of ~ 8, depending on the squeezing factor of the reference detection regime.
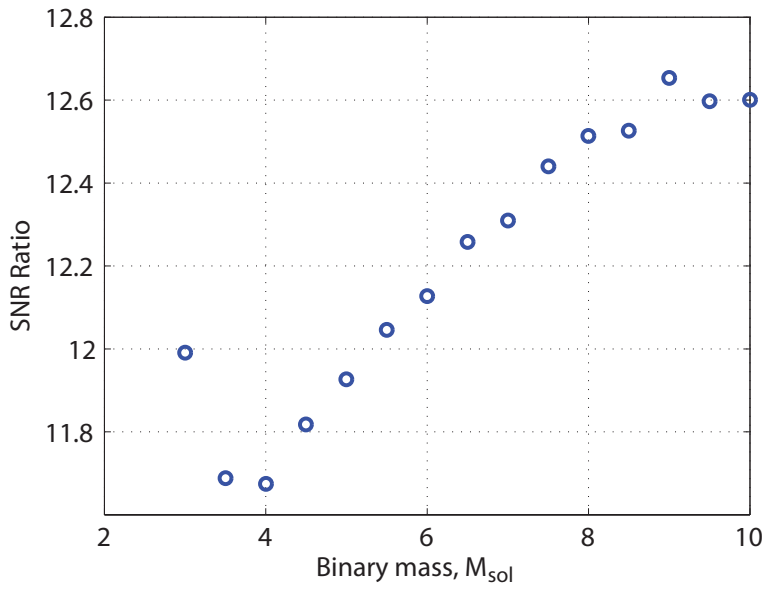
Figure 7.8.: The ratio of SNRs for a shot noise limited and a thermal noise limited detector with dynamical tuning
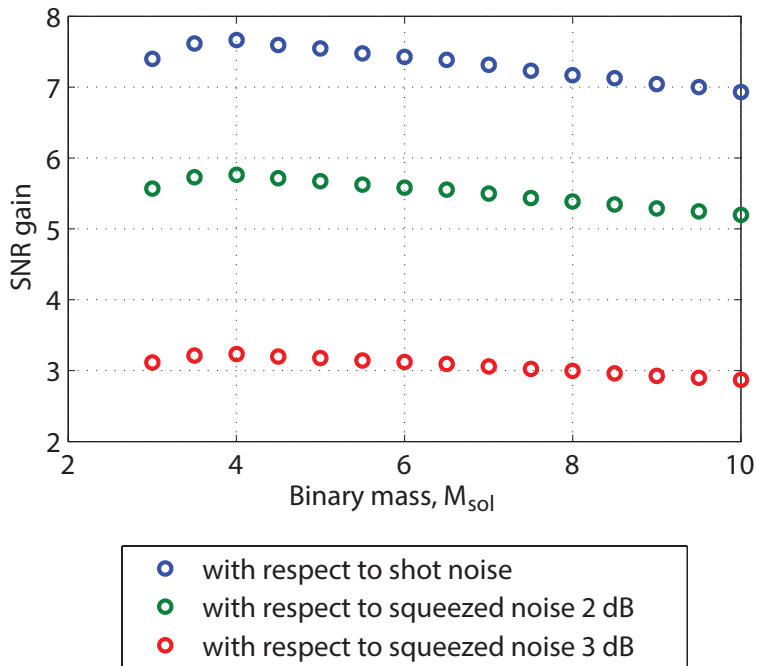
Figure 7.9.: The SNR gain of the dynamical tuning compared to broad band configuration, assuming that dynamical tuning is thermal noise limited

Summary and outlook

In this thesis we have studied the so-called dynamical tuning, a method of detecting chirp GW signals, during which the instantaneous signal frequency is tracked by the detuning of the detector.

We have repeated the frequency-domain consideration of a Fabry-Perot cavity and of a Michelson-based interferometer, considered in [47]. The resulted sensitivity allowed us to make a quasi-stationary model of a dynamically tuned detection with full quantum (both shot and radiation pressure) and displacement noise. It is a generalization of the approach from [52], where the analogous task was performed for the shot-noise-limited detection.

We have developed a time-domain method of analysis, since the detector, performing dynamical tuning, operates in a non-stationary regime (detuning of the SRC rapidly changes in time to match the frequency of the signal). We have considered the response of the detector to the shot noise injected through the dark port and lossy optical elements, and to differential motion of the end-mirrors, caused by GW signal and displacement noise. We found that although the optical fields describing vacuum fluctuations transform non-trivially inside the non-stationary detector, the output shot noise remains delta-correlated for arbitrary realistic motions of the SRM.

Using the signal response to the differential end-mirror motion we have defined a dynamical resonance, when the phase shifts of light, caused by the GW evolution and by the SRC detuning are canceled. We have studied a so-called resonant tracking of a signal, when the detuning of the SRC keeps the ideal dynamical resonance with the chirp frequency. We established that the detection during perfect resonant tracking of a chirp signal with negligible rate of amplitude displays a so-called virtual stationarity, when the field oscillations inside the detector possesses the corresponding stationary value. If the amplitude of a GW changes significantly, as in a chirp GW, the amplitude of the output photocurrent would have the shape of the low-pass-filtered GW amplitude. In principle, the fast changes of signal frequency and amplitude as well as of the SRM position cause transient effects. However, by properly adjusting the

mirror motion to the signal frequency, the corresponding transient effects are canceled by each other, leaving only the amplitude related ones.

Assuming a shot noise limited detector, the enhancement factor in SNR of a dynamically tuned detector over the current broadband GEO 600 configuration is 17. The analogous values with respect to the 2 dB and 3 dB squeezing in the reference detector gives 12 and 4 respectively. The influence of dynamical effects in the chirp signal detection is of the order of 15 percent. However we can neglect them if we perfectly track the signal frequency, because then the detector becomes displacement noise limited, so there are no transient effects of the gravitational wave with respect to displacement noise. Also the current level of displacement noise reduces the SNR enhancement factor down to 7, 5 and 3 correspondingly.

These number are the upper limit for the SNR gain for dynamical tuning with the theoretically predicted displacement noise, and we could achieve the value of 17, 12 and 4 if we could decrease the thermal noise sufficiently. The enhancement values will also be modified when we take into account the error of the resonant tracking that will cause a contribution of both shot and displacement noise into the dynamical tuning sensitivity.

The set of SNRs for the dynamical tuning we presented in section 7.2 was obtained with very special assumptions: (i) the SRM tracks resonantly the frequency of the chirp signal, (ii) the detector is considered to be either thermal, or shot noise limited. The inevitable error in the SRM position during its motion makes perfect resonant tracking of the signal impossible, preventing the signal and displacement noise from reaching their maximal amplification in comparison to shot noise. Even a small error, comparable with the band-width of the dynamically tuned detector, i.e. 8 Hz, makes the influence of shot and displacement noise of the same order.

The calculation of the SNR for both noise terms, using (6.7), requires in this case a numerical solving of the integral equation (6.5) with the composite detector noise, which can be in principle calculated with an arbitrary precision,

$$B_{\text{tot}}(t_1, t_2) = B_\eta^{\text{tot}}(t_1, t_2) + B_{\text{th}}(t_1, t_2), \tag{7.19}$$

where the items from the sum should be taken from (4.94) and (3.55) respectively. The solution of (6.5) allows also to estimate the influence from the signal tracking error, as it was done in [52], giving us the realistic benefits of the dynamical tuning.

In all the real GW detectors, a DC readout is used instead of a homodyne detection. The additional leak of laser light from the power recycling cavity of a Michelson based interferometer, caused by dark-fringe offset, becomes an equivalent local homodyne oscillator. The leaking power on the photodiode depends on SRC detuning, and therefore becomes time-dependent during a dynamical tuning detection. The filtering of the new time-dependent "DC"-part of the photo-current requires new solutions in the signal processing.

The considered Michelson configuration is used only in GEO 600, while the other GW detectors, namely Advanced LIGO, Advanced VIRGO and the Einstein Telescope, have Fabry-Perot cavities in the arms. The time-domain model for their layout may be obtained by the development of the described time-domain model. However, the shot and the displacement noise of these detectors have similar proportions as

depicted in FIG. 7.6, therefore the thermal-noise-limited configurations will give a good approximation for the maximal sensitivity gain which is possible by the implementation of dynamical tuning.

Brief CGS and SI based eletricity basics

Laws of electrical interaction are conventionally expressed in units of the two systems: CGS (centimeter, gram, second) and SI(french: Systeme international). Basis for the units in SI-system is definition of currency, Ampere. Ampere is the current in two infinite parallel conductors, placed on the distance of 1 meter from each other, causing the interaction force between them of 2×10^{-7} newtons. The unit of charge, 1 coulomb, is a charge, transmitted by current of 1 Ampere flow through a cross-section during 1 second. The CGS system is based on the charge definition. The unit of charge in it is the charge of two point particles, separated from each other by the distance of 1 cm, creating the force of one dyne. The Coulomb's Law in both systems:

$$\vec{F} = \frac{q_1 q_2}{r^2} \frac{\vec{r}}{|\vec{r}|} \text{ in CGS-system,} \tag{A.1a}$$

$$\vec{F} = \frac{1}{4\pi\epsilon_0} \frac{q_1 q_2}{r^2} \frac{\vec{r}}{|\vec{r}|} \text{ in SI-system.} \tag{A.1b}$$

Here $\frac{1}{4\pi\epsilon_0} = 9 \times 10^9 \frac{Nm^2}{C^2}$

Because the force, acting the between the particles, is defined by charges and distances, and is independent from the units system, the charge unit of CGS-system has a one-to-one correspondence with coulombs:

$$1 \, \text{coulumb} = 3 \times 10^9 \, \text{units CGS.} \tag{A.2}$$

The equation for interaction of particle with electrical field is the same for both systems:

$$\vec{F} = \vec{E}q. \tag{A.3}$$

The boundary between the units of the fields, the force and charge in both units defines the boundary for the units of eletrical field E:

$$1\,\text{V/m} = \frac{1}{3} \times 10^{-4}\,\text{units CGS.} \tag{A.4}$$

The law of Ampere-Bio-Savar-Laplace for the magnetic field, caused by an elementary current in units of the both systems is:

$$d\vec{H} = \frac{I}{c}\frac{d\vec{l} \times \vec{r}}{r^3} \text{ in SI-system,} \tag{A.5a}$$

$$d\vec{H} = \frac{2I}{cr}\frac{d\vec{l} \times \vec{r}}{r^3} \text{ in CGS-system.} \tag{A.5b}$$

The boundary for the units of magnetic field in both systems is, therefore:

$$1\,\text{A/m} = 4\pi \times 10^{-3}\,\text{units CGS.} \tag{A.6}$$

And in the end, the force of Lorentz, caused by this field, is defined in both units as following:

$$\vec{F} = q\left[\vec{v} \times \vec{B}\right] \text{ in SI-system} \tag{A.7a}$$

$$\vec{F} = \frac{q}{c}\left[\vec{v} \times \vec{B}\right] \text{ in CGS-system.} \tag{A.7b}$$

Fields in GEO 600 layout

B.1. Input-output relation

The layout of the detector is represented in figure 2.1. All the values used in this appendix could be found in tables 2.1 and 2.2.

Similar to the fields in a Fabry-Perot cavity, it is convenient to split the fields, propagating in GEO 600, into the zeroth and the first order terms. Again the zeroth order mode fields are sourced by the well-stabilized laser, and the perturbation, caused by the noise sources and the GWs, make contribution only to the first order terms.

The reflections of the laser field on the optical elements of GEO 600 as well as propagation in vacuum, described in this section, are based on formulas of the reflection from the mirrors, (1.12a) and (1.12b), and of the phase shift. The 50/50 reflections from the beam splitter are described similarly:

$$J = i\frac{\sqrt{2}}{2}E - \frac{\sqrt{2}}{2}H.$$

(B.1)

It is convenient to write the input-output relations of the optical elements in GEO 600 (figure 2.1) sorted by parts of optical paths and approximation orders.

1. Power recycling arm (between the beamsplitter and the PRM).

a. Zeroth approximation:

$$D = iT_\mathrm{p}A - R_\mathrm{p}C, \tag{B.2a}$$

$$E = De^{ik_\mathrm{p}L_\mathrm{i}}, \tag{B.2b}$$

$$F = i\frac{\sqrt{2}}{2}I - \frac{\sqrt{2}}{2}L, \tag{B.2c}$$

$$C = Fe^{ik_\mathrm{p}L_\mathrm{i}}, \tag{B.2d}$$

$$B = iT_\mathrm{p}C - R_\mathrm{p}A. \tag{B.2e}$$

b. First approximation:

$$\hat{\mathrm{d}}(\omega) = iT_\mathrm{p}\hat{\mathrm{a}}(\omega) - R_\mathrm{p}\hat{\mathrm{c}}(\omega) + 2iR_\mathrm{p}k_\mathrm{p}X_\mathrm{i}(\Omega)C, \tag{B.3a}$$

$$\hat{\mathrm{e}}(\omega) = \hat{\mathrm{d}}(\omega)e^{ikL_\mathrm{i}}, \tag{B.3b}$$

$$\hat{\mathrm{f}}(\omega) = i\frac{\sqrt{2}}{2}\hat{\mathrm{i}}(\omega) - \frac{\sqrt{2}}{2}\hat{\mathrm{l}}(\omega), \tag{B.3c}$$

$$\hat{\mathrm{c}}(\omega) = \hat{\mathrm{f}}e^{ikL_\mathrm{i}}, \tag{B.3d}$$

$$\hat{\mathrm{b}}(\omega) = iT_\mathrm{p}\hat{\mathrm{c}}(\omega) - R_\mathrm{p}\hat{\mathrm{a}}(\omega) - 2iR_\mathrm{p}k_\mathrm{p}X_\mathrm{i}(\Omega)A. \tag{B.3e}$$

2. North arm (upwards from the beamsplitter).
a. Zeroth approximation:

$$K = i\frac{\sqrt{2}}{2}H - \frac{\sqrt{2}}{2}E, \tag{B.4a}$$

$$N = Ke^{ik_\mathrm{p}L_\mathrm{n}}, \tag{B.4b}$$

$$M = iA_\mathrm{n}R - R_\mathrm{n}N, \tag{B.4c}$$

$$L = Me^{ik_\mathrm{p}L_\mathrm{n}}. \tag{B.4d}$$

b. First approximation:

$$\hat{\mathrm{k}}(t) = i\frac{\sqrt{2}}{2}\hat{\mathrm{h}}(t) - \frac{\sqrt{2}}{2}\hat{\mathrm{e}}(t), \tag{B.5a}$$

$$\hat{\mathrm{n}}(t) = \hat{\mathrm{k}}(t - L_\mathrm{n}/c)e^{ik_\mathrm{p}L_\mathrm{n}}, \tag{B.5b}$$

$$\hat{\mathrm{m}}(t) = iA_\mathrm{n}\mathrm{r}(t) - R_\mathrm{n}\hat{\mathrm{n}}(t) - 2iR_\mathrm{n}k_\mathrm{p}x_\mathrm{n}(t)N, \tag{B.5c}$$

$$\hat{\mathrm{l}}(t) = \hat{\mathrm{m}}(t - L_\mathrm{n}/c)e^{ik_\mathrm{p}L_\mathrm{n}}. \tag{B.5d}$$

3. East arm (between the beamsplitter and the PRM).
a. Zeroth approximation:

$$J = i\frac{\sqrt{2}}{2}E - \frac{\sqrt{2}}{2}H, \tag{B.6a}$$

$$S = Je^{ik_\mathrm{p}L_\mathrm{e}}, \tag{B.6b}$$

$$T = iA_\mathrm{e}U - R_\mathrm{e}S, \tag{B.6c}$$

$$I = Te^{ik_\mathrm{p}L_\mathrm{e}}. \tag{B.6d}$$

b. First approximation:

$$\hat{j}(t) = i\frac{\sqrt{2}}{2}\hat{e}(t) - \frac{\sqrt{2}}{2}\hat{h}(t), \tag{B.7a}$$

$$\hat{s}(t) = \hat{j}(t - L_e/c)e^{ik_pL_e}, \tag{B.7b}$$

$$\hat{t}(t) = iA_e\hat{r}(t) - R_e\hat{s}(t) - 2iR_ek_px_e(t)S, \tag{B.7c}$$

$$\hat{i}(t) = \hat{t}(t - L_e/c)e^{ik_pL_e}. \tag{B.7d}$$

4. Signal recycling arm (between the beamsplitter and the SRM).
a. Zeroth approximation:

$$G = i\frac{\sqrt{2}}{2}L - \frac{\sqrt{2}}{2}I, \tag{B.8a}$$

$$W = Ge^{ik_pL_s}, \tag{B.8b}$$

$$O = -R_sW, \tag{B.8c}$$

$$H = Oe^{ik_pL_s}, \tag{B.8d}$$

$$Y = iT_sW. \tag{B.8e}$$

b. First approximation:

$$\hat{g}(t) = i\frac{\sqrt{2}}{2}\hat{l}(t) - \frac{\sqrt{2}}{2}\hat{i}(t), \tag{B.9a}$$

$$\hat{w}(t) = \hat{g}(t - L_s/c)e^{ik_pL_s(t)}, \tag{B.9b}$$

$$\hat{o}(t) = iT_s\hat{z}(t) - R_s\hat{w}(t) + 2iR_sk_pX_O(\Omega)W, \tag{B.9c}$$

$$\hat{h}(t) = \hat{o}(t - L_s/c)e^{ik_pL_s(t)}, \tag{B.9d}$$

$$\hat{y}(t) = iT_s\hat{w}(t) - R_s\hat{z}(t). \tag{B.9e}$$

The notations of transmission and reflectivity coefficients used in these relations are denoted in figure 2.1. There are no sources of electromagnetic waves of zeroth order from the SRM and the end-mirrors. The quantities L_n, L_e, L_p and L_s are correspondingly the lengths of north, east arms and the distances from the beamsplitter to the PRM and the SRM.

Because of the dark-port condition of GEO 600 on the beamsplitter, the fields inside the detector are divided in two modes: the power recycling, formed by the PRM and the end-mirrors, and the signal recycling, formed by the SRM and the end-mirrors. So the fields inside the detector maybe separately considered in these modes and in two different approximations.

B.2. Zeroth approximation in the power recycling mode. Dark-fringe port and dark-fringe offset

As it was mentioned, the light of zeroth mode in detector is constant. Any field inside the power recycling mode, e.g. E, is a superposition of three parts: of the field come

from the laser E_A, of the field, originated from the same field E, propagated through the north E_{n} and the east E_{e} arms, and reflected from the PRM:

$$E = E_A + E_{\mathrm{n}} + E_{\mathrm{e}}. \tag{B.10}$$

The field E_A, coming from laser, is transmitted through the input mirror iT_{p} and propagates from the PRM to the beamsplitter $e^{ik_{\mathrm{p}}L_{\mathrm{i}}}$:

$$E_A = AiT_{\mathrm{p}}e^{ik_{\mathrm{p}}L_{\mathrm{i}}}. \tag{B.11}$$

The field, propagating through the north arm, is the field E, reflected from beam-splitter $-\frac{\sqrt{2}}{2}$, propagated through the north arm $e^{ik_{\mathrm{p}}L_{\mathrm{n}}}$, reflected from the north end mirror $-R_{\mathrm{n}}$, passed back through the north arm $e^{ik_{\mathrm{p}}L_{\mathrm{n}}}$, reflected again from the beamsplitter $-\frac{\sqrt{2}}{2}$, and finally traveled twice through from the beamsplitter to the PRM $e^{2ik_{\mathrm{p}}L_{\mathrm{i}}}$, reflected in between from it $-R_{\mathrm{p}}$:

$$E_{\mathrm{n}} = \frac{1}{2}R_{\mathrm{n}}R_{\mathrm{p}}e^{2ik_{\mathrm{p}}(L_{\mathrm{n}}+L_{\mathrm{i}})}E. \tag{B.12}$$

In the similar way, the field coming through the east arm is twice propagated through the east arm and from the beamsplitter to the PRM $e^{2ik_{\mathrm{p}}(L_{\mathrm{i}}+L_{\mathrm{e}})}$, twice transmitted through the beamsplitter $\left(i\frac{\sqrt{2}}{2}\right)^2$, and once reflected from the PRM and the east mirror $(-R_{\mathrm{e}})(-R_{\mathrm{p}})$:

$$E_{\mathrm{e}} = -\frac{1}{2}R_{\mathrm{e}}R_{\mathrm{p}}e^{2ik_{\mathrm{p}}(L_{\mathrm{i}}+L_{\mathrm{e}})}E. \tag{B.13}$$

The substitution of these fields into (B.10) gives the explicit equation for the field on the beamsplitter:

$$E = iT_{\mathrm{p}}e^{ik_{\mathrm{p}}L_{\mathrm{i}}}A + \frac{1}{2}R_{\mathrm{p}}e^{2ik_{\mathrm{p}}L_{\mathrm{i}}}E\left(e^{2ik_{\mathrm{p}}L_{\mathrm{n}}}R_{\mathrm{n}} - e^{2ik_{\mathrm{p}}L_{\mathrm{e}}}R_{\mathrm{e}}\right) \tag{B.14}$$

The interference on the beamsplitter of two fields, reflected from the end mirrors, is described by the sum in the brackets. The superposition of the fields can be adjusted by tuning of the end-mirrors positions and therefore of the lengths of arms L_{e} and L_{e}.

The dark-fringe port is the operation regime of GEO 600, when the fields reflected from the end mirror interfere destructively towards the dark port, and constructively towards the laser port. The dark-port condition is therefore:

$$2ik_{\mathrm{p}}L_{\mathrm{n}} = 2ik_{\mathrm{p}}L_{\mathrm{e}} + i\pi + 2i\pi n, n \in N. \tag{B.15}$$

With the condition of dark-port, the field on the beamsplitter (B.14) becomes:

$$E = iT_{\mathrm{p}}e^{i\omega_{\mathrm{p}}\frac{L_{\mathrm{i}}}{c}}A - \frac{1}{2}R_{\mathrm{p}}e^{2ik_{\mathrm{p}}L_{\mathrm{i}}}Ee^{2ik_{\mathrm{p}}L_{\mathrm{e}}}(R_{\mathrm{e}} + R_{\mathrm{n}}). \tag{B.16}$$

This equation is equivalent to the equation for the field inside the Fabry-Perot cavity with formed by the mirrors with reflectivities R_p and

$$R_f = \frac{R_e + R_n}{2} \tag{B.17}$$

and separated by the distance $L_i + L_e$ (compare with (1.15)). We call this an equivalent power recycling cavity (PRC). The field E in this cavity is considered on the distance L_i from the first mirror. Therefore the solution for the field in the PRC is an Airy function again:

$$E = \frac{iT_p e^{ik_p L_i} A}{1 + R_p R_f e^{2ik_p(L_i + L_e)}}. \tag{B.18}$$

We are interested in the strongest amplitude of laser field on the end-mirrors, therefore we want the power recycling cavity to be in resonance. The resonance condition, as it follows from (B.18), is:

$$e^{ik_p(L_i + L_e)} = i. \tag{B.19}$$

The field in resonantly enhanced PRC is therefore:

$$E_{res} = \frac{iT_p e^{ik_p L_i} A}{1 - R_p R_f}. \tag{B.20}$$

The field can be represented in terms of half-bandwidths:

$$1 - R_p R_f \approx (\gamma_p + \gamma_f) 2\tau, \tag{B.21}$$

where

$$\gamma_p = \frac{T_p^2 c}{4L}, \tag{B.22a}$$

$$\gamma_f = \frac{\gamma_n + \gamma_e}{2} = \frac{(T_e^2 + T_n^2)c}{8L} \tag{B.22b}$$

are the bandwidth, corresponding to each mirror separately (compare to (1.19)).

In the real interferometer the signal, coming from the dark port, requires a reference field, a local oscillator, as it was mentioned in section 1.5. It is technically inconvenient to use a local oscillator, sourced from the detector laser, in the large-scale interferometer. To have a referent beam in these circumstances the interference on the beamsplitter is set to a slight offset from the dark-fringe, causing a small constant field to dark port. Then the dark-port condition (B.15) turns to:

$$2ik_p L_n = 2ik_p L_e + \delta\phi_F + i\pi + 2i\pi n, n \in N. \tag{B.23}$$

The field inside the power-recycling cavity for the dark-port for this offset is

$$E = \frac{iT_p A e^{ik_p L_i}}{1 - \frac{1}{2} R_p e^{2ik_p(L_i + L_e)} (e^{i\delta\phi_F} R_n + R_e)}. \tag{B.24}$$

In the approximation of small dark-fringe offset and high reflectivities:

$$R_\mathrm{p} \approx R_\mathrm{n} \approx R_\mathrm{e} \approx 1, \tag{B.25a}$$

$$\delta\phi_F \ll 1, \tag{B.25b}$$

the resonant condition for the power recycling mode is:

$$2k_\mathrm{p}\left(L_\mathrm{i} + L_\mathrm{e}\right) = -\frac{\delta\phi_F}{2}. \tag{B.26}$$

Then the resonant field on the beamsplitter of the GEO 600 with dark-fringe offset is:

$$E_\mathrm{res} \approx \frac{iT_\mathrm{p}Ae^{ik_\mathrm{p}L_\mathrm{i}}}{1 - \frac{1}{2}R_\mathrm{p}(e^{i\delta\phi_F/2}R_\mathrm{n} + e^{-i\delta\phi_F/2}R_\mathrm{e})} \approx \frac{iT_\mathrm{p}Ae^{ik_\mathrm{p}L_\mathrm{i}}}{2\tau(\gamma_\mathrm{p} + \gamma_\mathrm{f})}. \tag{B.27}$$

Therefore, in the linear approximation, which is very good for 40 pm dark-fringe offset, the power on the beamsplitter is independent from the offset.

B.3. Zeroth approximation in the signal recycling mode

The zeroth approximation of field inside a signal recycling cavity, as everywhere else is a constant. The field inside the signal recycling mode, e.g H on Fig.2.1, is a superposition of two parts: of the field come from the field E of power recycling mode, and of the field come from the field H of the signal recycling mode: both after one round-trip through the north and east arms.

1. The path of field E:

a. through the north arm: it is once reflected from and once transmitted through the beamsplitter, has twice propagated both through the north arm and between the beamsplitter and the SRM, and is once reflected from the north mirror and the SRM each: $-\frac{\sqrt{2}}{2} \times i\frac{\sqrt{2}}{2} \times e^{2i\omega_\mathrm{p}\frac{L_\mathrm{n}+L_\mathrm{s}}{c}} \times (-R_\mathrm{s}) \times (-R_\mathrm{n})$.

b. through the east arm: it is once transmitted through and once reflected from the beamsplitter, has twice propagated both through the east arm and between the beamsplitter and the SRM, and is once reflected from the east mirror and the SRM each: $i\frac{\sqrt{2}}{2} \times \left(-\frac{\sqrt{2}}{2}\right) \times e^{2i\omega_\mathrm{p}\frac{L_\mathrm{e}+L_\mathrm{s}}{c}} \times (-R_\mathrm{s}) \times (-R_\mathrm{e})$.

2. The path of field H:

a. through the north arm: it is twice transmitted through the beamsplitter, has twice propagated through both the north arm and between the beamsplitter and the SRM, and is once reflected by the north mirror and the SRM each: $\left(i\frac{\sqrt{2}}{2}\right)^2 \times e^{2i\omega_\mathrm{p}\frac{L_\mathrm{n}+L_\mathrm{s}}{c}} \times (-R_\mathrm{s}) \times (-R_\mathrm{n})$.

b. through the east arm: it is twice reflected by the beamsplitter, has twice propagated through the east arm and between the beamsplitter and the SRM, and once reflected by the east mirror and the SRM each: $\left(-\frac{\sqrt{2}}{2}\right)^2 \times e^{2i\omega_\mathrm{p}\frac{L_\mathrm{e}+L_\mathrm{s}}{c}} \times (-R_\mathrm{s}) \times (-R_\mathrm{e})$.

The equation for the field H may be easily derived from these considerations:

$$H = E \left(-\frac{1}{2} i R_{\mathrm{s}} e^{2ik_{\mathrm{p}}L_{\mathrm{s}}} (R_{\mathrm{n}} e^{i2k_{\mathrm{p}}L_{\mathrm{n}}} + R_{\mathrm{e}} e^{i2k_{\mathrm{p}}L_{\mathrm{e}}}) \right) +$$
$$+ H \left(\frac{1}{2} R_{\mathrm{s}} e^{2ik_{\mathrm{p}}L_{\mathrm{s}}} (R_{\mathrm{e}} e^{i2k_{\mathrm{p}}L_{\mathrm{e}}} - R_{\mathrm{n}} e^{i2k_{\mathrm{p}}L_{\mathrm{n}}}) \right). \quad \text{(B.28)}$$

The terms in the brackets are dependent on the arms length difference. Under the dark port condition (B.23) the field inside the signal recycling mode, keeping the terms of the first order of smallness, reads:

$$H = -\frac{E\frac{1}{2} i R_{\mathrm{s}} e^{i\delta_\phi} (-R_{\mathrm{n}} e^{i\delta\phi_{\mathrm{f}}/2} + R_{\mathrm{e}} e^{-i\delta\phi_{\mathrm{f}}/2})}{1 - R_{\mathrm{s}} R_{\mathrm{f}} e^{i\delta_\phi}}, \quad \text{(B.29)}$$

where:

$$L = \frac{L_{\mathrm{e}} + L_{\mathrm{n}}}{2}, \quad \text{(B.30a)}$$
$$\delta_\phi = 2k_{\mathrm{p}} (L + L_{\mathrm{s}}). \quad \text{(B.30b)}$$

The additional factors of $e^{i\delta\phi_{\mathrm{f}}/2}$ and $e^{-i\delta\phi_{\mathrm{f}}/2}$, multiplied by R_{n} and R_{e} in the denominator of (B.29) are canceled in the first-order approximation. The whole expression is similar to the expression for the Fabry-Perot cavity (see (1.15)), but with some equivalent input laser power, therefore the signal recycling mode is conventionally described as an equivalent signal recycling cavity (SRC), formed by the mirrors with reflectivities R_{s} and R_{f}, and detuned from the laser frequency by the angle δ_ϕ. The power of the light inside the SRC is dependent from the constant differential displacement of the mirrors. However, if the lengths of the arms would precisely obey the dark-port condition, the zeroth order field will turn to zero.

The field H, transformed to the frequency language reads:

$$H \approx -\frac{1}{2} E e^{i\delta_\phi} \frac{i(\gamma_{\mathrm{n}} - \gamma_{\mathrm{e}} - i\delta\omega_{\mathrm{df}})}{\gamma_{\mathrm{s}} + \gamma_{\mathrm{f}} - i\delta}, \quad \text{(B.31)}$$

where

$$\gamma_{\mathrm{s}} = \frac{T_{\mathrm{s}}^2 c}{4L}, \quad \text{(B.32a)}$$
$$\delta = \frac{\delta_\phi}{2\tau}, \quad \text{(B.32b)}$$
$$\delta\omega_{\mathrm{df}} = \delta\phi_{\mathrm{f}}/2\tau. \quad \text{(B.32c)}$$

The quantity $\delta\omega_{\mathrm{df}} = \delta\phi_{\mathrm{f}}/2\tau$ is length difference between north and east arms, derived in frequency. The half band-width, corresponding to the losses in the arms γ_{f} is defined in (B.22). The single phase shifts are supposed to be very small and neglected.

The dependence of the power of the light inside the SRC is shown in figure B.1.
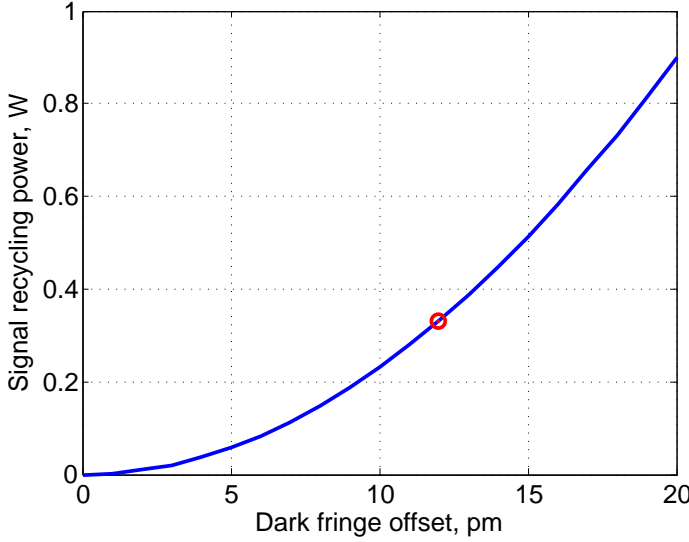
Figure B.1.: Power of laser field inside the signal recycling mode. Differential losses. Dependence on the dark-fringe port.

B.4. DC-readout

The laser field in the dark port outside the detector is determined by the field inside the SRC (B.31). The expression for the amplitude of light on the photodetector reads, derived using (B.8), reads:

$$Y \approx -\frac{1}{2}Ee^{-ik_{\mathrm{p}}L_{\mathrm{s}}}\frac{T_{\mathrm{s}}(\gamma_{\mathrm{N}} - \gamma_{\mathrm{e}} - i\delta\omega_{\mathrm{df}})}{\gamma_{\mathrm{s}} + \gamma_{\mathrm{f}} - i\delta} = Y_0 e^{i\phi_Y}, \qquad (B.33)$$

where

$$Y_0 = -\frac{1}{2}E\frac{T_{\mathrm{s}}\sqrt{(\gamma_{\mathrm{N}} - \gamma_{\mathrm{e}})^2 + \delta\omega_{\mathrm{df}}^2}}{\sqrt{(\gamma_{\mathrm{s}} + \gamma_{\mathrm{f}})^2 + \delta^2}}, \qquad (B.34a)$$

$$\phi_Y = \phi_E - k_{\mathrm{p}}L_{\mathrm{s}} + \arctan\frac{\delta\omega_{\mathrm{df}}}{\gamma_{\mathrm{N}} - \gamma_{\mathrm{e}}} - \arctan\frac{\delta}{\gamma_{\mathrm{s}} + \gamma_{\mathrm{e}}}. \qquad (B.34b)$$

The quantity ϕ_E is a phase of the light amplitude E.

This small output piece of light, referred to as a DC component, is usually used as a local oscillator for the homodyne detection. Easy to see, that the phase of the DC component may be changed by varying the dark-fringe offset. Its dependence is shown in Fig.B.2.
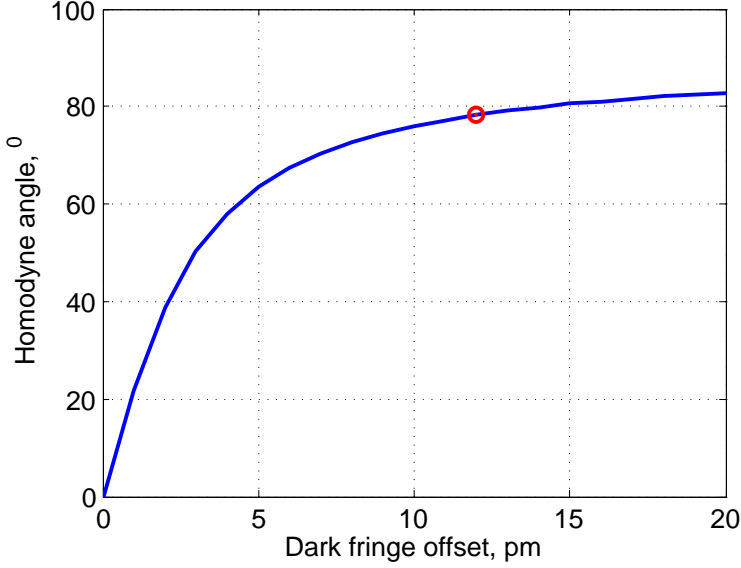
Figure B.2.: Homodyne angle of the local oscillator.

B.5. First approximation in the power recycling mode

The first approximation carries all the noises and perturbations. The field inside the power recycling mode, e.g. $\hat{e}(\omega)$, is formed, unlike the fields in zeroth approximation, by a bigger number of sources. The behavior of light inside the detector is described by the input-output relations (B.3), (B.5), (B.7) and (B.9) and depicted in FIG2.1. The sources of electromagnetic field inside, described here, may be conveniently ordered as following:

1. The sources at the mirrors are the injections of the ground state, and the leak from the fields of zeroth order, caused by the mirror motion (compare with (1.12a),(1.12b)):

a. The field, sourced at the PRM, $iT_p\hat{a}(\omega) + 2iR_p k_p X_i(\Omega)C$ propagates the distance between the PRM and the beamsplitter: e^{ikL_i}.

b. The field, sourced at the north mirror, $iA_n\hat{r}(\omega) - 2iR_n k_p X_n(\Omega)N$ propagates once through the north arm, is reflected once from from both the beamsplitter and the PRM and propagates twice between the beamsplitter and the PRM: $e^{ikL_n + 2L_i} \times \left(-\frac{\sqrt{2}}{2}\right) \times (-R_p)$.

c. The fields, sourced at the east mirror, $iA_e\hat{u}(\omega) - 2iR_e k_p X_e(\Omega)S$ propagates once through the east arm, is transmitted once through the beamsplitter, is reflected once from the input mirror and propagates twice between the beamsplitter and the PRM $e^{ikL_e + 2L_i} \times \left(i\frac{\sqrt{2}}{2}\right) \times (-R_p)$.

151

2. The fields of the first order of smallness, leaking from the signal recycling mode $\hat{\mathrm{h}}(\omega)$ (see section B.6).

a. The part of this field come through the north arm is once transmitted through and once reflected from the beamsplitter, is once reflected from each of the north and the input mirrors, and propagates twice through each of the north and the input arms: $\left(i\frac{\sqrt{2}}{2}\right) \times \left(-\frac{\sqrt{2}}{2}\right) \times (-R_\mathrm{n}) \times (-R_\mathrm{p}) \times e^{2ik(L_\mathrm{i}+L_\mathrm{n})}$.

b. The part of the field come through the east arm is once reflected by and once transmitted through the beamsplitter, is once reflected from each of the east and the input mirrors and propagates twice through each of east and input arms: $\left(-\frac{\sqrt{2}}{2}\right) \times \left(i\frac{\sqrt{2}}{2}\right) \times (-R_\mathrm{e}) \times (-R_\mathrm{p}) \times e^{2ikL_\mathrm{i}+L_\mathrm{e}}$.

3. The fields of the first order of smallness originated from the considered field $\hat{\mathrm{e}}(\omega)$, made one round-trip through the PRC.

a. The part of this field come through the north arm is twice reflected from the beamsplitter, is once reflected from each of the north and the input mirrors, and propagates twice through each of the north and the input arms: $\left(-\frac{\sqrt{2}}{2}\right) \times \left(-\frac{\sqrt{2}}{2}\right) \times (-R_\mathrm{n}) \times (-R_\mathrm{p}) \times e^{2ik(L_\mathrm{i}+L_\mathrm{n})}$.

b. The part of this field come through the east arm is twice transmitted through the beamsplitter, once reflected from each of the east and the input mirrors, and is twice passed through each of the east and the input arms: $\left(i\frac{\sqrt{2}}{2}\right) \times \left(i\frac{\sqrt{2}}{2}\right) \times (-R_\mathrm{e}) \times (-R_\mathrm{p}) \times e^{2ik(L_\mathrm{i}+L_\mathrm{e})}$.

Note that $C \approx -Ee^{-ik_\mathrm{p}L_\mathrm{i}}$, $S = i\frac{\sqrt{2}}{2}Ee^{ik_\mathrm{p}L_\mathrm{e}}$ and $N = -i\frac{\sqrt{2}}{2}Ee^{ik_\mathrm{p}L_\mathrm{n}}$. The equation for the field inside the cavity is:

$$\hat{\mathrm{e}}(\omega) = iT_\mathrm{p}\hat{a}(\omega)e^{ikL_\mathrm{i}} - 2ik_\mathrm{p}R_\mathrm{p}X_\mathrm{i}Ee^{ikL_\mathrm{i}}e^{-ik_\mathrm{p}L_\mathrm{i}} -$$

$$-\frac{\sqrt{2}}{2}iR_\mathrm{p}e^{ik2L_\mathrm{i}}\left(iA_\mathrm{e}\hat{u}(\omega)e^{ikL_\mathrm{e}} - A_\mathrm{n}\hat{r}(\omega)e^{ikL_\mathrm{n}}\right) -$$

$$- iR_\mathrm{p}k_\mathrm{p}Ee^{2ikL_\mathrm{i}}e^{ik_\mathrm{p}L_\mathrm{e}}\left(R_\mathrm{e}X_\mathrm{e}(\Omega)e^{ikL_\mathrm{e}} + R_\mathrm{n}X_\mathrm{n}(\Omega)e^{ikL_\mathrm{n}}\right) -$$

$$-i\frac{1}{2}R_\mathrm{p}e^{2ikL_\mathrm{i}}\left(R_\mathrm{n}e^{2ikL_\mathrm{n}} + R_\mathrm{e}e^{2ikL_\mathrm{e}}\right)\hat{h}(\omega) - \frac{1}{2}R_\mathrm{p}e^{2ik_\mathrm{p}L_\mathrm{i}}\left(R_\mathrm{e}e^{2ikL_\mathrm{e}} - R_\mathrm{n}e^{2ikL_\mathrm{n}}\right)\hat{\mathrm{e}}(\omega).$$

$$(\mathrm{B.35})$$

This expression may be simplified under the usual assumptions of the dark-port conditions (B.23), highly reflective mirrors(B.25), cavity resonant conditions, and smallness of dark-fringe offset (B.26) we used for the zeroth order terms with an additional assumption of the small frequencies of signal spectrum:

$$\Omega \ll \omega_\mathrm{p}, \tag{B.36}$$

The first term is already simple enough.

In *the second term* the phase shift $2\dfrac{\Omega L_\mathrm{i}}{c}$ is negligible because of the low values of signal frequency and of the short distance between the PRM and the beamsplitter.

$$\hat{e}_2(\omega) = 2ik_{\mathrm{p}}R_{\mathrm{p}}X_{\mathrm{i}}E. \tag{B.37}$$

The third term in the expression, with the injected fields of ground state oscillations from the end-mirrors, can be represented as an equivalent ground state insertion from the equivalent mirror:

$$\hat{e}_3(\omega) = iA_{\mathrm{f}}\hat{q}_1(\omega)e^{ikL_{\mathrm{i}}}, \tag{B.38}$$

where

$$A_{\mathrm{f}} = \sqrt{\frac{A_{\mathrm{e}}^2 + A_{\mathrm{n}}^2}{2}}, \tag{B.39a}$$

$$\hat{q}_1(\omega) \approx \frac{A_{\mathrm{e}}}{\sqrt{A_{\mathrm{e}}^2 + A_{\mathrm{n}}^2}}\hat{u}(\omega) - \frac{A_{\mathrm{n}}}{\sqrt{A_{\mathrm{e}}^2 + A_{\mathrm{n}}^2}}\hat{r}(\omega) \tag{B.39b}$$

are the equivalent losses of the mirror and the annihilation operator of the equivalent ground state oscillations. The creation and annihilation operator chosen in this way remarkably fits the necessary commutation relation:

$$\left[\hat{q}_1(\omega)\hat{q}_1^\dagger(\omega')\right] = 2\pi\delta(\omega - \omega'). \tag{B.40}$$

The fourth term, carrying the information about motion of the end-mirrors may be simplified as following:

$$\hat{e}_4(\omega) \approx i2Ek_{\mathrm{p}}X_+(\Omega). \tag{B.41}$$

This term is equivalent to the response of the field with zeroth term E inside a cavity on the equivalent mirror with motion of the end mirrors common displacement:

$$X_+(\Omega) = \frac{X_{\mathrm{e}}(\Omega) + X_{\mathrm{n}}(\Omega)}{2}. \tag{B.42}$$

The fifth term in (B.35), describing the contribution from the signal recycling mode, is simplified, using also the half bandwidths (B.22), giving:

$$\hat{e}_5(\omega) \approx \frac{1}{2}i\left(\frac{A_{\mathrm{e}}^2}{2} - \frac{A_{\mathrm{n}}^2}{2} + i\delta\phi_{\mathrm{f}}\right)\hat{h}(\omega) \approx i\tau(\gamma_{\mathrm{e}} - \gamma_{\mathrm{n}} - i\delta\omega_{df})\hat{h}(\omega), \tag{B.43}$$

where ω_{df} is an equivalent frequency version of dark-fringe offset:

$$\omega_{\mathrm{df}} = \frac{\phi_{\mathrm{f}}}{2\tau}. \tag{B.44}$$

This contribution is the same, as the contribution from the power recycling mode into signal recycling mode for the terms of zeroth order (compare with section (B.3)). The ratio of this contribution with respect to contribution to the shot noise, injected from the laser port is of the order:

$$\frac{\frac{1}{2}R_{\mathrm{p}}\left|\frac{A_{\mathrm{e}}^2}{2} - \frac{A_{\mathrm{n}}^2}{2} + i\delta\phi_{\mathrm{f}}\right|}{T_{\mathrm{p}}} \sim 2 \times 10^{-3} \tag{B.45}$$

The sixth part in (B.35), consisting of terms with $\hat{e}(\omega)$ put together, and considered with the transformations during one round-trip inside the power recycling mode, is required tj find the field explicitly:

$$
\hat{e}_6(\omega) \approx \left[1 - \frac{1}{2} R_\text{p} e^{2i\Omega\tau} \left(R_\text{e} + R_\text{n} \right) \right] \hat{e}(\omega) \approx
$$

$$
\approx 2\tau \left(\gamma_\text{p} + \gamma_\text{f} - i \left(\Omega + \frac{\delta\omega_{df}}{2} \right) \right) \hat{e}(\omega). \quad \text{(B.46)}
$$

The transformation of the field during one round-trip inside the power recycling mode is equivalent to the one of a Fabry-Perot cavity (compare with transformations described in (1.24d) and (1.25b)).

The simplified solution of (B.35), constructed from the simplified terms above, then reads

$$
\hat{e}(\omega) = \frac{iT_\text{p}\hat{a}(\omega)e^{ikL_\text{i}} + iA_\text{f}\hat{q}_1(\omega)e^{ikL_\text{i}} + i2Ek_\text{p}\left(X_+(\Omega) - X_\text{i}(\Omega) \right)}{1 - \frac{1}{2}R_\text{p}e^{2i\Omega\tau}\left(R_\text{e} + R_\text{n} \right)} +
$$

$$
+ \frac{1}{2} \frac{i\left(\frac{A_\text{e}^2}{2} - \frac{A_\text{n}^2}{2} + i\delta\phi_\text{f} \right)\hat{h}(\omega)}{1 - \frac{1}{2}R_\text{p}e^{2i\Omega\tau}\left(R_\text{e} + R_\text{n} \right)} \approx
$$

$$
\approx \frac{i\sqrt{\frac{\gamma_\text{p}}{\tau}}\hat{a}(\omega)e^{ikL_\text{i}} + i\frac{k_\text{p}}{\tau}X_\text{src}(\Omega)E + i\sqrt{\frac{\gamma_\text{f}}{\tau}}\hat{q}_1(\omega)}{\gamma_\text{p} + \gamma_\text{f} - i\Omega} -
$$

$$
- \frac{\frac{1}{2}\left(\gamma_\text{e} - \gamma_\text{n} + i\delta\omega_{df} \right)\hat{h}(\omega)}{\gamma_\text{p} + \gamma_\text{f} - i\Omega}, \quad \text{(B.47)}
$$

where

$$
X_\text{src}(\Omega) = X_+(\Omega) - X_\text{i}(\Omega) \quad \text{(B.48)}
$$

is an equivalent single mirror motion, introducing the same signal into first order terms of fields in the power recycling mode of GEO 600, as the joint motion of the PRM and the end-mirrors in the SRC.

The equation (2.1) is equivalent to the expression of the fields inside a Fabry-Perot cavity (compare with (1.24b) and (1.25b)). The field carries the information about the common end-mirror motion (B.42) and the differential mode of ground-state field injections (B.39b). The field from the orthogonal mode is injected only with the leaking from signal recycling mode due to dark-fringe offset and the differential end-mirror losses.

B.6. First approximation in the signal recycling mode.

The perturbations and noise inside GEO 600 affect the first approximation field in the signal recycling mode as well. We consider the behavior and sources for the first order terms of field, using equations (B.3), (B.5), (B.7) and (B.9), and looking in FIG.2.1. The sources of the first order electromagnetic fields, e.g. $\hat{\mathrm{h}}(\omega)$, inside the signal recycling mode may be ordered, similarly to previous section, as following:

1. The sources at the mirrors are the injections of the ground state, and the leak from the zeroth order fields due to the mirror motion (see (1.12a),(1.12b)):

a. The field, sourced at the SRM, $iT_s\hat{z}(\omega)$ (the leaks from the zeroth order fields due to the SRM motion are negligible here) propagates between the SRM and the beamsplitter: e^{ikL_s}.

b. The field, sourced at the north mirror, $iA_n\hat{r}(\omega) - 2iR_n k_p X_n(\Omega)N$ propagate once through the north arm, is transmitted once through the beamsplitter, is reflected once from the SRM, and propagates twice between the SRM and the beamsplitter: $e^{ik(L_n+2L_s)} \times \left(i\frac{\sqrt{2}}{2}\right) \times (-R_s)$.

c. The field, sourced at the east mirror, $iA_e\hat{u}(\omega) - 2iR_e k_p X_e(\Omega)S$ propagates once through the east arm, is reflected once from the beamsplitter, is reflected from the output mirror, and propagates twice between the SRM and the beamsplitter: $e^{ik(L_e+2L_s)} \times \left(-\frac{\sqrt{2}}{2}\right) \times (-R_s)$.

2. The field of the first order of smallness, leaking from the power recycling mode $\hat{\mathrm{e}}(\omega)$ (see section B.5).

a. The part of this field come through the north arm is once reflected from and once transmitted through the beamsplitter, is once reflected from each of the north mirror and the SRM, and propagates twice through the north mirror and between the SRM: $\left(-\frac{\sqrt{2}}{2}\right) \times \left(i\frac{\sqrt{2}}{2}\right) \times (-R_n) \times (-R_s) \times e^{2ik(L_s+L_n)}$.

b. The part of the field come through the east arm is once transmitted through and once reflected from the beamsplitter, is once reflected from each of the east mirror and the SRM, and propagates twice through the east arm and between the SRM and the beamsplitter: $\left(i\frac{\sqrt{2}}{2}\right) \times \left(-\frac{\sqrt{2}}{2}\right) \times (-R_e) \times (-R_s) \times e^{2ik(L_I+L_s)}$.

3. The field of the first order of smallness originated from the considered field $\hat{\mathrm{h}}(\omega)$, made one trip-through the SRC.

a. The part of this field come through the north arm is twice transmitted through the beamsplitter, is once reflected from each of the north mirror and of the SRM, and propagates twice through the north arm and between the SRM and the beamsplitter: $\left(i\frac{\sqrt{2}}{2}\right) \times \left(i\frac{\sqrt{2}}{2}\right) \times (-R_n) \times (-R_s) \times e^{2ik(L_I+L_s)}$.

b. The part of the field come through the east arm is twice reflected from the beamsplitter, is once reflected from each of the east mirror and the SRM, and propagates twice through the east arm and between the SRM and the beamsplitter: $\left(-\frac{\sqrt{2}}{2}\right) \times \left(-\frac{\sqrt{2}}{2}\right) \times (-R_e) \times (-R_s) \times e^{2ik(L_s+L_e)}$.

Noting that $S = i\frac{\sqrt{2}}{2}Ee^{ik_{\mathrm{p}}L_{\mathrm{e}}}$ and $N = -\frac{\sqrt{2}}{2}Ee^{ik_{\mathrm{p}}L_{\mathrm{n}}}$, we get the following equation for the field:

$$
\begin{aligned}
\hat{\mathrm{h}}(\omega) = {} & iT_{\mathrm{s}}\hat{z}(\omega)e^{ikL_{\mathrm{s}}} + \frac{\sqrt{2}}{2}e^{ik2L_{\mathrm{s}}}R_{\mathrm{s}}\left(iA_{\mathrm{e}}\hat{u}(\omega)e^{ikL_{\mathrm{e}}} + A_{\mathrm{n}}\hat{r}(\omega)e^{ikL_{\mathrm{n}}}\right) + \\
& + R_{\mathrm{s}}k_{\mathrm{p}}e^{2ikL_{\mathrm{s}}}E\left(R_{\mathrm{e}}X_{\mathrm{e}}(\Omega)e^{ik_{\mathrm{p}}L_{\mathrm{e}}}e^{ikL_{\mathrm{e}}} + R_{\mathrm{n}}X_{\mathrm{n}}(\Omega)e^{ik_{\mathrm{p}}L_{\mathrm{n}}}e^{ikL_{\mathrm{n}}}\right) - \\
& -i\frac{1}{2}R_{\mathrm{s}}e^{2ikL_{\mathrm{s}}}\left(R_{\mathrm{n}}e^{2ikL_{\mathrm{n}}} + R_{\mathrm{e}}e^{2ikL_{\mathrm{e}}}\right)\hat{\mathrm{e}}(\omega) + \frac{1}{2}R_{\mathrm{s}}e^{2ik_{\mathrm{p}}L_{\mathrm{s}}}\left(R_{\mathrm{e}}e^{2ikL_{\mathrm{e}}} - R_{\mathrm{n}}e^{2ikL_{\mathrm{n}}}\right)\hat{\mathrm{h}}(\omega).
\end{aligned}
\tag{B.49}
$$

Similar to the previous section, this equation for the field may be simplified. The assumptions for the simplification are: the dark-port condition (B.23), high reflectivity of the mirrors (B.25), the SRC detuning condition (B.30b), the smallness of dark-fringe offset (B.26), and the smallness of signal frequencies (B.36).

The first term of (B.49) requires no further simplification.

The second term, describing the injected through the end-mirrors ground state oscillations, can be represented as an equivalent ground state insertion from the equivalent mirror:

$$
\hat{\mathrm{h}}_2(\omega) \approx iA_{\mathrm{f}}\hat{q}_2(\omega)e^{ikL_{\mathrm{s}}},
\tag{B.50}
$$

Where

$$
\hat{q}_2(\omega) \approx \frac{A_{\mathrm{e}}}{\sqrt{A_{\mathrm{e}}^2 + A_{\mathrm{n}}^2}}\hat{u}(\omega) + \frac{A_{\mathrm{n}}e^{i\delta\phi_F}}{\sqrt{A_{\mathrm{e}}^2 + A_{\mathrm{n}}^2}}\hat{r}(\omega)
\tag{B.51}
$$

is an equivalent annihilation operator of a mode of ground state oscillations. The annihilation and the corresponding creation operator appear to be the normalized quantum annihilation and creation operators:

$$
\left[\hat{q}_2(\omega)\hat{q}_2^{\dagger}(\omega')\right] = 2\pi\delta(\omega - \omega').
\tag{B.52}
$$

The modes of ground state electromagnetic fluctuations, injected into signal recycling and power recycling modes obey the following commutation relation:

$$
\left[\hat{q}_1(\omega)\hat{q}_2^{\dagger}(\omega')\right] = 0,
\tag{B.53}
$$

meaning $\hat{q}_1(\omega)$ and $\hat{q}_2(\omega)$ are orthogonal.

In this simplification we noticed that detunings caused by the difference Ω of the considered and pumping frequencies contribute the negligible value.

The third term, carrying the information about the end-mirrors motion may be simplified in the following way:

$$
\hat{\mathrm{h}}_3(\omega) \approx 2R_{\mathrm{s}}Ek_{\mathrm{p}}X(\Omega)
\tag{B.54}
$$

This term is equivalent to the response that a field would have in a cavity with zeroth term of field E with the equivalent differential motion of the end-mirror:

$$
X(\Omega) = \frac{X_{\mathrm{e}}(\Omega) - X_{\mathrm{n}}(\Omega)}{2}.
\tag{B.55}
$$

The fourth term, describing the contribution from the power recycling mode, is simplified, using (B.22):

$$\hat{h}_4(\omega) \approx -\frac{1}{2}iR_s\left(\frac{A_e^2}{2} - \frac{A_n^2}{2} + i\delta\phi_F\right)\hat{e}(\omega) \approx -i\tau(\gamma_e - \gamma_n + i\delta\omega_{df})\hat{e}(\omega). \qquad (B.56)$$

The fifth part in (B.35), consisting of terms with $\hat{h}(\omega)$ put together includes the description of the transformation of the field during one round-trip inside the signal recycling mode:

$$\hat{h}_5(\omega) \approx \left[1 - R_s R_f e^{i\delta_\phi}\right]\hat{h}(\omega) \approx 2\tau\left(\gamma_s + \gamma_f - i\left(\Omega + \delta\right)\right)\hat{h}(\omega). \qquad (B.57)$$

As well as in the power recycling mode, the transformation of the field during one round-trip inside the signal recycling mode is equivalent to the one of a Fabry-Perot cavity (compare with transformations described in (1.24d) and (1.25b)).

The simplified solution of (B.49), constructed from the simplified terms above, then reads

$$\hat{h}(\omega) \approx \frac{iT_s\hat{z}(\omega)e^{ikL_s} + iA_f\hat{q}_2(\omega)e^{ikL_s} + 2R_sEk_pX(\Omega)}{1 - R_sR_fe^{i\delta_\phi}} -$$

$$- \frac{\frac{1}{2}iR_s\left(\frac{A_e^2}{2} - \frac{A_n^2}{2} + i\delta\phi_F\right)}{1 - R_sR_fe^{i\delta_\phi}}\hat{e}(\omega) \approx$$

$$\approx \frac{i\sqrt{\frac{\gamma_s}{\tau}}\hat{z}(\omega)e^{ikL_s} + i\sqrt{\frac{\gamma_f}{\tau}}\hat{q}_2(\omega)e^{ikL_s} + \frac{R_sk_p}{\tau}X(\Omega)E}{\gamma_s + \gamma_f - i\left(\delta + \Omega\right)} -$$

$$- iR_s\frac{\gamma_e - \gamma_n + i\delta\omega_{df}}{2\left(\gamma_s + \gamma_f - i\left(\delta + \Omega\right)\right)}\hat{e}(\omega). \quad (B.58)$$

As for the power recycling mode, the equation (2.2) is equivalent to the expression for the fields inside a Fabry-Perot cavity (see (1.24b) and (1.25b)) with the pumping field E. The field perturbations carry the information about the differential end-mirror motion (B.55), as if it was caused by the motion of the equivalent mirror, and the common mode of ground-state field injections (B.51). The signal from the common mirror motion and differential mode of ground-state injections are injected with the leaks from the power recycling mode with the term $\hat{e}(\omega)$. This term however also depends on $\hat{h}(\omega)$. The solution for the first order field inside the SRC, got by the substitution of the field $\hat{e}(\omega)$ from the PRC (2.1), gives after linear expansion of the

derived denominator:

$$\hat{h}(\omega) \approx \left[\frac{i\sqrt{\frac{\gamma_s}{\tau}}\hat{z}(\omega)e^{ikL_s} + i\sqrt{\frac{\gamma_f}{\tau}}\hat{q}_2(\omega)e^{ikL_s} + \frac{R_s k_p}{\tau}X(\Omega)E}{\gamma_s + \gamma_f - i(\delta + \Omega)} - \right.$$

$$\left. -iR_s \frac{\gamma_e - \gamma_n + i\delta\omega_{df}}{2(\gamma_s + \gamma_f - i(\delta + \Omega))} \frac{i\sqrt{\frac{\gamma_p}{\tau}}\hat{a}(\omega)e^{ikL_I} + ik_p\frac{X_{src}(\Omega)}{\tau}E + i\sqrt{\frac{\gamma_f}{\tau}}\hat{q}_1(\omega)}{\gamma_p + \gamma_f - i\Omega} \right] \times$$

$$\times \left(1 - \frac{iR_s(\gamma_e - \gamma_n + i\delta\omega_{df})^2}{4(\gamma_s + \gamma_f - i(\delta + \Omega))(\gamma_p + \gamma_f - i\Omega)}\right) \quad \text{(B.59)}$$

There is a source of field inside the power recycling mode corresponding to each of the sources in the signal recycling mode, that have the same order of amplitude. Thus we could estimate the corrections to the field from each of the sources, caused by the leaks from the power recycling mode:

1) The signal, caused by the injections of the ground-state oscillations through the SRM $\hat{z}(\omega)$ is stronger than signal from the ground-state injections through the PRM by factor of:

$$\left| \frac{(\gamma_e - \gamma_n + i\delta\omega_{df})\sqrt{\frac{\gamma_p}{\gamma_s}}}{\gamma_p + \gamma_f - i\Omega} \right| \sim 10^{-2}, \quad \text{(B.60)}$$

2) Both signals, caused by the SRC mode $\hat{q}_2(\omega)$ of ground state injections with respect to the PRC mode $\hat{q}_1(\omega)$, and by the differential mirror motion $X(\Omega)$ with respect to the common mirror motion $X_{src}(\Omega)$, are stronger by factor of:

$$\left| \frac{(\gamma_e - \gamma_n + i\delta\omega_{df})}{\gamma_p + \gamma_f - i\Omega} \right| \sim 0.2. \quad \text{(B.61)}$$

3) The additional correction, caused by the double leaks of the field from the signal recycling mode to the power recycling mode and back again:

$$\left| \frac{(\gamma_e - \gamma_n + i\delta\omega_{df})^2}{(\gamma_p + \gamma_f - i\Omega)(\gamma_s + \gamma_f - i(\delta + \Omega))} \right| \sim 10^{-3}. \quad \text{(B.62)}$$

All these three influence of leaking gives the corrections in factor of the order of less than 4% in power, and therefore are considered negligible.

The boundary for the spectrum width of signals in the time-domain models

Even though the fields inside the signal recycling cavity are considered in the time-domain to include the response on the SRM motion, we cannot ignore their wave properties and frequency band of spectrum. Since the detector is designed to operate in dark-port, separating fields into the signal recycling and the power recycling mode, the spectral components should be within a certain limit, to remain within its mode.

The interference on the beamsplitter for a frequency component ω and corresponding to it wave vector k of the signal reads, taking into account the strict dark-fringe condition with dark-fringe offset for the carrier frequency (B.23) (see notations in table 2.1):

$$e^{2ikL_{\mathrm{e}}} + e^{2ikL_{\mathrm{n}}} = e^{2ikL_{\mathrm{e}}}(1 - e^{ik_{\mathrm{p}}\Delta L} e^{i\Omega\pi/\omega_{\mathrm{P}}} e^{i\Omega\delta L_{\mathrm{df}}/c}). \tag{C.1}$$

The factor in brackets is responsible for the interference. The dark port condition is valid only for those frequencies, for which the correction to the dark-fringe offset in these brackets is negligible. The conditions for the Ω for this is the following:

$$(\Omega \ll \omega_p) \cap \left(\Omega \ll \frac{c}{\Delta L}\right). \tag{C.2}$$

The second condition here is stronger. Since the arm length difference is of the order of 10 cm, the Dark Port condition (B.23) is valid for all the fields in the signal recycling cavity if:

$$\Omega \ll 10^9 \mathrm{rad/s}, \tag{C.3}$$

which is very relaxed, since the signal frequency of interest is of the order of 10^5 Hz.

Accumulated phase shifts during the propagation inside the
detector

D.1. Straight arms

Each term in the expression for the impulse response function (3.31) has an exponent, describing phase shift of the light during its round-trips inside the detector since the moment of its injection and until it goes out. The phase shifts in all the field terms consist of the same elementary items, describing the phase shift, caused by the SRM-displacement at the instance of reflection

$$\Delta\phi_k(t) = 2\omega_{\mathrm{p}} \frac{x(t - 2k\tau)}{c}, k \in N. \tag{D.1}$$

This item describes, which phase shift the light got during the reflection from the SRM occurred k roundtrips ago.

For the every impulse, injected inside the detector the phase shifts of the light components are summed one after the other, in a consequent train of the individual phase shifts, while the light makes round trips inside the detector. Therefore, the phase shift train in the past, the overall phase shift, which the impulse gets during its propagation inside the detector may be described using a following function:

$$\phi_n(t) = \sum_{k=1}^{n} \Delta\phi_k(t), \tag{D.2}$$

describing, how big phase shift gets the light, gone out of the detector at the instance t, injected $n + 1$ roundtrips before into the SRC, and made the first reflection from the SRM n roundtrips before its leaking out.

Similar to (D.1) we introduce the phase shift, that the light will get during a single reflection from the SRM occurring after k roundtrips inside the detector:

$$\Delta\phi_k^+(t) = 2\omega_{\mathrm{p}}\frac{x(t + 2k\tau)}{c}, k \in N. \tag{D.3}$$

Using this we may introduce a similar to $\phi_n(t)$ a phase shift train in the future:

$$\phi_n^+(t) = \sum_{k=1}^{n} \Delta\phi_k^+(t), \tag{D.4}$$

describing, the overall phase shift, that the light, injected into the detector at the instance t, will get within the next n round-trips inside the detector.

The single phase shifts from reflection in the past has the following property:

$$\Delta\phi_k(t - 2m\tau) = \Delta\phi_{k+m}(t), m \in N. \tag{D.5}$$

and therefore the phase shift train in the past has the consequent property:

$$\phi_n(t - 2m\tau) = \phi_{n+m}(t) - \phi_m(t), m \in N. \tag{D.6}$$

Analogous properties has the phase shift from the reflection in the future:

$$\Delta\phi_k^+(t + 2m\tau) = \Delta\phi_{k+m}^+(t), m \in N \tag{D.7}$$

and the future phase shift train:

$$\phi_n^+(t + 2m\tau) = \phi_{n+m}^+(t) - \phi_m^+(t), m \in N. \tag{D.8}$$

The phase shift from the reflection in the past is the future event for a time instances before the reflection. Via this phase shifts from the single reflections in the future and in the past are bound:

$$\Delta\phi_k(t) = \Delta\phi_{n-k}^+(t - 2n\tau), (n, k \in Z; n \geq k). \tag{D.9}$$

The same consideration binds the future and the past phase shift trains:

$$\phi_n(t) = \phi_n^+(t - 2(n + 1)\tau). \tag{D.10}$$

Both $\phi_n(t)$ and $\phi_n^+(t)$ has the same physical meaning, namely a phase shift after n round trips in the row. The total phase shift, accumulated from the single phase shifts, caused by the reflections from the SRM, contains the information about these single phase shifts. And vice a versa from these accumulated phase shifts one can restore the information about single phase shifts. Therefore, it is convenient to introduce the new accumulated phase shift, that light, injected in the beginning of measurements t_0, could get during the detection, without leaving the detector:

$$\Phi_n = \phi_n^+(t_0), \tag{D.11a}$$

$$\Phi_0 = 0, \tag{D.11b}$$

$$\Phi_k = 0, k \in Z, k < 0. \tag{D.11c}$$

By setting the values of the accumulated phase with negative indices to zero we assume that detector was tuned before the beginning of the measurements.

The accumulated phase shift has also the physical meaning described in subsection (4.3.1). This accumulated phase shift contains the information about all the phase shifts, that get the echoes of the injected impulse after going out of the detector, all the past phase shift trains:

$$\phi_n(t_1) = \phi_n(t_0 + 2N\tau) = \phi_n^+(t_0 + 2(N-n-1)\tau) = \Phi_{N-1} - \Phi_{N-n-1}. \quad \text{(D.12)}$$

The future phase shift trains could also be expressed via these accumulated phase shift:

$$\phi_n^+(t_1) = \phi_n^+(t_0 + 2N\tau) = \phi_{N+n}^+(t_0) - \phi_N^+(t_0) = \Phi_{n+N} - \Phi_N \quad \text{(D.13)}$$

For the convenience of the simulation in Matlab we could begin indices in $D.11a$ from one. Then the following change of indices takes would take place: $\Phi_{n'-1} = \Phi_n$

D.2. Delay line in arms

Assume the detector with the delayed line in arms. In this configuration the impulse reaches the signal recycling mirror, and hence gets the phase shift, only every N_{RT} round trips, where N_{RT} is the number of round trips inside the delay line. Keeping this in mind, we redefine the single phase shifts:

$$\Delta\phi_k(t) = 2\omega_{\mathrm{p}}\frac{x(t - 2kN_{\mathrm{rt}}\tau)}{c}, \quad \text{(D.14)}$$

$$\Delta\phi_k^+(t) = 2\omega_{\mathrm{p}}\frac{x(t + 2kN_{\mathrm{rt}}\tau)}{c}. \quad \text{(D.15)}$$

The phase shift trains (D.2-D.12) read therefore for the case of delayed line:

$$\phi_n(t) = \sum_{k=1}^{n} \Delta\phi_k(t), \quad \text{(D.16)}$$

$$\phi_n^+(t) = \sum_{k=1}^{n} \Delta\phi_k^+(t). \quad \text{(D.17)}$$

The properties of the phase shifts for delay lines are:

$$\Delta\phi_k(t - 2mN_{\mathrm{rt}}\tau) = \Delta\phi_{k+m}(t), m \in N, \quad \text{(D.18)}$$

$$\phi_n(t - 2mN_{\mathrm{rt}}\tau) = \phi_{n+m}(t) - \phi_m(t), m \in N, \quad \text{(D.19)}$$

$$\Delta\phi_k^+(t + 2mN_{\mathrm{rt}}\tau) = \Delta\phi_{k+m}^+(t), m \in N \quad \text{(D.20)}$$

and

$$\phi_n^+(t + 2mN_{\mathrm{rt}}\tau) = \phi_{n+m}^+(t) - \phi_m^+(t), m \in N. \quad \text{(D.21)}$$

The boundary conditions are following:

$$\Delta\phi_k(t) = \Delta\phi_{n-k}^+(t - 2nN_{\mathrm{rt}}\tau), (n, k \in Z; n \geq k). \tag{D.22}$$

$$\phi_n(t) = \phi_n^+(t - 2(n+1)N_{\mathrm{rt}}\tau). \tag{D.23}$$

We can correspondingly introduce the following accumulated phase shift:

$$\Phi_{n,m} = \phi_n^+(t_0 + 2m\tau), \tag{D.24a}$$
$$\Phi_{0,m} = 0; \tag{D.24b}$$

And express in terms of it the phase shift trains:

$$\phi_n^+(t_1) = \Phi_{n+N,m} - \Phi_{N,m}, \tag{D.25}$$

$$\phi_n(t_1) = \Phi_{N-1,m} - \Phi_{N-n-1,m}. \tag{D.26}$$

For convenience of simulations in Matlab we could also change the indices $\Phi_{n',m'} = \Phi{n-1, m-1}$.

Bibliography

[1] A. Einstein, "Approximate integration fo the field equations of gravitation," *The Collected Papers of Albert Einstein*, vol. 6, 1997.

[2] E. Flanagan and S. Hughes, "The basics of gravitational wave theory," *New Journal of Physics*, vol. 7, p. 204, 2005. http://iopscience.iop.org/1367-2630/7/1/204/

[3] A. Buonnano, "Gravitational waves", *Proceedings of Les Houches Summer School, Particle Physics and Cosmolgy: The Fabric of Spacetime*　Les Houches, France, 31 July - 25 August 2008.

[4] R. Blandford and K. Thorne, *Ph 136: Applications of Classical Physics*. California Insitute of Technology, Pasadena, 2003., 2006-2007. http://www.pma.caltech.edu/Courses/ph136/yr2006/0426.1.K.pdf

[5] K. Thorne, "Gravitational waves," *arXiv:gr-qc/9506086*, 1995. http://arxiv.org/abs/gr-qc/9506086

[6] K. D. Kokkotas, "Gravitational wave astronomy," *arXiv:0809.1602*, 2008.

[7] L. Ju, D. Blair, and C. Zhao, "Detection of gravitational waves," *Reports on Progress in Physics*, vol. 63, p. 1317, 2000. http://iopscience.iop.org/0034-4885/63/9/201/pdf/0034-4885_63_9_201.pdf

[8] M. Maggiore, "Gravitational wave experiments and early universe cosmology," *Phys.Rept.*, vol. 331, pp. 283–367, 2000. http://inspirehep.net/record/506400?ln=en

[9] M. Maggiore, "Stochastic backgrounds of gravitational waves," *Lectures given at the "Gravitational Waves: A Challenge to Theoretical Astrophysics"*, 2000.

[10] B. Allen and J. Romano, "Detecting a stochastic background of gravitational radiation: Signal processing strategies and sensitivities," *Physical Review D*, vol. 59, 1999.

[11] R. Brustein, M. Gasperini, M. Giovannini, and G. Veneziano, "Relic gravitational waves from string cosmology," *Physics Letters B*, vol. 361, no. 1-4, pp. 45 – 51, 1995. doi:http://dx.doi.org/10.1016/0370-2693(95)01128-D. http://www.sciencedirect.com/science/article/pii/037026939501128D

[12] A. Buonanno, M. Maggiore, and C. Ungarelli, "Spectrum of relic gravitational waves in string cosmology," *Phys. Rev. D*, vol. 55, pp. 3330–3336, Mar 1997. doi:10.1103/PhysRevD.55.3330. http://link.aps.org/doi/10.1103/PhysRevD.55.3330

[13] M. Gasperini and G. Veneziano, "String theory and pre-big bang cosmology," *arXiv:hep-th/0703055*, 2007.

[14] G. Bisnovatyi-Kogan and V. Rudenko, "Very high frequency gravitational wave background in the universe," *Classical and Quantum Gravity*, vol. 21, p. 3347, 2004. http://iopscience.iop.org/0264-9381/21/14/001

[15] R. O'Shaughnessy, V. Kalogera, and K. Belczynski, "Binary compact object coalescence rartes: the role of elliptical galaxies." *Astrophys. J.*, vol. 716, no. 1, 2010. http://m.iopscience.iop.org/0004-637X/716/1/615

[16] J. A. et al, "Predictions for the rates of compact binary coalescences observable by ground-base gravitational-wave detectors," *Classical and Quantum Gravity*, vol. 27, no. 17, 2010. http://iopscience.iop.org/0264-9381/27/17/173001/

[17] L. Santamaria, F. Ohme, P. Ajith, B. Brugmann, N. Dorband, M. Hannam, S. Husa, P. Mosta, D. Pollney, C. Reisswig, E. L. Robinson, and J. Seiler, "Matching post-newtonian and numerical relativity waveforms: Systematic errors and a new phenomenological model for nonprecessing black hole binaries," *Phys. Rev. D*, vol. 82, p. 064016, Sep 2010. doi:10.1103/PhysRevD.82.064016. http://link.aps.org/doi/10.1103/PhysRevD.82.064016

[18] P. Ajith, "Addressing the spin question in gravitational-wave searches: Waveform templates for inspiralling compact binaries with nonprecessing spins," *Phys. Rev. D*, vol. 84, p. 084037, Oct 2011. doi:10.1103/PhysRevD.84.084037. http://link.aps.org/doi/10.1103/PhysRevD.84.084037

[19] I. Kamaretsos, M. Hannam, S. Husa, and B. S. Sathyaprakash, "Black-hole hair loss: Learning about binary progenitors from ringdown signals," *Phys. Rev. D*, vol. 85, p. 024018, Jan 2012. doi:10.1103/PhysRevD.85.024018. http://link.aps.org/doi/10.1103/PhysRevD.85.024018

[20] I. Kamaretsos, M. Hannam, and B. S. Sathyaprakash, "Is black-hole ringdown a memory of its progenitor?" *Phys. Rev. Lett.*, vol. 109, p. 141102, Oct

166

2012. doi:10.1103/PhysRevLett.109.141102. http://link.aps.org/doi/10.1103/Ph ysRevLett.109.141102

[21] T. Damour, A. Nagar, and L. Villain, "Measurability of the tidal polarizability of neutron stars in late-inspiral gravitational-wave signals," *Phys. Rev. D*, vol. 85, p. 123007, Jun 2012. http://link.aps.org/doi/10.1103/PhysRevD.85.123007

[22] F. Pannarale, L. Rezzolla, F. Ohme, and J. S. Read, "Will black hole-neutron star binary inspirals tell us about the neutron star equation of state?" *Phys. Rev. D*, vol. 84, p. 104017, Nov 2011. doi:10.1103/PhysRevD.84.104017. http://link.aps.org/doi/10.1103/PhysRevD.84.104017

[23] B. F. Schutz, "Determining the hubble constant from gravitational wave observations," *Nature*, vol. 323, no. 310-311, 1986. http://www.nature.com/nat ure/journal/v323/n6086/abs/323310a0.html

[24] J. Weber, "Gravitational-wave-detector events," *Phys. Rev. Lett.*, vol. 20, pp. 1307–1308, Jun 1968. doi:10.1103/PhysRevLett.20.1307. http://link.aps.org/doi /10.1103/PhysRevLett.20.1307

[25] J. L. Levine, "Early gravity-wave detection experimentes, 1960-1975," *Physics in Perspective*, vol. 6, pp. 42–75, 2004.

[26] J. Taylor and J. Weisberg, "A new test of general relativity - gravitational radiation and the binary pulsar psr 1913+16," *Astrophysical Journal*, vol. 253, pp. 908–920, 1982.

[27] R. Hulse and J. Taylor, "Discovery of a pulsar in a binary system," *Astrophysical Journal*, vol. 195, pp. L51–L53, 1975.

[28] http://www.minigrail.nl/.

[29] http://www.auriga.lnl.infn.it/.

[30] https://www.advancedligo.mit.edu/.

[31] B. A. Abbot et al, "Ligo: the laser interferometer gravitational-wave observatory," *Reports on Progress in Physics*, vol. 72, no. 7, p. 076901, 2009. http://stacks.iop.org/0034-4885/72/i=7/a=076901

[32] http://www.geo600.org/.

[33] D. G. Blair, L. Ju, and C. Zhao, *Advanced Gravitational Wave Detectors*. Cambridge Univ PR, 2012.

[34] H. Grote, "The geo 600 status," *Class. Quantum Grav.*, vol. 27, no. 8, 2010. http://iopscience.iop.org/0264-9381/27/8/084003

[35] https://wwwcascina.virgo.infn.it/advirgo/.

[36] http://www.et-gw.eu/.

[37] B. Sathyaprakash et al, "Scientific objectives of einstein telescope," *Classical and Quantum Gravity*, vol. 29, no. 12, p. 124013, 2012. http://stacks.iop.org/0264-9381/29/i=12/a=124013

[38] https://www.elisascience.org/.

[39] P. Amaro-Seoane, S. Aoudia, S. Babak, P. Binetruy, E. Berti, A. Bohe, ChiaraCaprini, M. Colpi, N. J. Cornish, K. Danzmann, J.-F. Dufaux, J. Gair, OliverJennrich, P. Jetzer, A. Klein, R. N. Lang, A. Lobo, T. Littenberg, S. TMcWilliams, G. Nelemans, A. Petiteau, E. K. Porter, B. F. Schutz, A. Sesana, RobinStebbins, T. Sumner, M. Vallisneri, S. Vitale, M. Volonteri, and H. Ward, "Low-frequency gravitational-wave science with elisa/ngo," *Classical and Quantum Gravity*, vol. 29, no. 12, p. 124016, 2012. http://stacks.iop.org/0264-9381/29/i=12/a=124016

[40] J. Hough, "Proposal for a joint german-british interferometric gravitational wave detector," *MPQ Report*, vol. 147, 1989.

[41] B. Willke et al, "Status of geo 600," *Classical and Quantum Gravity*, vol. 21, no. 5, p. S417, 2004. http://stacks.iop.org/0264-9381/21/i=5/a=006

[42] I. Zawischa, M. Brendel, K. Danzmann, C. Fallnich, M. Heurs, S. Nagano, V. Quetschke, H. Welling, and B. Willke, "The geo 600 laser system," *Classical and Quantum Gravity*, vol. 19, no. 7, p. 1775, 2002. http://stacks.iop.org/0264-9381/19/i=7/a=374

[43] B. J. Meers, "Recycling in laser-interferometric gravitational-wave detectors," *Phys. Rev. D*, vol. 38, pp. 2317–2326, Oct 1988. doi:10.1103/PhysRevD.38.2317. http://link.aps.org/doi/10.1103/PhysRevD.38.2317

[44] K. A. Strain and B. J. Meers, "Experimental demonstration of dual recycling for interferometric gravitational-wave detectors," *Phys. Rev. Lett.*, vol. 66, pp. 1391–1394, Mar 1991. doi:10.1103/PhysRevLett.66.1391. http://link.aps.org/doi/10.1103/PhysRevLett.66.1391

[45] Schnupp L., Presentation at European Collaboration Meeting on Interferometric Detection of Gravitational Waves   Sorrento, Italy, 1988.

[46] K. Somiya, Y. Chen, S. Kawamura, and N. Mio, "Frequency noise and intensity noise of next-generation gravitational-wave detectors with rf/dc readout schemes," *Phys. Rev. D*, vol. 73, p. 122005, Jun 2006. doi:10.1103/PhysRevD.73.122005. http://link.aps.org/doi/10.1103/PhysRevD.73.122005

[47] S. L. Danilishin and F. Y. Khalili, "Quantum measurement theory in gravitational-wave detectors," *Living Reviews in Relativity*, vol. 15, no. 5, 2012. doi:10.12942/lrr-2012-5. http://www.livingreviews.org/lrr-2012-5

[48] S. Hild, H. Grote, J. Degallaix, S. Chelkowski, K. Danzmann, A. Freise, M. Hewitson, J. Hough, H. Luck, M. Prijatelj, K. Strain, J. R. Smith, and B. Willke, "Dc-readout of a signal-recycled gravitational wave detector," *Classical and Quantum Gravity*, vol. 26, no. 5, p. 055012, 2009. http://stacks.iop.org/0264-9381/26/i=5/a=055012

[49] J. Degallaix, H. Grote, M. Prijatelj, M. Hewitson, S. Hild, C. Affeldt, A. Freise, J. Leong, H. Luck, K. A. Strain, HWittel, B. Willke, and K. Danzmann, "Commissioning of the tuned dc readout at geo 600," *Journal of Physics: Conference Series*, vol. 228, no. 1, p. 012013, 2010. http://stacks.iop.org/1742-6596/228/i=1/a=012013

[50] T. Fricke, N. Smith-Lefebvre, R. Abbott, R. Adhikari, K. Dooley, M. Evans, P. Fritschel, V. Frolov, K. Kawabe, J. Kissel, B. Slagmolen, and S. Waldman, "DC Readout Experiment in Enhanced LIGO," *Classical and Quantum Gravity*, vol. 29, no. 6, pp. 065 005+, feb 2012. doi:10.1088/0264-9381/29/6/065005. http://arxiv.org/abs/1110.2815

[51] A. Krolak, J. A. Lobo, and B. J. Meers, "Optimization of laser interferometers for the detection of gravitational waves from coalescing binaries," *Phys. Rev. D*, vol. 43, pp. 2470–2483, Apr 1991. doi:10.1103/PhysRevD.43.2470. http://link.aps.org/doi/10.1103/PhysRevD.43.2470

[52] B. J. Meers, A. Krolak, and J. A. Lobo, "Dynamically tuned interferometers for the observation of gravitational waves from coalescing compact binaries," *Physical Review D*, vol. 43, no. 6, 1993. http://prd.aps.org/abstract/PRD/v47/i6/p2184_1

[53] K. Cannon, R. Cariou, A. Chapman, M. Crispin-Ortuzar, N. Fotopoulos, MelissaFrei, C. Hanna, E. Kara, D. Keppel, L. Liao, S. Privitera, A. Searle, L. Singer, and AlanWeinstein, "Toward early-warning detection of gravitational waves from compact binary coalescence," *The Astrophysical Journal*, vol. 748, no. 2, p. 136, 2012. http://stacks.iop.org/0004-637X/748/i=2/a=136

[54] H. J. Kimble, Y. Levin, A. B. Matsko, K. S. Thorne, and S. P. Vyatchanin, "Conversion of conventional gravitational-wave interferometers into quantum nondemolition interferometers by modifying their input and/or output optics," *Phys. Rev. D*, vol. 65, p. 022002, Dec 2001. doi:10.1103/PhysRevD.65.022002. http://link.aps.org/doi/10.1103/PhysRevD.65.022002

[55] Y. Levin, "Internal thermal noise in the ligo test masses: A direct approach," *Phys. Rev. D*, vol. 57, pp. 659–663, Jan 1998. doi:10.1103/PhysRevD.57.659. http://link.aps.org/doi/10.1103/PhysRevD.57.659

[56] Y. Levin, "Fluctuation-dissipation theorem for thermo-refractive noise," *Phys. Lett. A*, vol. 372, pp. 1941–1944, 2008. http://www.sciencedirect.com/science/article/pii/S0375960107015964

[57] G. M. Harry, A. M. Gretarsson, P. R. Saulson, S. E. Kittelberger, S. D. Penn, W. J. Startin, S. Rowan, M. M. Fejer, D. R. M. Crooks, G. Cagnoli, and N. Nakagawa, "Thermal noise in interferometric gravitational wave detectors due to dielectric optical coatings," *Class. Quatnum Grav.*, vol. 19, no. 5, pp. 897–917, 2002. http://iopscience.iop.org/0264-9381/19/5/305

[58] Y. T. Liu and K. S. Thorne, "Thermoelastic noise and homogeneous thermal noise in finite sized gravitational-wave test masses," *Phys. Rev. D*, vol. 62, p. 122002, Nov 2000. doi:10.1103/PhysRevD.62.122002. http://link.aps.org/doi/10.1103/PhysRevD.62.122002

[59] A. Buonanno and Y. Chen, "Scaling law in signal recycled laser-interferometer gravitational-wave detectors," *Phys. Rev. D*, vol. 67, p. 062002, Mar 2003. doi:10.1103/PhysRevD.67.062002. http://link.aps.org/doi/10.1103/PhysRevD.67.062002

[60] C. Fabry and A. Perot, "Theorie et applications d'une nouvelle methode de spectroscopie interferentielle," *Annales de Chimie et de Physique*, vol. 16, pp. 115–144, 1899.

[61] A. Perot and C. Fabry, "On the application of interference phenomena to the solution of various problems of spectroscopy and metrology," *The Astrophysical Journal*, vol. 9, pp. 87–115, 1899.

[62] C. Fabry and A. Perot, "Measures of absolute wave-lengths in the solar spectrum and in the spectrum of iron," *The Astrophysical Journal*, vol. 15, pp. 73–96, 1902.

[63] T. Hicks, B. May, and N. Reay, "MgI emission in the night sky spectrum," *Nature*, vol. 240, pp. 401–402, 1972. http://www.nature.com/nature/journal/v240/n5381/abs/240401a0.html

[64] G. Hernandez, *Fabry-Perot Interferometers*. Cabridge University, 1986.

[65] J. Vaughan, *The Fabry-Perot Interferometers*. Bristol, England: Adam Hilger, 1986.

[66] R. Drever, G. Ford, J. Hough, I. Kerr, A. Munley, J. Pugh, N. Robertson, and H. Ward, "A gravity-wave detector using optical cavity sensing," in *Proceedings of the Ninth International Conference on General Relativity and Gravitation, Jena, 14-19 July*, E. Schmutzer, Ed. Cambridge University Press, 1989, pp. 265–267.

[67] R. Drever, J. Hall, F. Kowalski, J. Hough, G. Ford, A. Munley, and H. Ward, "Laser phase and frequency stabilization using an optical resonator," *Applied Physics B*, vol. 31, no. 2, pp. 97–105, 1983. doi:10.1007/BF00702605. http://dx.doi.org/10.1007/BF00702605

[68] A. A. Michelson and E. W. Morley, "On the relative motion of the earth and the luminiferous ether," *American Journal of Science*, vol. 34, no. 203, 1887.

[69] F. Khalili, "Nontrivial optical spring in non-symmetric interferometers: beyond the scaling law theorem," december 2012.

[70] M. Rakhmanov, "Dynamics of laser interferometric gravitational wave detectors," Ph.D. dissertation, California Insitute of Technology Pasadena, California, 2000.

[71] C. M. Caves, "Quantum-mechanical noise in an interferometer," *Phys. Rev. D*, vol. 23, pp. 1693–1708, Apr 1981. doi:10.1103/PhysRevD.23.1693. http://link.aps.org/doi/10.1103/PhysRevD.23.1693

[72] M. J. Lawrence, B. Willke, M. E. Husman, E. K. Gustafson, and R. L. Byer, "Dynamic response of a fabry-perot interferometer." *J. Opt. Soc. Am. B*, vol. 16, no. 4, 1999. http://dx.doi.org/10.1364/JOSAB.16.000523

[73] Walls D. F. and Milburn G. J., *Quantum Optics.* Springer, Berlin, 2008.

[74] L. Mandel and E. Wolf, *Optical coherence and quantum optics.* Cambridge University Press, Cambridge; New York, 1995.

[75] M. Scully and M. Zubairy, *Unknown Title.* Cambridge University Press, Cambridge; New York, 1997.

[76] A. Freise, "Finesse." http://www.gwoptics.org/finesse/

[77] B. R. Levin, *Theoretical Basis of Statistical Radio Techniques [in Russian].* Radio i svyaz, 1989.

[78] E. W. Kamen and J. K. Su, *Introduction to Optimal Estimation.* Springer, 1999.

[79] J. Neyman and E. S. Pearson, "On the problem of the most efficient tests of statistical hypotheses," *Phil. Trans. R. Soc. A*, vol. 231, no. 694-706, pp. 289–337, 1933. http://rsta.royalsocietypublishing.org/content/231/694-706/289.full.pdf+html

[80] B. J. Meers, A. Krolak, and J. A. Lobo, "Estimation of the parameters of the gravitational-wave signal of a coalescing binary system." *Physical Review D*, vol. 48, no. 8, 1993. http://prd.aps.org/abstract/PRD/v48/i8/p3451_1

[81] D. G. Blair, L. Ju, and C. Zhao, *Advanced Gravitational Wave Detectors.* Cambridge Univ PR, 2012, ch. 8, pp. 155–167.

[82] Geo 600 noise budget, http://www.geo600.uni-hannover.de/geocurves/, 2006,

[83] H. Luck, Private communication.

[84] H. Vahlbruch, S. Chelkowski, B. Hage, A. Franzen, K. Danzmann, and R. Schnabel, "Demonstration of a squeezed-light-enhanced power- and signal-recycled michelson interferometer," *Phys. Rev. Lett.*, vol. 95, p. 211102, Nov 2005. doi:10.1103/PhysRevLett.95.211102. http://link.aps.org/doi/10.1103/PhysRevLett.95.211102

[85] J. Abadie et al, "A gravitational wave observatory operating beyond the quantum shot-noise limit," *Nature Physics*, vol. 7, p. 962âĂŞ965, 2011. http://www.nature.com/nphys/journal/v7/n12/full/nphys2083.html

Publications

P1 D. Simakov, **Time-domain analysis of a dynamically tuned signal recycled interferometer for the detection of chirp gravitational waves from coalescing compact binaries**, submitted to *Physical Review D*

Curriculum Vitae

Personal Details

Name: Dmitry Simakov
Nationality: Russian Federation
Date of birth: 15th of November 1986
Place of birth: Brezhnev (USSR)
Family status: Single

University Education

03/2009 - present	Doctoral studies in Physics, Albert Einstein Institute (AEI), Hannover.
09/2003 - 01/2009	Physics, Fundamental Radiophysics and Physical Electronics, Moscow State University. *Graduated with diploma.*

Education

09/2000 - 06/2003	Lyceum #78 Named After Pushkin, Naberezhnye Tschelny. *Graduated with certificate of (complete) secondary general education.*
09/1993 - 06/2000	School 49, Naberezhnye Tschelny.

Working experience

10/2011 - 01/2013	Supervisor of the beginners practicum, Leibniz University, Hanover.